



The University of
Nottingham

UNITED KINGDOM • CHINA • MALAYSIA

**Manufacture and Structural
Characterisation of Novel Resorbable
Phosphate-Glass Microspheres for Bone
Repair Applications**

By

Uresha Patel
(B.Med.Sc, MSc)

Thesis submitted to the University of Nottingham for the
degree of
Doctor of Philosophy

June 2017

*I dedicate this thesis to my life teacher,
my late grandad*

G.S. Patel

Contents

ABSTRACT	v
ACKNOWLEDGMENTS	vii
LIST OF PUBLICATIONS	viii
ABBREVIATIONS AND NOMENCLATURE	x
COMPOUNDS AND ELEMENTS	xi
LIST OF FIGURES	xii
LIST OF TABLES	xviii
CHAPTER 1: INTRODUCTION AND REVIEW OF LITERATURE	1
1.1 Primary research motivation	1
1.2 Introduction	2
1.3 Fundamentals of bone and bone biology	3
1.3.1 Remodelling of bone.....	4
1.4 Osteoporosis	6
1.5 Phosphate glasses for therapeutic applications	10
1.5.1 Phosphate glass structure.....	12
1.5.2 Strontium containing PBGs.....	17
1.5.3 Phosphate invert glasses	20
1.6 Manufacture of microspheres	22
1.6.1 Borate based glass microspheres	23
1.6.2 Silicate based glass microspheres.....	26
1.6.3 Phosphate based glass microspheres.....	29
1.6.4 Porous glass manufacture	31
1.7 Summary	33
1.8 Aims and objectives	34
1.9 Thesis outline	35
CHAPTER 2: MATERIALS AND METHODOLOGY	36
2.1 Introduction	36
2.2 Glass manufacture and characterisation	36
2.2.1 Glass fabrication	36
2.2.2 Powder X-ray diffraction.....	38
2.2.3 Scanning electron microscopy/ Energy dispersive X-ray spectroscopy (SEM/ EDX).....	38
2.2.4 Density measurements.....	39

2.2.5	Thermal analysis via Differential scanning calorimetry	39
2.2.6	Fourier transform infrared spectroscopy	39
2.2.7	Solid state NMR	40
2.2.7.1	³¹ P NMR	40
2.2.7.2	²³ Na NMR	40
2.2.8	Dissolution studies.....	40
2.2.9	Ion release studies	41
2.2.9.1	Cation release	41
2.2.10	Anion release	42
2.3	Cytocompatibility studies	42
2.3.1	Cell culture	42
2.3.2	Cell metabolic activity.....	43
2.3.3	DNA content	43
2.3.4	Alkaline phosphatase activity	44
2.3.5	Cell morphology.....	44
2.3.6	Statistical analysis	45
2.4	Osteoclast culture	46
2.4.1	Cell culture	46
2.4.2	Tartrate-resistant acid phosphatase staining	47
2.5	Neutron Diffraction Theory and Application	47
2.5.1	An Introduction.....	47
2.5.2	Neutron source at ISIS	49
2.5.3	General materials diffractometer (GEM).....	49
2.5.4	Outline of Theory and Experimental Application	51
2.5.4.1	Differential cross section	51
2.5.4.2	Experimental Data Correction	52
2.5.4.3	Distinct and self-scattering	53
2.5.4.4	Total correlation function.....	55
2.6	Microsphere manufacture and characterisation	58
2.6.1	Flame spheroidisation	58
2.6.2	Porous microsphere manufacture.....	59
2.6.3	Post processing	59
2.6.4	Particle size analysis.....	60
2.6.5	Surface area via BET.....	60

2.6.6	Mercury porosimetry.....	60
2.6.7	Micro CT.....	61
2.6.8	PBG microsphere degradation and ion release	63
CHAPTER 3: PHYSICO-CHEMICAL PROPERTIES AND CYTOCOMPATABILITY OF Sr SUBSTITUTED PBG		
	PBG	64
3.1	Introduction	64
3.2	Powder XRD.....	64
3.3	EDX.....	65
3.4	Density.....	66
3.5	Thermal Analysis	67
3.6	Dissolution and ion release study	70
3.7	Cytocompatibility study.....	76
3.7.1	Cell metabolic activity.....	76
3.7.2	DNA content	78
3.7.3	Alkaline phosphatase activity	79
3.7.4	Cell morphology.....	81
3.8	Osteoclast feasibility study.....	84
3.9	Summary	88
CHAPTER 4: STRUCTURAL STUDY OF Sr SUBSTITUTED PBG		
	4.1 Introduction	89
4.2	Solid state NMR.....	90
4.2.1	³¹ P MAS NMR	90
4.2.2	²³ Na MAS NMR.....	92
4.3	FTIR	92
4.4	Neutron diffraction	94
4.4.1	Neutron diffraction experimental set-up	95
4.4.2	Diffraction patterns	95
4.4.3	Real-space correlation functions	98
4.4.5	Binary metaphosphate modifier environment.....	101
4.4.6	Multicomponent glass deconvolution.....	106
4.5	Summary	110
CHAPTER 5: TITANIUM INVERT PHOSPHATE GLASSES		
	5.1 Introduction	112
5.2	Powder XRD.....	113

5.3 EDX	114
5.4 Density	115
5.5 Thermal analysis	116
5.6 ³¹P MAS NMR spectroscopy	119
5.7 Dissolution studies	124
5.8 Ion release	126
5.8.1 Cation release	126
5.8.2 Anion release	129
5.9 Summary	131
6.1 Introduction	133
6.2 Glass powder production	133
6.3 Bulk microsphere manufacture	135
6.3.1 Gas flow rate.....	136
6.3.2 Collection distance determination	140
6.4 Novel porous microsphere manufacture	142
6.4.1 Altering porogen size	142
6.4.2 Altering porogen quantity	143
6.4.3 Two-step manufacture	144
6.4.4 Porogen binding methods	145
6.4.5 Oxy-acetylene assisted spheroidisation	147
6.5 Microsphere characterisation	153
6.5.1 Post processing porous microspheres	158
6.5.2 Optimised manufacturing procedure	164
6.5.3 Hypothesis on porosity formation within glass microspheres	165
6.5.4 Particle size analysis	168
6.5.5 Density, surface area and pore size	170
6.5.6 Micro CT analysis	175
6.6 Degradation study of PBG microspheres	181
6.7 Summary	194
7.1 Conclusions	196
7.2 Future work	201
7.3 A collection of images	203
REFERENCES	208

ABSTRACT

The principal focus for the materials developed in this thesis was for orthobiologics applications, particularly tailoring phosphate based glasses for the treatment of bone related disorders such as osteoporosis. The degradation and release of therapeutic ions from resorbable phosphate based glasses in aqueous media can potentially be tuned through compositional control.

Optimisation of glass formulations was carried out by investigating the physico-chemical and structural characteristics of glasses in two systems: (i) $40\text{P}_2\text{O}_5 \cdot (16-x)\text{CaO} \cdot 20\text{Na}_2\text{O} \cdot 24\text{MgO} \cdot x\text{SrO}$, where x is 0, 4, 8, 12 and 16 mol% i.e. multicomponent glasses and (ii) $(40-x)\text{P}_2\text{O}_5 \cdot 16\text{CaO} \cdot 20\text{Na}_2\text{O} \cdot 24\text{MgO} \cdot x\text{TiO}_2$, where $x = 3, 5, 7, 10$ and 12 . Furthermore, this project largely focused on the development and manufacture of phosphate based glasses into both non-porous and porous microsphere forms in the 63-125 μm size range using a novel, scalable, inexpensive production process.

The physico-chemical properties of glasses in system (i) assessed the thermal properties, dissolution rates and ion release profiles. A decrease in degradation rate was shown with initial addition of 4 mol% SrO, but further addition of SrO showed no significant change. The ion release profiles complemented this trend. The subtle changes in structure and dissolution rates observed for substitution of Ca with Sr were attributed to their similarities in terms of ionic size and charge. Cytocompatibility studies of SrO/CaO substitution revealed no cytotoxic effects when culturing osteoblast-like cells (MG63) onto glass discs. Cell metabolic activity appeared to be greatest for higher Sr containing (Sr12 and Sr16) glasses at later time points. However, no significant difference between glass compositions and DNA and ALP activity was observed.

Neutron diffraction, ^{23}Na and ^{31}P NMR and FTIR spectroscopy studies investigated the structural effects of substituting CaO with SrO within the glass system (i). ^{31}P solid-state NMR results showed similar amounts of Q^1 and Q^2 units for all of the multicomponent glasses investigated. The M-O coordinations

(M= Mg, Ca, Sr, Na) were determined for binary alkali and alkaline earth metaphosphates using neutron diffraction and broad asymmetric distributions of bond length were observed. Neutron diffraction results for the multicomponent glasses were consistent with a structural model in which the coordination of Ca, Sr and Na was the same as in the binary metaphosphate glass, whereas a definite shift to longer distances (r (Å)) of Mg-O bonds was observed.

Glass system (ii) manufactured invert phosphate glasses with a P_2O_5 content as low as 28mol%. Increasing Ti content increased functional properties such as thermal parameters and density, which were attributed to greater cross linking of phosphate units by Ti ions. The dissolution and ion release profiles of glasses in system (ii) were significantly reduced in comparison to those in glass system (i). However, the release of pyrophosphate units as degradation by products was achieved. ^{31}P MAS NMR studies suggested Ti ions behaved as a network former at lower concentrations of 3 mol%, and switched to behaving as network modifiers with addition of 5 mol% and above of TiO_2 .

This study also showed successful manufacture of both non-porous and highly porous resorbable phosphate glass microspheres with porosity levels of up to 71%, with a surface area of 0.3443 m^2/g and high levels of interconnectivity. Furthermore, the dissolution behaviour of these porous microspheres have shown evidence of the formation of hollow, shell-like precipitation layers.

This study demonstrated successful development of phosphate based glass compositions for use in orthopaedic related applications and developed a novel manufacturing process resulting in highly porous microspheres, via a single stage manufacturing process (for the first time), where the spherical morphology lends itself to easy delivery options via a minimally invasive route. Furthermore, the porous microspheres can potentially be combined with other biologics, such as stem cells and drugs for example, to provide a combinatorial effect to aid in the repair and regeneration of bone tissue

ACKNOWLEDGMENTS

My most sincere gratitude is expressed to my supervisors without whom this work would not have been possible. I am indebted to; Dr Ifty Ahmed for his continual support and guidance both academically and for the endless opportunities and encouragement provided during entrepreneurial activities. Dr Emma Barney and Dr Alex Hannon for their endless patience and never giving up on me during challenging characterisation and for their support throughout, and Dr Andrew Kennedy for his continual guidance and keeping me on track. Thank you.

Thank you to my friends and colleagues in the Biocomposites and Advanced Materials Research Group for the constant support and endless discussions; Fernando Barrera Betanzos, Dr Zakir Hossain, Magdalena Patel, Dr Nusrat Sharmin, Dr Chenkai Zhu, Dr Madhavie Perera, Menghao Chen, Sumaya Kabir, Caitriona McCarron, Ana Braz De Sousa, Towhid Islam, Harriet Parnell, Dr Gabriel Choong, Dr Andrew Parsons, Dr Reda Felfel, Michael Ward and Bryan Stuart are only to name a few. Thank you also to all the technical staff in Wolfson for their assistance.

I would like to extend this gratitude to the Science and Technology Facilities Council for funding this work.

A very special thank you to Arkish Patel for always being my rock and for the unconditional love, patience and understanding. I am grateful for your positivity and limitless encouragement.

I would like to express my deepest gratitude to my entire family, particularly Suril, Dipta and Kiran, for always believing in me and being my foundation and strength in life. This is for you also.

LIST OF PUBLICATIONS

Journal articles

1. K.M.Z. Hossain, **U Patel**, I Ahmed, *Development of microspheres for biomedical applications: a review*. Prog Biomater. 2015; 4:1-19.
2. **U. Patel**, R.M. Moss, K.M.Z Hossain, A.R. Kennedy, E.R. Barney, I. Ahmed, and A.C. Hannon, *Structural and physico-chemical analysis of calcium/strontium substituted, near-invert phosphate based glasses for biomedical applications*, Acta Biomater. 2017 (in press).

Conferences

1. **U. Patel**, A.R. Kennedy, A.C. Hannon, E.R. Barney, and I. Ahmed, **Poster title: Strontium phosphate based glasses for orthopaedic applications* UK society for biomaterials 14th annual conference and postgraduate day, 25th and 26th June 2015 Ulster, Belfast.
2. **U. Patel**, A.R. Kennedy, A.C. Hannon, E.R. Barney and I. Ahmed, **oral presentation title: Strontium enriched phosphate based glass microspheres for orthopaedic applications*, Society of Glass Technology - Glass Reflections, 7th to 9th September 2015, Cambridge, UK.
3. **U. Patel**, A.R. Kennedy, A.C. Hannon, E.R. Barney and I. Ahmed, **oral presentation title: Manufacture and Structural Characterisation of Phosphate Based Glass Microspheres*, ISIS Student Meeting 29-30 October 2015, Abingdon, UK.
4. **U. Patel**, E.R. Barney, A.R. Kennedy, A.C. Hannon, and I. Ahmed, **Poster title: Strontium phosphate based glasses for orthopaedic applications*, RSC Biomaterials Chemistry Meeting 7th – 8th January 2016, Birmingham, Uk.
5. **U. Patel**, K.M.Z Hossain, A.R. Kennedy, A.C. Hannon, E.R. Barney, and I. Ahmed, **Poster title: Calcium/strontium substituted phosphate based glasses for orthopaedic applications*. Front. Bioeng. Biotechnol. Conference Abstract: 10th World Biomaterials Congress, May 17th-22nd 2016, Montreal, Canada.

6. K.M.Z Hossain, **U. Patel**, and I. Ahmed, *Highly oriented PLA fibre reinforced tubular scaffold with shape recovery effect for cell guide applications*. Conference Abstract: 10th World Biomaterials Congress, May 17th-22nd 2016, Montreal, Canada.

7. I. Ahmed, **U. Patel**, K.M.Z Hossain, V. Sottile, D. Grant and B. Scammell, **Oral presentation title: Novel Microstructural Features in Resorbable Phosphate-Based Glass Microspheres*. United Kingdom Society of Biomaterials (UKSB). 15th Annual Conference. 30th June and 1st July 2016. University of Westminster, London.

8. **U. Patel**, K.M.Z Hossain, A.R. Kennedy, A.C. Hannon, E.R. Barney, and I. Ahmed, **Oral presentation title: Structural characterisation of calcium/strontium substituted phosphate based glasses*. Innovations in Biomedical Materials 2016. July 29 – 31st, Rosemeont Hyatt, Chicago, Illinois.

9. I. Ahmed, **U. Patel**, K.M.Z Hossain, V. Sottile, D. Grant and B. Scammell, *Oral presentation title: Novel Porous Resorbable Calcium Phosphate Microspheres for Biomedical Applications*. Innovations in Biomedical Materials 2016. July 29 – 31st, Rosemeont Hyatt, Chicago, Illinois.

10. I. Ahmed, **U. Patel**, K.M.Z Hossain, V. Sottile, D. Grant and B. Scammell *Novel microstructural features in phosphate glass microspheres for cell and biomaterial interactions*. Society of Glass Technology: Centenary Conference & 13th Symposium of the European Society of Glass Science and Technology. Glasses in Healthcare - Hench Memorial Symposium. 4-8th September 2016. University of Sheffield, UK.

11. **U. Patel**, E.R. Barney, A.C. Hannon and I. Ahmed, *Structural and physico-chemical analysis of calcium/ strontium substituted, near-invert phosphate based glasses for biomedical applications*, The 9th International Conference on Borate Glasses, Crystals and Melts and the 2nd International Conference on Phosphate Materials, 24th-28th July 2017, St. Anne's College, Oxford, UK.

ABBREVIATIONS AND NOMENCLATURE

3D	Three dimensional
ALP	Alkaline phosphatase
ANOVA	Analysis of variance
BET	Brunauer Emmet and Teller
BMD	Bone mineral density
BO	Bridging oxygen
<i>c.a.</i>	Circa
C.R.G	Controlled release glasses
CAII	Carbonic anhydrase II
DI	Deionised water
DMEM	Dulbecco's modified eagle media
DSC	Differential scanning calorimetry
EDX	Energy dispersive x-rays
FCS	Foetal calf serum
FGFR	Fibroblast growth factor receptors
FTIR	Fourier transform infrared
GEM	General materials diffractometer
HA	Hydroxyapatite
HBSS	Hanks balance salt solution
HMDS	Hexamthylsilazne
IUPAC	International union of pure and applied chemistry
MAS	Magic angle spinning
M-CSF	Macrophage colony stimulating factors
Me ₂ O	Alkaline earth modifier oxygen
MeO	Alkali earth modifier oxygen
Micro CT	Microcomputed tomography
MIP	Mercury intrusion porosimetry
NBO	Non-bridging oxygen
ND	Neutron diffraction
NHS	National health service
NMR	Nuclear magnetic resonance
OPG	Osteoprotegerin

PBG	Phosphate based glass
PBS	Phosphate buffer solution
PTFE	Polytetrafluoroethylene
PTH	Parathyroid hormone
RANK	Receptor activator of nuclear factor kappa-B
RANKL	Receptor activator of nuclear factor kappa-B ligand
SBF	Simulated body fluid
SEM	Scanning electron microscope
SERM	Selective estrogen receptor modulators
SSF	Simulate synovial fluid
T_c	Crystallisation temperature
TCP	Tissue culture plastic
TEOS	Tetraethoxysilane ethanol solution
T_g	Glass transition temperature
T_m	Melting temperature
TO	Terminal oxygen
T-O-F	Time of flight
TRAP	Tartrate resistant acid phosphatase
WHO	World health organisation
α MEM	Alpha minimum essential media

COMPOUNDS AND ELEMENTS

$(\text{SiO}_4)^{4-}$	Silicate	NaCO_3	Sodium carbonate
Au	Gold	NaH_2PO_4	Sodium dihydrogen phosphate
Ca	Calcium	Nb	Niobium
$\text{Ca}(\text{OH})_2$	Calcium hydroxide	P	Phosphorous
$\text{Ca}_{10}(\text{PO}_4)_6(\text{OH})_2$	Hydroxyapatite	P_2O_5	Phosphorous pentoxide
$\text{Ca}_3(\text{PO}_4)_2$	Calcium phosphate	PO_4^{3-}	Phosphate
CaCO_3	Calcium carbonate	Pt	Platinum
CaHPO_4	Calcium hydrogen phosphate	Rd	Rhodium
CaO	Calcium oxide	Sr	Strontium
Mg	Magnesium	SrCO_3	Strontium carbonate
$\text{MgHPO}_4 \cdot 3\text{H}_2\text{O}$	Magnesium hydrogen phosphate trihydrate	SrO	Strontium oxide
MgO	Magnesium oxide	Ti	Titanium
Na	Sodium	TiO_2	Titanium dioxide
Na_2O	Sodium oxide	V	Vanadium

LIST OF FIGURES

Figure 1.1: Illustration of the four main types of cells found residing in bony tissue.[15]	4
Figure 1.2: Illustration of RANK- RANK-L activation of osteoclasts adapted from N. Little et al. [17].....	6
Figure 1.3: Simplified schematic showing the glass transition behaviour.....	10
Figure 1.4: Schematic showing the four Q _n species which can be present in PBG's along with the classification of the groups corresponding to structure.....	13
Figure 1.5: Graphical illustration of MO mol% concentration on the relative theoretical Q ⁿ species in PBG.	16
Figure 1.6: (a) ³¹ P NMR spectra showing chemical shift to higher ppm with increasing Na ₂ O content in a 100-xP ₂ O ₅ ·xNa ₂ O glass system.[55] (b) adaption from Dohler et al.[53] showing ³¹ P NMR spectra and associated Q ⁿ species in a 50P ₂ O ₅ ·25CaO·25Na ₂ O glass.....	17
Figure 1.7: (a) Schematic model of PBG network structure showing entangled chain structures, (b) model of PBG invert structure showing no 3D network.[84].....	20
Figure 1.8: Schematic illustration adapted from Wang et al. [114] showing mechanism for production of hollow, porous HAP microspheres.....	24
Figure 1.9: SEM showing (a) 15CaO·10.63Li ₂ O·74.37B ₂ O ₃ (wt%) glass microsphere (b) hollow HA microsphere cross section formed by reacting glass microsphere in 0.02M K ₂ HPO ₄ @37°C, pH 9 for 48h showing the concentric bilayered structure (c) HA surface at high magnification.[107]	26
Figure 1.10: The effect of temperature on the solubility of various gasses in a soda-lime silica glass melt.[131]	32
Figure 2.1: The General materials diffractometer at ISIS [136] showing the large array of the detector banks and the sample tank position.	50
Figure 2.2: Time-of-flight spectra obtained for a) vanadium-niobium (VNb) showing near to no Bragg peaks and b) representative sample data is also shown. The scattering data for the rod allows the shape of the neutron flux to be removed from the scattering of the sample to give I(Q).	53
Figure 2.3: the corrected differential cross section data of bank 5 shown in black and I ^S (Q) of bank 5 shown in red of 40P ₂ O ₅ ·16CaO·20Na ₂ O·24MgO.....	54
Figure 2.4: The corrected and normalised I(Q) of 40P ₂ O ₅ ·16CaO·20Na ₂ O·24MgO from detector bank 0 (top) through to 7 (bottom). The first red line and last black and pink lines are not used in the merge due to difficulties in correcting.....	55
Figure 2.5: the low r region of the differential correlation function and correlation function (D(r) and T(r)), before normalisation (black), after normalisation (blue) and the -T ⁰ (r) (red) of 40P ₂ O ₅ ·16CaO·20Na ₂ O·24MgO.	57

Figure 2.6: (a) schematic of basic flame spheroidisation set up and (b) detailed schematic of feeder setup.....	58
Figure 2.7: (a) SEM image of non-porous microspheres after degradation at day 1, (b) threshold of microspheres done on ImageJ where the black regions show the microspheres and the white regions is air, and (b) outline of the measured microspheres using ImageJ.....	63
Figure 3.1: Powder XRD pattern of glass samples in the system $40P_2O_5 \cdot (16-x)CaO \cdot 20Na_2O \cdot 24MgO \cdot xSrO$ glass, where x is 0, 4, 8, 12 and 16 mol%.....	64
Figure 3.2: Composition of glass samples tested as measured by EDX. Dotted lines represent the target value. Error bars were determined by taking the standard deviation of three separate samples for each composition.....	65
Figure 3.3: Density and molar volume of the multicomponent glasses $40P_2O_5 \cdot (16-x)CaO \cdot 20Na_2O \cdot 24MgO \cdot xSrO$ glass. The ionic radius [149] and mass of calcium and strontium atoms, and the mass and radius ratios between the two are also shown.....	66
Figure 3.4: Thermal traces showing T_g , T_c and T_m of the multicomponent glass samples.	68
Figure 3.5: (a) The average mass loss per unit area ($g\ cm^{-2}$) for multicomponent glasses studied in ultra-pure water. (b) Shows the calculated degradation rate ($g/cm^2/hrs$) for each multicomponent glass ($n=3$) in ultra-pure water, deionised water (DI) and phosphate buffered saline (PBS).....	73
Figure 3.6: (a) Cumulative cation release profiles from the multicomponent glasses investigated, which were degraded in ultra-pure water ion release rates normalised to the surface area. (b) Concentration of ions released which were normalised to the initial glass composition.....	75
Figure 3.7: MG63 relative fluorescence as measured by Alamar blue assay, for cells grown on PBG samples in the system $40P_2O_5 \cdot (16-x)CaO \cdot 20Na_2O \cdot 24MgO \cdot xSrO$ ($x= 0, 4, 8, 12$ and 16). P40 indicates 0 mol% SrO and Sr_x indicates the SrO mol% in the glass. Error bars represent standard error of mean, $n = 15$. cell metabolic activity as measured by Alamar blue assay. Error bars represent standard error of mean, $n = 15$	77
Figure 3.8: MG63 cell proliferation as measured by Hoechst 33258 DNA assay, for cells grown on PBG samples in the system $40P_2O_5 \cdot (16-x)CaO \cdot 20Na_2O \cdot 24MgO \cdot xSrO$ ($x= 0, 4, 8, 12$ and 16). P40 indicates 0 mol% SrO and Sr_x indicates the SrO mol% in the glass. Error bars represent standard error of mean, $n = 12$	78
Figure 3.9: Alkaline phosphatase (ALP) activity of MG63 cells cultured on PBG samples in the system $40P_2O_5 \cdot (16-x)CaO \cdot 20Na_2O \cdot 24MgO \cdot xSrO$ ($x= 0, 4, 8, 12$ and 16). P40 indicates 0 mol% SrO and Sr_x indicates the SrO mol% in the glass. Data is normalised against DNA concentration at each time point. Error bars represent standard error where, $n = 12$	79

Figure 3.10: Representative SEM micrographs of human osteoblast-like cells (MG63) cultured on PBG compositions at day 3 and day 14. All samples show cell attachment and spreading resulting in the formation of a confluent cell layer.....	82
Figure 3.11: Staining of tartrate resistant acid phosphatase (TRAP) activity of cells seeded directly on the surface of glass discs in the series $40P_2O_5 \cdot (16-x)CaO \cdot 20Na_2O \cdot 24MgO \cdot xSrO$ glass at day 14.....	85
Figure 4.1 Solid-state (a) ^{31}P MAS NMR and (b) ^{23}Na MAS NMR data of multicomponent glasses investigated.....	91
Figure 4.2: FTIR spectra obtained for multicomponent glasses. The dotted lines indicate prominent bands in the spectra.....	93
Figure 4.3: distinct scattering, $i(Q)$, patterns of (a) binary metaphosphate glasses and (b) multicomponent glasses of composition $40P_2O_5 \cdot (16-x)CaO \cdot 20Na_2O \cdot 24MgO \cdot xSrO$, where x is 0, 4, 8, 12 and 16 mol%.....	96
Figure 4.4: (a) Total correlation functions, $T(r)$ of binary samples and, (b) $T(r)$ of multicomponent glasses, where the region before the dotted line is Fourier transformed using the step function and the region after the dotted line was Fourier transformed using the Lorch [142] function.....	99
Figure 4.5: SrP_2O_6 and CaP_2O_6 residual $T(r)$ where O...O peak has been subtracted from $T(r)$ leaving P-O and M-O peaks. Grey dashed line shows M-O peak fit.....	103
Figure 4.6: $NaPO_3$ residual $T(r)$ after scaling where O...O peak has been subtracted from $T(r)$ leaving P-O and M-O peaks. Grey dashed line shows M-O peak fit.....	105
Figure 4.7: $T(r)$ of multicomponent glasses showing small differences either side of the peak at 2.51\AA (dotted line) due to loss in Ca-O contribution (at short distances) and growth in Sr-O contribution (at long distances).....	107
Figure 4.8: Comparison of $T(r)$ between MgP_2O_6 and P40.....	108
Figure 4.9: M-O pair distribution simulations (after dotted line at 1.8\AA) of multicomponent glasses simultaneously fit on NXFi [182] where the $T(r)$ was Fourier transformed using the Lorch[142] function. The P-O bond distribution at low r before the dotted line were fit using the step modification function.....	110
Figure 5.1: Powder XRD patterns of glass samples in the system $(40-x)P_2O_5 \cdot 16CaO \cdot 20Na_2O \cdot 24MgO \cdot xTiO_2$ (where x = 0, 3, 5, 7, 10 and 12).....	113
Figure 5.2: composition of glasses investigated as determined by EDX and their target values as represented by the dotted line. Error bars were determined by taking the standard deviation of three separate samples for each composition.....	114
Figure 5.3: Representative image showing the effect of increasing Ti content on glass colour.	115

Figure 5.4: Density and molar value of glasses in the system $(40-x)P_2O_5 \cdot 16CaO \cdot 20Na_2O \cdot 24MgO \cdot xTiO_2$ (where $x = 0, 3, 5, 7, 10$ and 12).....	116
Figure 5.5: Thermal traces showing T_g , T_c and T_m of the Ti invert glass samples.....	117
Figure 5.6: T_g with increasing TiO_2 content.....	118
Figure 5.7: ^{31}P MAS NMR spectra of the Ti invert glass series showing deconvolution of the chemical shifts.....	120
Figure 5.8: Showing the two theoretical (solid line) models, and experimental (dashed line) of Q^0 , Q^1 and Q^2 species as a percentage. The solid grey and black line shows the theoretical Q^1 and Q^2 species if Ti was to behave as a network former.....	122
Figure 5.9: Basic structure of bisphosphonates.....	124
Figure 5.10: (a) Average mass loss of P30Ti10 and P33Ti7 glass discs when degraded in ultra-pure water over a 28 day period. (b) Shows the degradation rate of the Ti invert glasses compared to P40.	125
Figure 5.11: (a) Cumulative cation release and (b) release rates from P30Ti10 and P33Ti7.....	129
Figure 5.12: Cumulative anion release from P30Ti10 and P33Ti7 glass samples.....	131
Figure 6.1: (a) Image of the as quenched P40 glass, (b) & (c) SEM images of irregular particle morphology after grinding.....	134
Figure 6.2: Schematic and photograph of oxy-propane flame spheroidisation apparatus.....	135
Figure 6.3: (a) & (b) SEM image of non-porous microspheres produced using the oxy-propane set up.....	136
Figure 6.4: (a) flame length (c) particle size distribution & (e) SEM image of spheroidised microspheres at a gas flow rate of 1.5 L/min propane to 3 L/min oxygen, and, (b) flame length, (d) particle size distribution & (f) SEM image of spheroidised microspheres at a gas flow rate of 3 L/min propane to 7 L/min oxygen. Red X indicates the point at which powder is fed into the flame length.....	139
Figure 6.5: SEM images comparing spheroidisation efficiency of (a) microspheres manufactured using microparticle sizes between 200-300 μm , and (b) between 100-200 μm	140
Figure 6.6: Light microscopy images illustrating the spheroidisation efficiency of particles collected at various distances along the flight path of the apparatus from the orifice of the torch.....	141
Figure 6.7: SEM images showing effect of porogen size on porosity.....	142
Figure 6.8: SEM image showing effect of porogen quantity on yield of porous microspheres where (m) is microparticle and (p) is porogen ratio.....	143
Figure 6.9: (a) & (b) SEM image showing porous microspheres manufactured using a two stage process.....	144

Figure 6.10: (a), (b), (c) & (d) SEM images showing the outcomes of using a 2 stage spheroidisation process where porogen was mixed with porous microspheres pre spheroidisation and put through the flame a second time.....	145
Figure 6.11: (a) flame length of oxy-acetylene flame, and (b) in built powder feeder.....	147
Figure 6.12: (a) & (b) SEM images showing yield of non-porous microspheres using the oxy-acetylene spray gun.....	148
Figure 6.13: Displaying the effects of altering glass microparticle (63-125 μm) to porogen (45-63 μm) ratio on porosity and yield.....	149
Figure 6.14: True density of porous microspheres with varying porogen quantities.....	152
Figure 6.15: SEM images of (a) bulk and (b) porous microspheres where irregular and non-porous particles which were not included in parameter B in equation 20 are circled in red.....	153
Figure 6.16: (a) XRD trace of non-porous (NP) are porous microspheres with varying porogen percent, (b) XRD trace of porous microsphere (1:2) compared to neat and processed porogen.....	154
Figure 6.17: Thermal trace showing Tg of processed porogen, porous and non-porous microsphere and microparticles.....	155
Figure 6.18: (a) & (b) SEM images showing bulk material and pore edge respectively, and EDX analysis of these areas from microsphere cross sections.....	156
Figure 6.19: (a) & (b) SEM cross sections of porous microspheres using SrCO_3 as a porogen source, and the EDX analysis of the pore edges shown in (a) and (b).....	157
Figure 6.20: XRD trace of porous microspheres after acid washing in 0.25M acetic acid for 15, 30 and 60 seconds.....	161
Figure 6.21: XRD trace of porous microspheres after been subjected to acid wash in 0.5M acetic acid for 15, 30, 60 and 120 seconds.....	163
Figure 6.22: Flow diagram showing procedure of manufacturing porous microspheres.....	164
Figure 6.23: Schematic of the hypothesised process of porosity formation within the microspheres. The inner blue cone in the orange region indicates the hottest part of the flame and the blue tip of the flame indicates the coolest part of the flame.....	165
Figure 6.24: Illustration showing the effect of (a) high powder feeding rates and (b) low powder feeding rates.....	167
Figure 6.25: Histogram showing particle size distribution of the porogen, microparticles, non-porous, porous and acid washed microspheres.....	168
Figure 6.26: (a) showing density values of non-porous, porous and acid washed microspheres compared to the as quenched glass, and SEM images of cross sections of (b) non-porous spheres, (c) porous spheres and (d) SEM image of acid washed spheres.....	171

Figure 6.27: Displaying the cumulative intrusion of non-porous, porous and acid washed microspheres as obtained from mercury porosimetry, and their possible corresponding inflection points.....	174
Figure 6.28: Pore diameter against Log differential pore volume of non-porous, porous and acid washed microspheres.....	175
Figure 6.29: (a) grayscale image of 2D slice of high resolution imaged microspheres, (b) single selected full microsphere for analysis.....	176
Figure 6.30: 3D construction (a) of porous microsphere, and (b) cross section of porous microsphere.....	176
Figure 6.31: 3D reconstruction of porous microsphere showing (a) dimension of large inner pore, (b) dimension of an interconnected pore, and (c) pore strut size.....	177
Figure 6.32: (a), (c) and (e) Micro CT images of a specific area within a single porous microsphere showing interconnectivity, (b), (d) and (f) 2D slices of the specific area showing interconnectivity of pores. Cubic constant element for (a), (c) and (e) $x=y = 0.0965$ mm, $z = 0.106$ mm.....	179
Figure 6.33: (a), (b) and (c) Micro CT images showing connection points between pores, the red dashed lines represent the space occupied by larger pores. (d) Inverse of Micro CT skeleton showing points of connectivity. Cubic constant element for (a), (b), (c) and (d), $x=y = 0.0965$ mm, $z = 0.106$ mm.....	180
Figure 6.34: (a) 2D slice showing pore separation, where the red outlines show points of connection, (b) 3D reconstruction of pore separation, and (c) 3D reconstruction of separated pore morphology. Cubic constant element for (b) and (c), $x=y = 0.0965$ mm, $z = 0.106$ mm.....	181
Figure 6.35: SEM images of degraded non-porous microspheres at various time points showing the formation of precipitation and pitting corrosion as indicated by the arrows.....	187
Figure 6.36: EDX analysis of degraded bulk microspheres at day 28 showing a possible hydration layer and the formation of precipitation.....	188
Figure 6.37: Modal diameter of degraded microspheres as measured via ImageJ.....	189
Figure 6.38: Histogram displaying diameters of degraded microspheres as measured by ImageJ.....	189
Figure 6.39: SEM image of microsphere at day 14 showing the possible formation of precipitation shells with several layers.....	190
Figure 6.40: SEM images at day 28 after degradation showing (a) brittle precipitation layers formed on the outside of a P40 non-porous microsphere at low magnification (b) and (c) showing globular, loosely packed precipitation formation at high magnification, and (d) precipitation layer formation at high magnification.....	191
Figure 6.41: SEM images of degraded (a), (b), (c), and (d) porous microspheres at day 28, and (e) and (f) porous acid washed microspheres at day 14 and 21 respectively.....	192

Figure 6.42: (a) Cumulative cation release profiles and (b) release rate profiles for non-porous, porous and acid washed microspheres degraded in ultra-pure water.....**193**

Figure 6.43: pH of porogen, non-porous, porous and acid washed microspheres during degradation study in ultra-pure water.....**194**

Figure 7.1: SEM images of porous microspheres trialled with the compositions (a) and (b) Sr8, (c) $40P_2O_5 \cdot 38CaO \cdot 19Na_2O \cdot 2MgO \cdot 1TiO_2$ and (d) $40P_2O_5 \cdot 16CaO \cdot 17.5Na_2O \cdot 24MgO \cdot 2.5TiO_2$,.....**201**

LIST OF TABLES

Table 1.1 Summary of compact and spongy bone features [15].....**4**

Table 1.2: Displaying current osteoporotic treatments, their benefits and side effects..**8**

Table 1.3: A summary of common modifier oxides investigated in PBGs.....**11**

Table 1.4: Q^n characteristics.....**14**

Table 1.5: Mathematical expressions used to calculate the MO mol% concentration and relative theoretical Q^n species in PBG.....**16**

Table 2.1: Compositional information, showing the glass transition temperature of samples, and whether the sample was cast or quenched (represented by X).....**37**

Table 2.2: The cation calibration standards used along with their dilution factor and its equating concentration in ppm.**41**

Table 2.3: Displaying gas flow rates experimented with for flame spheroidisation.....**59**

Table 3.1: Glass transition, T_g , crystallisation, T_c , onset of crystallisation, T_{onset} first melting temperatures, T_m and second melting temperature, T_{m2} , for each composition is given along with the calculated thermal processing window, $T_{onset} - T_g$ of each glass..**68**

Table 4.1: Chemical shifts (ppm referenced using H_3PO_4) and relative concentrations of Q^n units determined by solid-state ^{31}P MAS NMR of each composition investigated and the calculated number of bridging oxygens (BOs) and non-bridging oxygens (NBOs) per PO_4 unit using equation 11.....**92**

Table 4.2: The FTIR wavenumbers (cm^{-1}) and band assignments attributed to the multicomponent glass samples.**94**

Table 4.3: The phosphorous environments in the binary and multi-component glasses, derived by fitting $T(r)$ using a step function.....**100**

Table 4.4: The modifier environments in the binary glasses, derived by fitting $T(r)$, and the refined Mg-O and O...O peak parameters used to simulate $T(r)$ s for the multicomponent glasses.**102**

Table 4.5: Displaying an exemplar (Sr8) sample composition files used to run the programme NXFit [182]**108**

Table 5.1: Compositional information on invert glasses investigated.....	112
Table 5.2: T_g , T_{onset} , T_c and T_m recorded for the Ti invert glass samples.....	118
Table 5.3: Chemical shifts (ppm referenced using H_3PO_4) and relative concentrations of Q^n units determined by solid-state ^{31}P MAS NMR of each composition investigated and the calculated number of bridging oxygens (BOs) and non-bridging oxygens (NBOs) per PO_4 unit using equation 11.....	121
Table 6.1: Shows the range and percentage of sizes obtained after grinding a batch (c.a.100g) of P40 at 500rpm for 2 minutes.....	134
Table 6.2: The effect on binding porogen to glass particles using Cellosize before spheroidisation and the effect of binding porogen to non-porous microspheres.....	146
Table 6.3: SEM images displaying internal features of porous microspheres manufactured using various glass microparticle to porogen ratios.....	150
Table 6.4: SEM images displaying the effect of acid washing porous microspheres in 2M and 1M of acetic acid for 1 and 2 minutes respectively.....	159
Table 6.5: SEM images displaying the effect of acid washing porous microspheres in 0.25M of acetic acid for various time points.....	159
Table 6.6: SEM images displaying the effect of acid washing porous microspheres in 0.5M of acetic acid for various time points.....	161
Table 6.7: Surface area of microspheres as measured by BET.....	172
Table 6.8: SEM images displaying representative samples of degraded non-porous, porous and acid washed microspheres at each time point after degrading in ultra-pure water.....	183

CHAPTER 1: INTRODUCTION AND REVIEW OF LITERATURE

1.1 Primary research motivation

An increasing worldwide ageing population is leading to an ever growing demand for the treatment of musculoskeletal related diseases and defects, such as osteoporosis. Fractures associated with this disease total around 60,000 hip, 50,000 wrist and 120,000 vertebral fractures in the UK each year.^[1] Treatment and associated healthcare costs for osteoporosis related fractures cost the UK £1.73 billion a year, and this figure is only destined to rise with the growing number of elderly patients.

In order to tackle the above issues, a novel technology comprising of resorbable porous phosphate based glass (PBG) microspheres has been developed, which has the potential to repair and regenerate bone tissue. These microspheres can be tailored to release therapeutic ions as degradation by products, which are beneficial for bone growth. The rate of release can also be tailored by simply altering the glass composition. Furthermore, the porous constructs can be loaded with alternate therapeutic components such as drugs, proteins, growth factors, cells or other biological components, providing a combinatorial effect.

PBG's are ideal materials for use in orthopaedic applications since their main constituents are characteristically native to bone (Ca^{2+} , Na^{2+} , Mg^{2+} , PO_4^{3-}) and have been widely investigated due to their fully resorbable, controlled degradation rates and biocompatible properties.^[2-6]

The spherical morphology of these novel microspheres confer additional advantages for example; spherical particles should be able to flow more efficiently down a syringe needle or cannula, thus enabling delivery of this technology via a minimally invasive (injection) route, thereby significantly reducing patient discomfort and trauma.

1.2 Introduction

The worldwide ageing population is generating greater demand on healthcare services to provide effective treatment for age related musculoskeletal diseases such as arthritis, trauma, tumours and osteoporosis. Techniques to replace, restore or regenerate bone is in greater clinical demand as evidenced via a recent study by Donaldson *et al.* [7] which revealed that fractures in England may be more common than was previously thought, with 1 in 2 middle aged women and 2 in 5 men aged 75 having experienced a fracture in their lifetime. In particular, osteoporosis related fractures have been reported at approximately 50 million worldwide.[8]

Surgical procedures responding to the rise in demand have resulted in the practice of 2.2 million bone grafting operations a year worldwide.[9] Although the market of drug treatments and prevention of osteoporosis is highly saturated, there still remains a lack of alternative treatments for the prevention of fractures.[10]

New technologies are now developing in the biomaterials field with a great deal of research focusing on tissue engineering and regenerative medicine. As technology has advanced through the years, the evolution of biomaterials has transitioned from first generation (bioinert materials), second generation (bioactive and biodegradable materials), to a rising interest of research being carried out on third generation biomaterials; aiming to repair and regenerate tissue.[11, 12]

This concept of “repair and regeneration” has been extensively translated to the orthopaedic field, with much research focused on regeneration of bone. Tissue repair has been described to occur via two routes; tissue engineering and *in situ* tissue regeneration. Tissue engineering may involve the use of resorbable scaffolds onto which cells of interest are seeded and cultured *in vitro*. Once the cells have proliferated and differentiated, the engineered construct is then implanted into the body where the affected tissue is replaced by the host tissue over time and the scaffold degrades away. On the other hand,

tissue regeneration involves some sort of bioactive biomaterial to trigger a response in the local environment leading to tissue repair. This bioactive material may release beneficial chemicals as its dissolution product at a controlled rate, either by diffusion or by the breakdown of the network, stimulating cells at the target site to regenerate tissue *in situ*.^[11]

Orthobiologics is of particular interest when aiming to prevent fractures from occurring, since this practice encourages engineered materials to promote the repair and regeneration of musculoskeletal tissue.^[13, 14]

1.3 Fundamentals of bone and bone biology

Bone is essentially a bioceramic composite material, which presents itself in a hierarchal manner with unique structural and mechanical properties. In order to successfully regenerate or repair bone, knowledge of the bone biology and its development are essential. Bone is formed of an extracellular matrix (25% water, 25% collagen fibres, and 50% mineralised salts) which surround the cells. There are four types of cells that reside in bone tissue; osteogenic cells, osteoblast, osteocytes and osteoclasts (Figure 1.1), all playing active roles in the formation and remodelling of bone.^[15] Ultimately it is the activity of the osteoblasts which secrete collagen fibres and other organic components which form the extracellular matrix, burying osteoblasts in their secretions and instigating the transformation to osteocytes. Furthermore, the matrix of bone can be conceived as an organic-inorganic composite; the organic component mainly comprising of collagen, proteoglycans, growth factors and matrix proteins, and the most abundant inorganic constituents are calcium phosphate ($\text{Ca}_3(\text{PO}_4)_2$), which combine with calcium hydroxide ($\text{Ca}(\text{OH})_2$) to form hydroxyapatite (HA) crystals ($\text{Ca}_{10}(\text{PO}_4)_6(\text{OH})_2$). During formation of the crystals, other mineral salts and ions are also deposited in the collagen fibre matrix, such as calcium carbonate, magnesium, and potassium fluoride, leading to calcification as the crystals harden.^[15, 16]

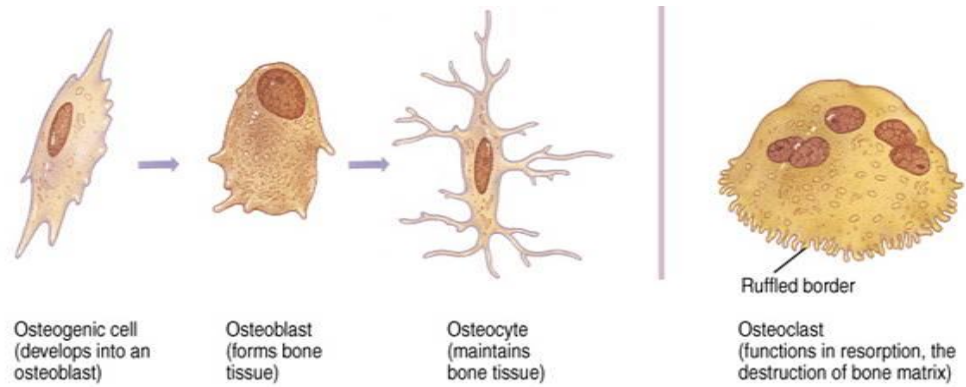


Figure 1.1: Illustration of the four main types of cells found residing in bony tissue. ^[15]

Bony regions may be classified as either compact bone tissue or spongy bone tissue as is summarised in Table 1.1. Around 80% of the human skeleton is compact bone and the remaining 20% is spongy bone. ^[15]

Table 1.1 Summary of compact and spongy bone features ^[15]

Compact bone	Spongy bone
(Cortical bone)	(Cancellous bone)
<ul style="list-style-type: none"> • Contains few spaces and is the strongest form of bone, providing protection and support as well as resisting day to day stresses and load • Composed of osteons (Haversian systems) • Osteons are aligned along stress lines • Interstitial lamellae are formed from older osteon fragments which have been partially destroyed during bone remodelling and are located in areas between osteons 	<ul style="list-style-type: none"> • Lighter bone which makes up the interior bone tissue of short, flat and irregular shaped bones. It is always covered by a protective layer of compact bone • Does not contain osteons • Lamella are arranged in this irregular lattice columns i.e. trabeculae , which have large spaces • Each trabeculae contain lacunae where osteocytes are housed

1.3.1 Remodelling of bone

Bone is one of the tissues in the human body that is capable of self-renewal (depending on the defect size). It is an ongoing process whereby old minerals and collagen is resorbed by osteoclasts, and new bone is deposited by

osteoblasts. There are several stimuli which trigger remodelling such as, biological stimuli (hormones), mechanical stimuli (exercise), diet, and inactivity. If the bone is subject to heavy loading, the new bone growth tends to be thicker and stronger than the previous bone. This new bone is also more resistant to fracture than the old bone.^[15] Ideally formation of new bone should match resorption of bone however; this is not always the case as is explained later in section 1.4.

Resorption of bone occurs as osteoclasts attach to bone and release protein digesting lysosomal enzymes and acids. The enzymes are involved in digesting collagen fibres and other organic components and the acid dissolves bone minerals. Trenches and tunnels of bone are removed via this process and by-products such as calcium, phosphorous and degraded proteins are engulfed via endocytosis. Once the osteoclast departs from the attacked area, osteoblasts then move in and fill the trenches with osteoid which later mineralises. Furthermore, the receptor activator of nuclear factor kappa – B (RANK) – RANK-ligand (RANK-L) pathway is initiated by activation of osteoblasts, which then stimulates osteoclast activity (Figure 1.2). In order to maintain this fine balance (between osteoblasts and osteoclasts), osteoblasts also produce osteoprotegerin, which acts as a blocking receptor of RANK-L, in turn moderating the differentiation of osteoclasts.^[17]

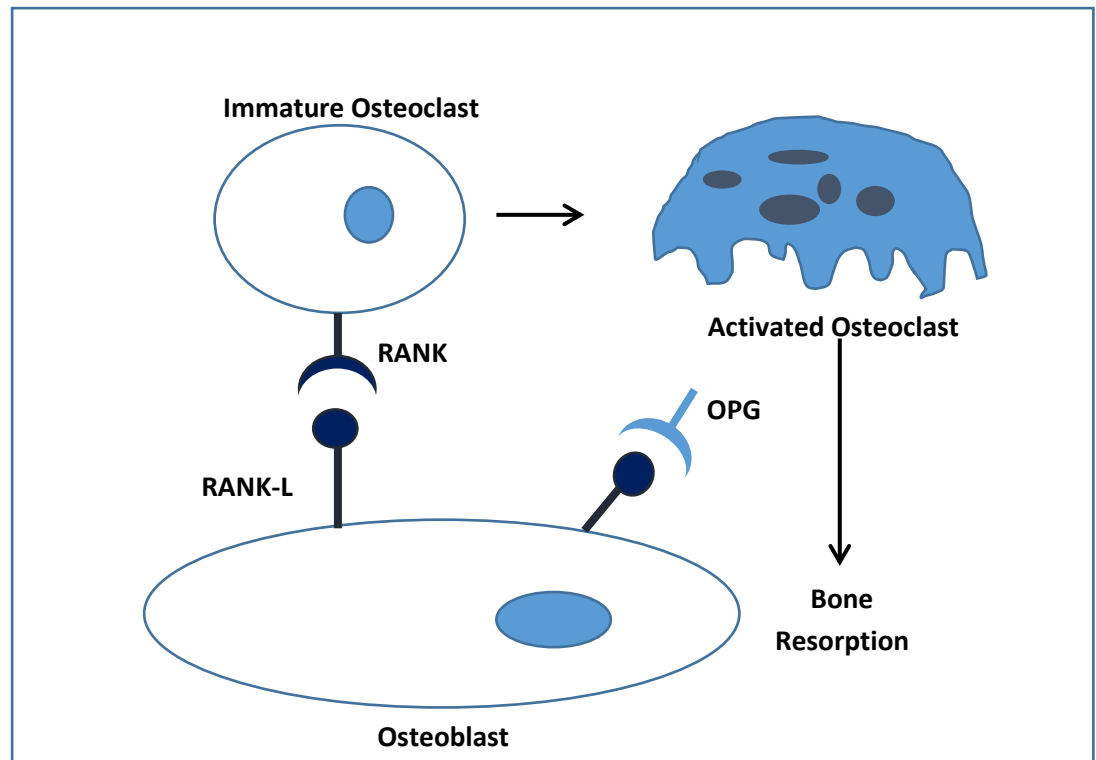


Figure 1.2: Illustration of RANK- RANK-L activation of osteoclasts adapted from N. Little et al. ^[17]

1.4 Osteoporosis

Osteoporosis is a bone related disease classified by a reduction in bone mineral density (BMD) and increase in brittleness, leading to eventual fracture. This is a major public health problem and due to the rise in the ageing population, the magnitude of this condition is vastly increasing. During the 1990's, the total annual cost to the UK associated with osteoporotic fractures was reported to be in the region of £740 million, with hip fractures being the most prevalent with 60,000 fractures occurring annually.^[18] The annual cost of treatment has rocketed to £1.73 billion, which is almost 2% of the National Health Services (NHS) budget, as reported by the national Osteoporosis society.^[1] In the year 2000, there were reported to be 1.6 million hip fractures, 1.7 million forearm fractures and 1.4 million vertebral fractures with the greatest number occurring in Europe.^[8] These figures clearly indicate that osteoporotic fractures have a significant impact on a large number of the population, particularly in

developed countries, and the direct medical costs have been predicted to rise to £2.2 billion by 2025.^[19]

Significant progress has been made over the last 2-3 decades regarding patient care, for example identification of individuals at risk of fracture before the first fracture is made possible by defining bone mineral density (BMD) as a T-score. The World Health Organisation (WHO) definition of osteoporosis states a BMD T-score which is <-2.5 SD or greater than that of the average value for a young healthy women.^[20]

Fragility fractures occur due to a greater activity of osteoclast bone resorption compared to osteoblast bone deposition, largely due to depletion of calcium in the body. Older women tend to be affected the most due to a fall in oestrogen production post menopause, and it is this hormone that largely modulates metabolism and mechanosensitivity of bone.^[15, 21] In males, there has also been a link to an increase in risk of osteoporosis with a fall in the sex steroid testosterone.^[22] Other than gender biases, there are other life style factors which also influence the risk of this bone disease such as increased consumption of alcohol, smoking, low levels of calcium and Vitamin D in diet, and lack of exercise.^[15]

Current treatments include administration of antiresorptive or anabolic treatments as outlined in Table 1.2. Antiresorptive treatments include those which ultimately inhibit osteoclast activity such as bisphosphonates, RANKL antibody, and selective estrogen receptor modulators (SERM) as well as calcium and vitamin D. Anabolic treatments comprise of teriparatide and parathyroid hormone (PTH), however, several of these have strong side effects associated with them as outlined by Langdahl and Harslof.^[23] Other challenges also exist when managing osteoporosis such as patient compliance and the surgeons who primarily focused on fracture treatment rather than prevention.

Table 1.2: Displaying current osteoporotic treatments, their benefits and side effects.

Medical treatment	Antiresorptive/ anabolic	Mode of action	Side effects	Ref.
Bisphosphonates e.g. Alendronate, Risedronate, Etidronate, Pamidronate	Antiresorptive	-Chemically stable derivatives of inorganic pyrophosphate. - Affinity to HA. -Suppresses osteoclast activity. -Leading clinical intervention of postmenopausal osteoporosis.	-Gastroesophageal irritation -Severe suppression of bone turnover - Optimal use requires adequate intake of calcium and Vitamin D before and during therapy. -Poor absorption of orally administered bisphosphonates. -Associated with osteonecrosis of the jaw, although rare.	[24] [25]
Hormone replacement therapy	Antiresorptive	-Hormone regulator of calcium homeostasis, increases bone formation and bone mass.	-Increased risk of breast cancer and cardiovascular diseases.	[23]
SERMs e.g. Raloxifene	Antiresorptive	- Reduced production of RANKL by osteoblasts thus inhibits osteoclast recruitment. -Bind to oestrogen receptors thus confers similar effects to oestrogen such as protection against bone loss and has additive effect on BMD.	-Not been shown to reduce incidence of fractures other than that of the vertebra. -Could play a role in renal failure.	[26]

<p>RANKL Inhibitors e.g. Denosumab</p>	<p>Antiresorptive</p>	<p>-Regulates osteoclast activity by inhibiting RANKL and RANK interaction. -Administered via subcutaneous injection and reduction in activity seen within first 24hours of administration.</p>	<p>-Potential immunological resistance to OPG. -Potential effects on the cardiovascular and immune systems. -Rarely causes osteonecrosis of jaw.</p>	<p>[27]</p>
<p>Strontium ranelate</p>	<p>Antiresorptive</p>	<p>-Maintains bone formation and decreases bone resorption. -Maintains bone mineralization. -Can replace calcium in bone and suppress bone resorption.</p>	<p>-Exact mechanism of action is still unknown. -Nausea, vomiting, venous thromboembolism.</p>	<p>[28]</p>
<p>Calcium and Vitamin D</p>	<p>Antiresorptive effect via suppression of PTH serum levels</p>	<p>-Reduces bone loss and stimulates bone mineralisation -Moderate antifracture efficacy</p>	<p>-Required alongside use of bisphosphonates -considered as a basic treatment for osteoporosis</p>	<p>[23, 29]</p>
<p>Rh-Parathyroid Hormones e.g. Teriparatide</p>	<p>Anabolic</p>	<p>-Stimulates bone formation and increase in BMD. -Increase cancellous BMD in postmenopausal women.</p>	<p>-Underlying mechanism not well understood -Nausea, fatigue, depression, urinary incontinence, palpitations, bone pain. -Little effect on cortical bone BMD.</p>	<p>[30, 31]</p>

1.5 Phosphate glasses for therapeutic applications

There are two main criteria a material must fulfil in order for it to be classed as a glass; there should be no evidence of long range order, i.e. no periodic atomic arrangement within the structure, and every glass should exhibit glass transformation behaviour. This is a time dependent behaviour which occurs over a specific temperature range known as the glass transformation region. In the area above and below the glass transition temperature (T_g), there is a linear variation in enthalpy/ volume with temperature however, in the vicinity of the T_g , a change in the slope of the curve occurs over several degrees. From this the T_g can be taken as the point at which the two lines of the extrapolations meet, as shown in Figure 1.3. Shelby^[32] defined glass as “any material which exhibits glass transformation behaviour”, which emphasises the fact that glass transformation occurs over a range of temperatures and cannot be characterised by a single temperature point however, in general, the onset of the glass transformation region is commonly taken as the T_g temperature as it is the most reproducible.^[32, 33] In summary, a glass may be termed as an amorphous, disordered material with no long range periodicity.

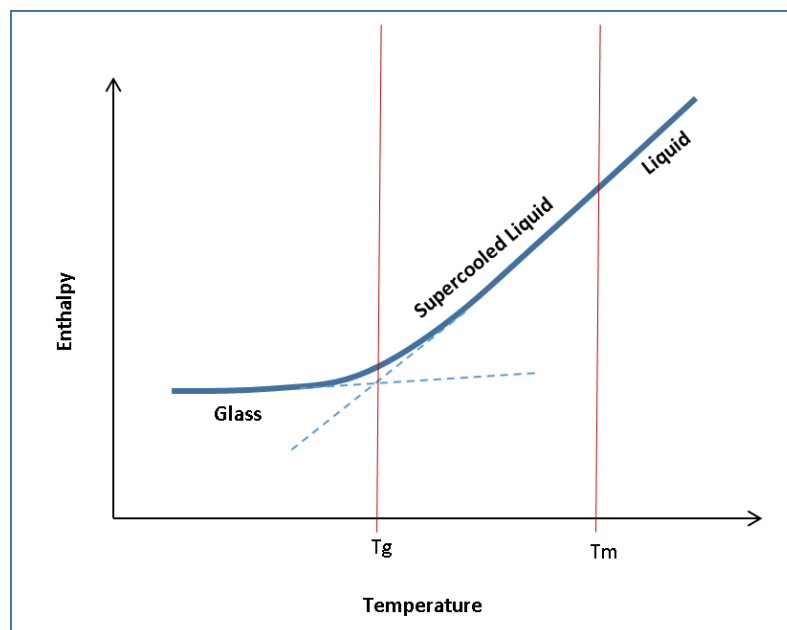


Figure 1.3: Simplified schematic showing the glass transition behaviour.

Phosphate based glasses have been long studied for use as biomedical materials^[2, 3, 34] due to their inherent properties such as its close chemistry to native bone, fully resorbable properties, controlled degradation rates, and biocompatible nature.^[2-6] The ability to control these properties, in particular the degradation rates, makes phosphate glasses extremely well suited for delivery of therapeutic ions. One of the first propositions for the use of PBG in biomedical applications was by Gilchrist *et al.*^[35] during the early 80's where a range of "controlled release glasses (C.R.G)" composed of a P₂O₅ network exerted no adverse effects on a L929 mouse fibroblast cell line over a 7 day period. These C.R.G's were also cast into rods and implanted in the lateral cortex of the tibia of six adult sheep where new bone formation was seen to fill the gap and replace the shrinking implant with no cytotoxic effects. Gilchrist *et al.*^[35] stated that control over degradation rates could range from a day to a decade when half the glass weight was made up of active ions so that the optimum rate of dissolution could be achieved. By altering the glasses physical form i.e. the particle size distribution (as rod, powder, foam, fibre or woven textile) the leaching characteristics and dissolution rates can be further altered.

The use of PBG's in both hard and soft tissue repair has been extensively studied^[2, 36, 37] and the benefits of adding therapeutic ions into bioactive materials have been summarised by Mourino *et al.*^[38] and Hoppe *et al.*^[39] A brief summary of some heavily investigated ions used to modify PBG can be seen in Table 1.3 below.

Table 1.3: A summary of common modifier oxides investigated in PBGs

Modifier Oxide	Effect	Reference
MgO	- Decreases the solubility of the glassy material. - Increasing Primary-derived human osteoblasts cell attachment.	[40, 41]
Fe ₂ O ₃	- Shown to significantly reduce degradation rate with addition of up to 5 mol% due to formation of higher resistant P-O-Fe bonds.	[42, 43]

CuO	<ul style="list-style-type: none"> - Conditionally immortal muscle precursor cell line derived from the H-2Kb-tsA58 immortomouse showed an increase in number with increasing Fe₂O₃ content. - Decrease in degradation rate with increasing CuO content. - Antimicrobial properties as seen by a decrease in the number of viable staphylococci. - Shown aneogenic potential as seen by formation of capillary-like network SVEC4-10 endothelial cells. 	[44, 45]
Ag₂O	<ul style="list-style-type: none"> - Low Ag contents have shown to have antimicrobial activities. - Decrease in degradation rates with increasing Ag content. 	[46]
CoO	<ul style="list-style-type: none"> - Found to encourage secretion of vascular endothelial growth factor by osteoblastic MG63 cells hence thought to encourage vascularisation. 	[47]

1.5.1 Phosphate glass structure

Historically there have been several theories surrounding the formation of glass. Initially during 1926 Goldschmidt suggested that glass formation occurred during cooling of melts containing tetrahedrally coordinated cations, where the cation to anion radius ratio was between 0.2 to 0.4. Although glass formers follow this rule, there are other elements such as BeO₂ which satisfy this rule but do not form a network. Following this proposal, Zachariasen led on to formulate an explanation of glass formation during 1932 which today has formed the basis for supporting glass structure formation. A summary of the random network theory can be seen below;^[32]

- 1) No oxygen atom should be linked to more than two cations
- 2) The coordination number of the cation should be small (i.e. 3 or 4)
- 3) Oxygen polyhedra do not share edges or faces but rather share corners
- 4) At least three corners are shared for 3D networks

In general all four rules should be satisfied in order for glass formation to occur.

The structural unit of PBG's are composed of PO₄³⁻ tetrahedral groups.^[48] The phosphorous atom is covalently bonded to three bridging oxygen's (BO) via a single bond, forming P-O-P bonds. The fourth terminal

oxygen atom (TO) is bound via a π bond, forming P=O bond, which is significantly shorter than the others.^[48, 49] The structure of the glass is denoted by Q^n terminology, where n represents the number of BO's per PO_4^{3-} tetrahedron and is illustrated in Figure 1.4.^[50]

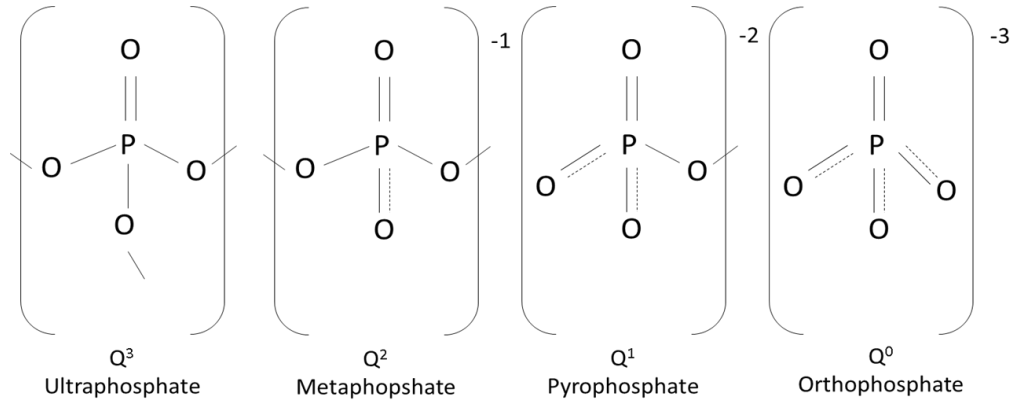


Figure 1.4: Schematic showing the four Q^n species which can be present in PBG's along with the classification of the groups corresponding to structure.

When considering the structure of vitreous P_2O_5 , each tetrahedral unit is connected to three other units via BO atoms, i.e. made up of Q^3 phosphate tetrahedra which have been confirmed by neutron diffraction studies.^[51, 52] The exceptionally hygroscopic behaviour of vitreous P_2O_5 limits its use significantly. In order to improve the chemical durability of this glass, various modifier oxides such as CaO and Na_2O are commonly added. Addition of alkali (MeO) and alkaline earth (Me_2O) oxides modifies this 3-dimensional network, causing depolymerisation and resulting in the formation of non-bridging oxygens (NBO). With increasing addition of MeO and Me_2O modifiers, the number of NBO's increases, thus Q^n species decreases. The fraction of two Q^n species for a specific formula can be predicted using the Q^n model.^[32] This model assumes only two Q^n species exists at a time in a glass system however, this is not always the case as evident from previous ^{31}P NMR studies^[53] and first-principles and classical molecular dynamics simulations.^[54] The general glass formula can be expressed as in Equation (1):

$$xM_nO \cdot 2(100 - x)P_2O_5 \quad (1)$$

where x is the mol% of MO in the glass system n is equal to 1 or 2. The total number of oxygens can be calculated by multiplying the number of oxygens introduced by each component times their concentration in the glass as shown in Equation (2):

$$\text{Number of oxygens} = x(1) + (100 - x)(5) \quad (2)$$

$$= x + (500 - 5x) \quad (2.1)$$

The total number of tetrahedra (e.g. $Q^3 + Q^2$) must equal to the number of glass network former atoms as indicated by Equation (3):

$$Q^3 + Q^2 = 2(100 - x) \quad (3)$$

Assuming that all the oxygens are associated with the glass former element by either bridged or non-bridged configurations, the number of oxygens is divided between the two Q^n species present at a time in the glass system. An expression of the resulting Q^n species along with their respective number of oxygens per tetrahedra can be expressed as is seen in Equation (4). The characteristics of the Q^n species are summarised Table 1.4.

$$\text{Number of oxygens} = Q^3(2.5) + Q^2(3) \quad (4)$$

Table 1.4: Q^n characteristics.

Characteristic	Q^3	Q^2	Q^1	Q^0
BO per tetrahedron	3	2	1	0
NBO per tetrahedron	1	2	3	4
Oxygens per tetrahedra	2.5	3	3.5	4

By equating Equations (2.1) and (4), the number of oxygens can be calculated as shown in Equation (5):

$$x + 500 - 5x = Q^3(2.5) + Q^2(3) \quad (5)$$

Making Q^3 the subject in Equation (6)

$$Q^3 = 200 - 2x - Q^2 \quad (6)$$

substituting (6) into (5):

$$x + 500 - 5x = [(200 - 2x) - Q^2](2.5) + Q^2(3) \quad (7)$$

which can be solved to give the amount of Q^2 species in the equivalent binary glass system with a x modifier content:

$$Q^2 = 2x \quad (8)$$

Equation (8) can then be combined with Equation (3) to give the concentration of Q^3 units:

$$Q^3 = 200 - 4x \quad (9)$$

It is then possible to calculate the theoretical x concentration of modifier oxide required to fully eliminate the Q^3 species from the glass structure, by setting Q^3 to 0 in Equation (9):

$$0 = 200 - 2x \quad (9.1)$$

Therefore

$$x = \frac{200}{4} \quad (9.2)$$

hence when $Q^3 = 0$, the mol. % of modifiers is equal to 50.

The same procedure can be used to derive expressions for the proceeding compositional regions created as the modifier content increases. Further addition of modifier oxides increases the concentration of NBOs, shifting the Q^n species to a region between Q^2 and Q^1 , followed by a region between Q^1 and Q^0 as the modifier content is further increased. Equations representing the Q^n

species concentration in the equivalent binary phosphate glass system can be seen in Table 1.5 and has been graphically illustrated in Figure 1.5.

Table 1.5: Mathematical expressions used to calculate the MO mol% concentration and relative theoretical Q^n species in PBG

Q^n species region	Equation	Modifier content (mol%) when $Q^n = 0$
$Q^3 - Q^2$	$Q^3 = 200 - 4x$	50
	$Q^2 = 2x$	0
$Q^2 - Q^1$	$Q^2 = 400 - 6x$	66.66
	$Q^1 = 4x - 200$	50
$Q^1 - Q^0$	$Q^1 = 600 - 8x$	75
	$Q^0 = 400 - 6x$	66.66

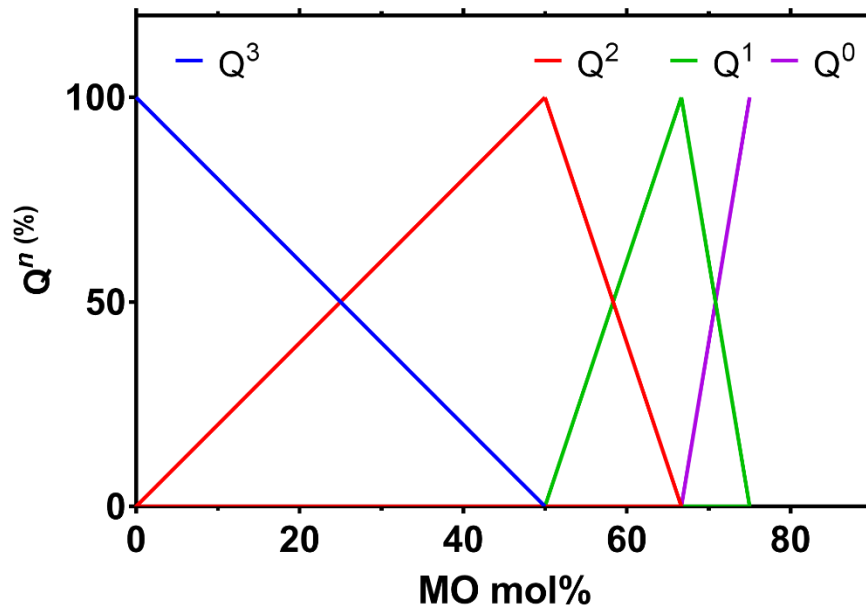


Figure 1.5: Graphical illustration of MO mol% concentration on the relative theoretical Q^n species in PBG.

The depolymerisation of phosphate networks with increasing addition of modifier oxides has been confirmed via ^{31}P MAS NMR, where the central peak in the spectra can be seen to shift to higher regions as the Q^n species transitions

from $Q^3 \rightarrow Q^2 \rightarrow Q^1 \rightarrow Q^0$. The area under the isotropic peaks along with the spinning side bands can be assigned to the contributing Q^n species as displayed in Figure 1.6. Data from ^{31}P NMR and predictions made using Q^n theory provide a complementary technique when understanding the medium range order of PBGs.^[32, 55, 56]

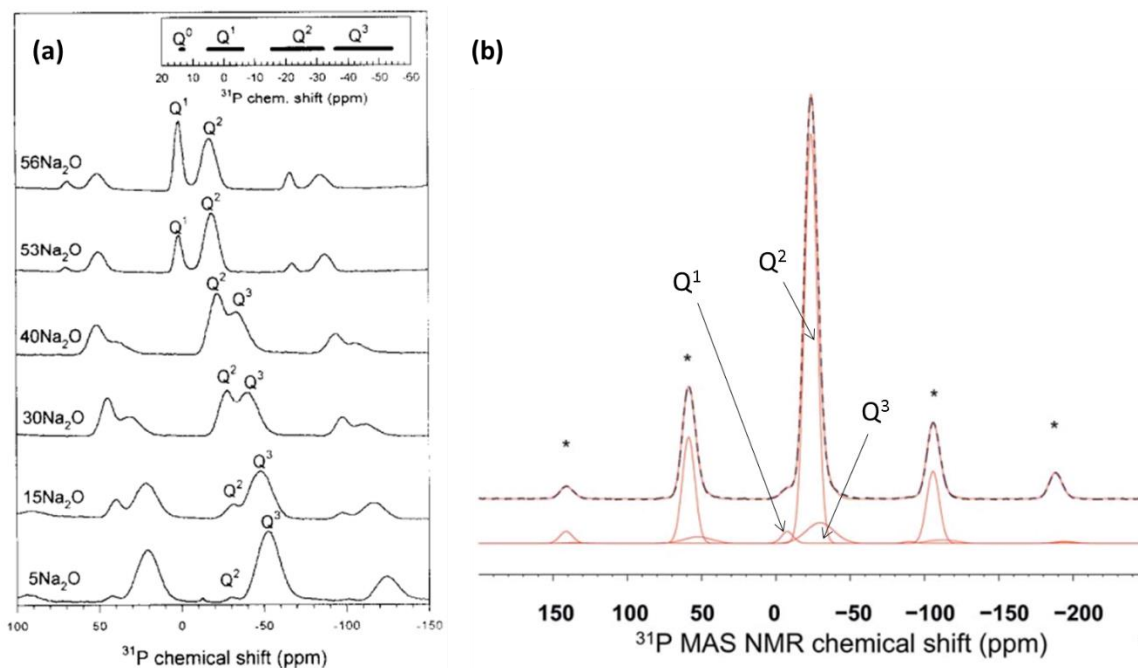


Figure 1.6: (a) ^{31}P NMR spectra showing chemical shift to higher ppm with increasing Na_2O content in a $100-x\text{P}_2\text{O}_5-x\text{Na}_2\text{O}$ glass system.^[55] (b) adaption from Dohler et al.^[53] showing ^{31}P NMR spectra and associated Q^n species in a $50\text{P}_2\text{O}_5-25\text{CaO}-25\text{Na}_2\text{O}$ glass.

1.5.2 Strontium containing PBGs

Research into bioactive glasses has focused extensively on tailoring glass properties to address specific clinical needs. The ability to introduce new oxides to the basic sodium-calcium phosphate glass network is of great interest as it allows properties such as their degradation rates to be tailored (see for example works studying the effect of MgO ,^[41] TiO_2 ^[57] and Fe_2O_3 ^[42]) and the addition of therapeutic ions for controlled release into the body.^[58]

One of the most common treatments for osteoporosis was administration of low doses (316–634 mg/kg per day Sr^{2+}) of strontium ranelate or strontium chloride for 9-26 weeks. This was shown to reduce bone resorption and

stimulate bone formation via increased replication of preosteoblastic cells. This is beneficial since it is the imbalance of bone deposition and resorption which leads to osteoporosis.^[59-61] The dual effect of strontium on bone metabolism has been investigated by researchers for use in orthopaedic applications.^[62-66] Recent studies have shown that addition of strontium ions to phosphate glasses has the potential to aid treatment of osteoporosis.^[62-64, 67, 68]

Substitution of calcium with strontium has been of interest as both play similar chemical roles since the two cations are divalent, and have a similar ionic size (Ca^{2+} 1.00 Å and Sr^{2+} 1.18 Å). Strontium is also known to follow a similar physiological pathway in humans as calcium, where a large portion accumulates in bone via ionic exchange of calcium for strontium, thus it has been used in bone therapies.^[69] However, controversy does exist in the use of strontium in bone health products due to its ability to displace calcium in the bone at high concentrations and reside there, which in turn leads to increased attenuation of x-rays, due to the higher atomic mass of Sr compared to Ca, leading to overestimation of BMD values due to the physical properties (i.e. mass) of Sr within bone.^[70-72]

The ease of substitution of these two cations within a glass system and the positive influence Sr has on bone metabolism has been shown to be an attractive area for research.^[64, 73, 74] Although the exact mechanism of how Sr influences osteoblastic activity is still unknown, studies have investigated the behaviour of cells such as osteosarcomas and mesenchymal stem cell lines towards Sr containing biomaterials.^[75-77] Strontium substituted hydroxyapatite nanocrystals showed increased levels of alkaline phosphatase (ALP), collagen type I and osteocalcin production in comparison to pure HA when cultured with an osteoblast-like MG63 cell line.^[78] Similarly, strontium substituted HA cultured with rat osteoblast cells derived from both healthy and osteopenic bone showed enhanced differentiation of osteoblasts of both healthy and osteopenic bone and increased levels of proliferation, ALP and collagen type I of osteopenic bone.^[79] Both of these studies found Sr to influence bone cells in a dose-dependent manner. Similarly, human osteosarcoma G-292 cells

cultured with Sr- doped gypsum revealed an increase in osteoblast proliferation also in a dose-dependent manner, with the lowest proliferation rate found with the highest investigated content of Sr (2.5%) in gypsum.^[80]

Investigation into the effects of strontium containing PBGs has also been reported, for example, human osteosarcoma cells were cultured with glass formulations of $50\text{P}_2\text{O}_5\cdot 30\text{CaO}\cdot (20-x)\text{Na}_2\text{O}\cdot x\text{SrO}$ ($x = 0, 1, 3 \text{ \& } 5$ mol%) resulting in greater cell attachment on compositions containing 1 and 3 mol% of SrO compared to those containing no SrO at 24 hours.^[64]

Similarly, a PBG composition $50\text{P}_2\text{O}_5\cdot (30-x) \text{CaO}\cdot 15\text{Na}_2\text{O}\cdot 5\text{TiO}_2\cdot x\text{SrO}$ ($x = 0, 1, 3 \text{ \& } 5$ mol%) resulted in greater cell growth of all Sr containing glasses at day 4 compared to Sr free glass and the control glass cover slips.^[81] A study with full substitution of CaO for SrO in the glass system $50\text{P}_2\text{O}_5\cdot (35-x)\text{CaO}\cdot 10\text{Na}_2\text{O}\cdot 5\text{TiO}_2\cdot x\text{SrO}$ ($x = 0, 3.5, 17.5 \text{ \& } 35$ mol%) showed comparable cell densities for all glass compositions to the tissue culture plastic (TCP) control. However, this value decreased for all Sr containing glasses after day 7, with the exception of the glass containing 17.5 mol% SrO which showed similar ALP activity at each time point and appeared to be greater than the TCP control.^[73] In contrast, when substituting CaO for SrO by 0-100% in an invert glass system; $30\text{P}_2\text{O}_5\cdot (60-x)\text{CaO}\cdot 7\text{MgO}\cdot 3\text{TiO}_2\cdot x\text{SrO}$ (where $x = 0, 17, 33, 50, 67, 83$ and 100) an increase in osteoblast like MC3T3-E1 cells on all glass compositions compared to the TCP control at day 3 and 5 was observed.^[74]

By incorporating strontium into a fully degradable material, it should be possible to achieve a controlled release of strontium into the body over time.

1.5.3 Phosphate invert glasses

Phosphate invert glasses typically contain <40mol% of the network former; P_2O_5 , thus consist of small pyro- (Q^1) and orthophosphate (Q^2) groups, which have larger mobility in the melt, and so are more prone to crystallisation during formation.^[82, 83] Unlike conventional glasses whose properties are governed by the network former, the property of invert glasses are largely dependent on the modifier cations that are present, and it is for this reason glasses with a P_2O_5 content below 40mol% are labelled “invert”.^[84]

The glassy state is not caused by chain entanglement or by a relatively stiff network, but rather by the interaction between cations and the small phosphate groups as illustrated in Figure 1.7. The high disorder responsible for forming these glasses is created by the addition of several modifier ions since the competition for the oxygen ions in the glass melt is exceedingly high, and so none can prevail, due to the “confusion” factor, hindering crystallisation and ordering process.^[84]

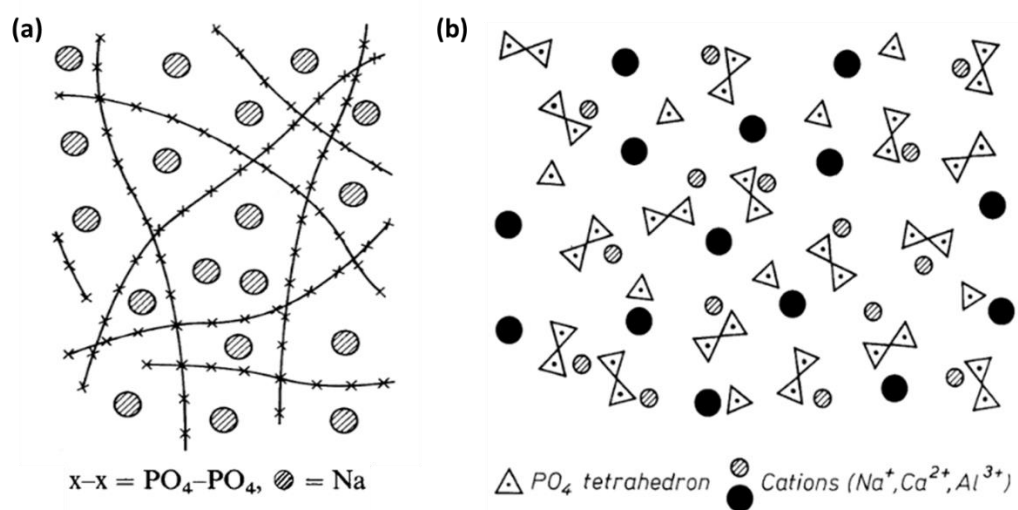


Figure 1.7: (a) Schematic model of PBG network structure showing entangled chain structures, (b) model of PBG invert structure showing no 3D network.^[84]

Motives behind the use of invert PBG in research have included reduction in dissolution rates, maintenance of neutral pH during dissolution, and to test the glass forming limits.^[85-88]

The very short chain structures of phosphate invert glasses were demonstrated in a study by Kasuga and Abe^[83] in $x\text{CaO}\cdot(90-x)\text{P}_2\text{O}_5\cdot y\text{TiO}_2\cdot(10-y)\text{Na}_2\text{O}$ compositions where the CaO content was 55 mol% or above. Kasuga *et al.*^[89] went on to demonstrate calcium phosphate apatite formation on $30\text{P}_2\text{O}_5\cdot 60\text{CaO}\cdot 10\text{TiO}_2$ phosphate invert glass by immersing samples in simulated body fluid (SBF) over a period of 20 days with a thickness of $\sim 10\ \mu\text{m}$. A thin gel layer was observed in the study onto which the apatite was deposited. This gel layer was proposed to act as a nucleating site for apatite formation.

The ion releasing abilities of $60\text{MO}\cdot 30\text{P}_2\text{O}_5\cdot 7\text{Na}_2\text{O}\cdot 3\text{TiO}_2$ (mol% M= Mg, Ca, Sr) were investigated by Lee *et al.*^[90] The study found glassification (parameter describing the glass forming ability) of the invert PBG containing MgO was easiest in comparison to Ca and Sr, and that it also released 2 to 3 times more ions than the others. Such behaviour was attributed to the larger amount of orthophosphates present in the MgO containing invert PBG. Lee *et al.*^[74] investigated a $30\text{P}_2\text{O}_5\cdot (x-60)\text{CaO}\cdot x\text{SrO}\cdot 7\text{MgO}\cdot 3\text{TiO}_2$ invert glass series on the dissolution and cell cytocompatibility behaviour. The addition of Mg^{2+} ions in the glass structure was shown to stabilise the glass as a result of its high field strength, which in turn lead to a higher number of MC3T3-E1 cell number attachment.

The intermediate role of MgO is determined by the phosphate chain lengths. When the $\text{MgO}/\text{P}_2\text{O}_5$ ratio is equal to 1 at the metaphosphate composition, anomalous property behaviour of the glasses have been observed.^[91, 92]

Other intermediate oxides of interest have been TiO_2 , as this oxide has shown to support glass formation in invert compositions.^[83, 93] When PBG's contain small Q^1 and Q^2 groups, like MgO, P-O-Ti bonds are created linking the groups.^[83, 94] Additionally, TiO_2 has shown to reduce the dissolution rate of PBGs due to the formation of crosslinks between TiO_4 or TiO_6 structural groups and phosphate tetrahedra.^[95-98]

1.6 Manufacture of microspheres

It is clear that bioactive resorbable glasses have huge potential in the biomedical field, and in order to utilise these glasses for various applications, it is important to fabricate the glass into practical morphologies for clinical applications. Spheres in particular provide the advantage of uniformity in size and shape, making delivery to the target tissue easier, as well as having increased surface area compared to irregular particles, which in turn could increase degradation rates allowing release of incorporated therapeutic ions. Spherical morphologies also allow for enhanced versatility in filling the shape of the defect compared to bulk scaffolds which tend to have predetermined shapes.^[99] Addition of porosity could further increase surface area allowing for efficient cell attachment, encapsulation and spreading, along with intrusion and extrusion of oxygen and nutrient by-products.^[100] Furthermore, porous spherical morphologies hold the capacity to enable the penetration of blood vessels, leading to an increase in cell viability throughout the entire construct. Microspheres can be defined as free flowing powders with particle sizes ranging from 1-1000 μm .

Material selection of microsphere manufacture can be application specific, for example, polymer-based porous microspheres have been extensively investigated for use as controlled drug delivery vehicles and delivery of biological components such as proteins, cells and growth factors.^[100, 101] Whereas ceramic and glass microspheres have been investigated for use in hard tissue regeneration, dental and orthopaedic applications and radionuclide applications.^[102-105] The main focus of this study was investigation into the manufacture of PBG microspheres and so the subsequent sections will cover glasses for microsphere manufacture however, in depth reviews of polymer and ceramic microspheres can be found by the following authors.^[99, 100, 106]

One particular fabrication method for producing glass spheres is via flame spheroidisation. This technique involves feeding ground glass particles through an oxy/fuel flame where the high temperatures and surface tensions created

cause re-melting and spheroidisation of the glass. Other techniques involve dropping crushed glass particles down a vertical tube furnace,^[107] cooling molten glass onto steel plates to create droplets,^[108] via the sol-gel route, and spray drying sols.^[109]

The following sections will focus on the production of microspheres from the three main glass families, borate, silicate and phosphate based glasses.

1.6.1 Borate based glass microspheres

Dysprosium lithium-borate microspheres have been formulated by Conzone *et al.*^[110, 111] for the treatment of rheumatoid arthritis, as well as in radiation synovectomy. Radioactive isotopes were chemically incorporated to the structure of the glass and flame spheroidised to fabricate microspheres in the size range of 5 and 15 μm . The radioactivity was then initiated via neutron activation, before delivery to the site of interest. The uniform size and shape of these microspheres are ideal for their use in radiation synovectomy. The solubility of this particular glass composition was found to be non-uniform; the soluble Li and B components of the glass dispersed into the simulated synovial fluid (SSF), whereas the insoluble dysprosium remained intact, resulting in a porous dysprosium phosphate- rich reaction product. This resulted in *c.a.* 80% weight loss of the microspheres after 64 days without changing the size and shape. The non-uniform behaviour was attributed to the soluble and non-soluble constituents of the glass rather than an outcome of spheroidisation, since similar results were observed for non-spheroidised particles.^[110, 111]

Following on from these findings, the resultant amorphous, porous reaction product was exploited, and a “novel” chemical process was described, yielding porous microspheres with the same size and shape as the starting product, but of a different composition. The non-uniform reaction process of dysprosium lithium-borate glass microspheres in phosphate containing solutions at 37°C presented porous microspheres with a specific surface area of around 200 m^2/g , pore volume of 0.2-0.4 cm^3/g and pore diameter of around 30nm.^[112]

Flame spheroidisation has also been utilised to fabricate hollow hydroxyapatite (HA) microspheres.^[113, 114] Firstly bulk $\text{Li}_2\text{O-CaO-B}_2\text{O}_3$ microspheres were created using this technique followed by immersion of the spheres in a phosphate buffer solution, resulting in heterogeneous precipitation of calcium phosphate. Following this the reacted spheres were subjected to heat treatment at 600°C for 4 hours to convert the amorphous calcium phosphate hollow shells into crystallised HA microspheres as illustrated in Figure 1.8.^[108, 113, 114]

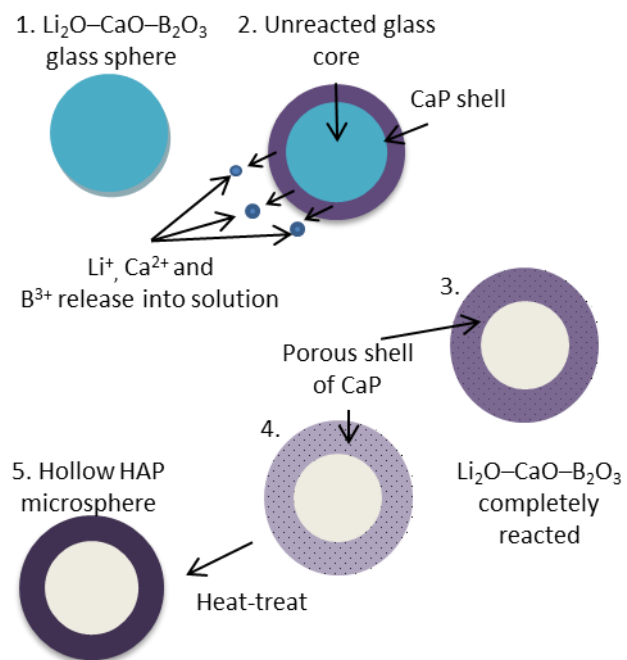


Figure 1.8: Schematic illustration adapted from Wang *et al.*^[114] showing mechanism for production of hollow, porous HAP microspheres

Post heat treatment resulted in improved strength of these microspheres, however an increase in brittleness was also observed. A study conducted by Huang *et al.*^[108] measured the strength of these hollow HA microspheres by direct unidirectional compression measured by a nano-mechanical testing machine. Compressive strengths were compared between the as prepared microspheres to the heat treated microspheres. It was found that the large surface area of the as prepared microspheres ($135 \text{ m}^2/\text{g}$), drastically fell after heat treating for 8 hours at 600°C , and on heat treating at 800°C , the surface area fell by a factor of more than 50 times to $2.6 \text{ m}^2/\text{g}$. This change in surface

area was translated in the rupture strength as microspheres heat treated at 800°C had a rupture strength of 35 ± 8 MPa as opposed to 1.6 ± 0.6 MPa for the as prepared hollow microspheres. It was suggested that the geometry of the spheres was more likely to effect the strength rather than the size, since experiments conducted on microspheres with diameters of ~ 500 and ~ 800 μm showed no difference in these properties, confirming that the compressive strength of structurally and compositionally homogenous porous spheres are independent of their size.^[108] An even greater specific surface area of 145 ± 5 m^2/g was achieved by Fu *et al.*^[107] when reacting the glass microspheres with 0.25M K_2HPO_4 at a reaction temperature of 60°C, as these parameters provided a high concentration of phosphate ions and a beneficial temperature, causing finer particle sizes of HA to form, resulting in a higher specific surface area. The same study found that reducing the reaction temperature (25°C) and the concentration of K_2HPO_4 (0.02 M) resulted in a larger ratio between the hollow core diameter to the external diameter of the microspheres, thought to be due to a more efficient packing of the fine HA particles.

Borate glasses are an ideal material to fabricate hollow microspheres due to their low network connectivity and ease of hydrolysis in acids or base. Scanning electron microscopy images (SEM) have shown these microspheres to consist of multiple porous layers which make up the shell wall of the hollow microspheres. In general it was found that the outer layer of the shells were smooth and less porous than the inner layer as shown in Figure 1.9. The most effectual variables on pore size has been found to be K_2HPO_4 concentration and reaction temperature with low solution concentrations (0.02 M) and high reaction temperatures (60°C) resulting in the smallest pore sizes (outer shell wall pore size of $\sim 10\text{nm}$). This reduction in pore size and formation of multiple layers is likely to occur due to densification of the HA shell and separation during the conversion reaction.^[107, 108]

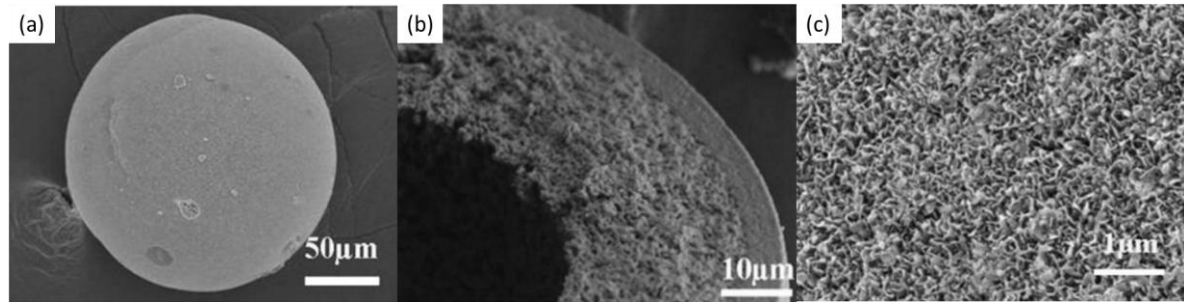


Figure 1.9: SEM showing (a) $15\text{CaO}\cdot 10.63\text{Li}_2\text{O}\cdot 74.37\text{B}_2\text{O}_3$ (wt%) glass microsphere (b) hollow HA microsphere cross section formed by reacting glass microsphere in $0.02\text{M K}_2\text{HPO}_4$ @ 37°C , pH 9 for 48h showing the concentric bilayered structure (c) HA surface at high magnification.^[107]

1.6.2 Silicate based glass microspheres

The most heavily investigated silicate based glass is 45S5 Bioglass[®] due to its inherent bone bonding ability.^[115, 116] Bioglass[®] was first discovered during the 1960's by Larry Hench^[115-117]. Thermal post processing of such glasses can pose difficulties due to the narrow thermal processing window, which can result in semi-crystalline materials. This semi crystalline behaviour has been investigated by Fu *et al.*^[118] where microspheres in the size range of 75-150 μm were fabricated using flame spheroidisation and immersed in K_2HPO_4 (5g to 500ml) in order to investigate the long term conversion to HA. In 10 years the 45S5 glass-ceramic microspheres only partially converted to a HA like material and it was concluded that immersion of these glass-ceramic 45S5 microspheres would take up to 45 years to convert to HA when immersed in 1.0 M K_2HPO_4 . Other silicate based glasses that have been flame spheroidised have been investigated by Martinelli *et al.*^[119] where flame spheroidisation again resulted in the formation of a glass-ceramic. Yttrium aluminosilicate ($45\text{Y}_2\text{O}_3\cdot 20\text{Al}_2\text{O}_3\cdot \text{SiO}_2$ (wt%)) microspheres in the size range of 20-50 μm were fabricated via flame spheroidisation for use in hepatic cancer treatment.^[120] This study investigated some of the main parameters which may influence microsphere production using a mathematical model to assess the process of glass particle spheroidisation. Parameters which may influence spheroidisation include:

- a) Physical properties:
 - i. Density
 - ii. Viscosity
 - iii. Thermal conductivity
 - iv. Particle size
- b) Flame properties:
 - i. Temperature profile
 - ii. Gas velocity
- c) Processing parameters
 - i. Geometry
 - ii. Particle feed ratio into the flame

The study concluded that spheroidisation of the glass is dependent on where the particle falls in the flame trajectory i.e. they should fall in the hottest area of the flame to increase spheroidisation efficiency.

Other glass-ceramic microspheres fabricated include aluminium iron silicate glasses, with a main crystalline phase of magnetite; suited to be used for thermotherapy for the treatment of liver cancers. Again, a flame spheroidisation technique was utilized to create microspheres with a target size distribution of 20-40 μm in order to allow easy flow through blood capillaries to the liver. In aiming to yield this specific sphere size, the authors used initial particle sizes of 38-63 μm , yet it was found that the resultant size distribution presented values greater than the original size distribution of irregular particles, with values surpassing 100 μm .^[119]

Further preparation methods previously used to create microspheres include the sol-gel method via the Stöber process.^[121] Hydrolysis and polycondensation of tetraethoxysilane ethanol solution (TEOS) has produced monodispersed silica microspheres (0.3 μm) due to repulsive forces encountered via the negative charges created under alkaline conditions. On addition of aluminium

nitrate enneahydrate ($\text{Al}(\text{NO}_3)_3 \cdot \text{H}_2\text{O}$) and silver nitrate (AgNO_3) dissolved in 2-methoxyethanol (MeOEtOH), amorphous microspheres ($0.4 \mu\text{m}$) coated in finer particles resulted, leading to aggregation of the samples. Although subsequent heat treatment at 1000°C formed larger microspheres ($8.8\text{--}10.1 \mu\text{m}$) with smoother surfaces, aggregation of the particles was not eliminated, and it was found that with increasing $\text{Al}(\text{NO}_3)_3 \cdot \text{H}_2\text{O}$ and AgNO_3 , aggregation increased linearly. The antibacterial agent release, i.e. silver ions, were only effective during initial submersion of these microspheres in ultrapure water, suggesting that silver nitrate incorporation occurred only on the surface of the spheres, creating a sort of short term antibacterial shell surrounding a silica core.^[122] An alternative method of adding aluminium tri-isopropoxide ($\text{Al}(\text{OC}_3\text{H}_7)_3$) powder to a partially hydrolysed TEOS was used to polycondense the solution in order to form Si – O – Al bonds. The silver ions were subsequently added to the aluminium triiso-propoxide/TEOS mixture in a solution of ammonia and silver nitrate and a centrifuge was used to separate solid products isolated from the solution. The resultant monodispersed microspheres had diameters ranging from $0.4 - 0.6 \mu\text{m}$ which did not change following subsequent heat treatment. Furthermore aggregation of the microspheres were not observed after application of heat, and release rates of silver ions in water were a lot more gradual than before. This more controlled release of silver ions was due to the fact that during fabrication of the microspheres, the silver ions enter the SiO_4 network accompanying aluminium ions in the form of $[\text{AlO}_4]^- \text{Ag}^+$, and ion exchange with H_3O^+ in the water slowly released Ag^+ ions from the microspheres. This alternative preparation method of silver-doped microspheres poses potential for use as antibacterial materials. Following on from this Masuda *et al.*^[123] further improved their fabrication method of creating these silver-doped silica glass microspheres by carrying out simultaneous hydrolysis and polycondensation of the TEOS with silver nitrate and aluminium nitrate solution, followed by addition of ammonia solution and centrifugal spinning, to separate monodispersed microspheres ($0.1 \mu\text{m}$). Heat treatment of the microspheres resulted in densification and reduction of micropores at temperatures above 700°C , and a reduction in the quantity of

silver ion release decreased with increasing temperature from 600-1000°C. Similar outcomes were seen with the antibacterial properties of the spheres with optimum antibacterial activity observed with microspheres heated treated at temperatures between 700-800°C.^[123]

1.6.3 Phosphate based glass microspheres

Phosphate based glasses are fully resorbable unlike silicate based glasses which can remain in the body for several years and can be post processed with a reduced risk of crystallisation. Various geometries have been produced from PBGs such as rods,^[2, 124] fibres,^[3, 43] woven textiles,^[125] scaffolds,^[126] and microspheres.^[103] Microsphere manufacture from phosphate based glasses is fairly recent and has been shown by Lakhkar *et al.*^[103] where a flame spheroidisation process was used to fabricate $50\text{P}_2\text{O}_5 \cdot 40\text{CaO} \cdot (10-x)\text{Na}_2\text{O} \cdot x\text{TiO}_2$ microspheres in the size range *c.a.* 10-200 μm . The study found spheroidisation of particles below 30 μm difficult due to agglomeration occurring at the feed apparatus. Larger particle sizes were also difficult to spheroidise due to limited flame residence time. Structural characterisation in terms of density and thermal properties such as T_g were found to be comparable to both discs and powders of the same composition, suggesting that flame spheroidisation did not affect the atomic structure of the glass but rather the morphology. The change in morphology expectedly increased degradation and ion release rates as a result of the increased surface area. This study also displayed positive biocompatibility results of the microspheres as MG63 cell attachment and spreading was observed by day 7 of culture. The microspheres appeared to have shown a stable substrate for osteoblastic cell proliferation.

Titanium doped PBG microspheres were suggested to be used as potential microcarriers to act as cell expansion platforms due to their stable surface. Guedes *et al.*^[127] investigated microspheres of the composition $50\text{P}_2\text{O}_5 \cdot 40\text{CaO} \cdot (7-x)\text{Na}_2\text{O} \cdot x\text{TiO}_2$ and in the size range of 63-106 μm on dissolution, ion release, and E12.5-13.5 CD-1 mouse embryo primary fibroblast activity. Cells cultured on the PBG microspheres containing 5mol% TiO_2 appeared to form bridges between adjacent microspheres after 7 days

however the degradation rates of the microspheres, in particular those containing 3 mol% TiO₂ resulted in an unstable surface for cell growth.

Lakhkar *et al.*^[128] went on to show enhanced proliferation of human mesenchymal stem cells and MG63 osteoblastic cells when cultured with the 5 mol% TiO₂ containing glass (50P₂O₅·40CaO·5NaO·5TiO₂) microspheres (50–100 μm) when compared to commercially available silica glass microspheres (Polysciences Inc., USA). The study also found that the condition in which the MG63 cells were cultured played an important role on the outcome, since those cultured in a bioreactor (spinner flask) showed a 24-fold increase in cells number over a 7 day period compared to an 8-fold increase when cultured under static conditions. It was evident from the study that it was not solely due to the mechanical forces exerted on the cells that resulted in an increase in cell number but that material chemistry may also have played an important role, as cell numbers seeded on the commercially available silica microspheres resulted in a 6-fold increase when cultured in a bioreactor (4500 series; Corning) and 7-fold increase when cultured in static conditions.

Alternate methods of microsphere production to flame spheroidisation have included the use of a vertical tubular furnace, where glass particles are introduced at the top of the surface and allowed to fall through, where the action of gravity and high temperatures reform the irregular particles into spheres. A study by Sene *et al.*^[129] investigated high P₂O₅ containing glass microspheres which showed resistance to crystallisation during spheroidisation and displayed advantageous chemical durability and cell viability which makes the spheres promising for use in radiotherapy applications.

1.6.4 Porous glass manufacture

Porosity can be defined as the ratio between void spaces/ pore volume and the bulk volume/ total volume occupied by the solid and is generally expressed as a percentage.

The International Union of Pure and Applied Chemistry (IUPAC) defines pore sizes based on the internal pore width:^[130]

- Micropores = <2 nm
- Mesopores = 2 nm – 5 nm
- Macropores = >50 nm

Introduction of porosity into spheres is of great advantage in the biomedical field, particularly to allow for penetration of cells throughout the structure.

Historically pore or bubble formation during a glass melt was deemed as undesirable defects.^[131] During batch melting, a large volume of gasses are released as the raw materials decompose. The solubility of these gasses in the glass melt can be defined as “the equilibrium concentration of dissolved gases in those liquids or melts at a given gas pressure and given temperature,”^[131] where the solubility of the gasses is highly dependent on temperature, glass composition and gas fugacities (function of gas partial pressure). On examination of molten silicates and borates, the solution of gasses in the molten state are a result of; i) chemical and ii) physical processes. i) Chemical reactions occur as gasses are released from salts in the molten state, such as H₂O, CO₂ and SO₃. Chemical solubility is proportional to the basicity of the melt. ii) Physical solubility is dependent on the interaction between gases and melts and the amount of physically dissolved gas is determined by the outer gas pressure, magnitude of the gas atoms/ molecules, temperature of the melt and the size and volume of the holes available in the melt.^[131] Figure 1.10 illustrates the dependence of temperature on the chemical solubility of gasses, where an increase in temperature decreases the chemical solubility of oxygen, carbon dioxide and sulphur but increases for nitrogen and water vapour in a soda-lime silica glass melt.

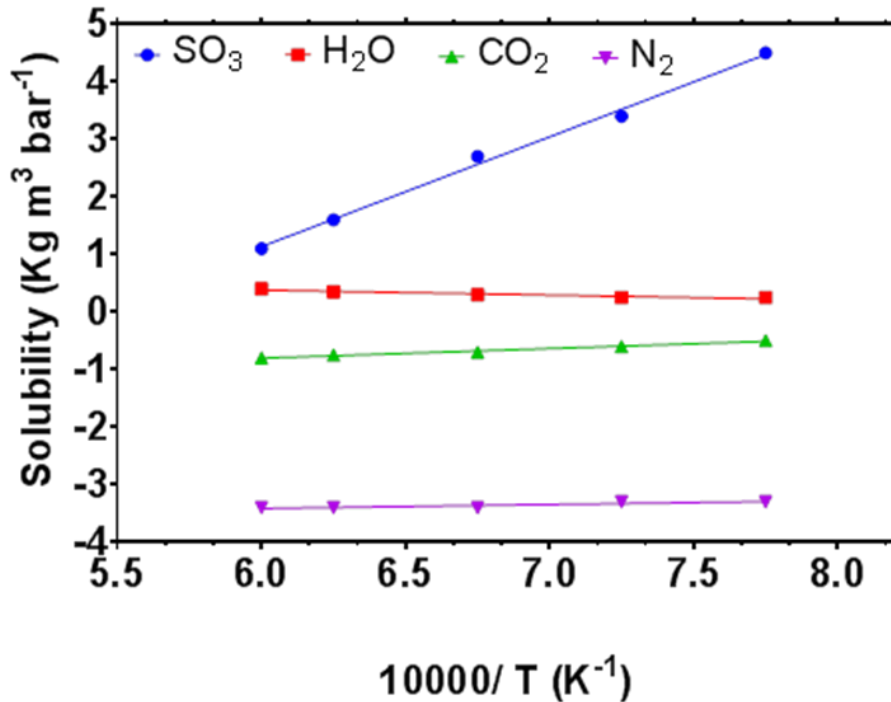


Figure 1.10: The effect of temperature on the solubility of various gasses in a soda-lime silica glass melt.^[131]

Shelby^[32] outlines several methods as to how bubbles may form during melting of glasses as summarised below:

- a) Physical entrapment of atmospheric gasses during batching or by the decomposition of batch components.
- b) Differing the particle size variation of batch components can increase the number of interstices in the unmelted batch.
- c) Agglomeration of particles which can encourage atmospheric gas entrapment within the agglomerate.
- d) Generation of O₂, CO₂ or H when metals come in contact with the melt.
- e) Supersaturation of gasses, for example in silica rich melts, carbon dioxide is present as CO₂ molecules, which enriches the melt, reacting with alkali-rich melts to form carbonate species. During the early stages of batching, the solubility of carbon dioxide is quite high, but during melting, local enrichment of silica occurs which converts the dissolved species to CO₂ molecules which has a lower solubility. This in turn locally saturates the melt with CO₂ bubbles.

Carbonates in group II of the periodic table become more thermally stable down the group, thus requiring more energy to decompose and release CO₂ as a by-product.

Calcium carbonate has previously been used as a pore generating agent in ceramics used in filtration applications.^[132] Previously, limestone was used as the pore generating agent which was mixed with the other components such as kaolin, potassic feldspar, albite, quartz and white clay, and compacted into samples by pressing. These samples were then degassed and sintered. Thermograms revealed the release of CO₂ from the CaCO₃ between 650 and 790°C thus degassing was carried out between 400 and 800°C. The release of CO₂ during this process resulted in smaller rounded pores, and formulations with higher CaCO₃ content resulted in a larger amount of closed pores as determined by density measurements.

Other materials which have utilised CaCO₃ as a pore forming agent included poly(lactic-co-glycolic acid)/ CaCO₃ microspheres.^[133] Microspheres were created using a solid/ oil/ water emulsion solvent evaporation technique. Microsphere morphology was found to have a solid centre with the surface covered in an even distribution of open macropores. The macropore sizes were found to reach 10 µm and a size dependent effect was observed where increasing the CaCO₃ size reduced macroporosity and resulted in irregular pit formation.

1.7 Summary

On reviewing the available literature it was apparent that release of therapeutic ions from phosphate based glasses and its relation to the structure of the glass is still not well understood. This project aimed to bridge this gap by gradually introducing a therapeutic ion to the glass network and understanding its effect on the glass structure and dissolution properties. Furthermore, previous studies showed the fabrication of PBG's into various morphologies such as fibres, textiles and microspheres, however, to date none have shown the incorporation of porosity to morphologies which can be delivered easily in a clinical setting such as microspheres.

1.8 Aims and objectives

The main aim of this project was to manufacture and characterise novel porous phosphate based glass microspheres suitable for use in biomedical applications, with a particular focus on minimally invasive injectable prophylactic, bone treatment options. The project also aimed to develop optimal glass formulations which could release therapeutic ions in a controlled manner, particularly for repair and regeneration of bone for the prevention of fragility fractures

The project objectives included:

- I. Introduction of strontium ions in to the PBG network which could be release to give beneficial, therapeutic effects.
- II. Asses the cytocompatability of Ca/Sr substituted PBG's using a MG63 cell line.
- III. Carry out structural characterisation to reveal the short and intermediate range order of the glass and to understand the interrelationship between durability, degradation and composition of the glass.
- IV. Optimise the manufacturing process to fabricate microspheres which could improve delivery to the site of interest in clinical settings.
- V. Introduce porosity to the microsphere structure
- VI. Optimise and characterise porosity in terms of yield of porous microspheres and their porosity levels

To the knowledge of the author, no work in the literature has previously presented on the manufacture of highly porous, PBG microspheres which could deliver therapeutic ions as a degradation by product and incorporate biological components for release.

1.9 Thesis outline

The outcomes of the aims and objectives have been divided into several chapters as outlined below:

Chapter 2: Outlines the materials and methods used throughout this thesis and the experimental detail regarding specific techniques such as neutron diffraction.

Chapter 3: Details the results and discussion on the physico-chemical analysis of calcium/ strontium substituted, near-invert phosphate based glasses in the system $40\text{P}_2\text{O}_5 \cdot (16-x)\text{CaO} \cdot 20\text{Na}_2\text{O} \cdot 24\text{MgO} \cdot x\text{SrO}$ glass, where x is 0, 4, 8, 12 and 16 mol%. This chapter also discusses the cytocompatibility of the glass discs when cultured with the MG63 cell line, and introduces preliminary findings when cultured with human derived osteoclasts.

Chapter 4: Expands on chapter 3, by discussing the short (atomic level) and medium range structure of the calcium/ strontium substituted glasses as determined by techniques such as ^{31}P and ^{23}Na NMR, FTIR and neutron diffraction.

Chapter 5: Outlines the results and discussions of invert phosphate glasses in the glass system $(40-x)\text{P}_2\text{O}_5 \cdot 16\text{CaO} \cdot 20\text{Na}_2\text{O} \cdot 24\text{MgO} \cdot x\text{TiO}_2$ (where x = 3, 5, 7, 10 and 12) explaining the physico-chemical properties of the glasses and the structure as determined via ^{31}P NMR. The aim of this chapter was to develop a glass system with a high pyrophosphate content.

Chapter 6: Explains a novel manufacturing technique to fabricate both non-porous and porous microspheres. This chapter discusses the developmental process of creating novel, highly porous microspheres and characterisation of the end product.

Chapter 7: Summarises the findings of all the work in this thesis and puts forward areas of future work.

CHAPTER 2: MATERIALS AND METHODOLOGY

2.1 Introduction

This chapter covers the manufacture of materials and experimental techniques used for characterisation throughout this thesis.

2.2 Glass manufacture and characterisation

2.2.1 Glass fabrication

All glass samples investigated in Chapter 3, 4 and 6 were produced using the following precursors; P_2O_5 , NaH_2PO_4 , $CaHPO_4$, $MgHPO_4 \cdot 3H_2O$, and $SrCO_3$ (Sigma Aldrich, UK), as were those studied in Chapter 5 with the replacement of $SrCO_3$ with TiO_2 , and NaH_2PO_4 with $NaCO_3$. All glass compositions along with their respective codes are displayed in Table 2.1. The sample preparation methods have also been highlighted in Table 2.1. The weighed precursors were thoroughly mixed and heated in a 5% Au/Pt crucible for Sr containing glasses and a Rh/Pt crucible for Ti containing glasses at 350°C for 30 minutes, followed by melting at 1150°C for the strontium substituted glasses or 1200 °C for titanium containing glasses for 1.5 hours. All Ti containing glasses were gently stirred every 30 minutes. The molten glass was then either quenched between two stainless steel plates or poured into preheated graphite moulds ($\sim 10^\circ C$ above T_g of each sample. NB the T_g in Table 2.1 was taken as the midpoint value) and annealed for 1h, followed by slow cooling to room temperature overnight.

Table 2.1: Compositional information, showing the glass transition temperature of samples, and whether the sample was cast or quenched (represented by X).

Glass code	P ₂ O ₅ (mol%)	CaO (mol%)	Na ₂ O (mol%)	MgO (mol%)	SrO (mol%)	TiO ₂ (mol%)	Melt Temp. (°C)	T _g (±1°C)	Melt quenched	Cast rod
CaP₂O₆	50	50	-	-	-		1150	-	X	-
NaPO₃	50	-	50	-	-		1150	-	X	-
MgP₂O₆	50	-	-	50	-		1150	-	X	-
SrP₂O₆	50	-	-	-	50		1150	-	X	-
P40	40	16	20	24	-		1150	450	X	X
Sr4	40	12	20	24	4		1150	447	X	X
Sr8	40	8	20	24	8		1150	447	X	X
Sr12	40	4	20	24	12		1150	447	X	X
Sr16	40	-	20	24	16		1150	443	X	X
P37Ti3	37	16	20	24	-	3	1200		X	-
P35Ti5	35	16	20	24	-	5	1200		X	-
P33Ti7	33	16	20	24	-	7	1200		X	-
P30Ti10	30	16	20	24	-	10	1200		X	-
P28Ti12	28	16	20	24	-	12	1200		X	-

2.2.2 Powder X-ray diffraction

A Bruker D500 X-ray diffractometer was used to determine the amorphous nature of the samples at room temperature with Ni-filtered CuK α radiation (λ 0.15418 nm), generated at 40 kV and 40 mA. A step size of 0.04° and step time of 2s was used over an angular range 2θ from 10° to 80°.

2.2.3 Scanning electron microscopy/ Energy dispersive X-ray spectroscopy (SEM/ EDX)

Samples were examined using the Philips XL30 (SEM) operated at 20 kV, in order to qualitatively examine the microparticles, bulk microspheres and porous microspheres manufactured. Representative samples were mounted onto a carbon tab attached to an aluminium stub and sputter coated with ~15nm of platinum.

To qualitatively examine internal structures, the microspheres were embedded in a cold set epoxy resin and polished with SiC paper followed by a diamond cloth. Industrial methylated spirit (IMS, Sigma Aldrich, UK, $\geq 99.5\%$) was used as a lubricating medium. Samples were then placed in an ultrasonic bath of IMS for 10 minutes and left to dry, followed by platinum sputter coating with a thickness of ~15nm.

Compositional analysis was carried out on flat samples which had been embedded in resin as mentioned above and carbon coated with a thickness of ~15nm. Energy dispersive X-ray spectroscopy (EDX) was conducted using Oxford Instruments INCA EDX system fitted with a Si-Li crystal detector. The EDX system was attached to the Philips XL30 scanning electron microscope and operated in backscattered electron mode, with an accelerating voltage of 20kV and a working distance of 10mm. Quantitative analysis was performed using stoichiometry normalised results with the following standards; NaAlSi₂O₆ (sodium), MgO (magnesium), GaP (phosphorous), SrF₂ (strontium), CaSiO₃ (calcium) and Ti (titanium). Analysis was conducted on three separate areas of each sample, and three separate samples were used for each category.

2.2.4 Density measurements

The density of each sample was measured three times using Micromeritics Accupyc1340 pycnometer, with helium as the displacement gas. For each measurement, a series of repeat readings were taken until a series of five results agreed within an error of $\pm 0.02\text{gcm}^{-3}$.

2.2.5 Thermal analysis via Differential scanning calorimetry

The energy change that occurred whilst the samples were heated was measured via differential scanning calorimeter (DSC). An empty pan measurement was carried out before experiments to represent the baseline from which the thermal heat flow traces for each sample were subtracted from in order to obtain specific heat capacity of the materials.

The T_g , crystallisation temperature (T_c), and melting temperature (T_m) of each glass sample was determined using a DSC TA Instruments Q600, UK. Around 40mg of each sample with particle size of 45-63 μm was heated in a platinum pan from 50°C to 1200°C using a heating rate of 10°C/minute in flowing Nitrogen gas (100ml/min). The T_g was taken as the onset of change in heat flow.

2.2.6 Fourier transform infrared spectroscopy

The Fourier transform infrared (FTIR) spectra were obtained using a Bruker Tensor-27 spectrometer (Germany) on absorption mode. Glass samples were ground to a fine powder (45-63 μm) and scanned in absorbance mode in the region of 4000 to 550 cm^{-1} (wave numbers) using standard pike attenuated total reflectance (ATR) cell (Pike technology, UK). The spectra were analysed using the OPUS™ software which included subtraction of air as background.

2.2.7 Solid state NMR

All Solid-state nuclear magnetic resonance (NMR) spectra were obtained via the EPSRC UK National Solid-state NMR Service at Durham using a 400 MHz Varian VNMRS spectrometer. Deconvolution of peaks was carried out using the programme fityk.^[134]

2.2.7.1 ³¹P NMR

Solid state ³¹P NMR experiments were conducted using a 4mm probe with a spinning speed of 11-12 MHz. The ³¹P spectra were recorded at a Larmor frequency of 161.87 MHz. A single pulse program with 300 second pulse delay and 4.4 μs pulse width was used. The spectra was referenced using H₃PO₄. Contributions from the respective spinning sidebands have been included in the measurements of the areas of the isotropic peaks for each site.

2.2.7.2 ²³Na NMR

Solid-state ²³Na NMR spectra conducted at a Larmor frequency of 105.78 MHz, with a 4mm probe at a spinning speed of 11-12 MHz. Again a single pulse program with a 1 second pulse delay and 4.4 μs pulse width was used and all spectra were referenced using 0.1 M aqueous NaCl.

2.2.8 Dissolution studies

The dissolution studies were conducted using glass discs (c.a. 9mm Ø by 5mm) degraded in 30ml of ultra-pure water (18.2 MΩ) and placed in either a borosilicate glass vial or polytetrafluorethylene (PTFE) tube. Samples were incubated (Memmert incubator IF160 plus (resolution of 0.1°C)) at 37°C. The media was replenished at each time point (1, 3, 7, 14, 21 and 28 days) with 30ml of fresh ultra-pure water and the pH (Seven Compact, PurePro, Mettler Toledo) was measured at each time point. This study was repeated using discs with a dimension of c.a. 9mm Ø by 10mm in deionised water (DI) and phosphate Buffered Saline (PBS) for the Sr glass series. At each time point, dimensions (height and width) of the discs and mass were recorded from which a) average mass loss and b) degradation rate were calculated as follows:

$$\text{a) } M = \frac{m_i - m_t}{SA}$$

b) Determined via the slope of best fit for each composition tested

Where m_i is the initial mass of the sample, m_t is the mass of degraded sample measured at time t , and SA is the surface area of the sample at time t .

2.2.9 Ion release studies

2.2.9.1 Cation release

The release of Ca^{2+} , Na^+ , Mg^{2+} and Sr^{2+} from the dissolution media at each time point were quantified using an ICS-1000 ion chromatography system (Thermo Scientific, Dionex, UK). An eluent of 20mM methanosulfonic acid (Sigma-Aldrich) was used. All specimens were analysed using a Dionex IonPac[®] CS12A 2mm x 250mm analytical column, and analysed under suppressed conductivity (CSRS 300 2mm, Thermo Scientific, Dionex). Results were calculated against a four-point calibration curve using a Combined Six Cation Standard II and Strontium (Sr^{2+}) 1000mg/l in water (Thermo Fisher Scientific). A stock solution containing the cations was prepared. From which serially diluted cation standards were prepared at the following dilution factors; 1:1024, 1:256, 1:64 and 1:16 (The equating ppm standards are shown in Table 2.2). Data analysis was performed using the Chromeleon[®] software, and the cumulative release per unit area of each sample was calculated.

Table 2.2: The cation calibration standards used along with their dilution factor and its equating concentration in ppm.

Cation	1:1024	1:256	1:64	1:16
Na⁺	0.197 ppm	0.789 ppm	3.156 ppm	12.625 ppm
Mg²⁺	0.244 ppm	0.977 ppm	3.906 ppm	15.625 ppm
Ca²⁺	0.485 ppm	1.941 ppm	7.766 ppm	31.063 ppm
Sr²⁺	0.485 ppm	1.953 ppm	7.813 ppm	31.25 ppm

2.2.10. Anion release

Phosphate anion release was conducted by Song Yi Baek (UCL, London) using a Dionex ICS-2500 ion chromatography system (Dionex, UK), fitted with a 25 μ l loop. All specimens were analysed using an IonPac AS16 anion exchange column (4mm x 250mm). A KOH (potassium hydroxide) eluent was used along with an Anion Self-Regenerating Suppressor. The sample run time was 30 minutes, with a gradient programme starting at 25 mM KOH. After 14 minutes this increased to 40 mM over 8 minutes and remained there for 4 minutes. Following this another linear increase to 60 mM in 1 minute took place and remained at 60 mM for 4.5 minutes. Following this, a linear decrease down to 25 mM over 1 minute took place. A 1000ppm stock solution of sodium phosphate tribasic (Na_3PO_4), trisodium trimetaphosphate ($\text{Na}_3\text{P}_3\text{O}_9$), pentasodium tripolyphosphate ($\text{Na}_5\text{P}_3\text{O}_{10}$), (Sigma, UK) and tetrasodium pyrophosphate ($\text{Na}_4\text{P}_2\text{O}_7$) (BDH, UK) was prepared. From which serially diluted 125, 50, 10, and 5 ppm standard solutions were obtained. Data analysis was performed using the Chromeleon[®] software, and the cumulative release per unit area of each sample was calculated.

2.3 Cytocompatibility studies

2.3.1 Cell culture

Osteoblast-like cells MG63 (obtained from European collection of cell cultures - ECACC) were cultured using sterile/aseptic techniques in Dulbecco's Modified Eagle Media (DMEM) supplemented with 10% foetal calf serum (FCS), 2% HEPES Buffer, 2% antibiotics- antimycotic agents, 1% L-glutamine, 1% non-essential amino acids (Gibco Invitrogen, UK) and 0.85 mM of ascorbic acid (Sigma Aldrich, UK), at 37°C in a humidified atmosphere of 5% CO_2 .

Cells were cultured in a 75cm² flask (Falcon, Becton, Dickinson and Company; UK) at 37°C in a humidified atmosphere of 5% CO_2 , until cells reached 80% confluency, after which the subconfluent cells were dissociated from the flask using warm (37°C) trypsin-EDTA (2.5g/L trypsin and 0.8 g/L EDTA) in 10mM

HEPES buffer. After 2 minutes of incubation, warm culture media was added to the flask to halt the reaction, and the cell suspension was transferred to universal tube followed by pellet formation via centrifugation at 1200 rpm for 4 minutes. The cell pellet was re-suspended in fresh culture media and the cell concentration was determined using a Haemocytometer where viable cells were identified with trypan blue and counted using a phase contrast microscope. Trypan blue is a dye exclusion test where viable cells do not take up the impermeable dye however, dead cells which are permeable take up the dye.

Cells were seeded onto the surface of each disc at a concentration of 40,000cells/cm² in a 48 well plate. The sample P40 and tissue culture plastic (TCP) were employed as a positive control. All samples were incubated for the following time points; Days 1, 3, 7 and 14. The culture media was changed at 2 day intervals.

2.3.2 Cell metabolic activity

At each time point, samples were washed three times with warm PBS (37°C). Alamar Blue solution (1:9 Alamar blue: Hanks Balanced Salt Solution (HBSS)) (1ml) was added to each well, and incubated for 90 minutes at 37°C, in an atmosphere containing 5% CO₂. The well-plate was then placed on a shaker at 150 rpm for a further 10 minutes. Aliquots of 100 µl were taken in triplicate from each well and transferred to a 96-well plate, including three blanks. An FLx800 fluorescence microplate reader (BioTek Instruments Inc.) was used to measure fluorescence at 530nm excitation and 590nm emission wavelength.

2.3.3 DNA content

Samples were washed at each time point, three times with warm (37°C) PBS and immersed in 1 ml of deionised water. Samples were freeze-thawed three times to lyse the cells and release nuclear content. Lysed samples were then thoroughly mixed using a vortex for 30-60 seconds and 100 µl of each sample was aliquoted into a 96-well plate. Hoechst 33258 stain was prepared (1 mg of BisBenzimide stain dissolved in 1 ml of double distilled water and diluted to 1:50 in TNE buffer) and DNA standards were prepared using calf thymus DNA

(Sigma, UK) and TNE buffer (10 mM Tris, 2M NaCl, and 1mM EDTA in deionised water, adjusted to pH 7.4) as a diluent, to generate a standard curve for DNA concentrations. Each well was then topped with 100 µl of Hoechst 33258 stain and agitated on a plate shaker. Fluorescence was measured at 360 nm excitation and 460 nm emission using a FLx800 microplate fluorimeter (BioTek Instruments).

2.3.4 Alkaline phosphatase activity

The Granustest 25 alkaline phosphatase assay (Randox, UK) was used to measure alkaline phosphatase activity. Aliquots of 50 µl of cell lysate (as prepared for cell proliferation assay in section 2.4) in triplicate were added to a 96-well plate and topped with 50 µl of alkaline phosphatase substrate (p-nitrophenyl phosphate 10 mmol.l⁻¹ in diethanolamine buffer 1 mol.l⁻¹ at pH 9.8, with MgCl₂ 0.5 mmol.l⁻¹). Plates were shaken gently for 5 minutes on a plate shaker and the absorbance was measured at wavelength of 405nm and 620nm using a ELx800 microplate colorimeter (BioTek Instruments).

2.3.5 Cell morphology

At each time point one disc of each composition was selected and washed three times in warm (37°C) PBS and fixed in 3% glutaraldehyde in 0.1 M sodium cacodylate buffer fixative for 30 minutes. Fixative was then replaced with 7% sucrose solution for 30 minutes. Specimens were then washed three times with 0.1 M cacodylated buffer for 5 minutes. Each sample was then covered in 1% osmium tetroxide in PBS for 45 minutes in a fume cupboard. This was followed by a dehydration process using a graded ethanol series (20% ethanol for 2 minutes, follow by subsequent washing in 30, 40, 50, 60, 70, 80, 90 and 100% ethanol for 5 minutes at each concentration) and dehydrating the samples in 100% ethanol for a second time for 5 minutes. The samples were then dried for 5 minutes using Hexamethyldisilazane (HMDS) (x2) to reduce artefacts such as shrinkage and surface structure collapse caused by the effects of surface tension when air dried following dehydration.

Samples were then mounted onto a carbon SEM stub and sputter coated with ~15nm of platinum. Morphology of the cells was visualised using a Philips XL30 scanning electron microscope operated at 10kV.

2.3.6 Statistical analysis

Average values and standard error were calculated for three iterations of the cytocompatibility experiment where each sample size was n=5. In addition, Average values and standard deviation were calculated for the dissolution samples. Statistical analysis was performed for the cell metabolic activity, DNA content, alkaline phosphatase activity, and the Ca/ Sr substituted PBG dissolution study using Prism software package (version 7.01, GraphPad Software, San Diego, CA, www.graphpad.com). Two-way analysis of variance (ANOVA) was calculated followed by a Tukey's multiple comparison test. The mean difference was considered to be significant at 0.05 and 95% confidence interval.

2.4 Osteoclast culture

All osteoclast culturing was carried out by Paul Millns (QMC, University of Nottingham).

2.4.1 Cell culture

Approximately 50 ml of human peripheral blood from a healthy adult donor was collected in lithium heparinised tubes. The blood was mixed in a 1:1 ratio with α MEM, and 25 ml of the blood was layered onto 14 ml of Histopaque 1077 (Sigma Aldrich, UK) and centrifuged at 400g for 30mins at 20°C. The buffy layer at the interface was then removed and diluted in 110 ml of α minimum essential media (α MEM), and again centrifuged at 300 g for 20 mins in order to isolate the monocytes.

The monocytes were then suspended in 5 ml of α MEM with 10% foetal calf serum (FCS), 100 μ /ml penicillin and 100 μ g/ ml streptomycin (PS) and 2 mM glutamine. 10 μ l of cells were then diluted with 10 μ l of 5% acetic acid. Cells were then counted and cell concentration was adjusted to 5x10⁶ cell / ml.

100 μ l of cells were seeded directly onto PBG discs (P40, Sr4, Sr8, Sr12 and Sr16) and incubated at 37°C in 7% CO₂ for 2hrs. Non-adherent cells were then removed by washing the discs twice with 200 μ l of α MEM without FCS. The final media contained 10% FCS, PS, Glutamine, macrophage-colony stimulating factor (M-CSF) 25ng/ml and RANKL 30ng/ml. The media was changed every 2-3 days and cells were cultured up to 14 days.

2.4.2 Tartrate-resistant acid phosphatase staining

The Sigma-Aldrich Tartrate-resistant acid phosphatase (TRAP) staining protocol was used. At day 14, all samples were washed three times with distilled water, and fixed with formalin by immersing in the solution for 30 seconds and thoroughly rinsed with deionised water. Then, 0.5 ml of Fast Garnet GBC base solution and 0.5ml of sodium nitrite solution were mixed in two test tubes each by gently inverting for 30 seconds and allowed to stand for 2 minutes. A Coplin jar of 45 ml of pre-warmed (37°C) deionised water, the Fast Garnet GBC base solution, 1 ml of the above prepared Naphthol AS-BI Phosphate Solution, and 2 ml of acetate solution was mixed as well as a second Coplin jar of 45 ml of pre-warmed (37°C) deionised water, the Fast Garnet GBC base solution, 1 ml of the above prepared Naphthol AS-BI Phosphate Solution, 2 ml of acetate solution and 1 ml of tartrate solution. The Coplin jars were warmed to 37°C in a water bath and the discs were added and incubated for 15 minutes at 37°C in the dark. Samples were then thoroughly rinsed in deionised water and counterstained for 2 minutes with Hematoxylin Solution, Gill No. 3. The samples were then washed for several minutes in alkaline tap water, air dried and viewed under a Zeiss Axiophot light microscope.

2.5 Neutron Diffraction Theory and Application

2.5.1 An Introduction

This section outlines the theory behind neutron diffraction (ND) techniques and the application of ND for the study of glass structure.

Neutrons are considered as either a wave or particle. Typically when discussing the production and detection of neutrons, the neutron can be considered to be a particle, and when interpreting the scattering from a sample, the neutron is considered as a wave. These wave-like particles interfere when scattering through samples if the wavelength is similar to the interatomic distances present in the sample. This is because de Broglie showed that the symmetry in

nature between particles and waves give a relationship between the wavelength, λ , of a neutron and its velocity, v :

$$\lambda = \frac{h}{m_n v} \quad (10)$$

Where h is the Planck's constant. Neutrons with wavelength similar to that of inter-atomic distances are called thermal neutrons. They are used in neutron diffraction because they produce interference effects as they pass through a material.

Neutron diffraction determines structure at the atomic level by using the inherent properties of the neutron. Neutrons have zero charge and are highly penetrating. A flux of neutrons interact directly with the nucleus of an atom, rather than the electron cloud as is the case for X-ray diffraction, and it is the amount of scattering from the nuclei of a material that occurs which is detected. This means that, unlike X-rays where the scattering intensity is proportional to the number of electrons in an atom or the atomic number, neutron scattering is dependent on the structure of the nuclei which varies haphazardly across the periodic table. As a result neutron diffraction allows for the detection of lighter elements in presence of heavier atoms. Furthermore, neighbouring atoms in the periodic table can have substantially different scattering lengths allowing easier distinguishability between elements, since the scattering intensity is not proportional to the number of electrons in an atom or the atomic number. In addition, neutrons have spin $\frac{1}{2}$ which is associated with the magnetic moment of the neutron (i.e. a non-zero magnetic dipole moment), so there is a magnetic interaction between a neutron and the (unpaired electron in the atoms in the) sample however, a detailed consideration of such magnetic interactions is beyond the scope of this thesis.

The interaction between a neutron and sample is relatively weak due to the lack of charge of a neutron, and thus ND is an intensity limiting experimental

technique. Nevertheless, by using large sample volumes (1 to 2cm³) and long counting times, respectable statistical accuracy can be achieved.

2.5.2 Neutron source at ISIS

Neutrons are produced via nuclear reactions in several ways; fission, photofission, spallation and fusion.^[135] All neutron diffraction experiments carried out in this work were conducted at ISIS, STFC Rutherford Appleton Laboratory, UK which is a pulsed neutron source. Isis is a neutron and muon source with 2 target stations and 27 instruments. The proton accelerator source is made up of an i) injector and ii) synchrotron. The i) injector consists of an ion source which produces negative hydrogen ions which are then eventually accelerated to 37% of the speed of light. The ii) synchrotron is composed of a ring of powerful magnets which focus and bend the beam into a ring. As the negatively charged hydrogen ions enter the synchrotron, a thin alumina foil strips the beam of electrons leaving behind a stream of protons which are then further accelerated using radio-frequency electric fields. The protons are then separated into two bunches travelling at 84% of the speed of light after *ca.* 10,000 revolutions. These proton bunches are then ejected at 50 Hz and collide with a tungsten target.

The tungsten target produces neutrons via spallation. As the high energy protons hit the target, neutrons are driven off from the nuclei of the target's atoms resulting in an intense pulse of neutrons. These neutrons are then slowed down by an array of hydrogen-containing moderators and directed towards an assortment of instruments, each optimised to examine various material properties.

2.5.3 General materials diffractometer (GEM)

All ND experiments in this study were conducted on the General Materials Diffractometer (GEM). GEM has been argued to be the world's leading material diffractometer, particularly for studying amorphous samples.^[136-138] One

property that gives this diffractometer its status is the large array of detectors, shown in Figure 2.1, which covers a wide scattering angle between 1.1° to 169.3° , and an azimuthal range of $\pm 45^\circ$.^[136] This large angular coverage yields data with high resolution and high stability over a wide Q range.^[137, 138]

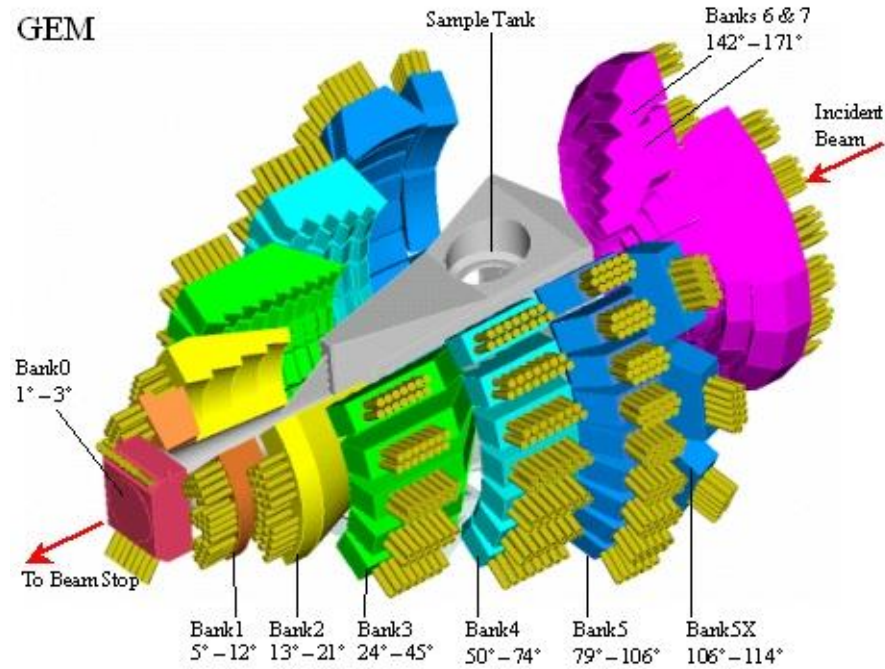


Figure 2.1: The General materials diffractometer at ISIS^[136] showing the large array of the detector banks and the sample tank position.

Since GEM is a pulsed source diffractometer it allows for time-of-flight (T-O-F) measurements. This involves measuring the time taken, t , for a neutron to travel the entire flight path, L (17.0m), from the moderator (which slows the neutron beam down to thermal energies) to the detector (ZnS scintillators) via the sample. The kinetic energy of the neutron determines this time. The detectors measure both the number of neutrons arriving at the detector (scattered neutron intensity) as well as the time taken for the neutron to arrive. Intensity of the scattered neutron (wavelength, λ) is measured as a function of time;

$$t = \frac{m_n}{h} L\lambda, \quad (11)$$

Where m_n is the neutron mass, h is Plank's constant.

2.5.4 Outline of Theory and Experimental Application

2.5.4.1 Differential cross section

During a ND experiment it is the differential cross section which is measured, defined as:

$$\frac{d\sigma}{d\Omega} = \frac{R_{tot}}{N\phi d\Omega} \quad (12)$$

Where R_{tot} is the number of neutrons scattered per second into a solid angle $d\Omega$, N is the total number of atoms in the sample and ϕ is the incident neutron flux on the sample. During a scattering experiment, an incident beam of neutrons with a wave vector \bar{K}_i and energy E_i is incident on a sample, scattering the neutron beam through an angle 2θ , resulting in a transfer of energy, $\hbar\omega$, and momentum, $\hbar\bar{Q}$, to the sample

$$\hbar\omega = E_i - E_f \quad (13)$$

$$\hbar\bar{Q} = \bar{K}_i - \bar{K}_f \quad (14)$$

Where E_f and \bar{K}_f are final energy and final wave vector respectively.

It is important to understand that during a ND experiment, the detector fixed at a scattering angle of 2θ records both elastic (total scattering) and inelastic scattering contributions. Since most glasses are an isotropic material, only the elastic scattering values are of importance when determining the structure. Henceforth, the energy transfer equals zero, and the magnitude of momentum transferred, Q , is given as

$$Q = \frac{4\pi \sin \theta}{\lambda} \quad (15)$$

Here the scattering intensity is dependent on the magnitude of the moment transfer $Q = |\bar{Q}|$ rather than the direction of \bar{Q} .

Inelastic scattering is corrected for in the programme GUDRUN. ^[139]

2.5.4.2 *Experimental Data Correction*

In order to achieve reliable structural information, it is necessary to carry out experimental corrections for any processes that may cause Q – dependent amplification or suppression of data. Vanadium foil is used to make containers for the glass samples due to its scattering being almost entirely incoherent (i.e. very low coherent scattering) and showing extremely small Bragg peaks which can easily be subtracted during the correction. For all experiments, data for a vanadium (V) or vanadium-niobium rod (V-Nb) were collected to normalise the scattering data on an absolute scale, removing the background flux from the sample data (see Figure 2.2). Measurements of the empty instrument and empty container were also obtained in order to carry out the appropriate corrections using the GUDRUN^[139] and ATLAS^[140] software. The following effects were corrected for:

- i) Detector dead time – where suppressed signals are corrected at the more intense regions caused by the inability of the detector to count a neutron periodically.
- ii) Background subtraction – to remove any contributions arising from the sample container or general background using data for the empty chamber
- iii) Absorption – when a neutron may be permanently absorbed by a nucleus
- iv) Attenuation – when further scattering events cause a reduction in the incident and scattered flux of neutrons. Data acquired from the vanadium rod.
- v) Multiple scattering – can add to further background signals when neutrons are scattered more than once.

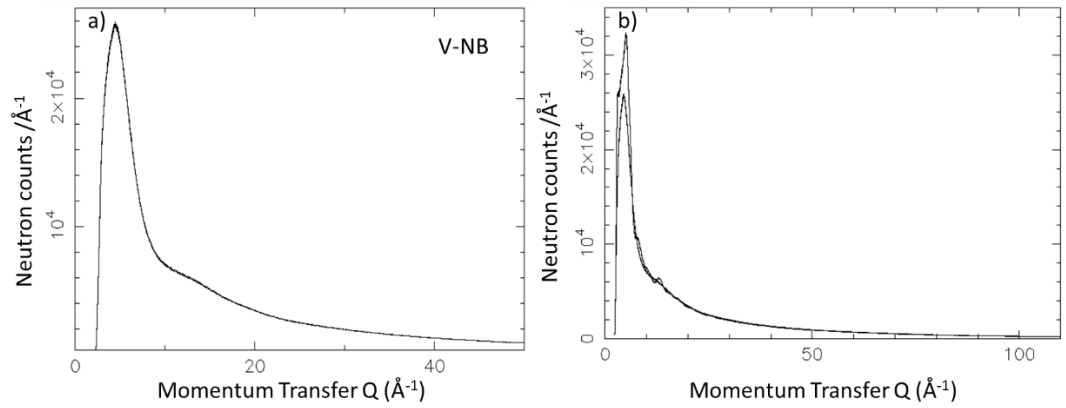


Figure 2.2: Time-of-flight spectra obtained for a) vanadium-niobium (V-Nb) showing near to no Bragg peaks and b) representative sample data is also shown. The scattering data for the rod allows the shape of the neutron flux to be removed from the scattering of the sample to give $I(Q)$.

2.5.4.3 Distinct and self-scattering

The total scattering, $I(Q)$, from the sample is calculated from the sum of the self-scattering (interference caused by waves scattered from the same nucleus), $I^s(Q)$, and the distinct scattering (interference between waves scattered from different nuclei), $i(Q)$. This is known as the interference function and is equivalent to differential cross section mentioned in equation 12:

$$\frac{d\sigma}{d\Omega} = I(Q) = I^s(Q) + i(Q) \quad (16)$$

Figure 2.3 shows the corrected differential cross section of $40P_2O_5 \cdot 16CaO \cdot 20Na_2O \cdot 24MgO$ where the Q -space data oscillates around the self-scattering level. The data has been corrected for the effects mentioned in section 2.5.4.2 and by the “Placzek correction”^[141] where Placzek first showed that there was no inelasticity effect for the distinct scattering, $i(Q)$.

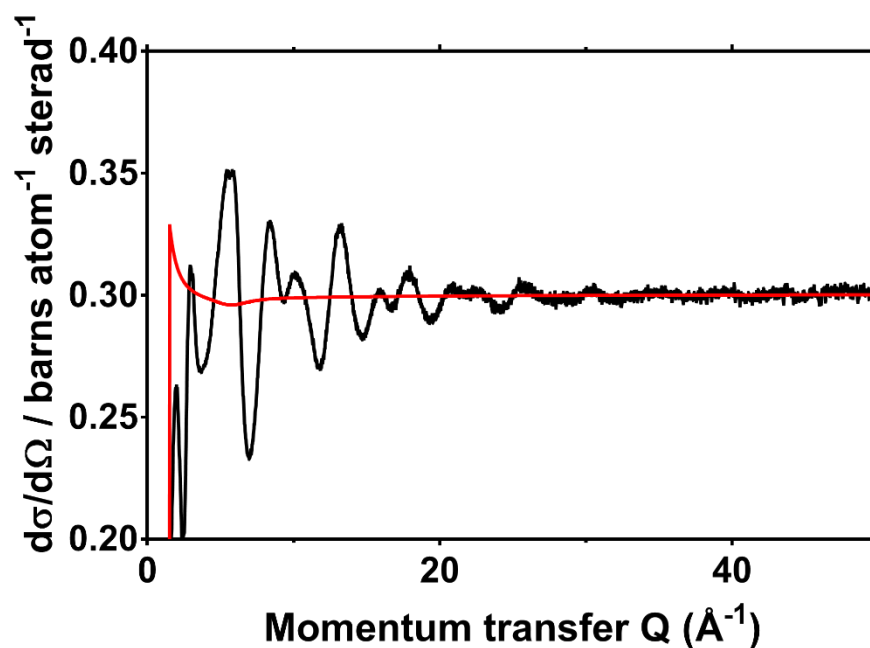


Figure 2.3: the corrected differential cross section data of bank 5 shown in black and $I^S(Q)$ of bank 5 shown in red of $40P_2O_5 \cdot 16CaO \cdot 20Na_2O \cdot 24MgO$

GUDRUN^[139] outputs data in the form of individual detector banks as shown in Figure 2.4. The $I^S(Q)$ is calculated for each scattering angle and each bank is then scaled so that the high Q region oscillates about $I^S(Q)$ as displayed in Figure 1.4. The Q_{max} (i.e. limit of useable data) was 50 \AA^{-1} for these experiments since at higher Q , the structural information is masked by instrument noise. The Placzek correction is applied to each detector bank (scattering angles) and in order to produce a final distinct scattering, $I(Q)$ over the whole Q range, the banks are merged together.

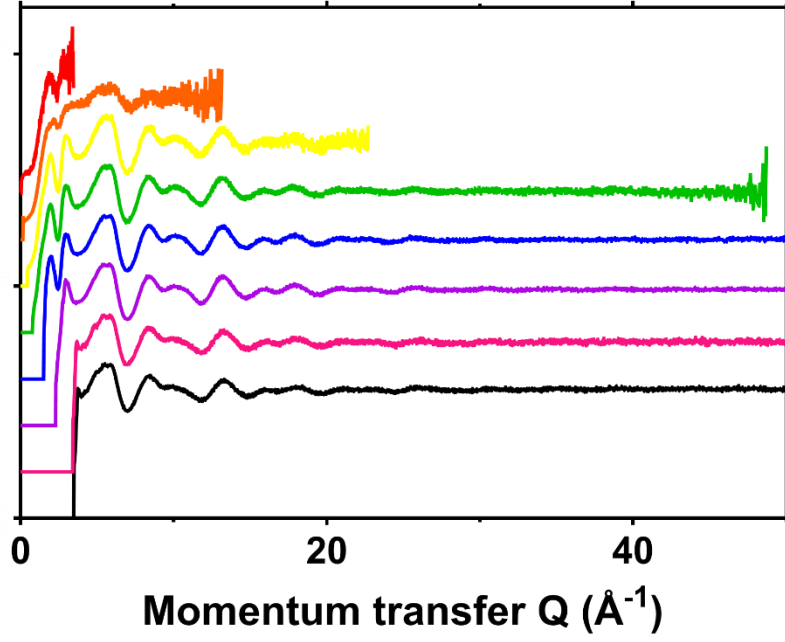


Figure 2.4: The corrected and normalised $I(Q)$ of $40P_2O_5 \cdot 16CaO \cdot 20Na_2O \cdot 24MgO$ from detector bank 0 (top) through to 7 (bottom). The first red line and last black and pink lines are not used in the merge due to difficulties in correcting.

2.5.4.4 Total correlation function

In order to relate the obtained reciprocal space data from a ND experiment to information in real space, a Fourier transformation of the experimental data is carried out using equation 17:

$$T(r) = T^0(r) + \frac{2}{\pi} \int_0^{\infty} Qi(Q)M(Q) \sin(rQ) dQ \quad (17)$$

Where $T^0(r)$ is the average density contribution to the correlation function ($T^0(r) = 4\pi r \rho_0 (\sum_{l=1}^N c_l \bar{b}_l)^2$), r is the distance between atoms, ρ^0 is the average atomic number density, N is the number of elements in the sample, and c_l and \bar{b}_l are the atomic fraction and coherent scattering for element l respectively. $M(Q)$ is a modification function (e.g. Lorch^[142] or step), which is used to take account of the fact that experimental data are only available up to some finite maximum momentum transfer, Q_{\max} , not infinity as in equation (11).

The resultant correlation function, $T(r)$, in real space can provide information on the different interatomic distances in the glass and the frequency of the occurrence of a specific interatomic distance is the weighted sum of all the possible partial correlation functions, $t_{ll'}(r)$, given by,

$$T(r) = \sum_{l,l'} c_l \bar{b}_l \bar{b}_{l'} t_{ll'}(r) \quad (18)$$

Structural information is gained by fitting Gaussians, convoluted with the resolution of the instrument, to $T(r)$. At short distances, where a peak in $T(r)$ arises from only one particular pair of elements (l and l') the peak area, $A_{ll'}$, interatomic distance, $r_{ll'}$, and the coordination number, $n_{ll'}$, can be calculated, according to:

$$n_{ll'} = \frac{A_{ll'} r_{ll'}}{(2 - \delta_{ll'}) c_l \bar{b}_l \bar{b}_{l'}} \quad (19)$$

Where $\delta_{ll'}$ is the Kronecker delta. It must be noted, in order to obtain accurate coordination numbers, the density and composition of the sample must be known and a normalisation of $T(r)$ should be applied.

In ND experiments, the region at low r (values less than the shortest interatomic distance in the glass) should ideally have a value of zero for $T(r)$. However, as shown in Figure 1.6 this is not always the case due to Fourier ripples and experimental noise in this region. In addition, in the area below 1 Å, an unphysical peak is usually observed as a result of imperfections in the experimental corrections. Nonetheless, $T(r)$ can be corrected to zero below a minimum distance.

Normalisation can be conducted by matching the differential correlation function, $D(r)$ slope, to the average density contribution, $T^0(r)$ and scaling the $i(Q)$ by the difference, resulting in a normalised $T(r)$ (i.e. ensuring $T(r)$ at low r is equal to zero) as displayed in Figure 2.5. In order for this normalisation to be accurate, which in turn determines the accuracy of the coordination number, it is crucial for the chemical composition to be well known so that the atomic fraction of element l is correct, and for the density of the sample to be

known as this determines the $T^0(r)$. It should be noted that coordination number can also be obtained from $D(r)$.

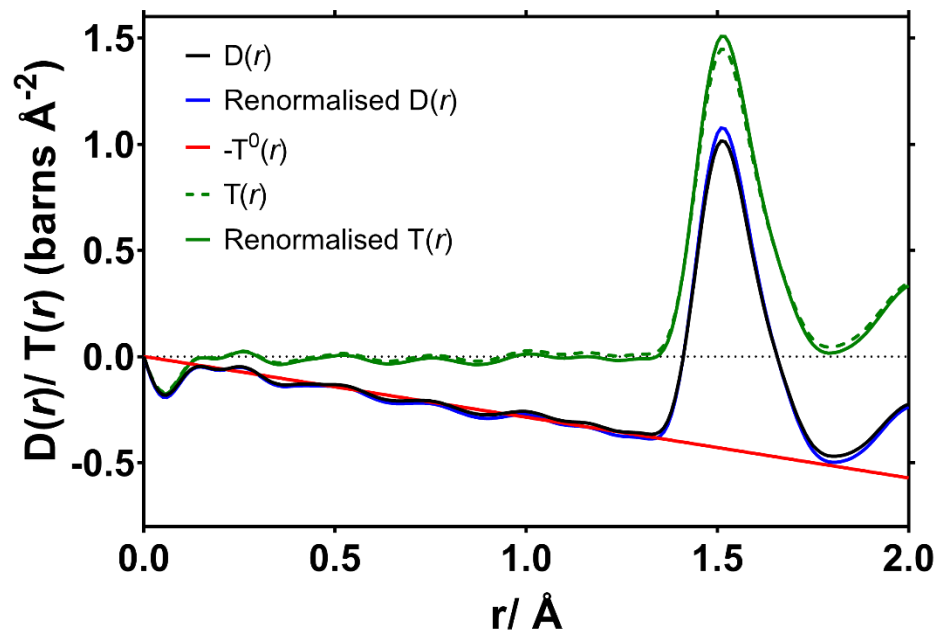


Figure 2.5: the low r region of the differential correlation function and correlation function ($D(r)$ and $T(r)$), before normalisation (black), after normalisation (blue) and the $-T^0(r)$ (red) of $40P_2O_5 \cdot 16CaO \cdot 20Na_2O \cdot 24MgO$.

2.6 Microsphere manufacture and characterisation

This section gives an overview of the materials and methods used in the manufacture and characterisation of PBG microspheres (non-porous and porous) however, developmental conditions are explained in chapter 6.

All microsphere manufacture was carried out using the P40 glass composition. The quenched glass (manufactured as explained in section 2.2.1) was ground into irregular microparticles using a planetary zirconia ball mill (Retsch Planetary Mill PM100), operated for 2 minutes at 500 rpm. Glass powder was separated into particle sizes ranging from 63-200 μm using stainless steel sieves (VWR International, UK) placed on an Octagon digital shaker.

2.6.1 Flame spheroidisation

The flame spheroidisation process (setup shown in Figure 2.6 below) was used and consisted of a funnel feeder with a mesh size of 200 μm , attached to a DC vibratory motor in order to obtain sufficient particle flow, a gas torch (BOC Cutting torch, UK and MK74 Thermal Spray gun Metallisation Ltd., UK), gas flowmeters (Platon, Roxspur, UK), and a series of collection vessels.

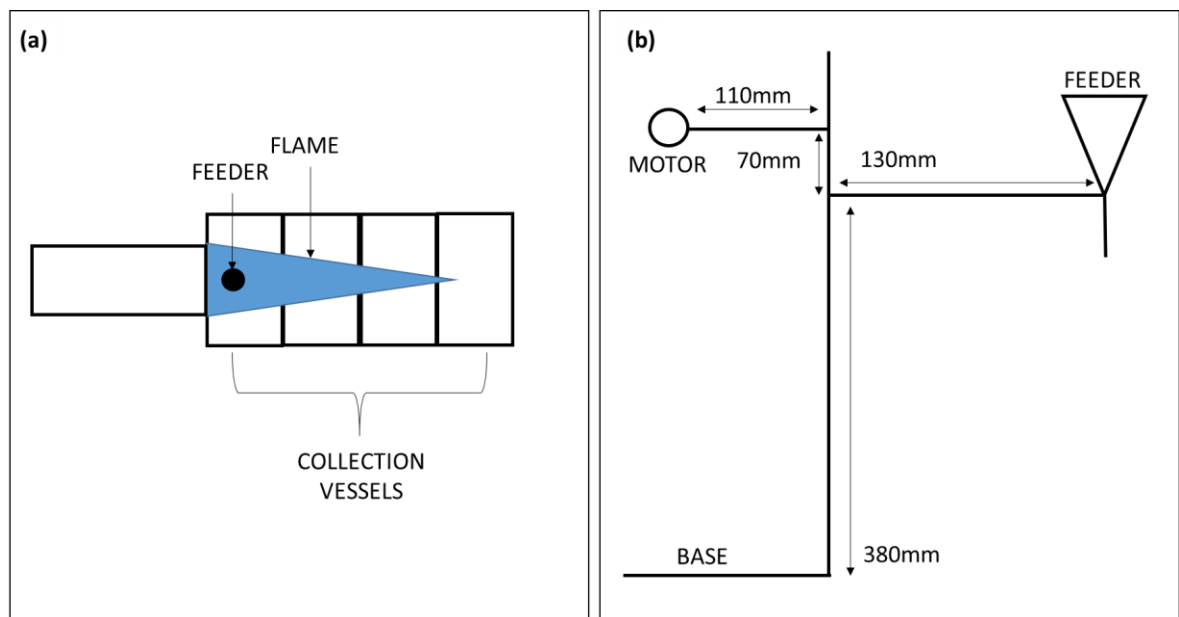


Figure 2.6: (a) schematic of basic flame spheroidisation set up and (b) detailed schematic of feeder setup.

The setup using the BOC cutting torch required oxy-propane gas. The flow rates are outlined in Table 2.3. A second thermal spray gun (MK74 thermal spray gun) was then used for spheroidisation which was operated with oxy-acetylene gas at equal flow rates of 4L/min.

Table 2.3: Displaying gas flow rates experimented with for flame spheroidisation

Spray Gun	O ₂ (L/min)	C ₃ H ₈ (L/min)	C ₂ H ₂ (L/min)
BOC cutting torch	3	7	
BOC cutting torch	1.5	3	
MK74 thermal spray gun	4		4

2.6.2 Porous microsphere manufacture

Glass microparticles in the size range of 63-125 μm were thoroughly mixed with CaCO₃ (Longcal P52, Longcliffe Quarries Ltd., Derby) on a 1:2 weight basis pre spheroidisation.

2.6.3 Post processing

Porous microspheres (3g) were submerged in 100ml of 0.5M of acetic acid (Sigma Aldrich, UK) for 160 seconds. The experiment was then halted by diluting the solution with 4 litres of deionised water. The solution containing the porous microspheres was then filtered through a funnel and filter paper (QL100, Fisher Scientific, UK). All collected microspheres were then left to dry in a 50°C oven over night.

2.6.4 Particle size analysis

Particle size analysis was performed by Mathew Coltman (University of Nottingham) using a Mastersizer 2000 instrument (Malvern, UK) which is based on the principle of laser diffraction. Particles were dispersed in a stream of gas and then passed through a laser beam to produce a scattering pattern. Measurements were taken in the range between 0.020 to 2000 μm , under the following conditions: particle refractive index 1.500, particle absorption coefficient 0.1, dispersant 1.000, and general calculation model for irregular particles. Two measurements for each particle type were taken and the data obtained was averaged by software Mastersizer 2000, ver. 5.40 from Malvern, UK.

2.6.5 Surface area via BET

Surface area measurements were carried out by David Mee (University of Nottingham). Surface area was measured using the Brunauer, Emmett, and Teller (BET) technique employing a Micromeritics ASAP 2020 instrument with krypton at 77K as the adsorption gas. The samples were degassed at 105°C overnight under vacuum, followed by backfilling with nitrogen prior to analysis.

2.6.6 Mercury porosimetry

Mercury intrusion porosimetry (MIP) was carried out using a Micromeritics Autopore IV 9500, which is capable of obtaining pressures between 0 to 345 kPa at low pressure and up to 228 MPa at high pressure, enabling characterisation of pore diameters ranging from $\sim 360 \mu\text{m}$ to $\sim 0.0055 \mu\text{m}$. Prior to any experiment, the samples were dried under vacuum at 50°C overnight to drive off any physisorbed water on the sample. A micromeritics 5cc powder penetrometer with 1cc intrusion volume was used for all samples. The sample weight used was above 20% of the stem volume in order to obtain accurate porosity measurements i.e. the sample weight was *c.a.* 1000 mg. An empty penetrometer was run before sample runs in order to calibrate the equipment.

The experimental procedure consisted of increasing the external pressure to the sample and thus forcing the non-wetting mercury into increasingly smaller pores in the microspheres. At each pressure step (once equilibrium has been reached) the apparent volume of mercury entering the sample was measured. The material was first placed in a low pressure port where the intruded volume was recorded as a function of pressure. This was followed by placing the sample in the high pressure port. The pressure was increased incrementally up to a maximum given ultimate pressure of 228 MPa. The process was then reversed by decreasing the pressure stepwise, which allowed the mercury to extrude from the solid material, thus generating an extrusion curve.

Despite a few limitations of this technique, such as the presence of hysteresis between the intrusion and extrusion regions, possible deformation and fracture of the porous structures under high pressure and the environmental and health concerns associated with mercury,^[143, 144] MIP is regarded as a standard measure for both macro- and mesopore size distributions.

2.6.7 Micro CT

Image analysis via microcomputed tomography (micro CT) provides a means of reconstructing three dimensional (3D) images of the microspheres allowing quantification of porosity including pore size, pore distribution and strut thickness. Such information can be used to complement results of porosity achieved by physical measurements such as MIP and SEM image analysis. A random sample of pre-acid washed (i.e. as manufactured) porous microspheres were tap filled into a 4 mm x 2 mm sample holder and a scan was conducted by Martin Corfield (University of Nottingham) using The XRADIA Versa XRM - 500. The first X-ray scan was performed at lower resolution (1 μm) where the energy of the scanner was 55 kV and the current 82 μA . The optical magnification was 4X and the image consisted of 994 slices. This was followed by a second scan performed at higher resolution (0.5 μm) where the energy of the scanner was 60 kV and the current 84 μA . The optical magnification was 20X and the image

consisted of 96 slices. The higher resolution scan honed in on a specific area where the greatest number of full spheres were observed in the field of view.

Image processing and characterisation were done in Scan IP package of Simpleware™ using the procedure set out by Otaru & Kennedy, 2016.^[145] This is a 3D image processing, analysis and model generation software package. The gray scale images were thresholded from shades of gray to black where black was the material and white was air. Post reconstruction of the 3D image, a smart mask process (with 10 iterations) was used to smooth the image and was preferred to a recursive Gaussian smoothing operation since it more accurately preserved the imported geometry, in particular the geometry of the small windows connecting the pores. Quantitative analysis was performed on the image using tools within the software and the volume, surface area and volume fraction were measured.

2.6.8 PBG microsphere degradation and ion release

Non-porous, pre and post acid washed P40 microspheres were screened between 100-125 μm stainless steel sieves (VWR International, UK) in order to narrow the particle size. 250mg of spheres were placed in 50ml of ultrapure water ($n = 3$) and degraded for 28 days. At each time point (days 0, 1, 3, 7, 14, 21 and 28), the media was replenished and a small representative sample was placed on a carbon stub and prepared for SEM image analysis as outlined in section 2.2.3. Cation release was measured at each time point as outlined in section 2.2.9.1.

Image J (Fiji)^[146] was used to measure the diameter of 150 ± 10 microspheres from all sample repeats ($n= 3$) for non-porous, pre and post acid washed microspheres at each time point. Microspheres touching the edge of the image and irregular particles were disregarded as displayed in Figure 2.7. This data was then used to determine the change in diameter over time.

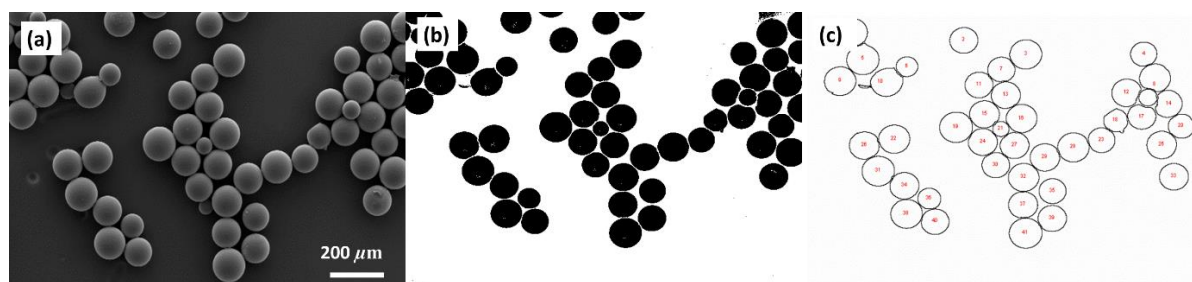


Figure 2.7: (a) SEM image of non-porous microspheres after degradation at day 1, (b) threshold of microspheres done on ImageJ where the black regions show the microspheres and the white regions is air, and (c) outline of the measured microspheres using ImageJ.

CHAPTER 3: PHYSICO-CHEMICAL PROPERTIES AND CYTOCOMPATABILITY OF Sr SUBSTITUTED PBG

3.1 Introduction

This chapter outlines the fundamental properties observed in the glass system $40\text{P}_2\text{O}_5 \cdot (16-x)\text{CaO} \cdot 20\text{Na}_2\text{O} \cdot 24\text{MgO} \cdot x\text{SrO}$ glass, where x is 0, 4, 8, 12 and 16 mol%. All glass samples in this chapter were melt quenched for XRD, EDX, density, and thermal analysis, and in disc form for the dissolution and ion release study, and for the cytocompatibility studies. Understanding such properties will aid in determining models of the glass structure. This chapter also presents the outcomes of a cytocompatibility study employing a MG63 human osteoblast-like cell line and the preliminary findings on the effect of Sr substitution in this glass system on human peripheral blood monocytes differentiation. The materials and methods used in the chapter are provided in Chapter 2.

3.2 Powder XRD

The powder XRD patterns of each glass composition can be seen in Figure 3.1, where a single broad peak spanned from $\sim 20^\circ$ to $\sim 40^\circ$. The lack of any sharp crystalline peaks confirmed the amorphous nature of the glasses under investigation.

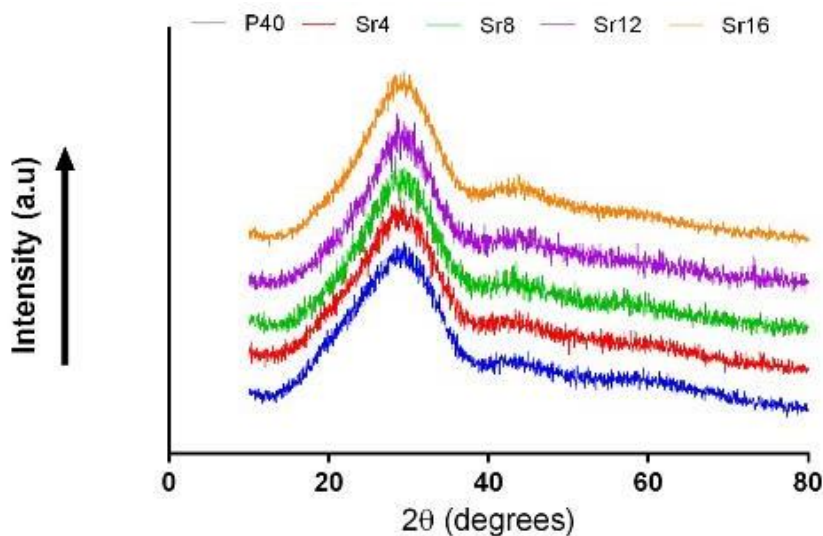


Figure 3.1: Powder XRD pattern of glass samples in the system $40\text{P}_2\text{O}_5 \cdot (16-x)\text{CaO} \cdot 20\text{Na}_2\text{O} \cdot 24\text{MgO} \cdot x\text{SrO}$ glass, where x is 0, 4, 8, 12 and 16 mol%.

3.3 EDX

The relative concentration of elements in each glass sample were analysed via EDX. Figure 3.2 shows confirmation that all samples were within 1-2% of the target mol% for each composition. A ~ 1 mol % reduction in CaO was accompanied by ~ 1 mol% increase in SrO compared to that of the target values. Similar increases/decreases in compositions and error margins have also been reported previously when investigating PBG and such discrepancies were attributed to losses occurring during melting, and/or due to the initial compositions of the precursor salts themselves, in particular those containing phosphate, due to its hygroscopic nature.^[5, 73, 147, 148]

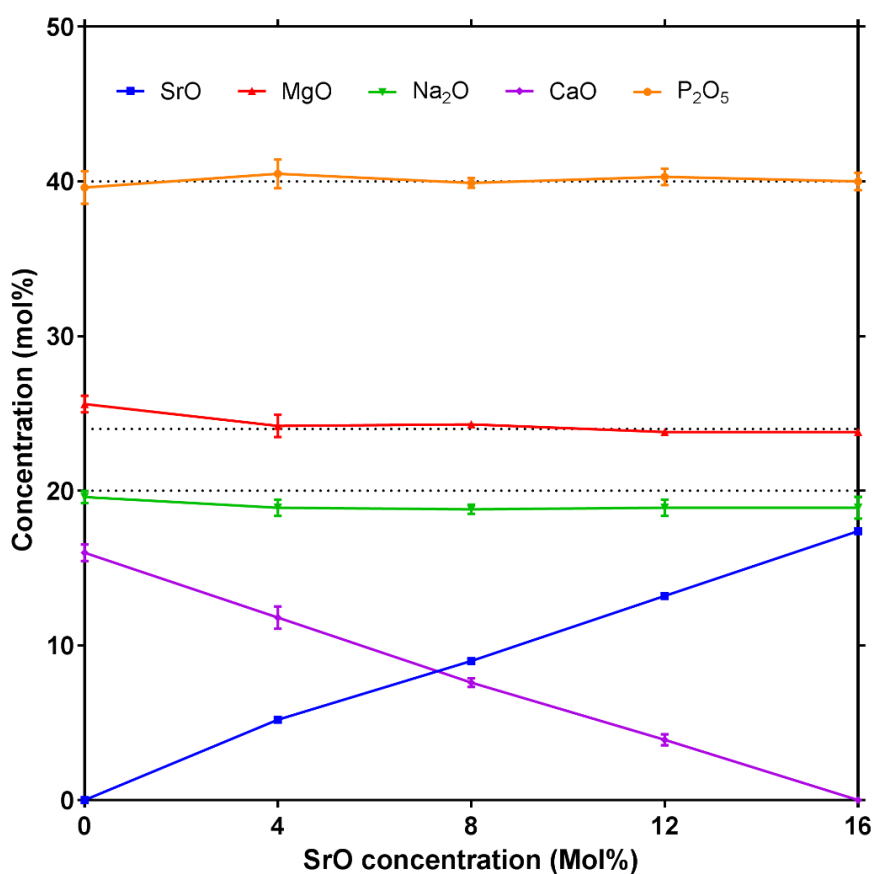


Figure 3.2: Composition of glass samples tested as measured by EDX. Dotted lines represent the target value. Error bars were determined by taking the standard deviation of three separate samples for each composition.

3.4 Density

Figure 3.3 shows the density and molar volume of the investigated glass series. The atomic mass of Sr is more than double that of calcium, resulting in an increase in density from 2.71 to 2.89 g/cm³ as SrO is substituted for CaO. Similarly, a small linear change in molar volume was observed across the compositional range (from 29.44 cm³ mol⁻¹ to 31.78 cm³ mol⁻¹) due to the similarity in ionic radii. The changes observed with increasing SrO content also correlated well with results of a previous study^[64] which reported a 0.04 g/cm³ increase on substituting 5mol% SrO for Na₂O in a series of glasses with composition 50P₂O₅·(20-x)Na₂O·30CaO·xSrO where x = 1, 3 and 5mol%. Al Qaysi *et al.*^[73] also reported a linear change from 2.6 g/cm³ to 3.0 g/cm³ when substituting SrO for CaO in a 50P₂O₅·10Na₂O·5TiO₂·(35-x)CaO·xSrO (where x = 0, 3.5, 17.5 and 35) glass system.

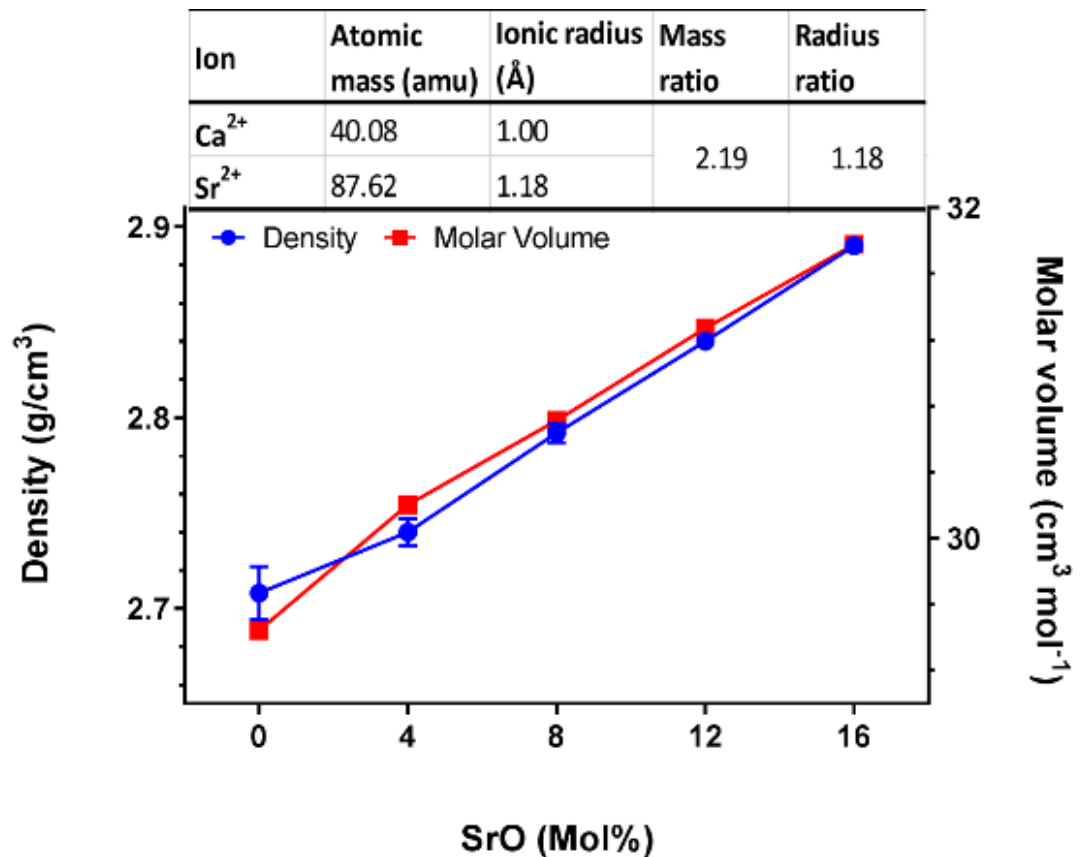


Figure 3.3: Density and molar volume of the multicomponent glasses 40P₂O₅·(16-x)CaO·20Na₂O·24MgO·xSrO glass. The ionic radius^[149] and mass of calcium and strontium atoms, and the mass and radius ratios between the two are also shown.

3.5 Thermal Analysis

The DSC traces of the multicomponent glasses investigated are shown in Figure 3.4 and the thermal parameters are displayed in Table 3.1. Results showed very little change in T_g when substituting strontium for calcium, with a decrease of only 3°C. Direct comparisons between this work and studies in the literature are made difficult by the very different modifier concentrations in the various glass series discussed. The small change in T_g observed in this study is attributed to the similar charges and M-O (where M is the modifier) bond strengths of Ca^{2+} and Sr^{2+} with both ions playing a similar role in the network structure^[64] and Lakhkar *et al.*^[150] observed comparable results to those reported here when substituting SrO for CaO in the PBG system $50\text{P}_2\text{O}_5 \cdot (30-x)\text{CaO} \cdot 17\text{Na}_2\text{O} \cdot 3\text{TiO}_2 \cdot x\text{SrO}$ (where $x = 0, 1, 3, 5$). Abou Neel *et al.*^[64] showed that when Sr^{2+} was substituted with Na^+ , a monovalent cation, in the PBG system $50\text{P}_2\text{O}_5 \cdot (20-x)\text{Na}_2\text{O} \cdot 30\text{CaO} \cdot x\text{SrO}$ (where $x = 0, 1, 3$ and 5 mol%), a large decrease in T_g , from 383 to 428°C was reported.

Work on silicate glass systems^[63, 67] has shown that the substitution of strontium for calcium resulted in an increase in T_g and this was suggested to be due to the expansion and disruption of the silicate glass network with increasing strontium concentration, due to the larger ionic radius of Sr compared to Ca. The different behaviours in the silicate and phosphate glass networks could be attributed to the presence of NBOs associated with P atoms in the phosphate glass network, and the non-existent double bonded oxygen in the silicate glasses, which enables formation of a continuous 3D glass network for silicate glasses.

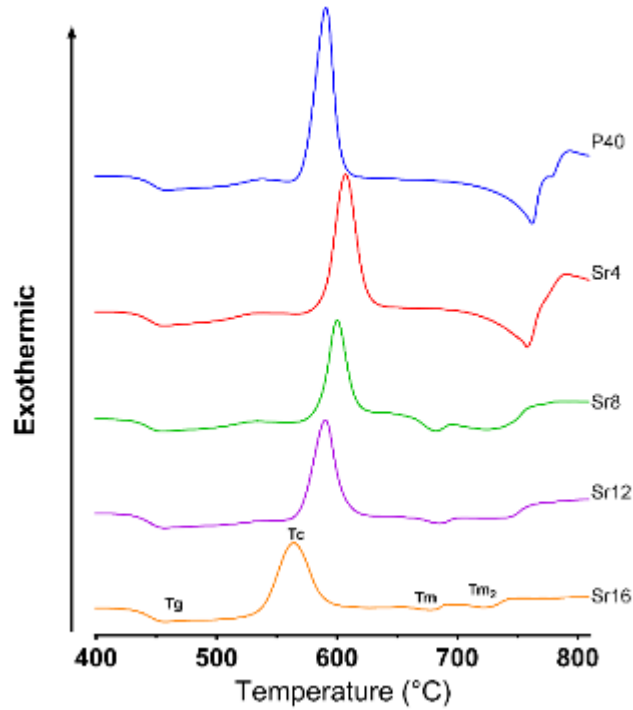


Figure 3.4: Thermal traces showing T_g , T_c and T_m of the multicomponent glass samples.

Table 3.1: Glass transition, T_g , crystallisation, T_c , onset of crystallisation, T_{onset} first melting temperatures, T_m and second melting temperature, T_{m2} , for each composition is given along with the calculated thermal processing window, $T_{onset}-T_g$ of each glass.

Glass code	T_g	T_{onset}	T_c	T_m	T_{m2}	$T_{onset}-T_g$
P40	435 ± 0	573 ± 0	591 ± 0	762 ± 0		123
Sr4	432 ± 1	588 ± 0	609 ± 0	759 ± 0		141
Sr8	431 ± 1	582 ± 1	601 ± 0	734 ± 0	854 ± 2	135
Sr12	431 ± 0	571 ± 0	589 ± 0	685 ± 1	742 ± 0	124
Sr16	432 ± 1	538 ± 0	565 ± 0	679 ± 0	725 ± 1	95

A distinctive crystallisation peak was seen to shift from 591°C for the host glass composition (P40) to 609°C with the addition of 4 mol% of SrO (Sr4), followed by a single melting peak. As more strontium was added to the glass (Sr8 – Sr16) the crystallisation temperature was seen to decrease to 565°C and the melting peaks became broader, less defined and reduced in area. With increasing addition of strontium to ≥ 8 mol% SrO two melt peak features were observed, which shifted to lower temperatures. This, coupled with the broadening of the crystallisation peak, was attributed to the potential presence of more than one crystalline phase. A recent study^[73] investigating the substitution of CaO for SrO in a fixed 50mol% P₂O₅ PBG system found that increasing SrO content led to a more prominent melting peak (which was not apparent in this study), and a reduction in the thermal processing window. The presence of two T_m peaks in PBG systems with fixed 45 and 50 mol% P₂O₅ have previously been correlated with the following two dominating crystal phases; sodium calcium phosphate (NaCa(PO₃)₃), and a beta calcium metaphosphate (CaP₂O₆), as reported by Ahmed *et al.*^[2] when investigating ternary 50P₂O₅·40CaO·10Na₂O and 55P₂O₅·35CaO·10Na₂O glass systems. They reported that the predominant crystal phase in both 45 and 50 mol% P₂O₅ ternary glasses was sodium-calcium phosphate. A NaCa(PO₃)₃ crystal phase was also found to be dominant in a previous study by Lakhkar *et al.*^[81] when investigating CaO substitution with SrO in a P₂O₅·Na₂O·CaO·TiO₂·SrO glass system

The materials thermal processing window; i.e. the gap between T_g and the onset of crystallisation, T_{onset} , can provide a good indication of the thermal stability of a glass system.^[32] The thermal processing window data in Table 3.1 showed that addition of a fifth component to the glass system (i.e. 4 mol% of SrO) increased the thermal processing window from 123°C to 141°C. This can be explained by increasing the energy barrier for the rearrangement of atoms in order to form a critical size defect i.e. the entropy of mixing increased.^[147, 151] Further substitution of CaO with SrO resulted in a gradual decrease in the thermal processing window which was suggested to be due to the lower field strength of Sr²⁺ (0.28 valence/Å²) compared to Ca²⁺ (0.33 valence/Å²) according

to Dietzel.^[74, 152] Dietzel's theory took into account both the size-ratios and field strengths of the ions; for example, on cooling a binary silicate melt, both cations compete for the oxygen ions in aiming to achieve the densest packing. The cation with the higher field strength will have most of the oxygen ions densely packing around it and the cation with the lower field strength is satisfied with a higher coordination number in relation to the anion complex formed by the other cation (e.g. $(\text{SiO}_4)^{4-}$). The decrease in thermal processing window with increasing Sr concentration correlated with the fact that the calcium free (Sr16) glass composition had to be cooled much more rapidly than the others to form a glass. Such findings agreed well with the work of Lee *et al.*^[74, 90] who observed a higher tendency of crystallisation with increasing SrO content in a $30\text{P}_2\text{O}_5 \cdot 7\text{MgO} \cdot 3\text{TiO}_2 \cdot (60-x)\text{CaO} \cdot x\text{SrO}$ and $30\text{P}_2\text{O}_5 \cdot 7\text{Na}_2\text{O} \cdot 3\text{TiO}_2 \cdot (60-x)\text{CaO} \cdot x\text{SrO}$ (mol %) glass system where x is 0-60. The narrowing of the thermal processing window with increasing SrO, may potentially make thermal post processing (such as extrusion and fibre drawing) of high strontium content phosphate glasses more difficult than for lower strontium containing formulations, particularly with lower P_2O_5 contents however, this could potentially be mitigated by increasing the P_2O_5 content.

3.6 Dissolution and ion release study

It is well known that the physico-chemical properties of phosphate glasses are largely dependent on the cations that modify the network.^[153] These cations are thought to take up the interstitial sites created between phosphate chains, increasing the glasses resistance to hydrolysis.^[153] As already mentioned, the field strength of Sr^{2+} is less than that of Ca^{2+} (as a result of the larger ionic radius) thus, it may be hypothesised that the degradation rate of the higher SrO containing glasses would be greater than those with less CaO. However, this was not the case as observed in this study. Instead, the initial addition of SrO to the glass (adding 4mol% SrO) caused a reduction in the dissolution rate as displayed in Figure 3.5 (a), suggesting that replacing Ca with Sr could increase cross linking between phosphate chains. The average mass loss per unit area decreased significantly ($P < 0.001$) on addition of 4 mol% strontium oxide from

$8.4 \times 10^{-4} \text{ g cm}^{-2}$ to $5.5 \times 10^{-4} \text{ g cm}^{-2}$ at 72 hours (see Figure 3.5 (a)). However, further addition of Sr in place of Ca had no significant effect on both average mass loss per unit area and the degradation rate. Figure 3.5 (b) shows the degradation rates for the multicomponent glasses determined via the slope of best fit for each composition tested using three different media; DI water, ultra-pure water and PBS. The rate remained similar for all the Sr containing glasses with the greatest change in rate occurring between P40 and Sr4 by $3 \times 10^6 \text{ g/cm}^2/\text{hrs}$ in ultra-pure water. The same trend was seen in both DI water and PBS with P40 degrading at a faster rate than the Sr glasses. A number of studies investigating the degradation profiles of strontium-containing phosphate glasses reported that their degradation rates were greater than the strontium-free glasses.^[81, 150, 154] However, it should be noted that these studies investigated PBGs with fixed P_2O_5 content of 50 mol%. The increased degradation profiles observed in the past studies were attributed to an expansion of the glass network with the addition of Sr, correlating with an increase in molar volume. However, although a small increase in molar volume was seen in this study, it did not exert any influence on the degradation of these glasses with fixed 40 mol% P_2O_5 (i.e. almost invert glass structure; invert glasses are those with a P_2O_5 content <40 mol%).^[82, 84]

The degradation rates between each strontium-containing glass in this study did not vary significantly in any of the media tested. One explanation for this could be due to the fact that these glasses are on the verge of an invert glass, and the various glass properties (e.g. degradation rate) of such glasses are not controlled by the glass (P_2O_5) network skeleton nor the entanglement of chains, but rather the interaction of cations with the phosphate groups.^[82, 86, 155, 156]

Furthermore, the compositions studied here had high concentrations of MgO present where Mg^{2+} has an even higher field strength ($0.53 \text{ valence}/\text{\AA}^2$ when 4-coordinated or $0.46 \text{ valence}/\text{\AA}^2$ when 6-coordinated) than Ca^{2+} and Sr^{2+} due to the increasing atomic number of the alkaline earth metals.^[90] This in turn would increase packing density and thus decrease dissolution rate, which, in turn would decrease ion release rates. According to Dietzel's rule,^[74, 152] MgO is

also known to behave as an intermediate oxide, acting as either a network modifier or can enter the phosphate network forming P-O-Mg bonds.

It was notable from Figure 3.5 (a) that the dissolution rates for the two samples (P40 and Sr16) containing four oxide components was higher than those containing five oxide components as those samples showed a lower and more constant dissolution rate. This observation suggested increased packing density and crosslinking caused with the addition of an extra cation, and greater structural frustration arising from the larger number of glass components leading to a smaller dissolution rate.

It is also of note that the Sr16 sample were more prone to crystallisation than the other multicomponent samples as indicated by the low values of T_{onset} and T_c in Table 3.1, suggesting that the greater frustration of the 5-component samples gave them a greater resistance to crystallisation.

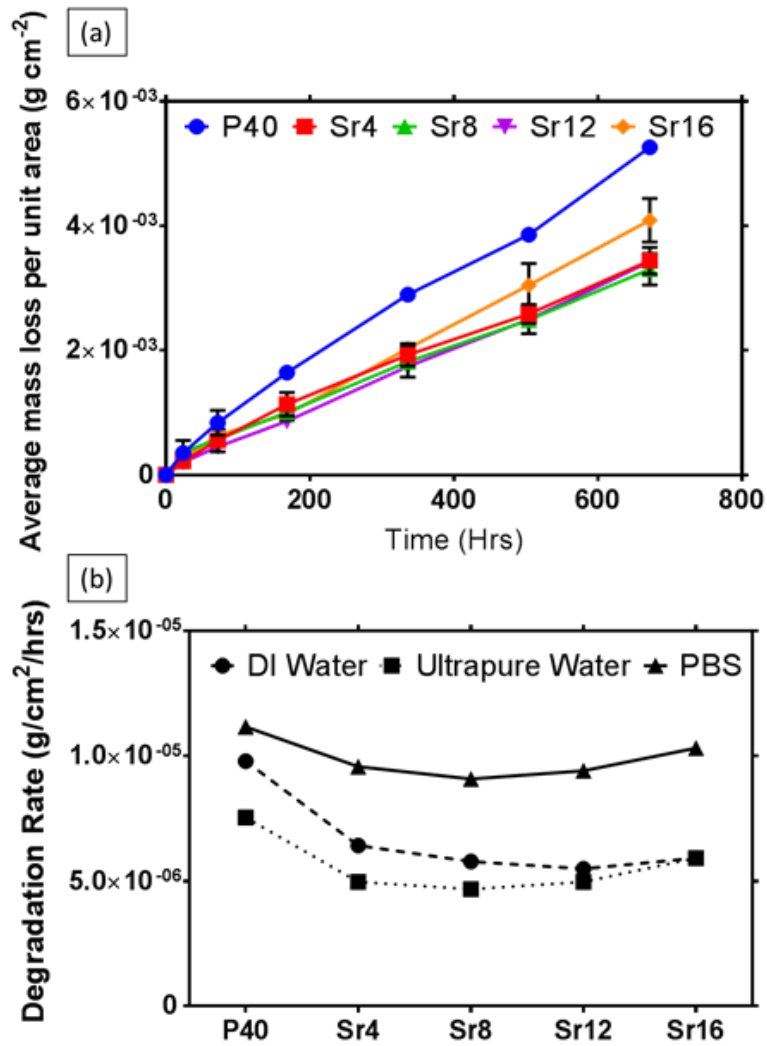
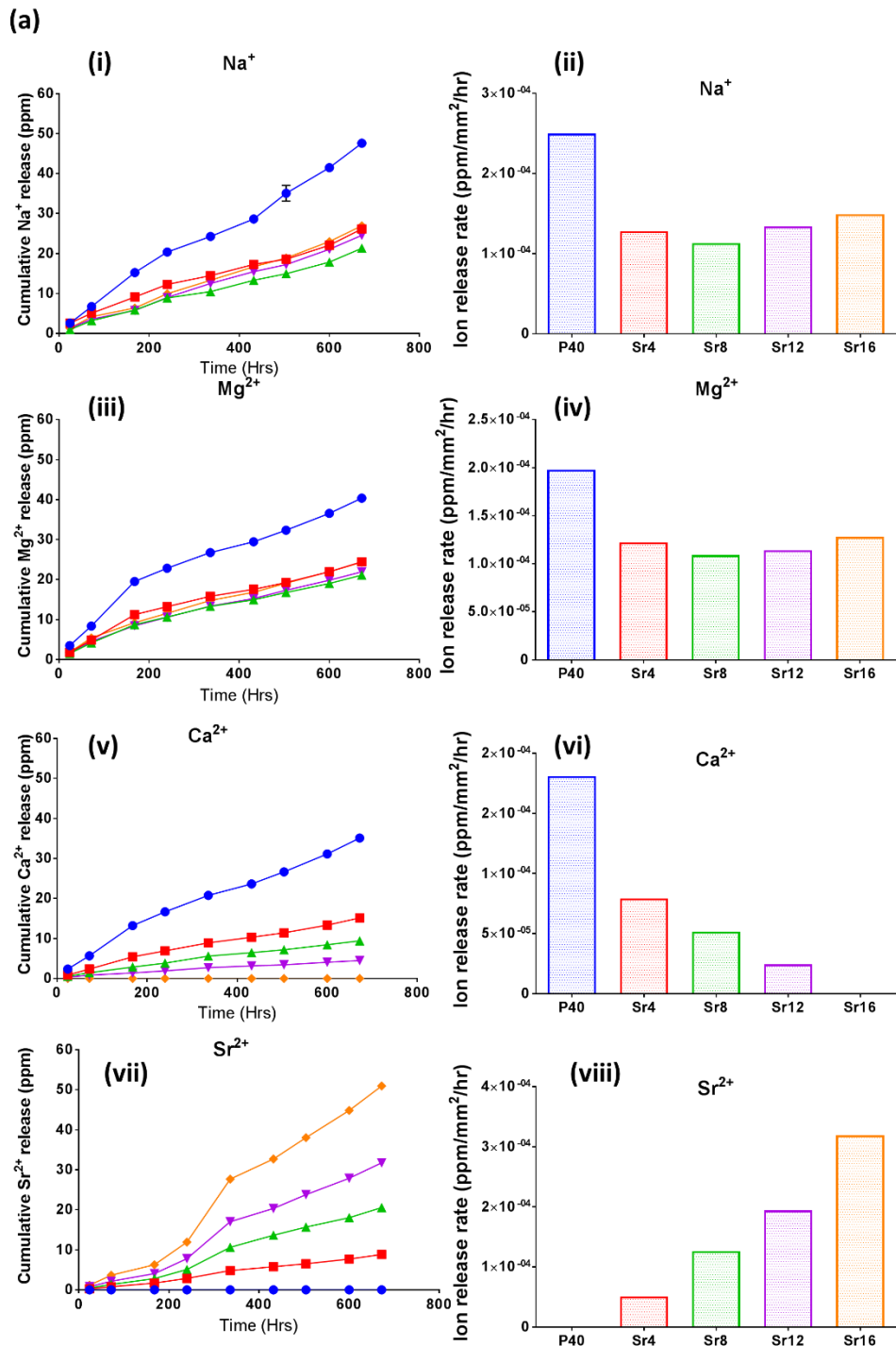


Figure 3.5: (a) The average mass loss per unit area (g cm^{-2}) for multicomponent glasses studied in ultra-pure water. (b) Shows the calculated degradation rate ($\text{g/cm}^2/\text{hrs}$) for each multicomponent glass ($n=3$) in ultra-pure water, deionised water (DI) and phosphate buffered saline (PBS).

The ion release studies were conducted for the following cations, Ca^{2+} , Na^+ , Mg^{2+} and Sr^{2+} . From the profiles observed (Figure 3.6 (a)), Na^+ and Mg^{2+} followed a similar trend to the degradation study where P40 released the highest concentration of cations over time, and strontium-containing glasses showed a consistent release of cations ranging from 0.27ppm for Sr4 at 24 hours to 50.95ppm for Sr16 at 672 hours. The correlation of ion release studies of Na^+ and Mg^{2+} have also been observed by Ahmed *et al* [4] where a cumulative release method was also used for a ternary based PBG. It was interesting to note that the concentration of Sr^{2+} released by the Sr16 glass where CaO was fully substituted with SrO, was greater than the Ca^{2+} released from the P40

samples containing 0 mol% SrO. As expected a gradual increase in SrO in the glass samples resulted in a gradual increase in the amount of strontium and reduction in calcium ions released. These release profiles of Sr^{2+} coupled with the degradation rate profiles provided evidence that it was possible to control the concentration of strontium ions released without affecting the rate of degradation.



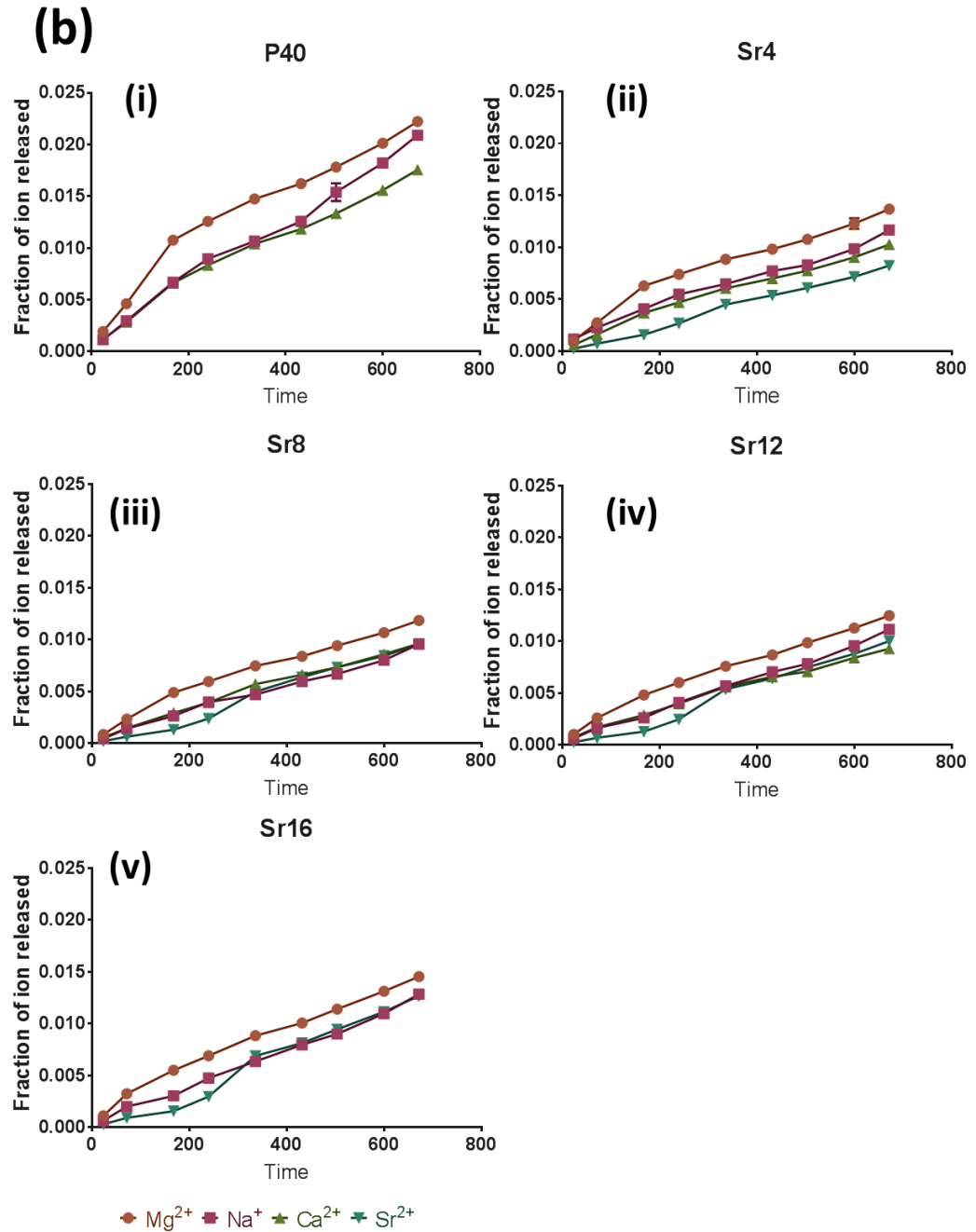


Figure 3.6: (a) Cumulative cation release profiles from the multicomponent glasses investigated, which were degraded in ultra-pure water ion release rates normalised to the surface area. (b) Concentration of ions released which were normalised to the initial glass composition

Figure 3.6 (b) shows the release of ions normalised to the initial glass composition. For all compositions it appeared as though Mg²⁺ ions The ability to retain both structural and physico-chemical properties of the glasses in this study suggested the possibility of fine tuning the release of therapeutic ions

such as Sr. Treatment for osteoporosis has involved oral administration of strontium ranelate at doses of 2g per day.^[70] This study has shown that degradation rates of Sr containing glasses could be maintained and that a linear rate of change of Sr release has been achieved with varying concentration. This study showed that it is possible to preserve the optimised properties of the glass formulation whilst also maintaining a predictable release rate of Sr ions.

3.7 Cytocompatibility study

The cytocompatibility of these Ca/Sr substituted near invert glasses was also investigated. The ability of this glass system to stimulate adherence, proliferation and differentiation of human osteoblast-like MG63 cells was investigated. A direct contact method was used in order to test the cytotoxicity of the glass samples with increasing SrO content, due to the high sensitivity associated with this method.

3.7.1 Cell metabolic activity

The Alamar blue assay was used to determine the effect of glass composition on cell metabolic activity of the human osteoblast-like cells MG63 over a period of 14 days. TCP and P40 were used as controls. Over the 14 day period, metabolic activity for all compositions was seen to increase as displayed in Figure 3.7, showing no cytotoxic effects on cell metabolic activity. The TCP control displayed significantly greater ($p < 0.05$) activity compared to the glass samples. At early time points of day 1 and 3, cell metabolic activity showed no significant difference between each sample. At day 7, Sr12 and Sr16 showed a significantly greater ($p < 0.05$) cell metabolic activity compared to P40, Sr4 and Sr8. At the later time point of day 14, again, Sr12 and Sr16 displayed a significantly greater ($p < 0.05$) cell metabolic activity compared to Sr8, suggesting higher concentrations of Sr encouraged metabolic activity of osteoblast like cells.

A dose dependent effect was previously observed by Caverzasio,^[157] where an increase in strontium ranelate concentration (up to 5mM) resulted in an increase in MCT3-E1 cell number, correlating with the increase in cell metabolic

activity observed in this study at higher concentrations. The exact mechanism as to how strontium ions influence the growth of osteoblasts is still unknown, although the dual mode of action of strontium ranelate has been evident both in vivo and in vitro.^[158] The mechanism as to how Strontium ranelate influenced osteoblast activity was briefly summarised by suggesting that enhanced progenitor differentiation into osteoblasts and regulation of osteoblast-induced osteoclastogenesis occurred.^[158, 159] Two mechanisms on the effect of strontium ranelate on osteoblast activity were proposed by Caverzasio and Thouverey;^[160] one involving the activation of the calcium sensing receptor which mediated osteoblastic cell growth, and the other suggestion was the activation of the Fibroblast Growth factor Receptors (FGFR) which was said to enhance the number of osteoblasts. Both mechanisms resulting in the mediation of osteoblastic cell growth and enhanced number of osteoblasts correlated well with what was observed in this study.

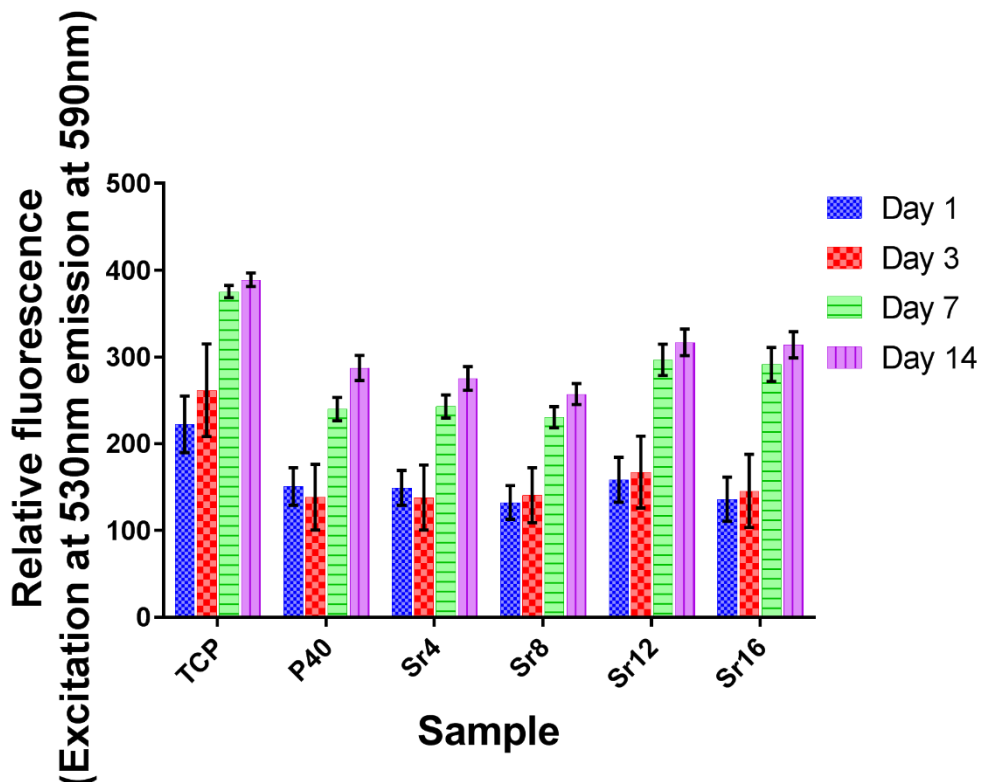


Figure 3.7: MG63 relative fluorescence as measured by Alamar blue assay, for cells grown on PBG samples in the system $40P2O_5 \cdot (16-x)CaO \cdot 20Na_2O \cdot 24MgO \cdot xSrO$ ($x = 0, 4, 8, 12$ and 16). P40 indicates 0 mol% SrO and Sr x indicates the SrO mol% in the glass. Error bars represent standard error of mean, $n = 15$. cell metabolic activity as measured by Alamar blue assay. Error bars represent standard error of mean, $n = 15$.

As described in section 3.6, the concentration of Sr^{2+} released over time increased with increasing Sr/Ca substitution, thus in accordance with this cytocompatibility study, it may be postulated that higher concentrations of Sr in these specific formulations, enhanced cell metabolic activity of osteoblast like cells.

3.7.2 DNA content

The effect of Sr concentration on cell proliferation was inferred by the DNA concentration of MG63 osteoblast-like cells cultured over a period of 14 days. The DNA concentration was measured by Hoechst 33258 DNA assay. Figure 3.8 showed that the DNA concentration for all samples was below $4.0 \mu\text{g ml}^{-1}$ across the time points and no significant difference ($p > 0.05$) was observed. The DNA concentration was seen to peak for all samples except Sr4 up to day 7, and marginally decrease at day 14 however, this decrease was not statistically significant.

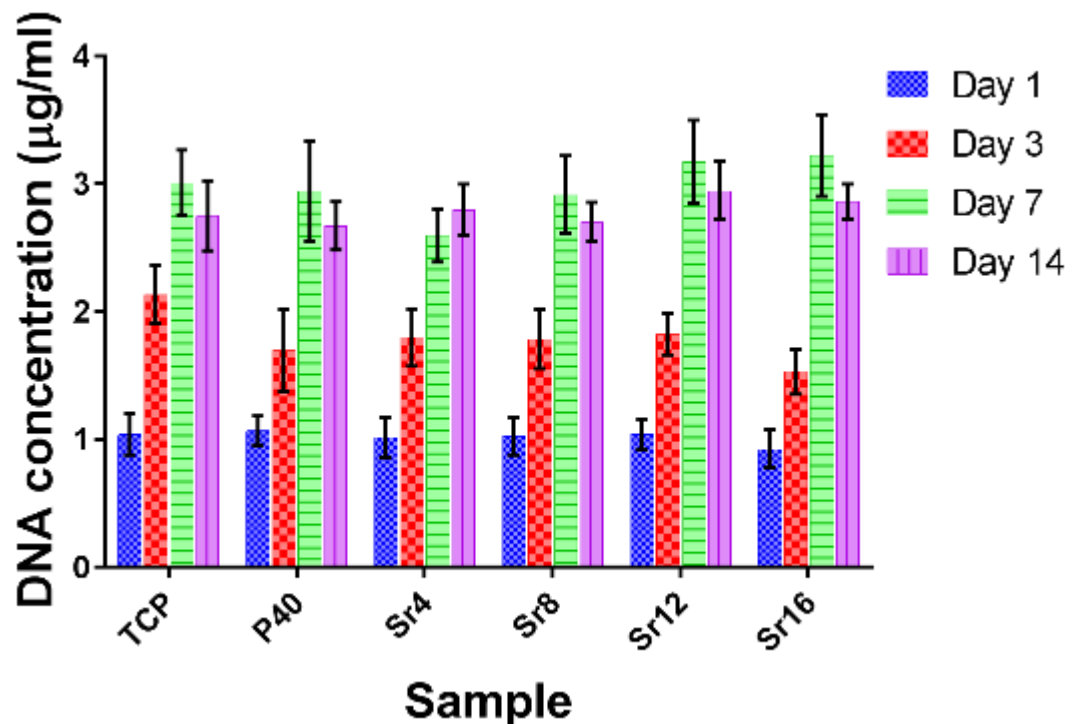


Figure 3.8: MG63 cell proliferation as measured by Hoechst 33258 DNA assay, for cells grown on PBG samples in the system $40\text{P}2\text{O}5 \cdot (16-x)\text{CaO} \cdot 20\text{Na}2\text{O} \cdot 24\text{MgO} \cdot x\text{SrO}$ ($x = 0, 4, 8, 12$ and 16). P40 indicates 0 mol% SrO and Sr_x indicates the SrO mol% in the glass. Error bars represent standard error of mean, $n = 12$.

The proliferation of cells as inferred by DNA concentration showed that Sr/Ca substitution had no significant effect on cell proliferation and was comparable to the TCP control at each time point. The DNA concentration and cell metabolic activity profiles were also comparable, both showing greater activity over time. Similarly, Boanini *et al.*^[161] showed that the incorporation of 5 and 10 atom% of Sr in hydroxyapatite did not differ in osteoblast proliferation in respect to the control (empty well plate) and proliferation appeared to be similar for both 5 and 10 atom% of Sr.

3.7.3 Alkaline phosphatase activity

The ALP activity was normalised to the DNA concentration of each sample. This was used as an early osteoblastic differentiation marker to determine the effect of Sr concentration on the activity of MG63 osteoblast-like cells at culture periods of 7 and 14 days as presented in Figure 3.9. The ALP activity is an early marker of cell matrix maturation and may act as a measure of cell mineralisation. The ALP activity of all samples appeared to slightly increase over time with the exception of Sr16 where a decrease was observed, however, all samples including the TCP control did not show a significant difference in ALP activity of each sample as determined via two-way ANOVA.

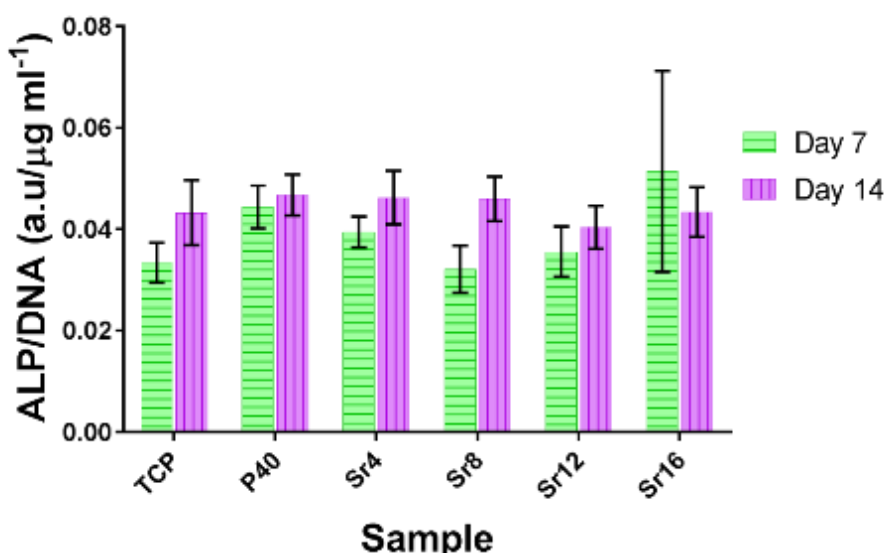


Figure 3.9: Alkaline phosphatase (ALP) activity of MG63 cells cultured on PBG samples in the system $40P2O5 \cdot (16-x)CaO \cdot 20Na2O \cdot 24MgO \cdot xSrO$ ($x = 0, 4, 8, 12$ and 16). P40 indicates 0 mol% SrO and Sr x indicates the SrO mol% in the glass. Data is normalised against DNA concentration at each time point. Error bars represent standard error where, $n = 12$.

The insignificant increase ($p > 0.05$) in ALP activity observed in this study suggested that Sr ion release and concentration had a more profound effect on the cell metabolic activity rather than on the ALP activity, and thus the differentiation of cells. In contrast, Lee *et al.*^[74] found SrO for CaO substitution in an invert PBG had no significant effect on MC3T3-E1 cell attachment and proliferation however, they did observe a slight increase in ALP activity at day 10 with increasing SrO concentration. Similarly higher ALP activity of MG63 cells with addition of Sr was seen by Al Qaysi *et al.*^[73] and an optimal Sr concentration of 17.5 mol% in the glass system $50P_2O_5 \cdot (35-x)CaO \cdot 10Na_2O \cdot 5TiO_2 \cdot xSrO$ ($x = 0, 3.5, 17.5$ & 35 mol%) was determined. A specific value for what the optimal concentration of Sr release is, to encourage osteoblastic cell activity such as proliferation remains controversial. An optimal concentration between 0.09 ppm and 1.75 ppm of Sr was shown to promote cell responses such as proliferation, ALP activity and early gene markers of bone differentiation.^[60, 75] Aina *et al.*^[162] found that concentrations of Sr between 1.21 and 3.24 ppm did not influence the proliferation of MG63 cells and suggested other ions released from the HA substituted with Sr may influence cell behaviour. This co-interaction was also suggested by Lee *et al.*^[74] where Mg^{2+} ions from the glass were suggested to encourage cell attachment and proliferation.

Addition of Sr into other biomaterials such as hydroxyapatite have revealed a significant heightening of ALP activity compared to the control (empty well) and with increasing Sr concentration (atom%), suggesting Sr influences osteoblast cell differentiation in a dose dependant manner.^[161] Usually, a down regulation in cell proliferation is coupled with an upregulation in ALP activity as maturation of the extracellular matrix takes place. However, in this study ALP activity remained stable suggesting a lack in extracellular matrix maturation, which complemented the increase in cell metabolic activity observed with time.^[163]

In line with the insignificant change in ALP activity observed in this study, an ongoing debate is present on the inhibitory effect of Sr^[164], as evident by a study by Wornham *et al.*,^[165] where osteoblast numbers and ALP activity of primary

osteoblasts from rat calvariae were unaltered when exposed to 0.01, 0.1 and 1mM of strontium ranelate and strontium chloride. The same study also showed a dose dependent reduction in mineralisation when compared to the control. However, it should be highlighted that Wornham *et al.*^[165] found strontium salts to have a positive effect on the ability of reducing osteoclast numbers, and thus reduction in formation of resorption pits using mouse marrow cultures on dentine surfaces.

3.7.4 Cell morphology

SEM imaging was used to visualise morphology of cells cultured on PBG disks at each time point. Figure 3.10 shows a representative SEM micrograph of MG63 cells on the PBG formulations investigated. Cells were seen to have attached by day 3 and a confluent layer across all sample compositions was observed at day 14. In general the SEM images showed equal densities of cells for all compositions at both day 3 and day 14. The cells appeared to be spindle like with lamellipodia and filopodia extending to neighbouring cells, leading to the formation of a confluent layer on all of the glass formulations investigated at both day 3 and 14. No apparent difference in cell morphology was observed between each of the compositions investigated.

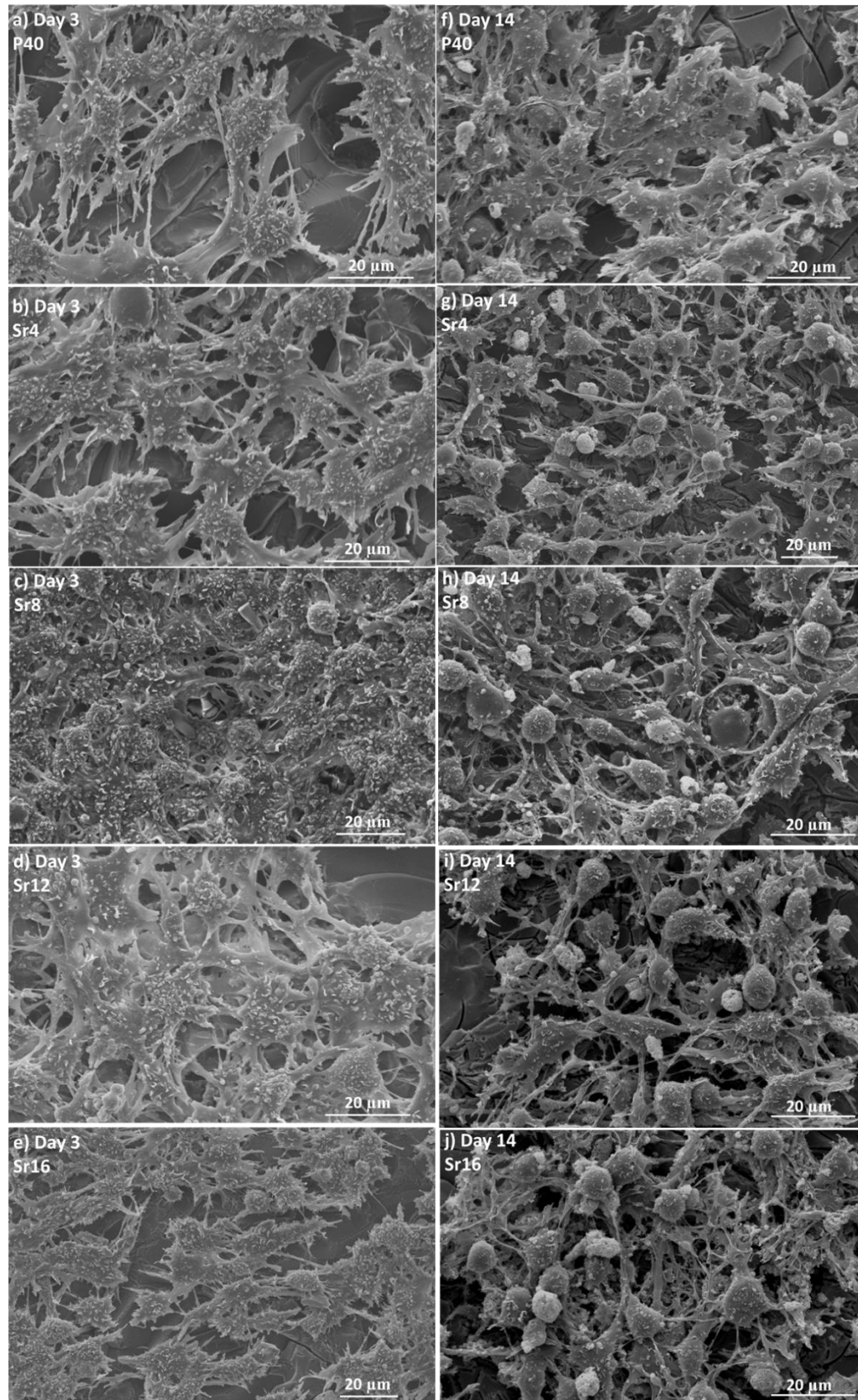


Figure 3.10: Representative SEM micrographs of human osteoblast-like cells (MG63) cultured on PBG compositions at day 3 and day 14. All samples show cell attachment and spreading resulting in the formation of a confluent cell layer.

The SEM micrographs obtained from this study complemented the cell metabolic activity as cell attachment and spreading could clearly be seen by day 3. Elongated, protrusive structures at the edge of the cells i.e. lamellipodia and filopodia were observed, allowing for cell-cell interaction and spreading across the surface of all PBG samples resulting in a confluent layer.^[166] At day 7, cells exhibited a flattened architecture, particularly for P40, Sr4 and Sr16. Cells did not favour a particular orientation and although the cell monolayer appeared fairly packed, large gaps were present. This was attributed to difficulties in sample preparation where the dehydration process using graded ethanol series followed by HMDS can cause cells to shrink, resulting in artefacts and breakage of the fragile cell membrane. Surface topography is well known to influence cell behaviour and physical characteristics such that cells preferentially align themselves to the direction of the surface pattern.^[167-169] Furthermore, the onset of cell attachment observed here at day 3 may be attributed to the stability of the phosphate glass surface, as slower degrading, more stable substrates have shown greater ability to support cell attachment.^[85, 127, 170] The influence of glass composition and degradation rate on cell behaviour was demonstrated by Skelton et al.,^[171] who demonstrated the lack of cell attachment, proliferation and increased cell death on a $50\text{P}_2\text{O}_5 \cdot (50-x)\text{CaO} \cdot x\text{Na}_2\text{O}$ ($x = 2, 4, 8, 8$ or 10) ternary PBG system. Such detrimental effects on cell behaviour were attributed to the unstable PBG surface during dissolution resulting in insufficient time for cells to adhere. This study demonstrated a more stable PBG surface arising from the higher number of network modifiers and low P_2O_5 content, resulting in greater cross-linking of phosphate chains. No obvious difference in morphology was observed with varying concentrations of SrO in the PBGs investigated.

Past studies have shown the inclusion of Sr into PBG's to positively influence the attachment and activity of osteoblast like cells.^[64, 81] Collectively, the results from this study showed CaO substitution with 0-100% SrO had no detrimental effect on cell activity in terms of attachment, proliferation and differentiation, with increased cell metabolic activity observed at later time points (day 7 and 14) for higher Sr containing glasses; i.e. Sr12 and Sr16. It may be postulated that this was caused by the fact that the culture media was replenished every two days, thus possibly resulting in lower concentrations of Sr²⁺ present in the media to show any substantial outcomes on cell activity. Furthermore, although an increase in Sr ion release was observed with increasing SrO in section 3.6, the degradation media used was ultra-pure water, whereas this study used cell culture media which may cause a different degradation behaviour to occur due to the presence of several ions in the culture media to begin with reducing the rate of degradation. One way of overcoming this would be to investigate the time limit for which the culture media is still effective and maintain the culture media with the samples for as long as possible to optimise the concentration of Sr²⁺. Alternatively an indirect testing method could be adopted whereby the samples are degraded in the culture media without the presence of cells and at each time point, the media for the cultured cells could be supplemented with the degradation product.

3.8 Osteoclast feasibility study

This study aimed to investigate the effects of varying Sr concentrations of the PBG formulations investigated on osteoclast activity in terms of osteoclastogenesis and resorption pit activity using human peripheral blood monocytes. Differentiation was induced by MCSF and RANKL. The number of multinucleated cells and osteoclast differentiation was determined using TRAP staining at day 14 as shown in Figure 3.11.

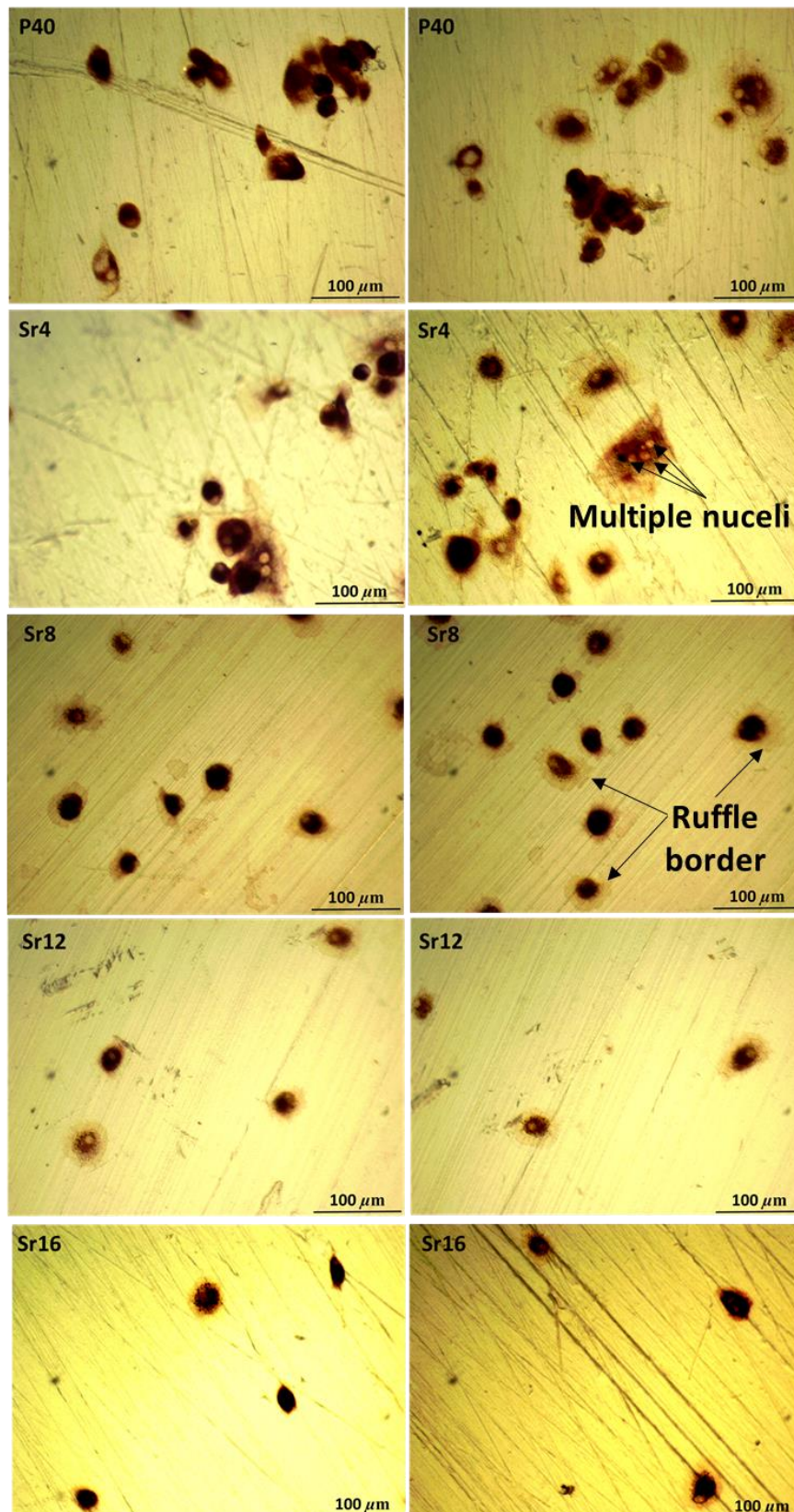


Figure 3.11: Staining of tartrate resistant acid phosphatase (TRAP) activity of cells seeded directly on the surface of glass discs in the series $40\text{P}_2\text{O}_5-(16-x)\text{CaO}\cdot 20\text{Na}_2\text{O}\cdot 24\text{MgO}\cdot x\text{SrO}$ glass at day 14.

Osteoclastogenesis can be characterised by multinucleated morphologies as a result of cell fusion, and is detected by TRAP-positive staining.^[172] From Figure 3.11 it was seen that the cells grown on the glass discs displayed larger, multinucleated cells for P40 and Sr4 compositions, however, with higher Sr concentrations (8, 12 and 16 mol%), cell sizes appeared to be smaller and were mononucleated which stained positive for TRAP activity. Interestingly, the mononucleated cells at higher Sr concentrations of 8 and 12 mol% appeared to display a more prominent ruffled border however, this remains unclear. The ruffle border is an extension of the plasma membrane enclosed by the actin ring, which enlarges into this highly convoluted structure. It is at this site (ruffle border) where protons and lysosomal proteases are released which demineralise and degrade the bone matrix.^[173] As has been seen with previous studies,^[66, 165, 172, 174] a dose dependent effect on the increasing concentration of strontium and formation of osteoclasts was observed in this study.

Various explanations have been proposed on the exact mechanism as to how strontium ions influence osteoclast activity. Previous studies have suggested Sr^{2+} ions may either prevent mature osteoclasts from eroding the surface, or inhibit osteoclast differentiation. This was demonstrated by the reduced TRAP activity and resorption of calcium phosphate (CaP) films by RAW624.7 cells, when cultured with dissolution media from a series of bioactive glasses in the series $46.46\text{SiO}_2 \cdot 1.07\text{P}_2\text{O}_5 \cdot 26.38\text{Na}_2\text{O} \cdot (23.08-x)\text{CaO} \cdot x\text{SrO}$ (mol%) where x was 0%, 10%, 50% or 100% of the CaO content.^[66] The effect of Sr containing CaP bone cements (58 wt.% α -TCP ($\alpha\text{-Ca}_3(\text{PO}_4)_2$), 25 wt.% calcium hydrogen phosphate (DCPA or monetite, CaHPO_4), 8.5 wt.% calcium carbonate (CaCO_3) and 8.5 wt.% hydroxyapatite ($\text{Ca}_{10}(\text{PO}_4)_6(\text{OH})_2$) where CaCO_3 is substituted with SrCO_3 by 0, 5, 10, 50 or 100 wt%) on osteoclastogenesis inhibition/ reduction and osteoclastic resorption has also been investigated using differentiated human peripheral blood mononuclear cells.^[172] This study cultured cells supplemented with SrCl_2 concentrations equivalent to the Sr^{2+} concentrations released by the CaP cements. It was found that Sr^{2+} concentrations up to 0.1 mM reduced TRAP and carbonic anhydrase II (CAII) activity, which altered the

actin cytoskeleton of osteoclasts and did not hinder osteoclastogenesis. At 5-10 mM of SrCl₂, a decrease in cell number was observed suggesting apoptosis of osteoclasts. Decreased CAII activity at concentrations of ≥5 mM SrCl₂ suggested inhibition of osteoclast differentiation. Furthermore, cells were directly seeded on to the CaP cements to investigate cellular resorption and osteoclastogenesis. At day 16, resorption lacunae ranging in diameter from 20-50 μm were detected for Sr free CaP cements, however, Sr containing cements resulted in smaller lacunae diameters as well as number of pits observed with increasing Sr concentration.^[172] Wornham *et al.*^[165] similarly observed a dose dependent effect on the formation of osteoclasts from marrow mononuclear cells, which correlated with the reduction seen in pit formation. It was concluded that Sr²⁺ ions affected the formation of osteoclasts rather than their resorptive activity. The dose dependent behaviour of Sr²⁺ concentration and inhibition of osteoclastic activity was also observed by Peng *et al.*^[174] whereby, the number of multinucleated cells differentiated from RAW624.7 cells in the presence of Sr containing culture media were significantly lower than the Sr free culture media. The findings of this study also demonstrated the necessity of osteoprotegerin (OPG) to be present for osteoclastogenesis and bone resorption to occur in the presence of Sr. Again, a reduction in the differentiation of osteoclasts and disruption of the actin cytoskeleton was demonstrated by Bonnelye *et al.*^[60] in the presence of Sr (ranelate).

Several difficulties were encountered when visualising resorption pits on the glass surface in this study, due to the transparency and inhomogeneous surface roughness of the glass discs as evident from Figure 3.11. A more robust study is required in order to complement what has already been carried out above and to obtain meaningful data on osteoclast activity such as the viability and differentiation of cells by DNA quantification. Assessment of osteoclastogenesis by TRAP staining may also be complemented with CAII which will also assess the enzyme activity of the cells. In order to overcome the problems faced with visualising the formation of pits, an indirect cell seeding method may be experimented with where the degradation products from the

PBG series were supplemented into the culture media and cells were seeded onto dentine discs.

3.9 Summary

Thermal analysis showed that the addition of Sr into a multicomponent 40mol% P_2O_5 glass had little effect on T_g . Initial substitution of CaO with SrO resulted in an increase in T_{onset} , T_c , and thermal processing window, followed by a gradual decrease with increasing substitution. This was attributed to the effect of increased crosslinking with the addition of a fifth cation to the glass network causing an increase in the thermal parameters; however, further addition resulting in a decrease in these parameters was attributed to the smaller field strength associated with Sr^{2+} compared to Ca^{2+} . The increased cross linking and packing density of these glasses were suggested to influence the decrease in dissolution rate with initial addition of SrO. Further addition of SrO had no significant effect on the degradation rate of the glass and suggested that phosphate glasses with compositions close to invert formulations (i.e. fixed with 40 mol% P_2O_5) could provide a means of releasing controlled quantities of Sr^{2+} ions without significantly hindering the degradation rate.

This study showed that the PBG compositions investigated were non-toxic to MG63 cells even at higher concentrations of SrO. The study also showed clear attachment and proliferation of cells when cultured directly on the surface of PBG's. Cell metabolic activity appeared to be greatest for higher Sr containing (Sr12 and Sr16) glasses at later time points however, formulations with increased Sr addition had no effect on cell proliferation and differentiation inferred via DNA and ALP assays respectively. The observations made in this study suggest it is possible to substitute CaO for SrO in a near invert PBG without detrimentally affecting cytocompatibility and cellular activity. The osteoclast feasibility study showed it was possible to directly seed human peripheral blood monocytes onto PBG discs which differentiate into osteoclasts within a 14day period. This early study suggested a dose dependent effect of Sr on osteoclastogenesis however further validation is required.

CHAPTER 4: STRUCTURAL STUDY OF Sr SUBSTITUTED PBG

4.1 Introduction

This chapter investigates the structural effects of substituting CaO with SrO in a $40\text{P}_2\text{O}_5 \cdot (16-x)\text{CaO} \cdot 20\text{Na}_2\text{O} \cdot 24\text{MgO} \cdot x\text{SrO}$ as quenched glass, where x is 0, 4, 8, 12 and 16 mol%. In this study Ca was substituted for Sr in order to minimise the changes in the glass structure; cations with the same valence and similar charge to size ratio can be easily substituted within glass structures.^[175] Although several studies on the structure of phosphate based glasses have been conducted,^[34, 153, 176-181] very little is known about the effect of cation substitution on the structure of complex, multicomponent, lower phosphate containing glasses (i.e. for phosphate glasses close to invert glass formulations). This is primarily due to the difficulties associated with the deconvolution of overlapping modifier–oxygen peaks in diffraction data. A previous study^[68] investigating Ca/Sr substitution in a $49.46\text{SiO}_2 \cdot 26.38\text{Na}_2\text{O} \cdot 1.07\text{P}_2\text{O}_5 \cdot (23.08-x)\text{CaO} \cdot x\text{SrO}$ (where $x = 0, 11.54, 23.08$) glass system used an isostoichiometric substitution method in order to determine the M-O environments in the neutron diffraction data, finding that Ca and Sr behaved in a similar manner in the glass structure. The M-O environments in this study were first of all determined for binary alkali and alkaline earth metaphosphates followed by simultaneous fitting of all the multicomponent compositions using the programme NXFit^[182] where the parameters of the binary metaphosphate glasses were used in the model.

Chapter 3 explained the physico-chemical properties of substituting CaO with SrO in the $40\text{P}_2\text{O}_5 \cdot (16-x)\text{CaO} \cdot 20\text{Na}_2\text{O} \cdot 24\text{MgO} \cdot x\text{SrO}$ glass, where x is 0, 4, 8, 12 and 16 mol%, and this chapter aimed to understand its atomic scale structure in order to understand the features observed in chapter 3.

³¹P and ²³Na NMR and FTIR were used in order to determine the medium to short range order of the glasses, and neutron diffraction studies were carried out in order to probe the short range structure at an atomic level. Structure determination allows tailoring of materials which can be highly beneficial when

aiming to release therapeutic ions at a controlled rate. All materials and methodology for this chapter has been outlined in Chapter 2.

4.2 Solid state NMR

4.2.1 ^{31}P MAS NMR

Both ^{31}P and ^{23}Na MAS NMR spectra can be seen in Figure 4.1. The two dominant isotropic peaks in the ^{31}P MAS NMR spectra (Figure 4.1 (a)) are at *c.a.* -8.0 ppm and -22 ppm and are ascribed to Q^1 and Q^2 units respectively.^[48, 183] The relative intensity of these features remained constant with Ca/Sr content. This behaviour arises due to the unchanged oxygen concentration in the glasses. For an alkali or alkaline earth phosphate glass with a composition of 100y mol% P_2O_5 , with y in the range from 0.5 to 0.333, there are expected to be only Q^2 and Q^1 units, with an abundance $Q^1=(1-2y)/y$ (and $Q^2=1-Q^1$). For the multicomponent glasses, $y=0.4$, and hence equal numbers of Q^2 and Q^1 units are expected. The equal number (50%) of Q^1 and Q^2 units in the glass series as shown in table 4.1, suggested that all of the modifiers are behaving as network modifiers. The network connectivity^[155] of the glasses can be calculated from the average number of BO per network forming tetrahedra. If the PBG contains only Q^1 and Q^2 units, then the average number of BO atoms in a PO_4 unit is given by:

$$N_{\text{BO}} = 2 - Q^1 \quad (11)$$

Here, Q^n indicates the fraction of P with n bonds to bridging oxygen, as determined by ^{31}P MAS NMR. This study showed a constant network connectivity $N_{\text{BO}} \approx 1.5$ as displayed in Table 4.1. This corresponded to the fact that the overall modifier content was constant throughout the glass series. This study found that, replacing calcium for strontium had minimal effects on the phosphorous environment as examined by MAS NMR, which corresponded well with the minimal effects observed on bulk characteristics, such as dissolution rates as outlined in Chapter 3, section 3.6.

From these results, an average chain length of four tetrahedra can be assumed based on two Q^1 units terminating either end of a chain of two Q^2 units. This assumption was made on the basis of there being no rings in the structure. For compositions close to metaphosphates ($O/P = 3.00$) it has been shown that cyclic phosphate ring structures can also exist,^[184] necessitating the formation of shorter chains or phosphate dimers (i.e. pyrophosphates).

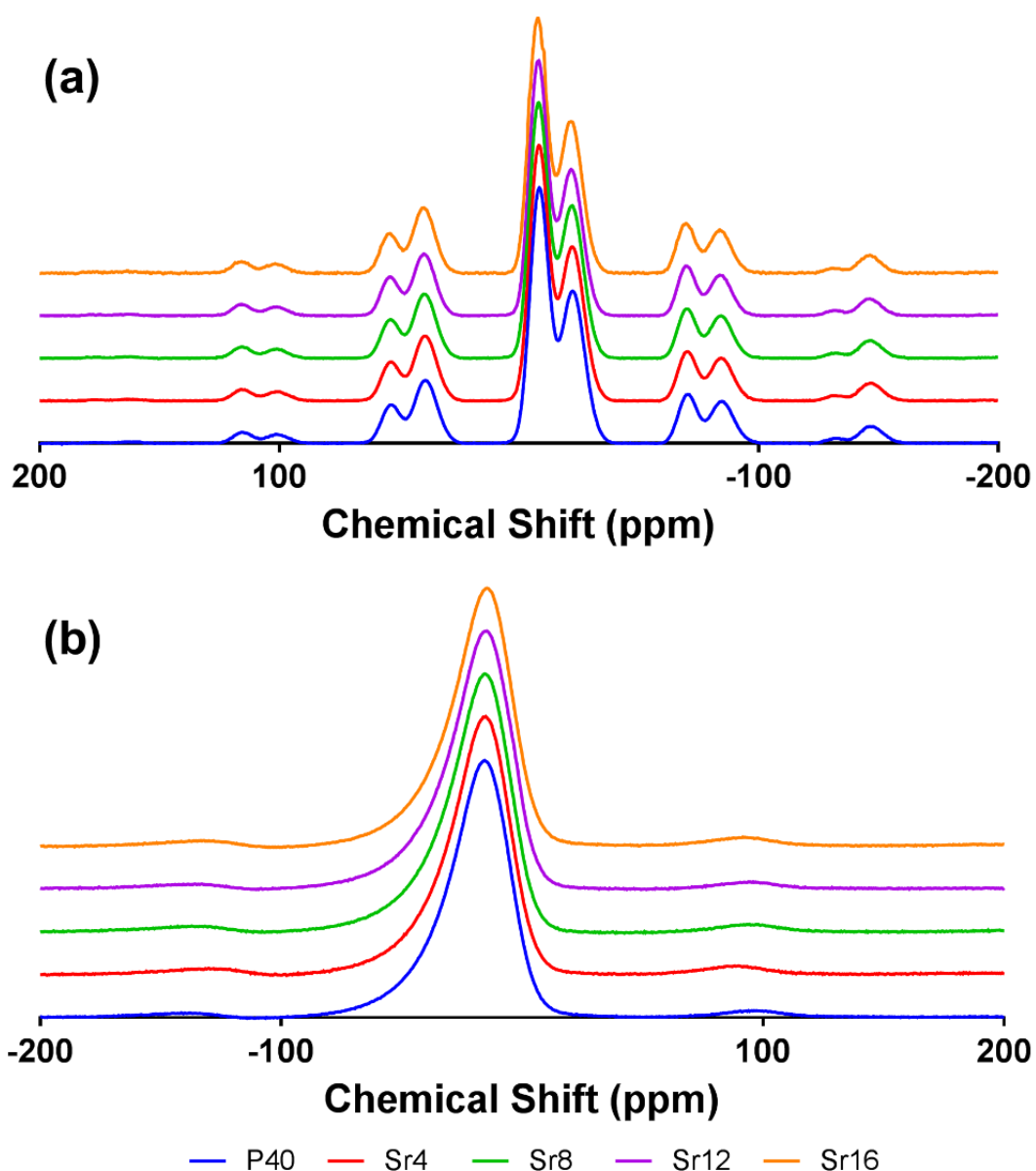


Figure 4.1 Solid-state (a) ^{31}P MAS NMR and (b) ^{23}Na MAS NMR data of multicomponent glasses investigated.

Table 4.1: Chemical shifts (ppm referenced using H_3PO_4) and relative concentrations of Q^n units determined by solid-state ^{31}P MAS NMR of each composition investigated and the calculated number of bridging oxygens (BOs) and non-bridging oxygens (NBOs) per PO_4 unit using equation 11.

Glass code	Intensity -8 ppm /% (Q^1)	Intensity -22 ppm /% (Q^2)	BO	NBO
P40	49	51	1.51	2.49
Sr4	49	51	1.51	2.49
Sr8	49	51	1.51	2.49
Sr12	50	50	1.50	2.50
Sr16	49	51	1.51	2.49

4.2.2 ^{23}Na MAS NMR

Figure 4.1 (b) shows each ^{23}Na MAS NMR spectrum. Unlike the two peaks observed with the ^{31}P MAS NMR, ^{23}Na MAS NMR exhibited a single, broad, slightly asymmetric peak at approximately 15 ppm.^[185, 186] Detailed information on the chemical environment for sodium is difficult to obtain from NMR due to the inability to eliminate second-order quadrupolar interactions and distribution of bond angles.^[185, 186] However, a study of the sodium environment in a binary sodium tellurite glass system found that increasing concentration of Na_2O in the glass, caused a change in chemical shift in the ^{23}Na MAS NMR spectra, which was attributed to a decrease in the sodium-oxygen coordination from six to five.^[187] The lack of change in chemical shift in this study indicated that substituting CaO for SrO had no effect on the local environment of sodium atoms in the glass.

4.3 FTIR

Figure 4.2 shows the FTIR spectra for the multicomponent glasses studied. The five prominent band positions (wavenumber cm^{-1}) are indicated by a dotted line and their assignments are shown in Table 4.2. The first two prominent absorption bands at 725 and 890 cm^{-1} were attributed to symmetric and

asymmetric stretching of P-O-P respectively.^[183] The bands near 990 and 1100 cm^{-1} have been assigned to symmetric and asymmetric stretching of chain end units associated with Q^1 units^[183, 188] and 1250 cm^{-1} for asymmetric stretching of NBO in a phosphorous atom in Q^2 units,^[73, 188, 189] (where the n in Q^n refers to the number of BO atoms in the PO_4 tetrahedral unit as discussed in Chapter 1, section 1.5.1). Both the peak intensity and position remained constant for all multicomponent glasses studied, suggesting similarities in structure between all compositions. Al Qaysi *et al.*^[73] investigated the FTIR spectra of Sr-containing phosphate glasses in the composition $50\text{P}_2\text{O}_5 \cdot 10\text{Na}_2\text{O} \cdot 5\text{TiO}_2 \cdot (35-x)\text{CaO} \cdot x\text{SrO}$ (where $x=0, 3.5, 17.5$ and 35), which showed an unexpected decrease in intensity for peaks at 900cm^{-1} associated with P-O-P asymmetric stretching of Q^2 units and an increase in peak intensity at 1100cm^{-1} associated with Q^1 units with increasing Sr content. The lack in variation between the samples examined in this study using FTIR was attributed to the fact that the O/P ratio (3.25) was constant for each sample, thus not influencing the network structure. These results corroborated well with the ^{31}P and ^{23}Na MAS NMR results showing that Sr for Ca substitution did not influence the structure.

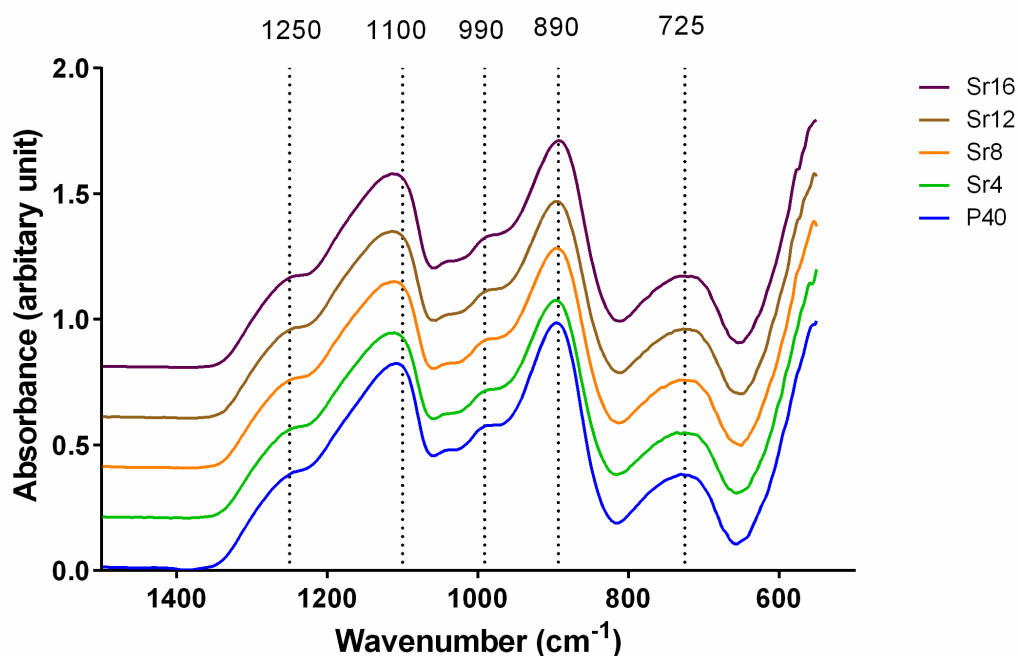


Figure 4.2: FTIR spectra obtained for multicomponent glasses. The dotted lines indicate prominent bands in the spectra.

Table 4.2: The FTIR wavenumbers (cm^{-1}) and band assignments attributed to the multicomponent glass samples.

Wavenumber (cm^{-1})	Assignment ^[73, 183, 188, 189]
1250	Asymmetric stretching of two NBO bonded to a phosphorous atom in Q^2 units
1100	Asymmetric stretching of Q^1 chain end units
990	Symmetric stretching of Q^1 chain end units
890	Asymmetric P-O-P stretching
725	Symmetric P-O-P stretching

4.4 Neutron diffraction

The Ca/Sr substituted glasses in this study can be classified as highly complex due to the relatively large number of modifying cations included in the structure. Such complexity renders the extraction of the local environment information exceedingly difficult due to the overlapping of modifier-oxygen (M-O) bonds with at least one other in the correlation function. In the case of Sr-O peak, which is of primary interest in this study, there is overlap in peaks arising from Na-O, Ca-O bonds and O...O distances.

Therefore, in order to provide information on such M-O peak parameters, neutron diffraction fits to the correlation function for the relevant binary metaphosphate compositions (CaP_2O_6 , SrP_2O_6 , MgP_2O_6 and NaPO_3) were obtained in addition to the multicomponent glasses. The M-O peak positions, widths and areas from fitting the correlation functions of the binary metaphosphate glasses were used to aid in the interpretation of the neutron diffraction data of the multicomponent glasses.

4.4.1 Neutron diffraction experimental set-up

All binary metaphosphate glass compositions were ground into irregular particles and contained in vanadium cylinders with a diameter of 10.3 mm and wall thickness of 40 μm . The multicomponent glasses were cast into solid rods and fixed to sample holders, and placed directly in the neutron beam. Once all interference patterns were collected, along with the vanadium rod, empty sample can and empty GEM, data was corrected and normalised as outlined in section 2.5.4.2.

4.4.2 Diffraction patterns

The distinct scattering functions $i(Q)$, for the binary metaphosphate and multicomponent glasses are shown in Figure 4.3 (a) and (b) respectively. The most prominent changes are highlighted in the main area of the graph displaying the low Q region and the insert shows the data to a maximum Q , of 50 \AA^{-1} , as used to Fourier transform the data. The high Q_{max} value used yields a narrow resolution in real-space. The lack of any Bragg peaks in the $i(Q)$ agrees with the XRD results displayed in Chapter 3.2 displaying amorphicity of the samples. Neutron diffraction experiments are highly sensitive to the presence of crystallinity due to the high penetration of neutrons and high resolution in reciprocal space.

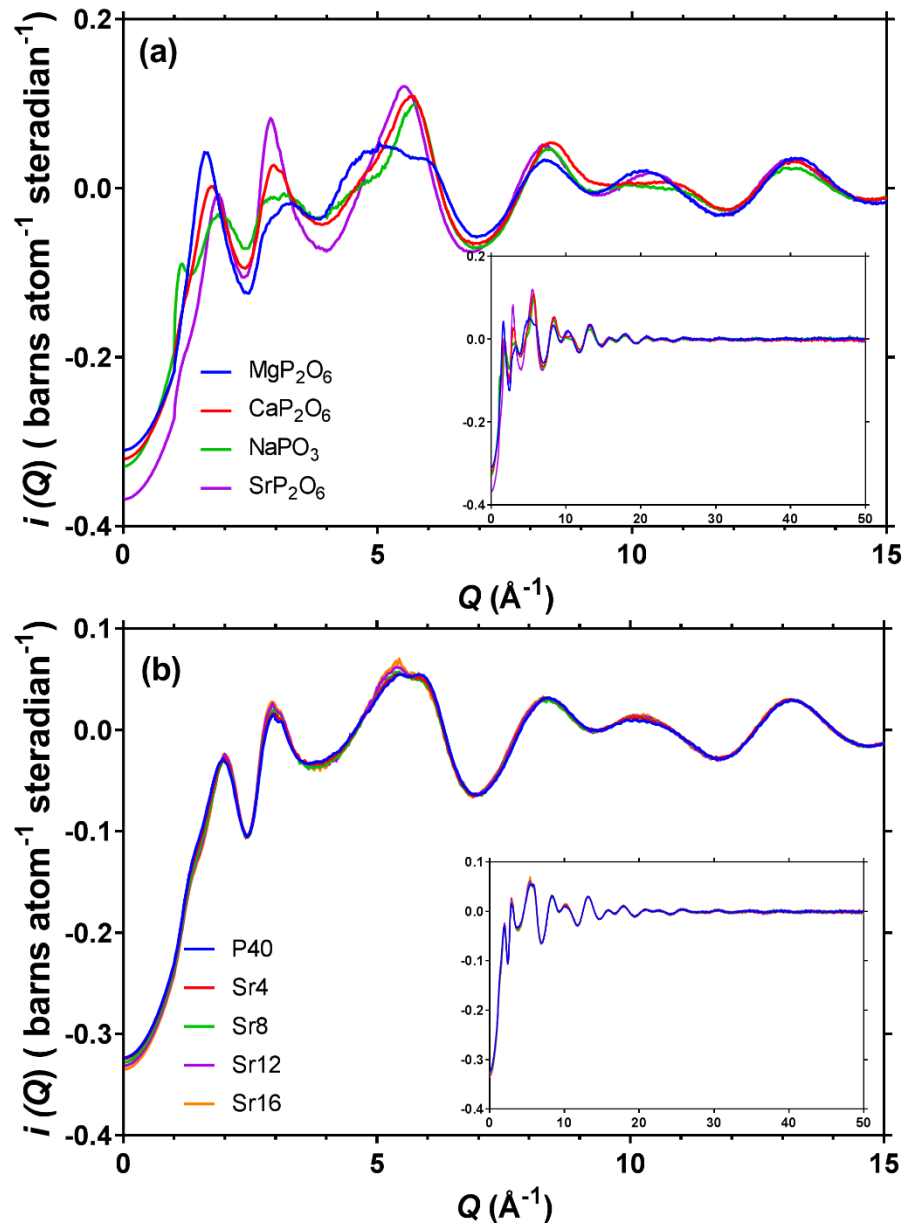


Figure 4.3: distinct scattering, $i(Q)$, patterns of (a) binary metaphosphate glasses and (b) multicomponent glasses of composition $40P_2O_5 \cdot (16-x)CaO \cdot 20Na_2O \cdot 24MgO \cdot xSrO$, where x is 0, 4, 8, 12 and 16 mol%.

The first sharp diffraction peak (FSDP) in $i(Q)$ in Figure 4.3 (a) is at 1.56 \AA^{-1} for MgP_2O_5 , which progressively shifts to higher Q with increasing alkaline earth radius. This shift is surprising, because the position of the FSDP can arise from the typical size of the cages formed by the network^[190] however, it should be noted that competing theories about the FSDP do exist.^[191, 192] It has previously been suggested, on the basis of molar volume studies, that an expansion of the silicate network occurs when strontium is substituted for calcium in silicate glasses.^[63, 67] However, this result does not provide support for an expansion of

the phosphate network as Sr substitutes for Ca. The next prominent peak observed for the alkaline earth metaphosphate compositions showed a reversal in these trends with the peak shifting from 2.95 to 3.3 Å⁻¹, as does the third peak at ca. 5.50 Å⁻¹ with the MgP₂O₆ glass also exhibiting a shoulder at lower Q .

The peaks in $i(Q)$ of the NaPO₃ glass are in very similar positions to those observed for the alkaline earth modifier glasses. However, there are two shoulders, one at 1.22 Å⁻¹, which was not present for the other binary metaphosphate compositions, and one at 4.86 Å⁻¹, which is similar to the shoulder in the correlation function for the magnesium glass, but has a significantly greater intensity. Such differences may be attributed to structural difference, possibly due to a bigger distribution of bond lengths or weaker, longer bonds.

The $i(Q)$ patterns shown in Figure 4.3 (b) for the multicomponent glass series show a decrease in intensity below the FSDP, and increase in intensity at *c.a.* 3Å and an increase in intensity at 5Å which match the $i(Q)$ patterns of the binary metaphosphate glasses. Furthermore, almost no change in the FSDP with composition was observed for the multicomponent glasses, suggesting that the size of the network frame is not altered significantly by the substitution of Ca with Sr.

4.4.3 Real-space correlation functions

The total correlation functions, $T(r)$, for the binary metaphosphate and multicomponent glass series are displayed in Figure 4.4 (a) and (b) respectively. In order to best show the clear split in the first prominent peak, the step modification function was used when calculating the $T(r)$ (as outlined in equation 17 (chapter 2)), in the region at low r preceding the dotted line (at 1.8 Å) in Figure 4.4. The $T(r)$ for the region subsequent to the dotted line at high r was calculated using the Lorch^[142] modification function. The step modification function results in narrower real-space resolution of $T(r)$, although at the expense of greater termination ripples which may mask real peaks at higher r . Both binary metaphosphate and multicomponent glass spectra showed a prominent peak at *ca.* 1.51 Å and *ca.* 1.62 Å relating to the P-O nearest neighbour distances. This was in agreement with previous studies^[180, 181, 193]. The shorter distance of this split peak was attributed to P-NBO, and the longer distance to P-BOs.^[176]

Although better separation of the P-BO and P-NBO peak was observed using the step modification function, there was still insufficient separation to constrain the fits, thus, in order to obtain reliable results, consistent between the samples, for the P-O peak it was necessary to constrain the ratio of the two coordination numbers for the P-NBO and P-BO. For the binary metaphosphate compositions shown in Figure 4.4 (a), the coordination numbers of the P-NBO and P-BO contributions were constrained at a ratio of 1:1, since for a composition of 100y mol% P₂O₅, the ratio is calculated as $\frac{n_{p-BO}}{n_{p-NBO}} = 4y - 1$. Thus, for the multicomponent glasses in Figure 4.4 (b), the coordination numbers for one peak was fixed at 0.6 of the other, which was also consistent with the ³¹P MAS NMR results shown in Table 4.1.

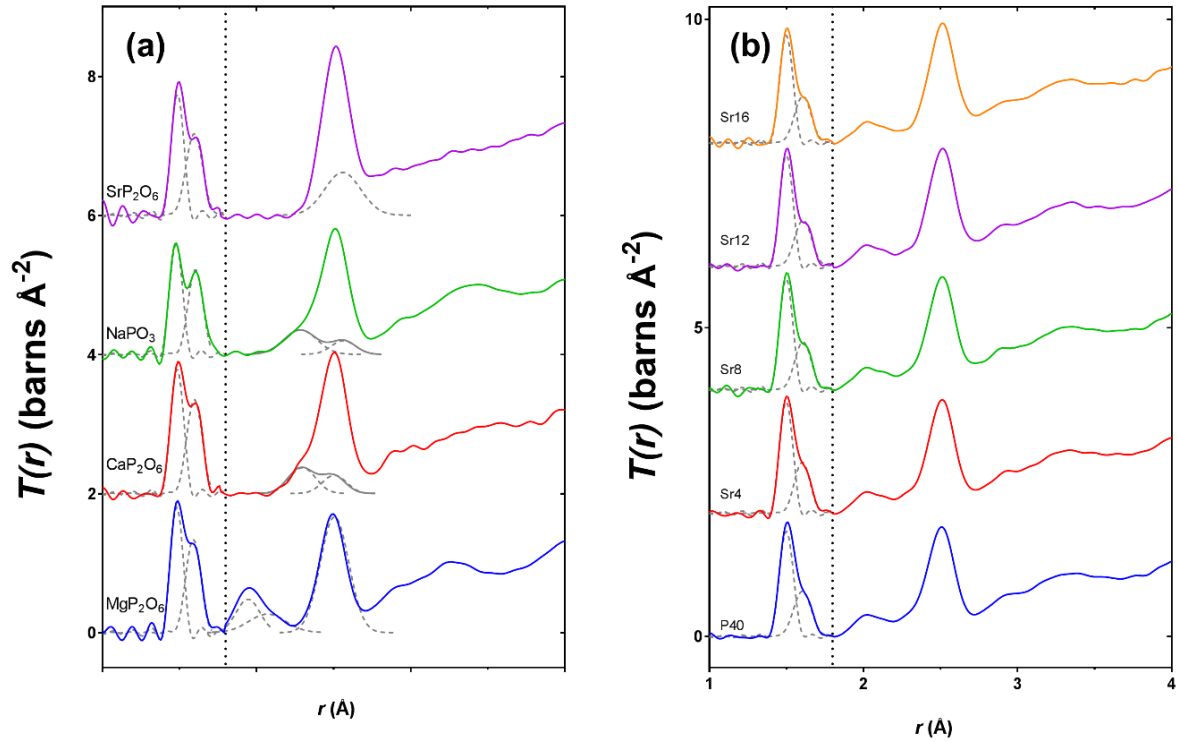


Figure 4.4: (a) Total correlation functions, $T(r)$ of binary samples and, (b) $T(r)$ of multicomponent glasses, where the region before the dotted line is Fourier transformed using the step function and the region after the dotted line was Fourier transformed using the Lorch^[142] function.

The resultant P-O coordination numbers from this study as derived by equation 19 (chapter 2) were between 3.77 and 4.00. The errors on the data points in the measured neutron spectra were determined by counting statistics (i.e. for N counts the standard deviation is \sqrt{N}), and these were propagated through the various stages of data reduction and correction so as to determine the standard deviation on the data points for $i(Q)$. The statistical errors on $i(Q)$ were then propagated through the Fourier transform $T(r)$. The errors on $T(r)$ were taken into account in the fits to $T(r)$. giving rise to the statistical errors on the fit parameters reported in Table 4.3. The expected P-O coordination number of these tetrahedral glasses is four. However, it is common for the P-O coordination numbers to be slightly lower than the expected value due to the dampening of peaks at high Q arising from Q - resolution (in reciprocal-space).^{[194], [56]} What was also apparent was that the variation in bond lengths amongst the multicomponent glasses ($\pm 0.04 \text{\AA}$) was not as great at that

observed for the binary metaphosphate glasses ($\pm 0.10 \text{ \AA}$), suggesting that calcium for strontium substitution has very little effect on the P-O bond lengths.

Table 4.3: The phosphorous environments in the binary and multi-component glasses, derived by fitting $T(r)$ using a step function.

Sample	Atom pair $l - l'$	Bond length ($r_{ll'}/\text{\AA}$)	Bond length variation ($\langle u_{ll'}^2 \rangle^{1/2}/\text{\AA}$)	Coordination number ($n_{ll'}$)
MgP₂O₆	P-NBO	1.4822 (4)	0.0347 (5)	1.92 (1)
	P-BO	1.5998 (7)	0.0465 (6)	1.92 (1)
	P-O sum			3.83 (2)
CaP₂O₆	P-NBO	1.4848 (4)	0.0375 (4)	2.00 (1)
	P-BO	1.5969 (6)	0.0483 (5)	2.00 (1)
	P-O sum			4.00 (2)
SrP₂O₆	P-NBO	1.4869 (4)	0.0356 (4)	1.88 (1)
	P-BO	1.5962 (8)	0.0527 (7)	1.88 (1)
	P-O sum			3.77 (2)
Na₂P₂O₆	P-NBO	1.4776 (8)	0.0365 (8)	1.93 (2)
	P-BO	1.604 (1)	0.046 (1)	1.93 (2)
	P-O sum			3.86 (4)
P40	P-NBO	1.49995 (5)	0.04196 (5)	2.458 (2)
	P-BO	1.6039 (1)	0.0565 (1)	1.475 (1)
	P-O sum			3.932 (3)
Sr4	P-NBO	1.4988 (2)	0.0386 (3)	2.435 (9)
	P-BO	1.6031 (6)	0.0494 (6)	1.461 (5)
	P-O sum			3.90 (1)
Sr8	P-NBO	1.4990 (1)	0.0383 (1)	2.407 (5)
	P-BO	1.6079 (3)	0.0522 (3)	1.444 (3)
	P-O sum			3.851 (8)
Sr12	P-NBO	1.4997 (2)	0.0383 (3)	2.41 (1)
	P-BO	1.6083 (7)	0.0541 (6)	1.445 (7)
	P-O sum			3.85 (2)
Sr16	P-NBO	1.4992 (3)	0.0394 (3)	2.38 (1)
	P-BO	1.6070 (8)	0.0530 (7)	1.430 (6)
	P-O sum			3.81 (2)

The P-NBO and P-BO measured for the multicomponent glasses in this study (Table 4.3) are in good agreement with previous studies for PBGs.^[178, 179] An increase in the P-NBO bond length from 1.4822 Å for the MgP₂O₆ binary metaphosphate glasses to 1.49995 Å for P40 was found, as was also the case

for the P-BO bond lengths with a smaller increase from 1.5998 Å for MgP₂O₆ to 1.6039 Å for P40. Such a change is caused by the depolymerisation of the network as the modifier content is increased.^[195]

4.4.5 Binary metaphosphate modifier environment

Deconvolution of the modifier-oxygen (M-O) environment required a systemic approach due to the overlap in M-O bonds and O...O distances. Fits were first made to the Mg-O and O...O distances in the MgP₂O₆ samples due to the clear separation of these two peaks in the $T(r)$ as shown in Figure 4.4 (a). In contrast, for all other samples studied, there is significant overlap in the M-O and O...O peaks. Thus $T(r)$ for MgP₂O₆ provided both a clear measurement of the Mg-O coordination, and a clear measurement of the O...O peak that can be used to aid the interpretation of the results for the other binary metaphosphate samples.

The Mg-O peak in $T(r)$ showed a clear asymmetry, with an extended tail on the long distance side, thus it was best modelled using two peaks at 1.945 Å and 2.07 Å. A total coordination number of 5.0 was obtained as shown in Table 4.4, however a larger error was associated with this, due to the over estimation of the two peak fit components. Earlier reports on MgP₂O₆ glasses have shown insufficient real-space resolution to reveal the asymmetry observed in the Mg-O peak, however, later reports with greater resolution have shown such asymmetry. The distribution in coordination numbers reported in the later reports are in good agreement with that found in this study ranging from 5.3 to 6.3.^[91, 196-200] It must be mentioned that none of the previous studies have had a Q_{max} as high as the one used in this study, and this is the first time that MgP₂O₆ has been measured with sufficient resolution that there is insignificant overlap with the Mg-O and O...O peaks in $T(r)$.

On comparison to crystalline structures, the coordination number measured in this study is lower than when Mg is octahedrally coordinated by oxygen.^[201] It is of note that studies of magnesium silicate glasses also find an asymmetric distribution of Mg-O distances,^[202] and coordination numbers less than 6.

Table 4.4: The modifier environments in the binary glasses, derived by fitting $T(r)$, and the refined Mg-O and O...O peak parameters used to simulate $T(r)$ s for the multicomponent glasses.

Sample	Atom pair $l - l'$	Bond length ($r_{ll'}/\text{Å}$)	Bond length variation ($(\langle u_{ll'}^2 \rangle)^{1/2}/\text{Å}$)	Coordination number ($n_{ll'}$)	M-O valence (e)
MgP₂O₆	Mg-O	1.945 (1)	0.066 (4)	2.6 (5)	1.30
	Mg-O	2.07 (3)	0.11 (1)	2.4 (5)	0.87
	Mg-O sum			5.0 (7)	2.17
	O-O	2.5059 (9)	0.084 (1)	4.29 (4)	
CaP₂O₆	Ca-O	2.299 (2)	0.078 (2)	2.91 (6)	1.19
	Ca-O	2.506 (2)	0.069 (2)	2.10 (7)	0.49
	Ca-O sum			5.01 (9)	1.68
SrP₂O₆	Sr-O	2.559 (1)	0.111 (1)	5.10 (6)	1.55
Na₂P₂O₆	Na-O	2.284 (2)	0.100 (3)	2.58 (6)	0.70
	Na-O	2.564 (3)	0.070 (5)	1.20 (7)	0.15
	Na-O sum			3.77 (9)	0.85
Multicomponent Sr-series glasses	Mg-O	2.00	0.07	2.44	1.06
	Mg-O	2.09	0.09	2.62	0.90
	Mg-O sum			5.06	1.96
	O-O	2.51	0.08	4.15	

The O...O peak in the $T(r)$ of the MgP₂O₆ glass was fitted with a single peak and resulted in a coordination number of 4.29 (4).

Unlike the clear separation of the Mg-O peak seen in $T(r)$ for MgP₂O₆, the M-O peak in the other binary metaphosphate glasses largely overlaps with the O...O peak and so direct fitting of the M-O distances to $T(r)$ cannot be determined. Thus, the O...O peak fit parameters (see Table 6; bond length = 2.5059, peak width = 0.084 and coordination number = 4.29) from the MgP₂O₆ sample were then used to model the O...O peak in the other alkaline earth binary metaphosphate glasses, since all (Ca and Sr) except Na binary metaphosphate samples have the same stoichiometry, thus it may be assumed that the O...O peak is similar in each sample. This O...O peak was subtracted from the $T(r)$ to reveal the P-O and M-O contributions, as shown in Figure 4.5 for SrP₂O₆ and CaP₂O₆.

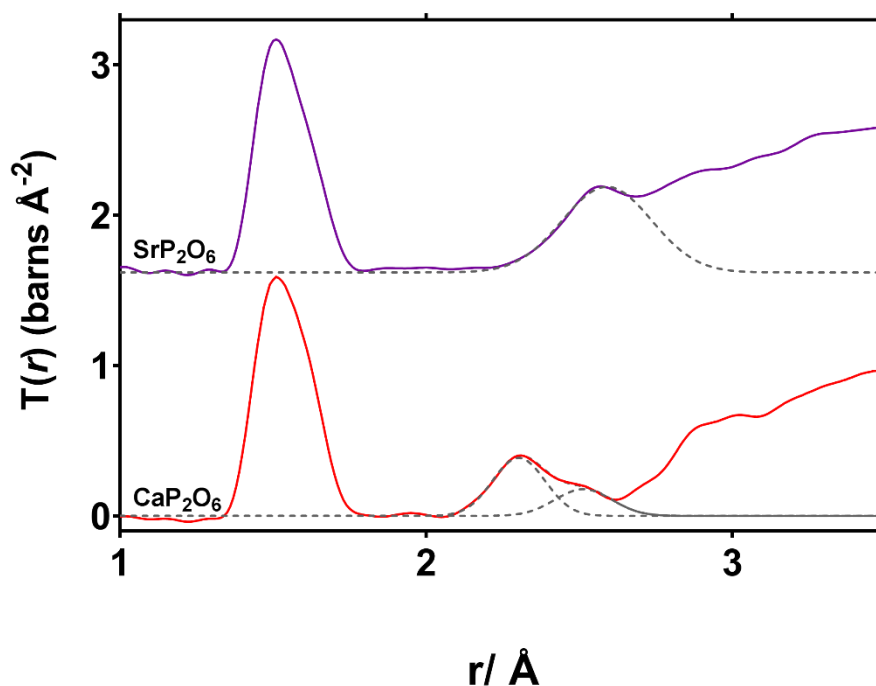


Figure 4.5: SrP_2O_6 and CaP_2O_6 residual $T(r)$ where $\text{O}\dots\text{O}$ peak has been subtracted from $T(r)$ leaving P-O and M-O peaks. Grey dashed line shows M-O peak fit.

The Ca-O peak was best fit with two peaks centred at 2.299 (2) Å and 2.506 (2) Å yielding a coordination number of 5.01 (9) (see Table 4.4). This is consistent with the prediction that five Ca-O bonds of length 2.306 Å are required to satisfy bond valence,^[203] but is a significantly lower coordination number than observed in calcium metaphosphate crystals, where coordination numbers of 6 are observed (where bond lengths are assumed to be shorter than 2.55 Å).^[204] A study by Wetherall et al.^[181] highlighted a range of coordination numbers for Ca-O such as 5.2 at a distance of 2.35 Å, which was similar to this study, and an additional coordination number of 1.7 at a distance further than the range studied here, at 2.86 Å.

Alternatively, Sr-O correlations required only a single peak to best model the Sr-O bond length distribution. The peak centred at 2.559 Å yielded a coordination number of 5.10 (6), which was lower than that predicted by the bond valence, as Sr-O bond lengths of 2.582 Å are predicted to result in coordination numbers of 7.^[203] The coordination number from this study does however, correlate well with that observed in a SrP₂O₆ crystal when the upper limit for bond lengths was restricted to 2.7 Å.^[205] Hoppe *et al.*^[206] previously determined a coordination number of 6 for Sr-O at a bond length of 2.552 Å, which is in reasonable agreement to that found in this study.

The discrepancy in coordination numbers observed in these binary metaphosphate glasses when compared to the Ca and Sr metaphosphate crystals may arise due to the overlapping with longer bond correlations in the glass. There are several M-O bonds that are longer than 2.6 Å in the crystals, a length scale in the correlation functions where a number of different interatomic distances are present. Such complications with resolving Ca-O and Sr-O environments due to the overlap of the M-O peaks with other correlations has previously been observed.^[181, 196]

The addition of Na into the glass network of the NaPO₃ glass composition altered the coefficients for each partial correlation ($C_i, \bar{b}_i, \bar{b}_i'$) in equation 9 (chapter 2) as one Mg ion is replaced by two Na ions. Therefore, it was necessary to scale the experimental data for the NaPO₃ glass and the O...O peak taken from the MgP₂O₆ glass by the respective partial correlation function coefficients for $t_{oo}(r)$ before subtracting the O...O peak. Once the subtraction had been successfully carried out, the residual correlation function was rescaled and the sodium-oxygen peak was fitted as shown in Figure 4.6.

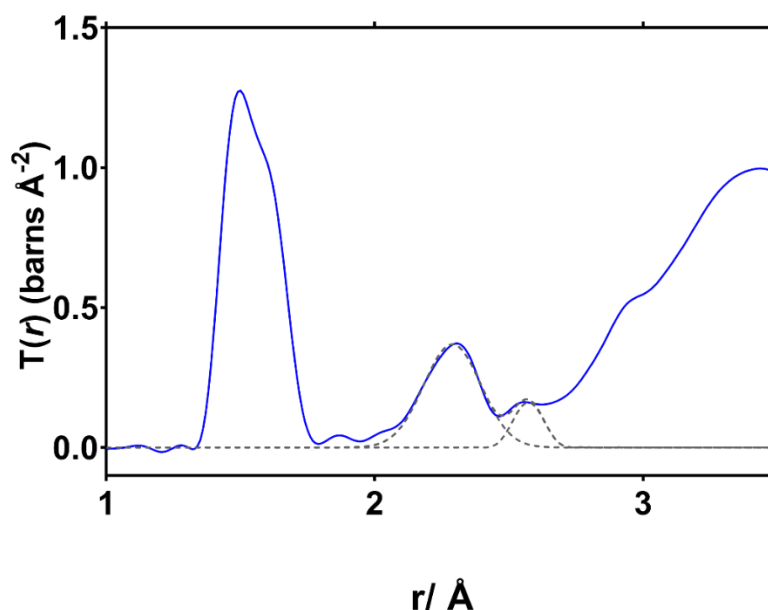


Figure 4.6: NaPO_3 residual $T(r)$ after scaling where $\text{O}\dots\text{O}$ peak has been subtracted from $T(r)$ leaving P-O and M-O peaks. Grey dashed line shows M-O peak fit.

In order to best fit the Na-O bond length distribution two peaks were required. The obtained coordination number for the Na-O contribution was 3.77 (9) with a bond length of 2.284 and 2.564 Å. A coordination number of 4 was given by bond valence calculations for Na-O bonds of length 2.31 Å which is fairly similar to the one obtained in this study. A NaPO_3 crystal has been shown to contain sodium ions with three bonds to oxygen that are shorter than 2.4 Å, and up to three more bonds in the range of 2.4 - 3 Å.^[207] Pickup *et al.*^[193] measured the Na-O coordination for a sodium metaphosphate glass composition to have a coordination number of ~4 using a single peak at a bond length of 2.33 Å. However, this fit was only achieved when including a Na-Na correlation beyond $r = 3\text{Å}$. This was justified by the fact that each polyhedral will share edges resulting in Na-Na correlations since each NBO is shared by two Na^+ ions.

In summary, we have found that in binary metaphosphate glasses M-O (M=Mg, Ca, Sr, Na) coordination numbers are smaller and M-O bond lengths are shorter than in corresponding crystals. The distributions of M-O bond lengths are broad and asymmetric. Two peaks were required to model the Ca-O, Na-O and Mg-O environments, which is consistent with previous neutron diffraction studies published by Martin *et al.*^[68, 175] on silicate based glasses.

4.4.6 Multicomponent glass deconvolution

The modifier environments such as the bond length, coordination number and peak positions of the multicomponent glasses could not be fit in the same way as for the binary metaphosphate glasses due to the numerous M-O contributions which overlap. Figure 4.4 (b) shows a great deal of similarity between correlation functions for the Sr-series multicomponent glasses. The only small differences were observed either side of the major peak at *c.a.* 2.51Å as shown in Figure 4.7, where a loss in Ca-O contribution at shorter distances between *c.a.* 2.15 – 2.40 Å, and growth of the Sr-O contribution at longer distances between *c.a.* 2.45 – 2.95 Å was observed as Ca is substituted for Sr. For this reason, all five multicomponent glass series were fit simultaneously, using the single set of peak parameters ($r_{ll'}$, $\langle u_{ll'}^2 \rangle^{1/2}$ and $n_{ll'}$) obtained from fitting the binary metaphosphate glasses as displayed in Table 4.4 using the programme NXFit.^[182] NXFit is a programme which optimises structural parameters of amorphous materials using neutron pair-distribution functions. Fits are made to the experimentally derived data as best as possible using the Nelder-Mead method, resulting in the output of coordination number, atomic separation and disorder parameter for each atomic correlation used in the fitting process. This version of NXFit took into account the correct real-space resolution function but did not evaluate errors on the fitted parameters.

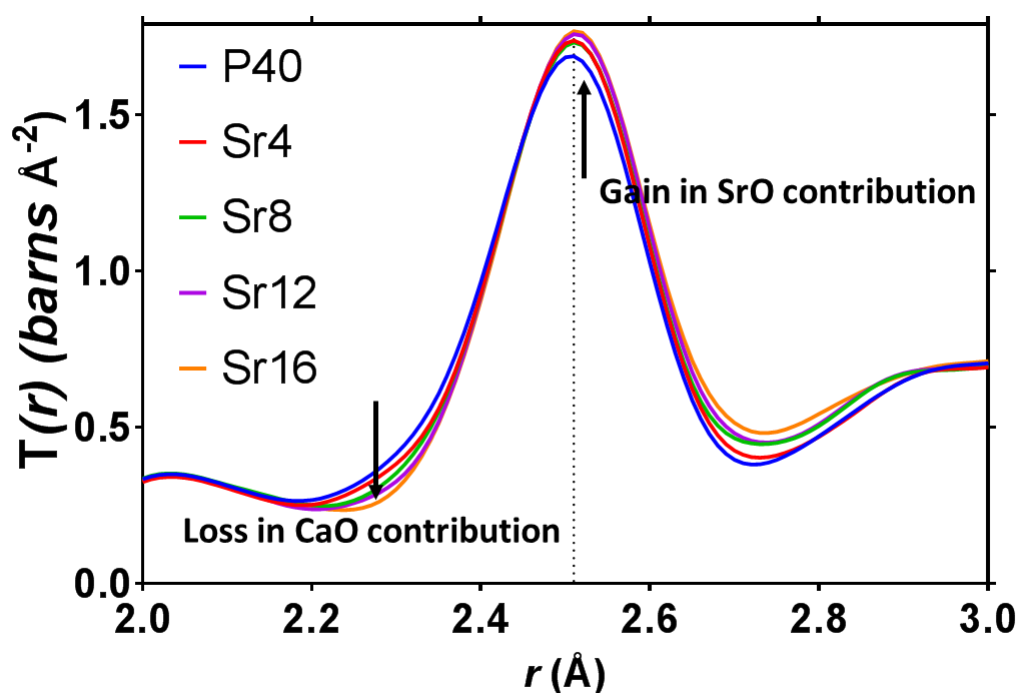


Figure 4.7: $T(r)$ of multicomponent glasses showing small differences either side of the peak at 2.51\AA (dotted line) due to loss in Ca-O contribution (at short distances) and growth in Sr-O contribution (at long distances).

A series of files were set up in order to provide information about the sample and diffraction measurements as summarised in Table 4.5. The Ca-O, Na-O and Sr-O parameters were fixed due to the lack of evidence in change, however, the O...O distance was allowed to vary by bond length $\pm 0.5\text{\AA}$, coordination number ± 1.5 and peak width $\pm 0.5\text{\AA}$ and the Mg-O bond parameters were allowed to vary by bond length $\pm 0.5\text{\AA}$, coordination number ± 3.0 and peak width $\pm 1.5\text{\AA}$. The Mg-O distance contributions were not fixed due to the clear shift in peak position of the clearly resolved peak at *c.a.* 2.0\AA when comparing the binary and multicomponent glasses (See Figure 4.8). As shown in equation 18 (chapter 2, section 2.5.4.4), the Mg-O contribution is weighted by the Mg atomic fraction, C_{Mg} , therefore the Mg-O peak for P40 (24 mol% MgO) has roughly half the size of the peak for MgP_2O_6 (50 mol% MgO). The P-O peak was included in the fit due to the small overlap in the Mg-O and P-O peak. The short range order of the multicomponent glasses were modelled between 1.5\AA and 2.65\AA . The fitting procedure involved the use of the Lorch^[142] modification function.

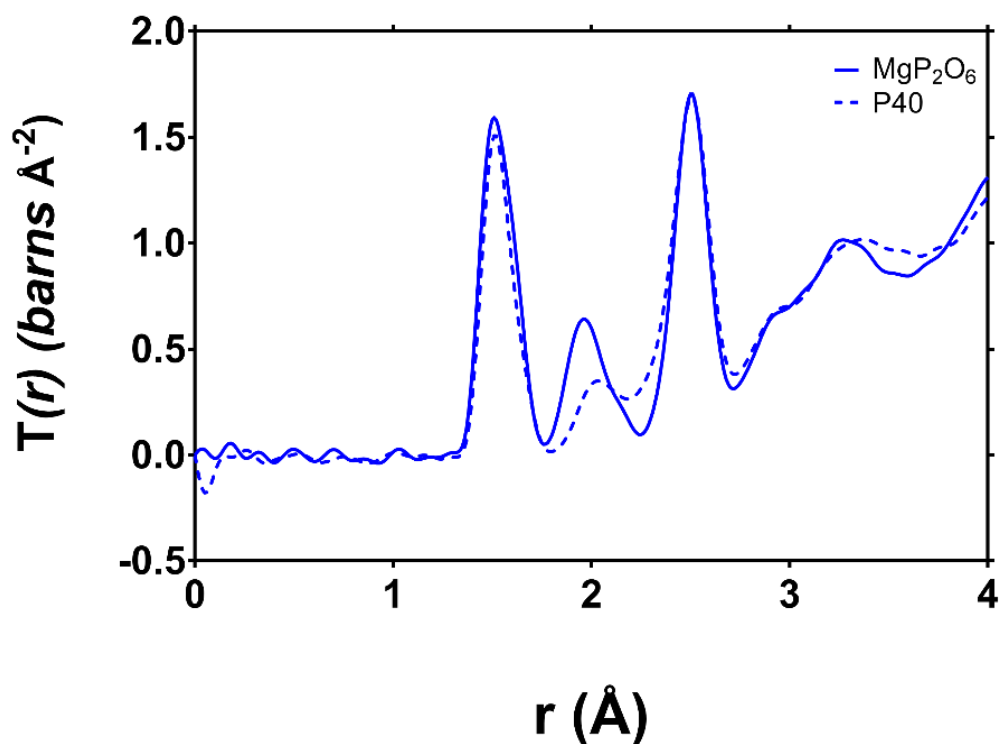


Figure 4.8: Comparison of $T(r)$ between MgP_2O_6 and P40

Table 4.5: Displaying an exemplar (Sr8) sample composition files used to run the programme NXFit^[182]

File Type	Description	Example		
Neutron data file	Experimentally derived neutron total correlation function ($T(r)$)			
Neutron scattering factor file	This contain the sample composition where the atom type is distinguished by its atomic number (Z), scattering length (b_l) and atomic fraction of each atom (c_i)	Z	b_l	c_i
		15	5.13	0.19048
		20	4.7	0.01905
		8	5.803	0.61905
		12	5.375	0.05714
		11	3.63	0.09524

		38	7.02	0.01905		
Initial parameters file	Defines the starting parameters for individual atomic pair correlations including interatomic bond length, coordination number, peak width, followed by the atomic pair defined by the number referred to the position in the scattering factor file	$R_{ll'}$	$N_{ll'}$	$C_{ll'}$	<i>atom l</i>	<i>atom l'</i>
		1.499	2.40	0.0416	1	3
		1.601	1.54	0.058	1	3
		2.299	2.91	0.075	2	3
		2.506	2.10	0.069	2	3
		2.284	2.58	0.100	5	3
		2.564	1.20	0.07	5	3
		1.945	2.6	0.066	4	3
		2.07	2.4	0.11	4	3
		2.506	4.29	0.084	3	3
		2.559	5.10	0.111	6	3
Fits constraints file	Defines the constraint of each parameter by a bounds file	$\Delta R_{ll'}$	$\Delta N_{ll'}$	$\Delta \delta_{ll'}$		
		0	0	0		
		0	0	0		
		0	0	0		
		0	0	0		
		0	0	0		
		0.5	3.0	1.5		
		0.5	3.0	1.5		
		0.5	1.5	0.5		
		0	0	0		

The optimised fit results, shown in Table 4.4, showed consistency with the structural model in which the modifier environment does not change as Ca is substituted for Sr in each glass, and where Na-O, Ca-O and Sr-O particularly remains the same as in the binary metaphosphate compositions. However, some clear changes in the Mg-O environment were observed when comparing the results obtained for the binary and multicomponent glasses. The position of the Mg-O peak shifted to longer distance from 1.945 Å and 2.07 Å to 2.00 Å and 2.09 Å. However, only a small increase in coordination number was found from 5.0 (7) to 5.06. This result correlated with a previous structural study where a shift to higher r was seen with a reduction in P₂O₅ content and

increasing MgO, associated with the compaction of the glass structure.^[91] The anomalous behaviour of Mg-O in terms of varying coordination number and peak position is one which has been of interest to researchers due to its intermediate behaviour and its effect on the modification of the phosphate glass network.^[91, 208] The fits to the modifier-oxygen contributions as shown in Figure 4.9 are satisfactory for all compositions with the exception of Sr16 where the residual is noisier in the region between ~ 2.2 Å and ~ 2.7 Å.

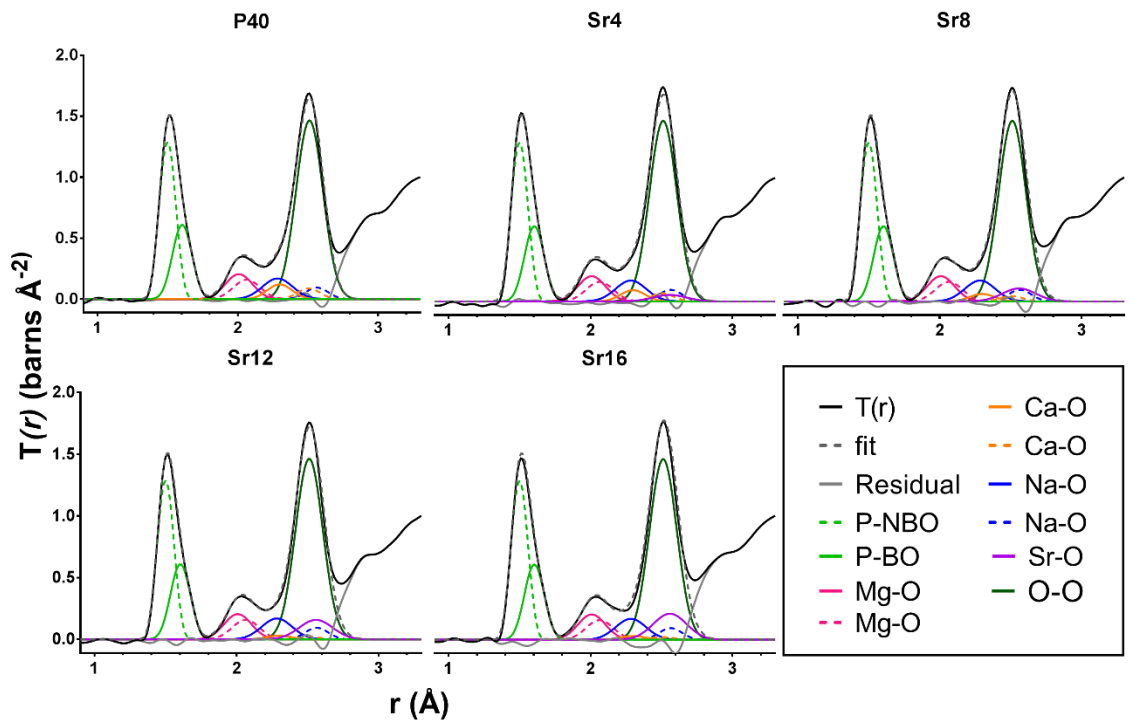


Figure 4.9: M-O pair distribution simulations (after dotted line at 1.8 Å) of multicomponent glasses simultaneously fit on NXFit^[182] where the $T(r)$ was Fourier transformed using the Lorch^[142] function. The P-O bond distribution at low r before the dotted line were fit using the step modification function.

4.5 Summary

In summary, this study has found that fitting the multicomponent glasses simultaneously using NXFit^[182] results in satisfactory fits to all modifier environments at the expense of not obtaining error values for the fit parameters. This is the first time to the author's knowledge that the correlation functions of complex, multicomponent glasses have been deconvoluted by fitting multiple data sets simultaneously. Using the modifier-oxygen

parameters obtained by fitting to the $T(r)$ of the binary compositions provided satisfactory fits to the equivalent environments in the multicomponent glasses. The Ca-O and Sr-O coordination numbers were determined as 5.01(9) and 5.10(6) respectively, however, it is most likely that the Sr-O distribution includes an additional contribution at longer distances, beyond the range that was able to be probed. The neutron correlation functions for the multicomponent glasses are consistent with a structural model in which the coordination of Ca, Sr and Na is the same as in the binary metaphosphate glass. On the other hand, the Mg-O bonds in the multicomponent glasses are shifted to longer distance than for the binary metaphosphate glass. The neutron diffraction data acquired suggested that CaO/SrO substitution in phosphate glasses with fixed 40 mol% P_2O_5 (i.e. close to invert systems) did not significantly change the modifier-oxygen environment, suggesting that, in agreement with FTIR and NMR results, the addition of SrO did not disrupt the glass network.

Chapter 3 showed a decrease in the dissolution rate with the addition of a fifth cation to the glass structure when compared to the four-component glasses. This was attributed to the increased cross-linking and packing density arising from the addition of SrO, or due to the increased structural frustration associated with a larger number of components. These findings corroborated the structural investigation.

CHAPTER 5: TITANIUM INVERT PHOSPHATE GLASSES

5.1 Introduction

This chapter investigated the development of invert phosphate glasses by reducing P_2O_5 content and adding TiO_2 in the glass system $(40-x)P_2O_5 \cdot 16CaO \cdot 20Na_2O \cdot 24MgO \cdot xTiO_2$ (where $x = 0, 3, 5, 7, 10$ and 12), to investigate novel formulations with potential for use in treating bone related diseases such as osteoporosis. All glass samples investigated were as quenched. Generally, invert glasses have a higher tendency to crystallise due to the increased mobility of phosphate groups/ chains in the melt, and thus the addition of TiO_2 was investigated in order to inhibit crystallisation.^[85]

The phosphate structural units in invert compositions consist mainly of pyro- and orthophosphate groups.^[82, 89] In this study, the pyrophosphate groups were primarily of interest since they are structurally related to bisphosphonates, which are currently administered as drugs to suppress bone loss in osteoporotic patients via osteoclast apoptosis.^[25, 209]

Thus the main aim of this study was to fabricate invert PBGs consisting largely of pyrophosphate and orthophosphate groups by reducing the phosphate content as shown in Table 5.1 (with their respective glass codes). This chapter outlines the results and discussion and the materials and methodology used here can be found in chapter 2.

Table 5.1: Compositional information on invert glasses investigated

Glass code	P_2O_5 (mol%)	CaO (mol%)	Na_2O (mol%)	MgO (mol%)	TiO_2 (mol%)
P40Ti0	40	16	20	24	0
P37Ti3	37	16	20	24	3
P35Ti5	35	16	20	24	5
P33Ti7	33	16	20	24	7
P30Ti10	30	16	20	24	10
P28Ti12	28	16	20	24	12

5.2 Powder XRD

The powder XRD patterns displayed in Figure 5.1 showed a single broad peak which spanned from $\sim 20^\circ$ to $\sim 40^\circ$ along with absence of sharp crystalline peaks confirming the amorphous nature of all glass samples investigated.

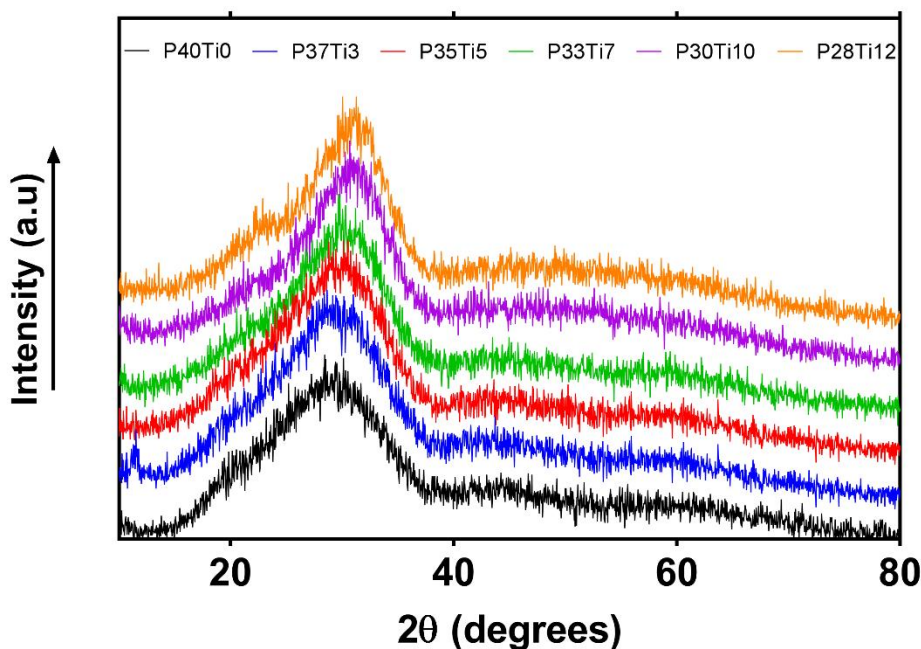


Figure 5.1: Powder XRD patterns of glass samples in the system $(40-x)\text{P}_2\text{O}_5 \cdot 16\text{CaO} \cdot 20\text{Na}_2\text{O} \cdot 24\text{MgO} \cdot x\text{TiO}_2$ (where $x = 0, 3, 5, 7, 10$ and 12).

Phosphate invert glasses are composed of shorter chain units which have greater mobility in the melt, and thus have a higher tendency to crystallise.^[85] It has been shown that the addition of TiO_2 can impede crystallisation by the formation of crosslinks between TiO_4 or TiO_6 structural groups and the phosphate tetrahedra.^[85] The large charge to size ratio of Ti^{4+} ions has been shown to prevent crystallisation and improve glass formation.^[151]

The formation of crosslinks between phosphate units and Ti^{4+} units not only hinders crystallisation but also reduces the solubility of the glasses.^[85] Hitherto, the lowest P_2O_5 content reported without traces of crystallinity has been 30mol%,^[90, 210, 211] This study showed it was possible to melt quench PBG's with a P_2O_5 content as low as 28 mol% and with a high TiO_2 content of 12 mol%.

5.3 EDX

The relative concentration of elements in each glass sample were analysed via EDX and are displayed in Figure 5.2. All glass compositions were within 1-2 mol% of the target composition. Figure 5.3 shows a representative image of the melt quenched glass compositions where increasing the Ti content led to increasingly darker colouration of the glass. Phosphate glasses containing Ti are known to become purple due to the formation of Ti^{3+} ions during melting as a result of the redox of Ti^{4+} .^[94, 212] Decolourisation can be achieved by oxidising the glass via annealing for long periods of time in O_2 atmospheres above the glass T_g ; However, this was not of importance in this study.

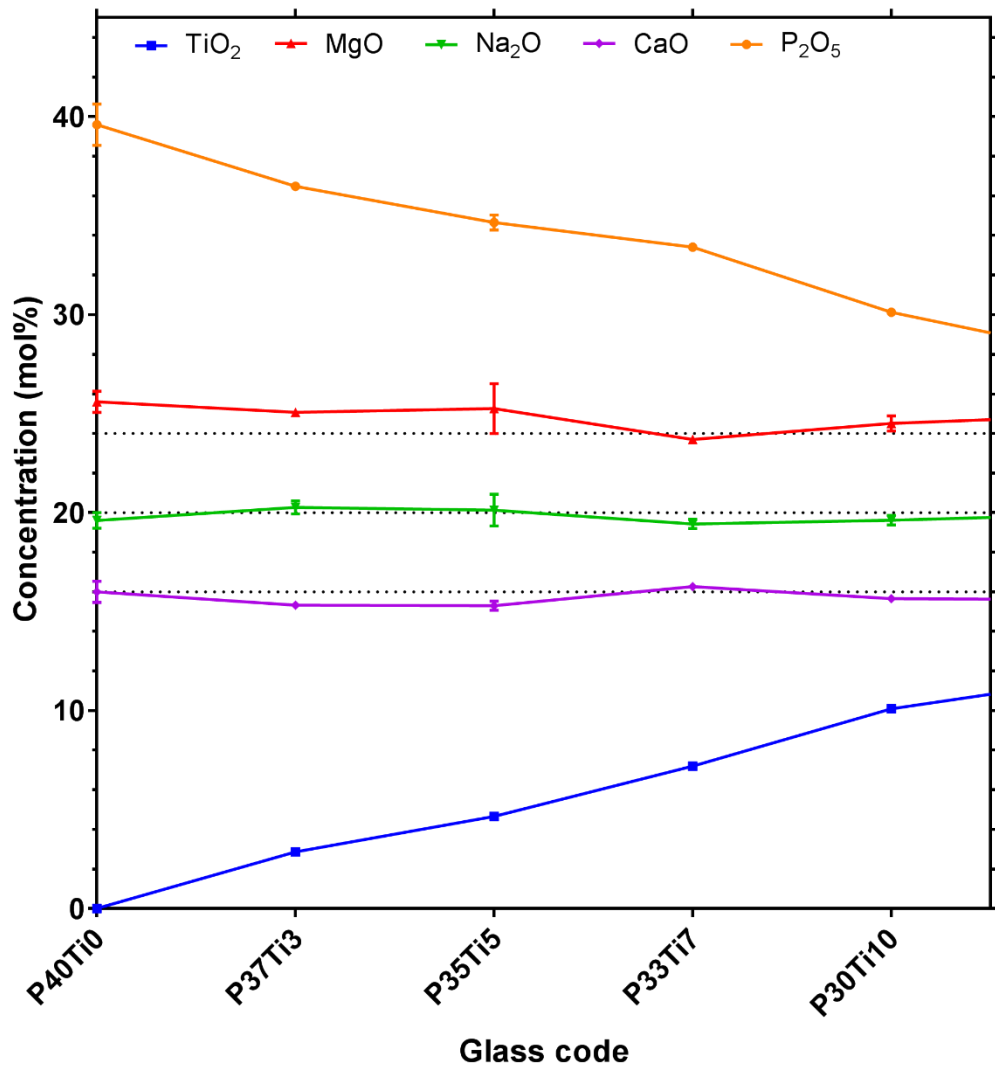


Figure 5.2: composition of glasses investigated as determined by EDX and their target values as represented by the dotted line. Error bars were determined by taking the standard deviation of three separate samples for each composition.



Figure 5.3: Representative image showing the effect of increasing Ti content on glass colour.

5.4 Density

With increasing Ti content, the density of the glass increased from 2.697 g/cm^3 for P37Ti3 to 2.846 g/cm^3 as displayed in Figure 5.4. As the density gradually increased, a change in gradient was observed from around 5 mol%. In conjunction with the increasing density as TiO_2 content increased, the molar volume decreased, suggesting a compaction of the glass network, possibly due to stronger P-O-Ti bonds as a result of the small ionic radius and large charge of Ti^{4+} .^[97] These stronger P-O-Ti bonds increased the O/P ratio from 3.25 to 4 when increasing Ti content from 0 mol% to 12 mol%, which in turn, caused depolymerisation of the phosphate network.^[97, 213] The trends observed here correlate well with the findings of other works where increasing Ti concentration led to an increase in density and more compact structure.^[214, 215]

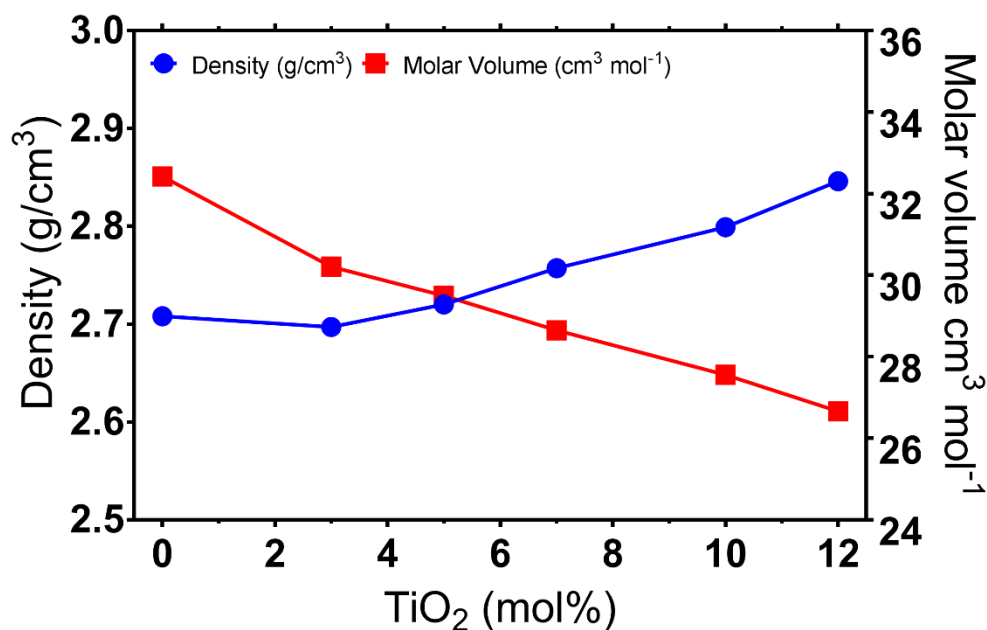


Figure 5.4: Density and molar value of glasses in the system $(40-x)P_2O_5 \cdot 16CaO \cdot 20Na_2O \cdot 24MgO \cdot xTiO_2$ (where $x = 0, 3, 5, 7, 10$ and 12).

5.5 Thermal analysis

The increase in density observed in section 5.4 correlated with the increase in T_g seen in the thermal traces as shown in Figure 5.5 and 5.6. With increasing Ti content, the T_g increased from 435°C to 515°C as shown in Table 5.1. The increase in T_g suggested structural cross-linking between the shorter phosphate chains and the Ti polyhedral. The first T_c peak for the glass compositions studied was seen to shift to higher temperatures with increasing Ti content, as well as becoming broader. Overlapping T_c peaks were observed for P33Ti7, P30Ti10 and P28Ti12 compositions which has previously been seen in a $50P_2O_5 \cdot 40CaO \cdot 7-xNa_2O \cdot xTiO_2$ (where $x = 3, 5, \text{ and } 7$)^[103]. The increase in both T_g and T_c suggested densification of the glass structure with increasing Ti content resulting from the formation of P-O-Ti bonds with high Ti content.^[83, 216] The onset of crystallisation gradually shifted to higher temperatures with increasing Ti content from 0 to 7 mol%, which then progressively decreased with further addition of TiO₂ to 10 and 12 mol%. This suggested the presence of different Ti-O groups changing from network formers (TiO₅) to network modifiers (TiO₆) with increasing TiO₂ content.^[217]

Furthermore, P35Ti5 and P33Ti7 showed additional T_c peaks, as did P30Ti10 however, the T_c point in the successive peaks for this composition were difficult to identify due to the overlapping behaviour. Multiple T_c peaks suggested the presence of several phases and the increasing nucleating ability of TiO_2 which could induce phase separation during cooling of the molten glass, due to its immiscibility at lower temperatures.^[216, 217] furthermore, nucleation and crystallisation is favoured by Ti^{3+} ions compared to Ti^{4+} ions.^[84] Again more than one melting peak was observed for the glass compositions and no distinct pattern was identified.

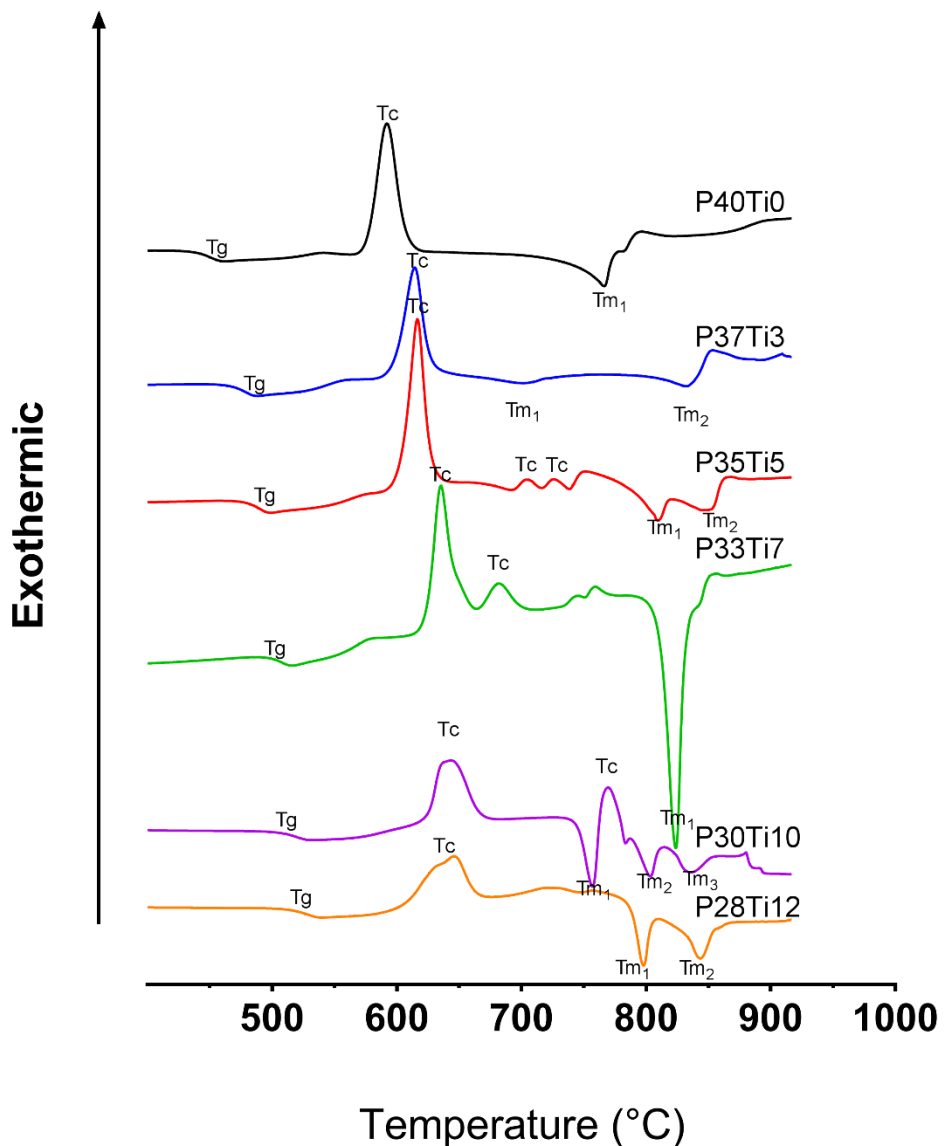


Figure 5.5: Thermal traces showing T_g , T_c and T_m of the Ti invert glass samples.

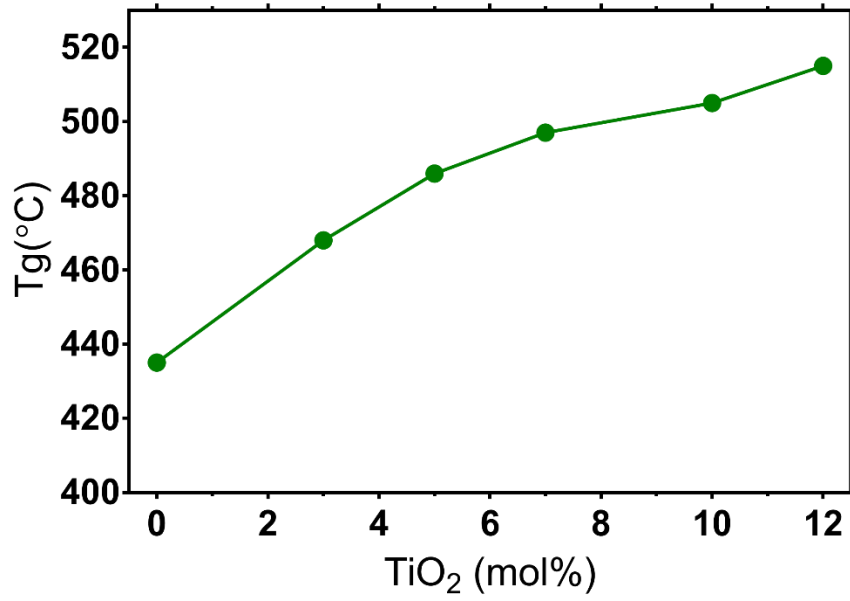


Figure 5.6: T_g with increasing TiO_2 content.

Table 5.2: T_g , T_{onset} , T_c and T_m recorded for the Ti invert glass samples

Glass code	T_g	T_{onset}	T_c	T_{onset2}	T_{c2}	T_{onset3}	T_{c3}	T_m	T_{m2}	T_{m3}
P40Ti0	435	573	591					762		
P37Ti3	468	598	614					702	833	
P35Ti5	486	610	625	703	711	725	733	816	859	
P33Ti7	497	625	638	668	683			821		
P30Ti10	505	622	639					755	800	832
P28Ti12	515	601	645					796	842	

5.6 ^{31}P MAS NMR spectroscopy

Figure 5.7 shows the ^{31}P MAS NMR spectra of the Ti invert glasses investigated. The peak intensities displayed in the spectra were assigned to Q^2 , Q^1 and Q^0 units. The network appeared to depolymerise with increasing addition of Ti as indicated by the decrease in Q^2 units and increase in Q^1 units as shown in Table 5.3, which was consistent with an increase in O/P ratio. The spectra obtained for P30Ti10 and P28Ti12 showed no Q^2 units but instead displayed a positive chemical shift associated with Q^1 and Q^0 units. Furthermore, the ^{31}P MAS NMR data confirmed that all glass compositions were invert as only pyro- and orthophosphate units were detected, however it should be noted that longer chains may be present. Previous work^[83, 218] on invert glasses complement the results seen in this study.

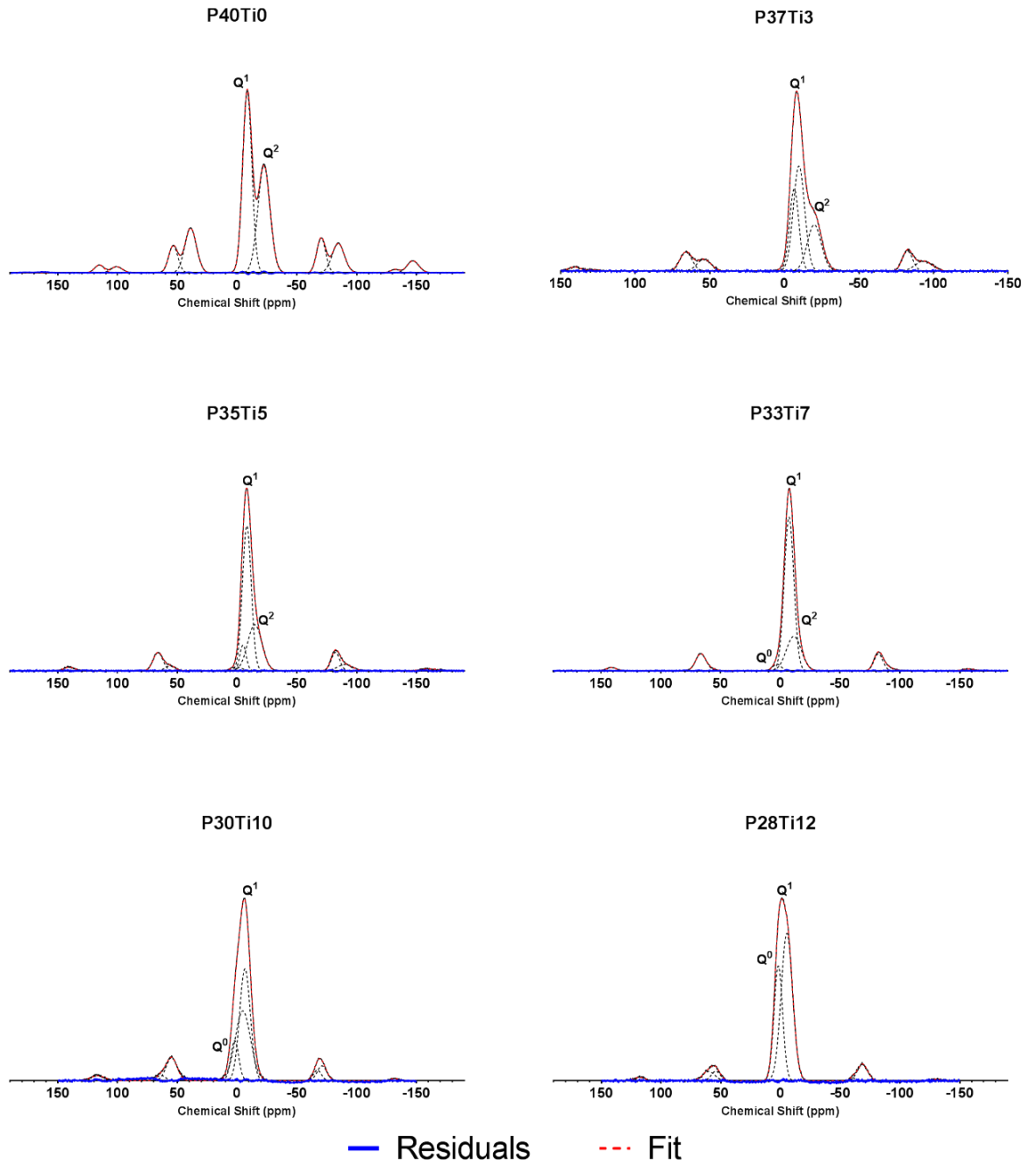


Figure 5.7: ^{31}P MAS NMR spectra of the Ti invert glass series showing deconvolution of the chemical shifts.

Table 5.3: Chemical shifts (ppm referenced using H_3PO_4) and relative concentrations of Q^n units determined by solid-state ^{31}P MAS NMR of each composition investigated and the calculated number of bridging oxygens (BOs) and non-bridging oxygens (NBOs) per PO_4 unit using equation 11.

	Intensity (ppm) Q^0	Intensity (ppm) Q^1	Intensity (ppm) Q^2	% Q^0	% Q^1	% Q^2	BO	NBO
P40Ti0	0	-8.00	-22.00	0	49	51	1.51	2.49
P37Ti3	0	-9.76	-15.03	0	52	48	1.48	2.52
P35Ti5	0	-8.13	-14.76	0	58	42	1.42	2.58
P33Ti7	2.84	-7.24	-11.24	2	74	23	1.2	2.76
P30Ti10	1.95	-6.57	0	17	83	0	0.83	3.17
P28 Ti12	1.81	-5.36	0	37	63	0	0.63	3.37

With increasing Ti content, the number of NBOs exceeded that of the number of BOs. This is explained by the breaking of P-O-P bonds as TiO_2 is added to the phosphate network, resulting in the formation of terminal oxygens and a non-continuous structure i.e. short chains/ groups.

It has been suggested that TiO_2 can behave as either a network former by creating ionic cross linking between NBO's of two different chains,^[97, 213] or as a network modifier.^[86, 152] In order to investigate the behaviour of TiO_2 in this study, the theoretical fraction of Q^n species present was calculated using the O/P ratio for each glass composition. To do this it was assumed that only two Q^n species were present in any glass. Different models were produced when TiO_2 was treated as i) a network modifier, and ii) a network former. The following calculations on the assumption that only two Q^n species were present:

$$Q^{na} = \left(\frac{O/P - Q_{o/p}^{nb}}{0.5} \right) * 100 \quad (13)$$

Where, Q^{na} , is the Q^n species percentage to be calculate, and, $Q_{o/p}^{nb}$, is the O/P ratio of the second Q^n species assumed to be present in the glass structure. The same equation 13 was used for calculating the Q^n species when assuming TiO_2 behaved as a network former. However, the O/P ratio included the Ti contribution. Figure 5.8 shows the theoretical Q^n percentage compared to the experimental value with increasing TiO_2 content.

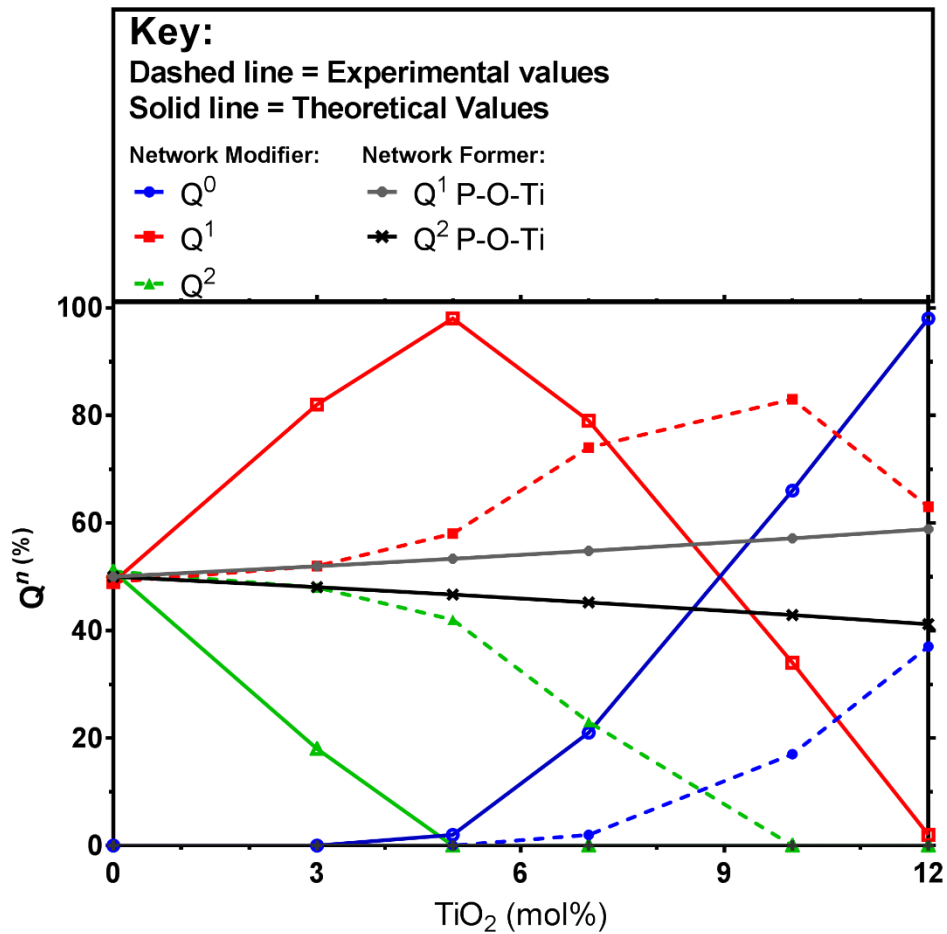


Figure 5.8: Showing the two theoretical (solid line) models, and experimental (dashed line) of Q^0 , Q^1 and Q^2 species as a percentage. The solid grey and black line shows the theoretical Q^1 and Q^2 species if Ti was to behave as a network former.

The experimental data from this study showed that TiO_2 behaved as a network former (P-O-Ti) up to 3 mol%, thereafter the experimental data closely followed the same trend as the theoretical model behaving as a network modifier. Although the theoretical values have a shift by 4mol%. This deviation between 3-5 TiO_2 mol% complements the change in gradients observed with T_g and density values in the 3-5 mol% region, providing evidence that structural

changes can have direct effects on the physico-chemical properties. This study showed that when TiO_2 behaved as a network modifier, the ionic crosslinking between chains resulted in an increase in T_g and more compact structure as shown by the decrease in molar volume as evident in Figures 5.6 and 5.4 respectively.

Figure 5.8 showed that the experimental values for Q^1 units did not quite reach 100% Q^1 since some Q^0 units appeared when TiO_2 was *c.a.* 7 mol%. The observation in this study of Ti-O groups behaving as a network former at low TiO_2 concentration, and switching to network modifiers with increasing TiO_2 content complemented suggestions made previously by Monem *et al.*^[217] Glass forming ions in phospho-silicate glasses have been shown to be present as Ti^{4+} and glass modifying ions were present as Ti^{3+} , where the Ti^{3+} content was strongly dependent on the amount of titanium in the glass.^[219] Brow *et al.*^[218] previously showed the presence of both distorted octahedral (TiO_6) and tetragonal pyramidal (TiO_5) units in binary titanium phosphate and ternary calcium titanium phosphate glasses made by quenching between copper blocks. These units were later related to TiO_5 groups which strengthened the network by acting as glass network formers, and TiO_6 groups which behaved as network modifiers with progressive depolymerisation of phosphate chains with increasing TiO_2 .^[217]

The main objective of developing invert PBGs in this study was to increase the quantity of pyrophosphate groups within the glass system with the aim to release these anions/groups as degradation by-products. The reason for this was due to the close relationship between bisphosphonates (a therapeutic drug used for osteoporotic patients which disrupts osteoclast activity) and pyrophosphates.^[220] The two phosphate groups in the bisphosphonate structure have a high affinity for hydroxyapatite crystals. Furthermore, these two phosphate groups are required for cell-mediated antiresorptive activity. Altering either of the phosphate groups can ultimately effect the biochemical potency of the drug.^[221] The hydroxyl groups in bisphosphonates have the ability to bind to calcium in the bone, and the R^2 structural moiety bound to the

structural carbon (Figure 5.9) is the determinant for the potency for the inhibition of bone resorption.^[222] In addition to this, many earlier studies have shown the ability of pyrophosphates to inhibit the dissolution of hydroxyl apatite crystals^[223] which led to the development of experimental studies to show the inhibition of bone resorption by bisphosphonates.^[221] Therefore, the two Ti invert glass compositions with the highest concentration of Q¹ units; P30Ti10 and P33Ti7 were selected to be investigated further to evaluate their degradation by-products in ultra-pure water.

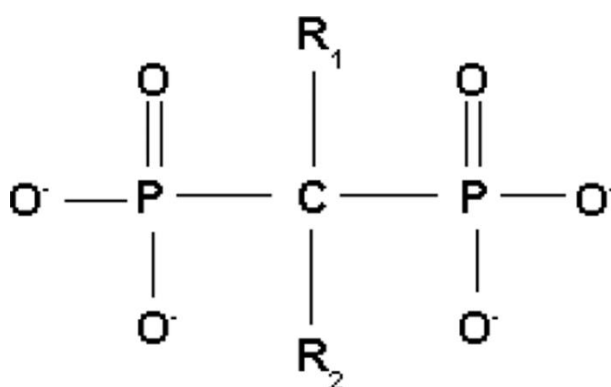


Figure 5.9: Basic structure of bisphosphonates.

5.7 Dissolution studies

Figure 5.10 displays the average mass loss per unit area of the two compositions investigated further (i.e. P30Ti10 and P33Ti7) where glass discs (c.a. 9mm \varnothing by 5mm) were degraded in ultra-pure water. The rates of degradation were also measured. When compared to the P40 glass disc, the rate of degradation of the two Ti invert glasses were considerably lower where the trend was P40 > P33Ti7 > P30Ti10. These relatively slower degradation rates were reflected in the very low ion release profiles shown in Figure 5.11 and 5.12. Such observations where increasing Ti content in PBG reduced the rate of degradation has been seen previously.^[85, 86, 96, 103, 224, 225] This was attributed to the increase in cross linking stability by TiO₂ and the compaction of the glass structure due to the smaller ionic radius and greater charge of Ti ions compared to the other modifier ions such as Ca²⁺, Mg²⁺ and Na⁺.^[81, 226]

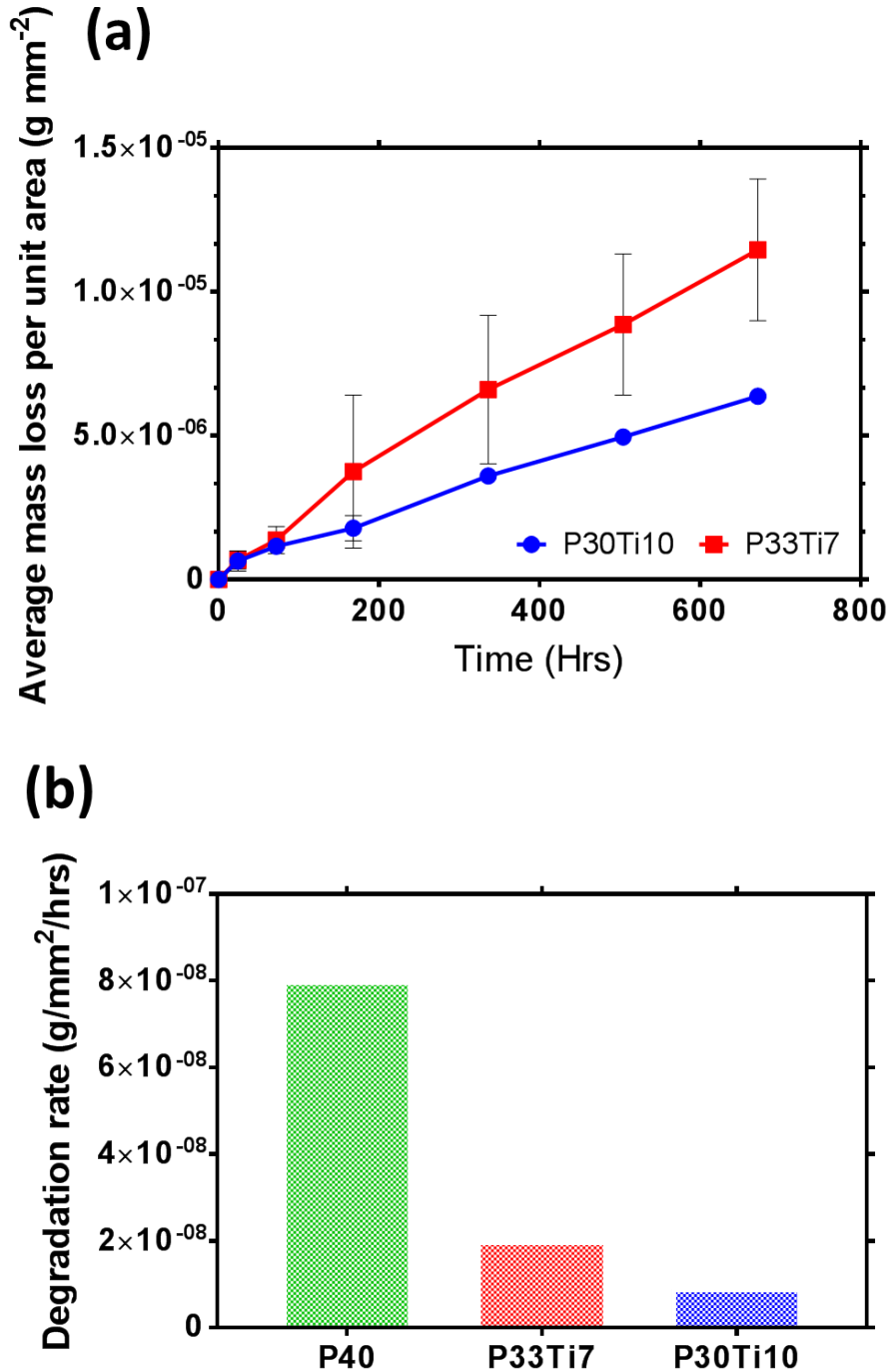


Figure 5.10: (a) Average mass loss of P30Ti10 and P33Ti7 glass discs when degraded in ultra-pure water over a 28 day period. (b) Shows the degradation rate of the Ti invert glasses compared to P40.

The increase in durability with addition of Ti, when compared to P40 was previously explained by the formation of Ti-O-P crosslinks which hindered chain hydration.^[218] Vogel *et al.*^[227] also found invert PBGs to be more resistant to hydrolysis than polyphosphate glasses. The elevated durability and resistance to hydrolysis seen in this study for P30Ti10 and P37Ti12 was due to the glasses being both invert and containing high TiO₂ content, since the glassy state of invert glasses was caused by the interaction of cations and phosphate groups rather than chain entanglement or stiff networks.

5.8 Ion release

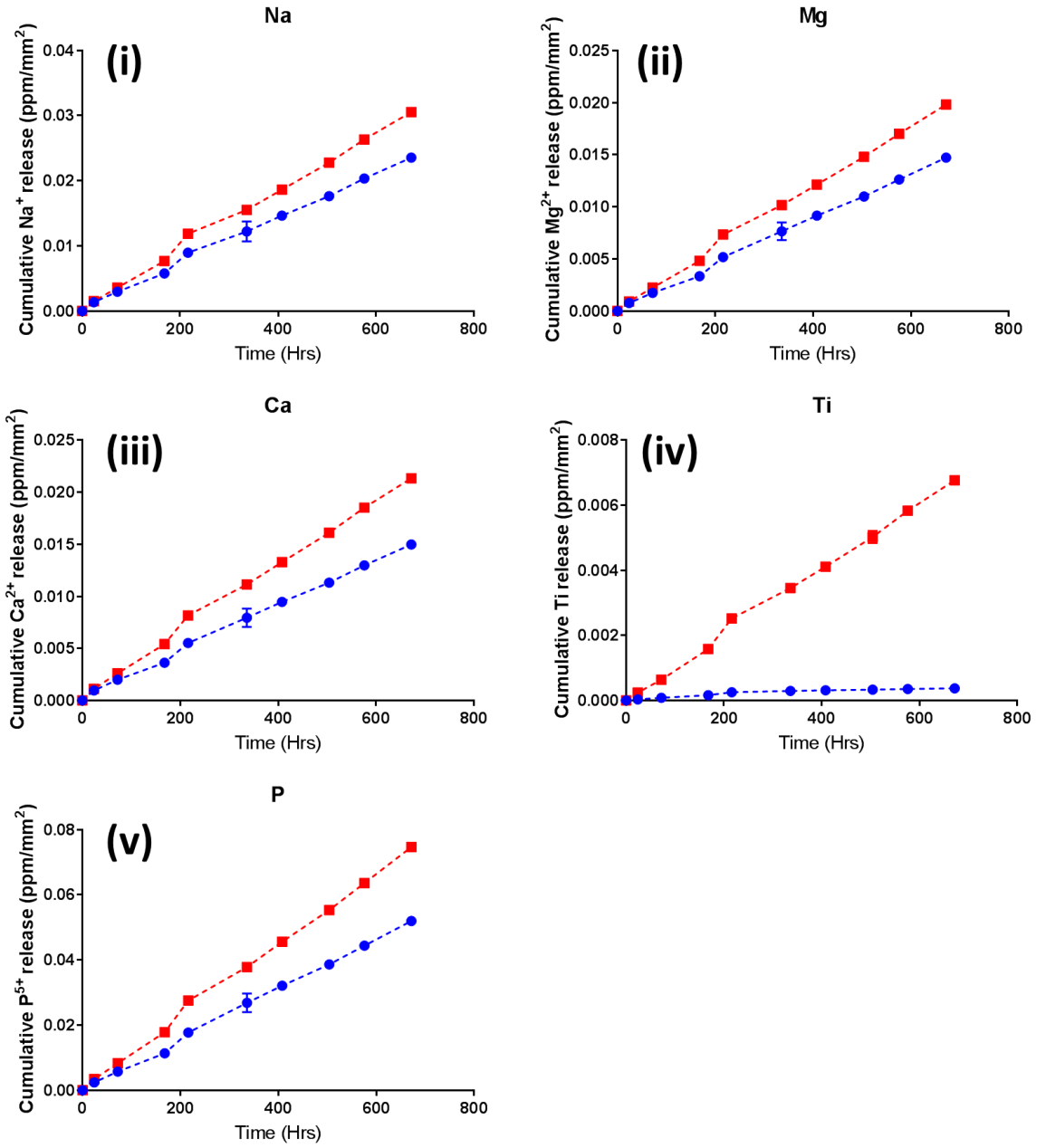
5.8.1 Cation release

The cation release studies were conducted by Saul Vazquez Reina at The University of Nottingham. It should be noted that the ICP method used analysed the total Ti concentration which included all possible chemical species of Ti released by the glass samples. The ion release profiles displayed in Figure 5.11 reflected the minimal degradation profiles observed in Figure 5.10. The cumulative ion release of Ca²⁺, Na⁺, Mg²⁺, P⁵⁺ and the Ti ions displayed a linear increase with time up to 168 hours, where a sudden increase in the release of ions was observed which again followed a linear trend. Interestingly this was not observed for the Ti ions released from the composition P30Ti10, and although this sample contained a greater amount of TiO₂ compared to the sample P33Ti7, the cumulative release of Ti ions was significantly less (<0.05) where P33Ti7 release 0.0068 ppm of Ti ions compared to 0.0004 ppm by P30Ti10 at 672 hours. This inverse compositional dependence of Ti ions has also been seen previously in a 50P₂O₅·30CaO·(20-x)Na₂O·xTiO₂ (where x = 0, 5, 10 and 15) glass system,^[215] and 50P₂O₅·40CaO·(10-x)Na₂O·xTiO₂ (where x = 0, 1, 3 and 5).^[216]

The release rate of cations from P33Ti7 was greater than that of P30Ti10, where the largest quantity of cations released was shown by Na^+ followed by P^{5+} > Ca^{2+} > Mg^{2+} > Ti ions. Such miniscule quantities of ions released from these glass compositions and the slow rates of degradation suggests that the release of phosphate ions (pyro or ortho etc) would also be low and slow. However, such glass compositions could find more promising use in applications such as in photonics or glass to metal seals since such low quantities of ions released would have little therapeutic effect for orthopaedic applications. Further work could involve investigating less durable compositions with high ortho- and pyrophosphate units.

Although previous studies on the dissolution of phosphate invert glasses containing TiO_2 have shown relatively low ion release,^[228] this study appeared to show the lowest ion release quantities. This could possibly be explained by the fairly high concentration of MgO content in these studies. According to Dietzel's rule,^[152] MgO is known to behave as an intermediate oxide where it may act as a network modifier or as a network former. Its fate is dependent on the field strength (Z/a^2 where Z is the ion charge and a^2 is the M-O bond distance) of the ion, where a value usually ranging between 0.1 to 0.4 is classified as a network modifier, and a higher field strength in the range of 1.5 and 2 is classified as a network former. If MgO was to enter the network and behave as a glass network former, this would both impede crystallisation and enhance durability of the glasses, however, even if they were to behave as modifiers, MgO would still improve the glass forming ability by preventing crystallisation due to its larger charge to size ratio in comparison to other modifiers in this glass system (Na^+ and Ca^{2+}) as well as improve the durability of the glass by effectively forming cross links between phosphate groups as seen previously.^[82, 151, 229]

(a)



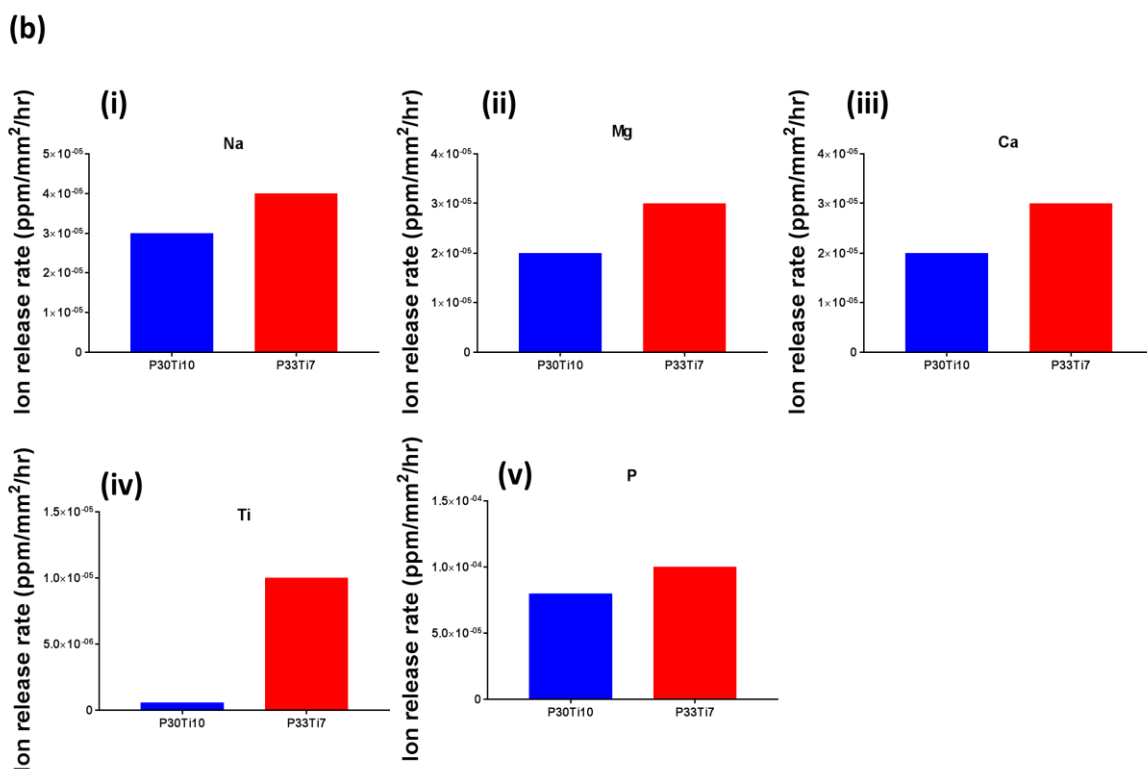


Figure 5.11: (a) Cumulative cation release and (b) release rates from P30Ti10 and P33Ti7.

6.8.2 Anion release

The cumulative anion release of different phosphate species were carried out by Song Yi Beck at University College London. The anions released shown in Figure 5.12 for samples P30Ti10 and P33Ti7 are represented as orthophosphate (PO_4^{3-}), pyrophosphate ($\text{P}_2\text{O}_7^{4-}$), and linear polyphosphate ($\text{P}_3\text{O}_{10}^{5-}$), although only ortho-, pyro- and metaphosphates were observed from the ^{31}P NMR data, suggesting initial ion release of polyphosphate may break down into shorter chains. Interestingly anion release was detected only after 168 hours. The greatest phosphate units released was found to be linear polyphosphate ($\text{P}_3\text{O}_{10}^{5-}$), where sample P30Ti10 appeared to release approximately 0.01ppm more $\text{P}_3\text{O}_{10}^{5-}$ than P33Ti7 from c.a. 400 hours, increasing linearly over time. Orthophosphate units showed a rapid linear increase in release between 168 and 408 hours, followed by a plateau at 0.046 ppm for P33Ti7 and 0.051 ppm for P30Ti10 at 408 hours.

A similar observation was made with the pyrophosphate units, where a linear increase was observed between 168 and 408 hours for the P33Ti7 sample, followed by a plateau at a maximum release of 0.012 ppm. Such plateau-like profiles for anionic release have been observed previously and correlated well with this study.^[215] The P33Ti7 sample appeared to release a considerably greater quantity (0.011 ppm) of pyrophosphate units compared to P30Ti10, however, of the three phosphate units detected, pyrophosphate quantities was the lowest measured. As seen with the cation release measurements shown in section 5.8.1, such small quantities of anions released would have little therapeutic effect but the stability of the glasses would have better use in alternate applications such as in photonics or glass to metal seals.

The highest anion species release measured was the orthophosphate groups however, it should be noted that all samples were analysed after the final time point of 672 hours, and although all precaution was taken to hinder further phosphate degradation during storage by refrigerating samples, there is a possibility of longer phosphate chains to break down into the smaller constituents in the degraded media during storage. F. Döhler *et al.*^[53] found that larger chain structures were easier to dissolve as this occurs via chain hydration which has a significantly lower activation energy compared to that of P-O-P hydrolysis, which is the prominent method of dissolution occurring for smaller units such as ultraphosphate glasses. The presence of linear polyphosphates also suggests the possibility of the smaller ortho- and pyrophosphate units to form into longer units when stored in the degradation media. In conclusion, again the low anion release correlated with the low degradation rates observed in section 5.7. This study has shown the successful release of pyrophosphate units by the sample P33Ti7.

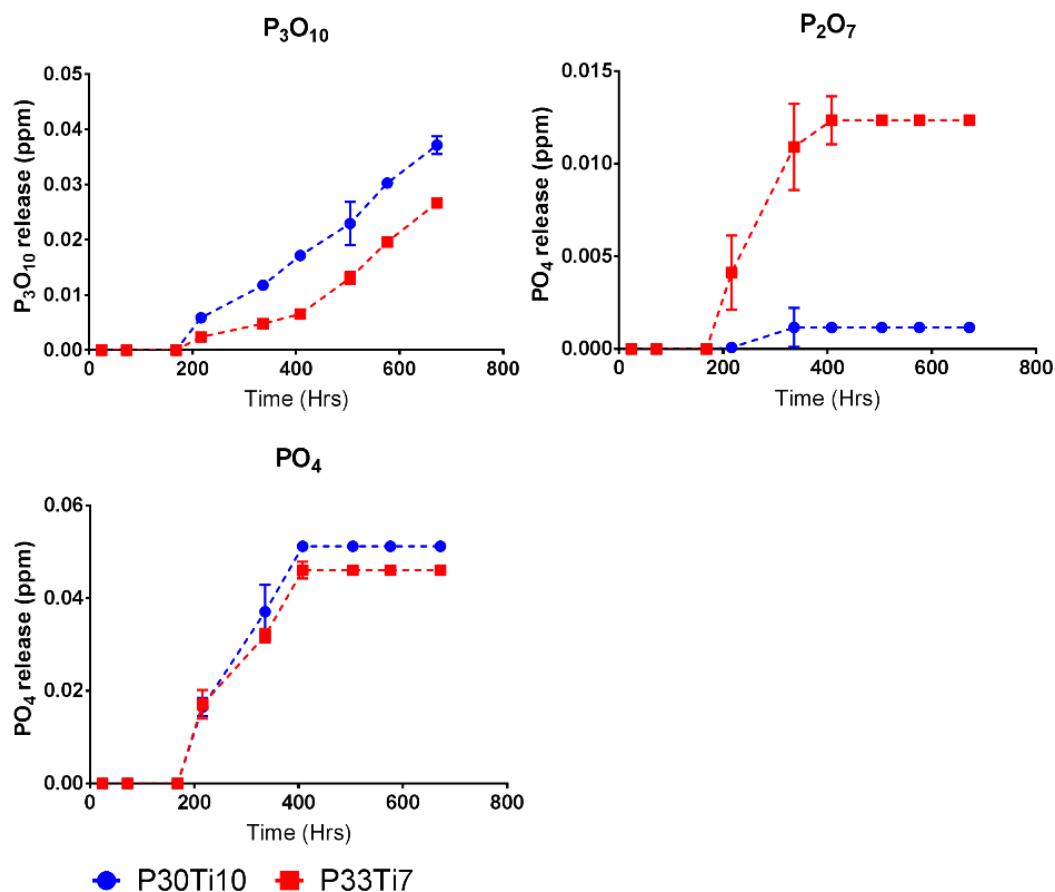


Figure 5.12: Cumulative anion release from P30Ti10 and P33Ti7 glass samples.

5.9 Summary

This study showed the successful fabrication of fully amorphous PBGs with a phosphate content as low as 28 mol%, and titanium content of 12 mol%. ³¹P MAS NMR studies confirmed all glass compositions to be invert, i.e. composed of short pyro- and orthophosphate units as opposed to long entangled chains. Furthermore, ³¹P MAS NMR suggested Ti ions to behave as a network former at lower concentrations of 3 mol%, and switch to behaving as network modifiers with addition of 5 mol% and above of TiO₂. Increasing addition of titanium oxide resulted in an increase in T_g , attributed to greater cross linking of phosphate units by Ti ions due to the larger size to charge ratio of the ion compared to the other network modifiers. Such behaviours were reflected in the dissolution studies of these glasses where addition of TiO₂ drastically reduced solubility of the PBG compared to TiO₂ free glasses (P40).

Additionally, cation and anion release were found to complement the slow degradation rates observed and were found to release nano-levels of ions. Furthermore, the sample P33Ti7 successfully released pyrophosphate units as a degradation by product.

CHAPTER 6: MANUFACTURE OF NOVEL PBG MICROSPHERES

6.1 Introduction

This chapter provides an outline of the manufacture of PBG microspheres and introduces for the first time, a novel technique to fabricate porous PBG microspheres, via flame spheroidisation. The composition of $40\text{P}_2\text{O}_5 \cdot 16\text{CaO} \cdot 20\text{Na}_2\text{O} \cdot 24\text{MgO}$ (denoted P40) was used for all trials and characterisation. The materials and methodology have been outlined in Chapter 2, section 2.6 however, this chapter explains developmental conditions in more detail.

PBG's were manufactured into microspheres with the aim of producing a more clinically applicable material morphology which could be delivered to the site of interest with ease as well as provide added advantages other than the release of biotherapeutic ions alone. For example, a synergistic effect could be taken advantage of, by successfully manufacturing porous microspheres, within which stem cells could be loaded, thus providing added value from the release of therapeutic ions to both aid in the repair and regeneration of bone tissue and potentially influence the stem cells down specific lineages to assist in the regeneration of new tissue.^[230]

6.2 Glass powder production

All microspheres were manufactured using the quenched P40 glasses which were ground into powder form with irregular morphologies (see Figure 6.1). An optimal grinding procedure was attained at 500rpm for 2 minutes as this resulted in the vast majority of a starting batch of *c.a.* 100g of the glass microparticles to fall within the target range of 63-200 μm as shown in Table 6.1. Glass particles were then separated using stainless steel sieves in the size ranges outlined in Table 6.1 and shaken for 15 minutes on an Octagon digital sieve shaker.

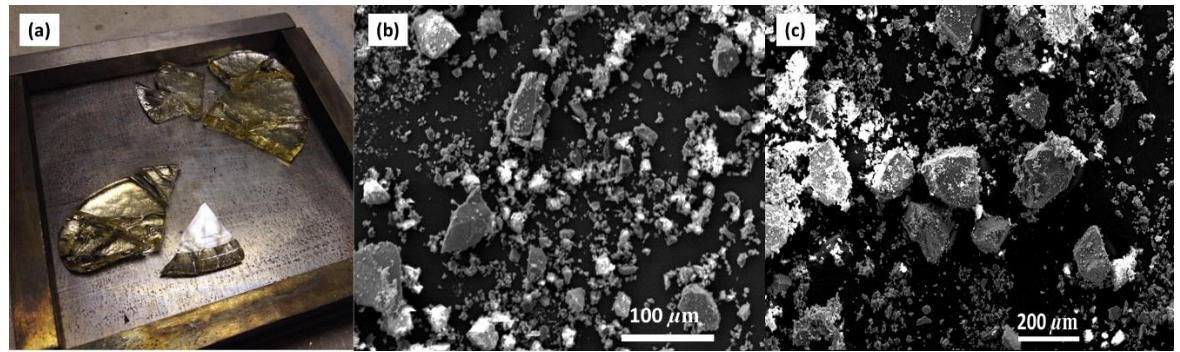


Figure 6.1: (a) Image of the as quenched P40 glass, (b) & (c) SEM images of irregular particle morphology after grinding.

Table 6.1: Shows the range and percentage of sizes obtained after grinding a batch (c.a.100g) of P40 at 500rpm for 2 minutes

Particle size (μm)	Average quantity collected (%)
>500	1.0 ± 0.3
500-300	1.7 ± 0.3
300-250	2.3 ± 0.5
250-200	9.1 ± 6.7
200-100	35.5 ± 5.8
100-63	30.0 ± 5.5
63-45	19.2 ± 0.5
<45	2.2 ± 0.1

6.3 Bulk microsphere manufacture

Microsphere size range can impact on delivery rate of therapeutic ions, since smaller particles have larger surface area to volume ratios thus increasing ion release rates.^[106] Initial feasibility studies were conducted using microparticles in the size range 100-200 μm since this fell within the ideal size for delivery down a standard 11 (inner \varnothing 2.38 mm) or 13 (inner \varnothing 1.80 mm) gauge needle commonly used in vertebroplasty.^[231]

Irregular shaped microparticles were passed through a flame spheroidisation apparatus as displayed in Figure 6.2. The apparatus comprised of a blow torch (BOC Cutting torch, UK and Metallisation Ltd., UK) utilising oxy-propane fuel, gas flowmeters (Platon, Roxspur, UK), a vibratory funnel feeder and a collection vessel. A DC motor was also attached to the feeder, to assist the stable flow of the microparticles during feeding. Hossain *et al.*^[232] investigated the effect of powder feed-rate and energy exchange between soda-lime-silica glass particles and plasma, where the rate was found to strongly influence the transfer of energy linearly to particles, which in turn was suggested to affect particle residence time in the plasma trajectory. This study found that the voltage applied to the motor had to be varied depending on batch size.

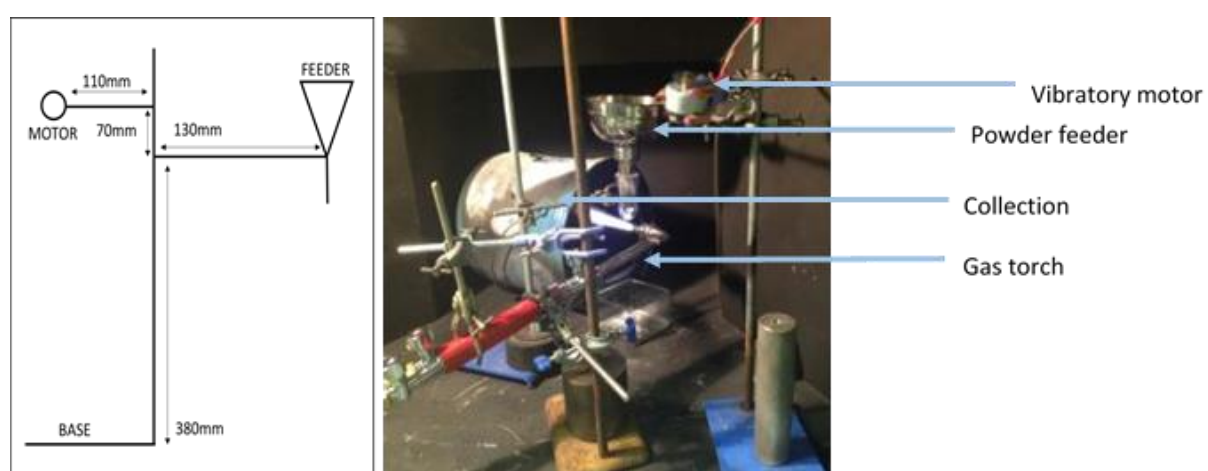


Figure 6.2: Schematic and photograph of oxy-propane flame spheroidisation apparatus.

The resultant spherical morphology of the particles can be seen in Figure 6.3 and the formation can be explained by the high temperatures of the oxy-propane flame which reduced the viscosity as the glass melted and created surface tension in the trajectory of the flame, which forced the irregular particles to develop a spherical morphology.

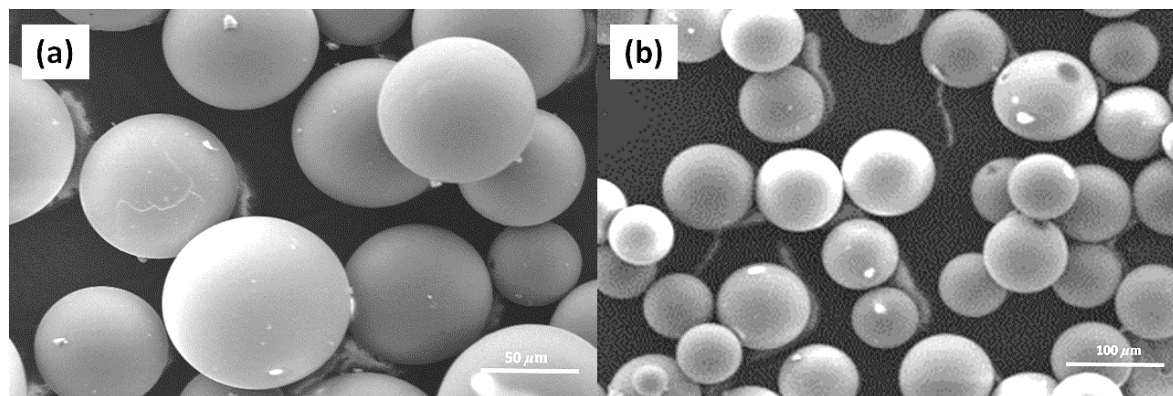


Figure 6.3: (a) & (b) SEM image of non-porous microspheres produced using the oxy-propane set up.

6.3.1 Gas flow rate

The rate of gas flow displayed obvious differences in flame length, where higher flow rates of 3 L/min of propane to 7 L/min of oxygen resulted in a longer flame length (300 mm) compared to 1.5 L/min propane to 3 L/min of oxygen, which resulted in a shorter (210 mm) flame length as shown in Figure 6.4. The effect of flame length can be seen on particle size distribution and spheroidisation efficiency as the higher flow rates resulted in a better spheroidisation efficiency compared to the lower flow rate where more irregular particles could be seen in Figure 6.4 (c). The higher flow rate also showed a broader size distribution between 80 and 200 μm as seen in Figure 6.4 (e) compared to the narrower distribution in Figure 6.4 (b).

This could have possibly been due to a greater particle residence time within the flame, increasing the chances of particles colliding and fusing together, forming larger spheres. A gas flow rate of 3 L/min of propane to 7 L/min of oxygen was used going forward. When experimenting with gas flow rates it was important to maintain a gas ratio closer to a neutral flame, since an oxidising flame would shorten the flame length and a carbonising flame could run the risk of introducing impurities such as carbon into the final product. Furthermore, the gas flow rate would also alter the flame temperatures, for example, an oxidizing flame is hotter than a neutral flame.

Flame length is an important parameter as this can determine the degree of spheroidisation, since the longer the microparticles are within the flame trajectory, the greater the chance of spheroidisation. However, in order to achieve longer flame lengths, higher gas ratios were required, which in turn could increase flame velocity, also effecting particle residence time. Other factors such as the starting size of the microparticles also played an important role since, larger particle sizes were likely to have a greater mass, thus may either fall directly through the flame or were unlikely to reach a temperature higher than the glass T_g whilst in the flames trajectory, due to their greater volumes and so may not have completely spheroidised as shown in Figure 6.5. The spheroidisation efficiency of microspheres manufactured from microparticle starting size ranges of 200-300 and 100-200 μm was calculated as follows:

$$\eta_s = \frac{B}{A} \times 100 \quad (20)$$

Where A is equal to the total number of particles counted in the SEM image, and B is the number of spherical particles. All irregular particles such as those circled in Figure 6.5 were excluded in parameter B. The spheroidisation efficiency of microspheres manufactured from a starting microparticle size range of 200-300 μm was 77% and 98% for microspheres manufactured from a starting size of 100-200 μm .

Small microparticle sizes also run the risk in lack of spheroidisation due to the fact that their mass may be much lower, which in turn can be carried away from the flames trajectory by the gas velocity, causing the particles to get caught in the spray either side of the flames trajectory. Such behaviour has been explained by Bortot *et al.*^[120] where a model was used to calculate the spheroidisation efficiency of various particle sizes. This study suggested that it was not the particle residence time in the flame alone that influenced spheroidisation but a combination of temperature-time that the particles were subjected to that influenced spheroidisation, since the viscosity of the material needed to be low enough and/or the temperature needed to be sufficiently high in order for the effects of surface tension to form a sphere. However, it is also well recognised that smaller particles would require lower temperature profiles for melting.

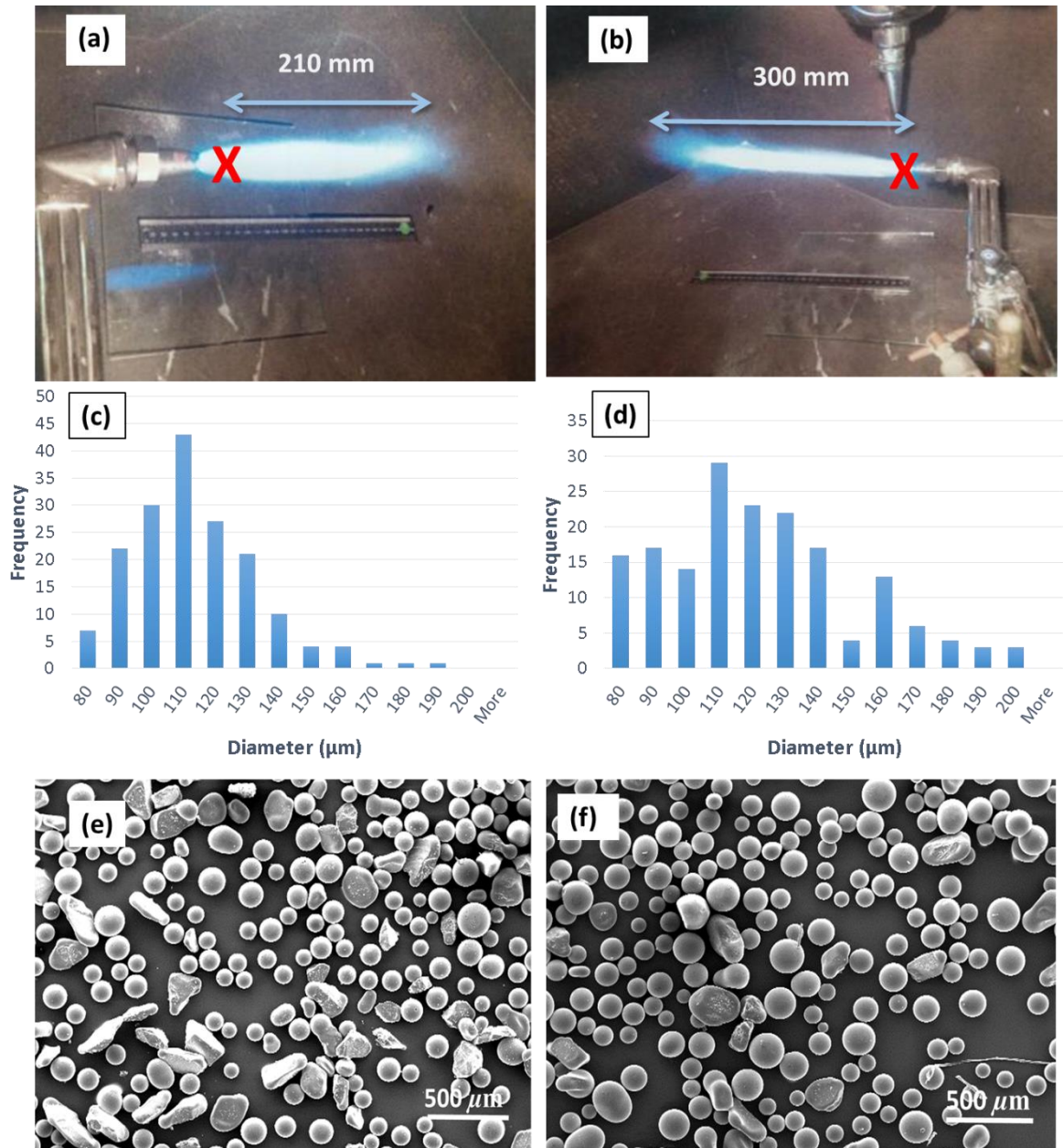


Figure 6.4: (a) flame length (c) particle size distribution & (e) SEM image of spheroidised microspheres at a gas flow rate of 1.5 L/min propane to 3 L/min oxygen, and, (b) flame length, (d) particle size distribution & (f) SEM image of spheroidised microspheres at a gas flow rate of 3 L/min propane to 7 L/min oxygen. Red X indicates the point at which powder is fed into the flame length.

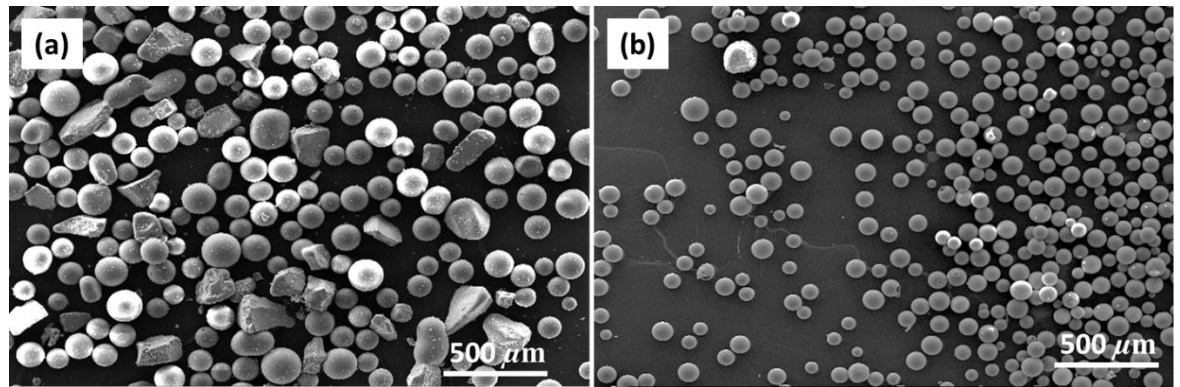


Figure 6.5: SEM images comparing spheroidisation efficiency of (a) microspheres manufactured using microparticle sizes between 200-300 μm , and (b) between 100-200 μm .

6.3.2 Collection distance determination

In order to determine the optimum distance of collection vessel, particles were collected along the entire flight path of the apparatus after spheroidisation, and sphericity and yield were determined qualitatively by observation under a light microscope. Figure 6.6 illustrates the spheroidisation efficiency at various distances between 0-500 mm from the orifice of the torch nozzle. It was observed that collections furthest away from the orifice resulted in a higher yield of spherical morphologies. This was attributed to i) the mass of the particles, as larger heavier particles were unlikely to travel the entire flame trajectory and, ii) the flame residence time; where particles with lower mass were able to maintain enough velocity to be sustained in the entire flame trajectory and reach a high enough temperature in order form microspheres.

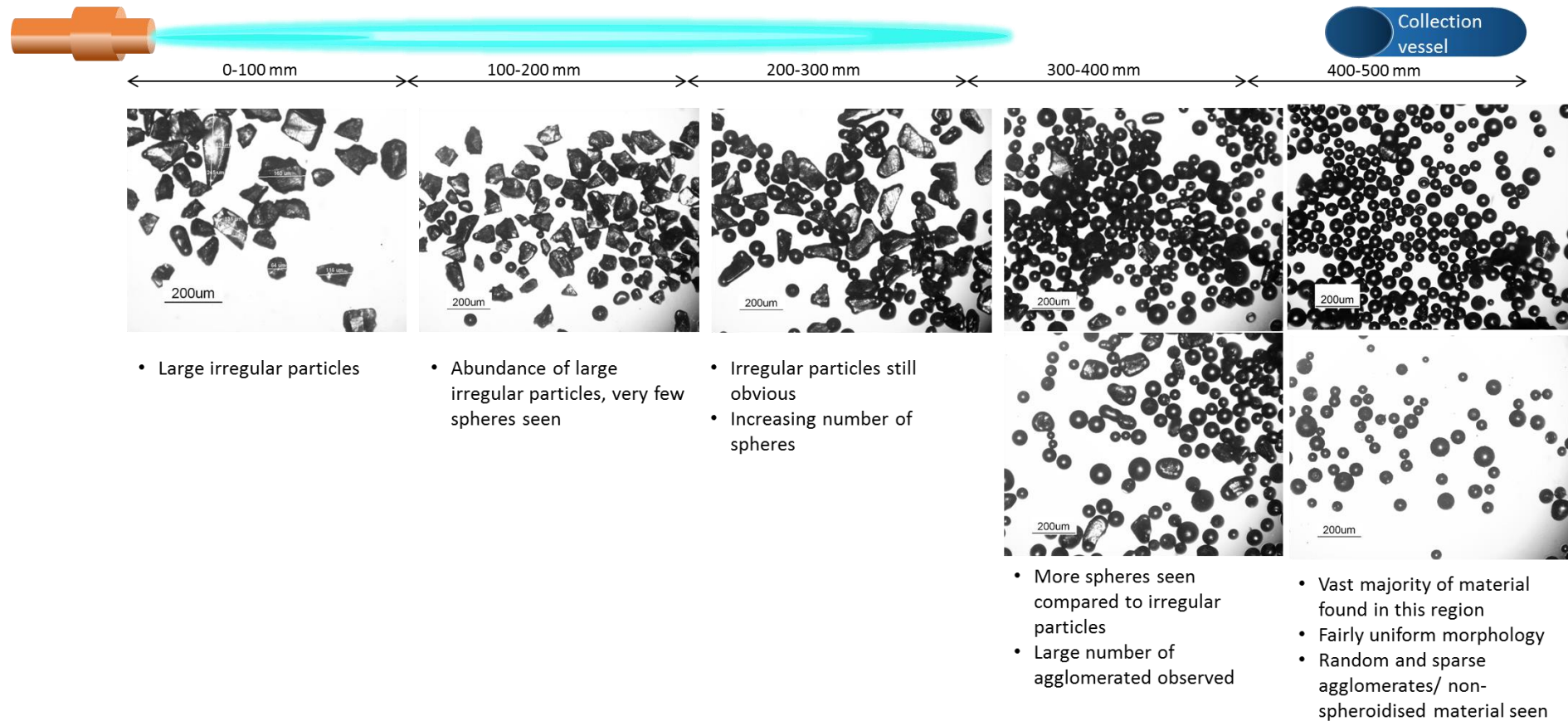


Figure 6.6: Light microscopy images illustrating the spheroidisation efficiency of particles collected at various distances along the flight path of the apparatus from the orifice of the torch.

6.4 Novel porous microsphere manufacture

This section explains the never done before development of highly porous, interconnected PBG microspheres which was outline as one of the aims to enable loading of biological factors such as stem cells for example.

Pore or bubble formation in glasses is dependent on the solubility and diffusion of gasses in the glass melt, and are usually deemed as undesirable melt defects.^[131] The most common gasses present in glass melts are water vapour, oxygen and carbon dioxide.^[233] This study aimed to deliberately encourage the formation of pores by introducing CO₂, due to its high solubility in glass melts as shown in Figure 1.10 (chapter 1). The porosity introduced into the microspheres developed was obtained via a novel single stage manufacturing process. The irregular shaped microparticles were mixed with a porogen namely calcium carbonate (CaCO₃) at the pre spheroidisation stage. CaCO₃ will be referred to as porogen from this point forward.

6.4.1 Altering porogen size

Parameters such as porogen size and quantity were first investigated. Figure 6.7 shows the qualitative effect of varying porogen size with regards to pore size produced and distribution of pores when mixing the porogen on a 1:1 ratio of glass microparticles to porogen.

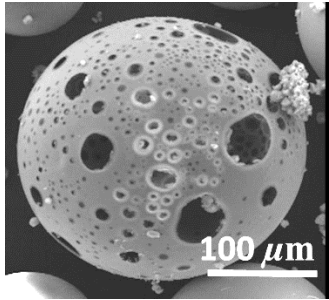
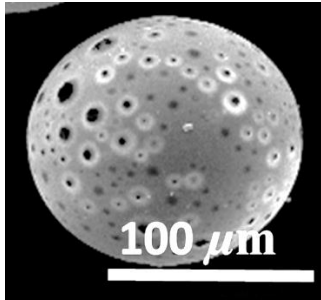
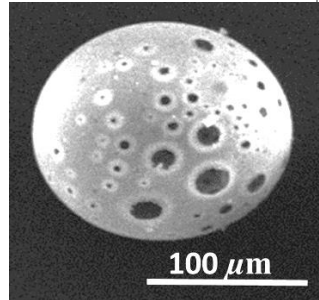
<i>Porogen sizes</i>	<i>45-63 μm</i>	<i>100-200 μm</i>	<i>200-300 μm</i>
<i>SEM image of outcome</i>			

Figure 6.7: SEM images showing effect of porogen size on porosity

SEM images of the porous microspheres manufactured using varying porogen sizes showed no obvious differences in the number of pores on the surface when observed qualitatively. However, a porogen size range of 45-63 μm appeared to show greater distribution in pore sizes when viewing SEM images by eye, thus the manufacturing methods following this all used a porogen size range of 45-63 μm .

6.4.2 Altering porogen quantity

The quantity of porogen mixed with glass microparticles pre-spheroidisation was also investigated as shown in Figure 6.8.

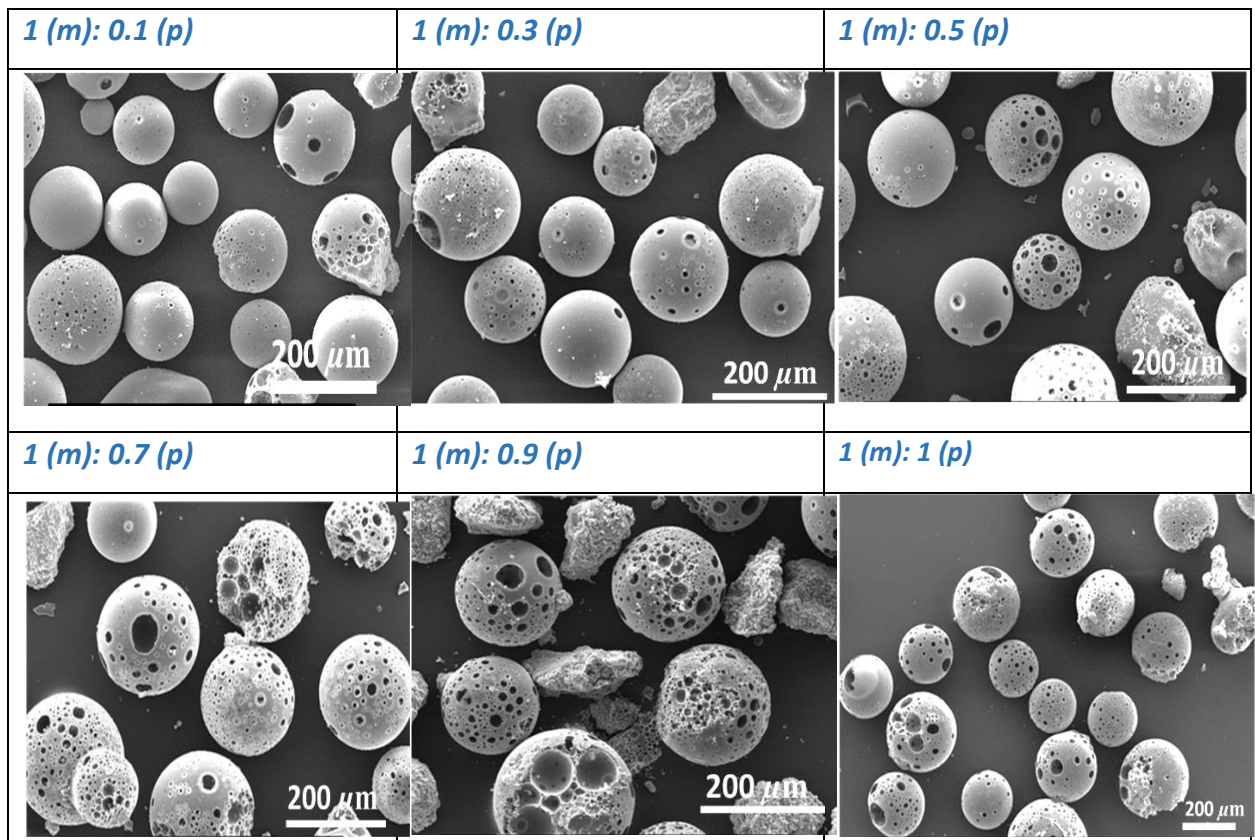


Figure 6.8: SEM image showing effect of porogen quantity on yield of porous microspheres where (m) is microparticle and (p) is porogen ratio

Figure 6.8 showed that increasing porogen quantity resulted in a gradual increase in the yield of porous spheres compared to the number of non-porous spheres as seen in the SEM images in Figure 6.8. This increase appeared to be obvious until a porogen ratio of 0.7, where the number of porous to non-porous

microspheres appeared to level off when examined qualitatively. Subsequent investigations aimed to optimise the level of porosity for each microsphere by investigating alternate ways of introducing the porogen other than by introducing the microparticles and the porogen together at the same time pre-spheroidisation.

6.4.3 Two-step manufacture

A two-stage method for yielding porous spheres was investigated when aiming to optimise porosity of microspheres. First, non-porous microspheres were manufactured in the size range of 100-200 μm using the standard flame spheroidisation technique. These non-porous microspheres were then combined with porogen in the size range of 45-63 μm at a glass microparticle to porogen mass ratio of 1: 0.2. Figure 6.9 shows that this method resulted in a shell type formation, and porosity appeared to be more uniform resulting in a honeycomb-like structure. It may be postulated that the velocity at which the spherical particles travelled through the flame trajectory may have been faster than the irregular shaped particles, enabling less time for the gasses to dissolve and enter the glass melt, which then cooled creating a shell-like structure. Such restriction to the pores from the outer surface was not deemed ideal for use as stem cell carriers and thus this two stage process was not carried forward.

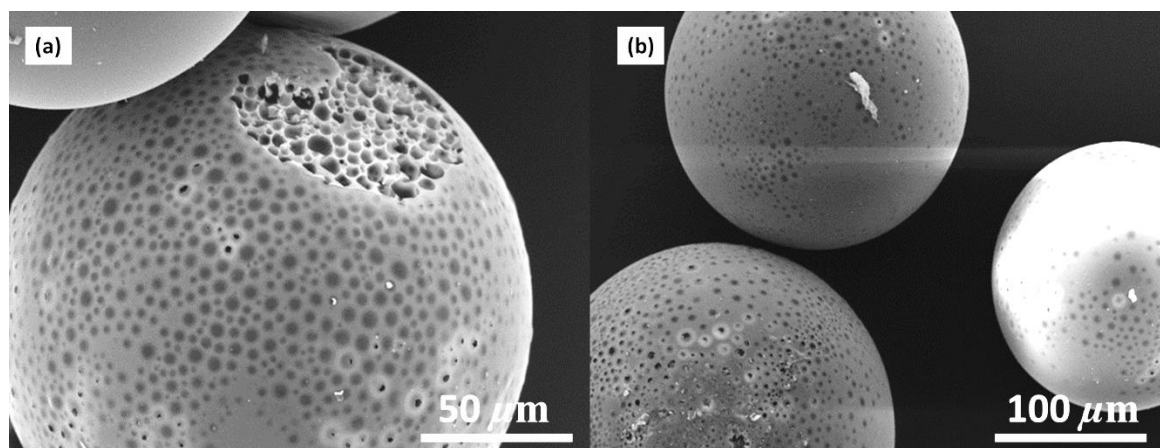


Figure 6.9: (a) & (b) SEM image showing porous microspheres manufactured using a two stage process.

This two-stage method was further adapted by mixing porous 100-200 μm microspheres with a porogen size range of 45-63 μm at a ratio of 1: 0.2 pre

spheroidisation, in aiming to improve porosity. Figure 6.10 showed that this method had a reverse effect and in fact closed off the pores on the outer surface. This may have been due to insufficient flame residence time of the microspheres since the initial porous microspheres would begin to re-melt and the gasses would dissolve in the glass liquid towards the beginning of the flame simultaneously closing off the surface pores due to surface tension created in the molten state, the microspheres may then have been ejected from the flames trajectory before allowing for the gasses (CO_2) created during porogen combustion, to escape. Thus, resulting in a highly porous inner structure and a solid outer shell in most cases.

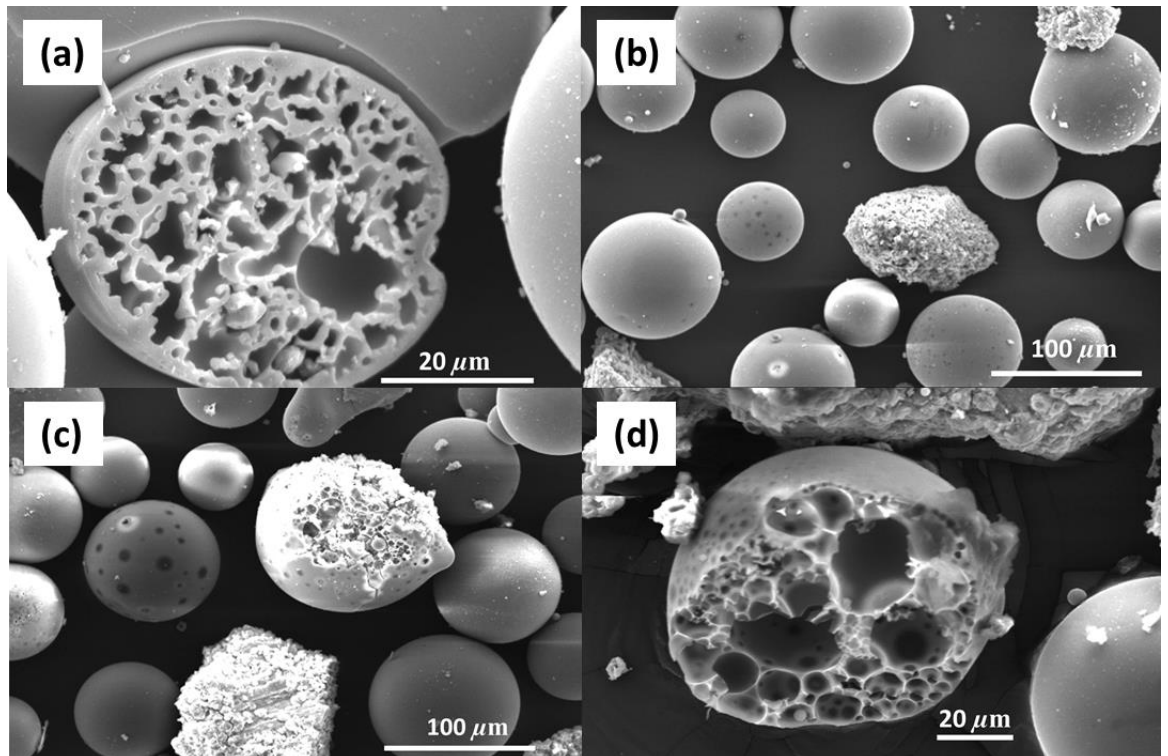


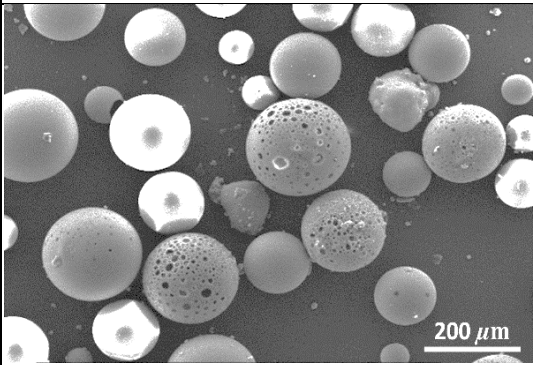
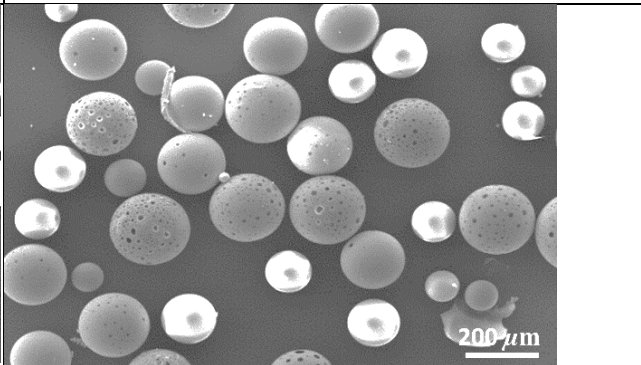
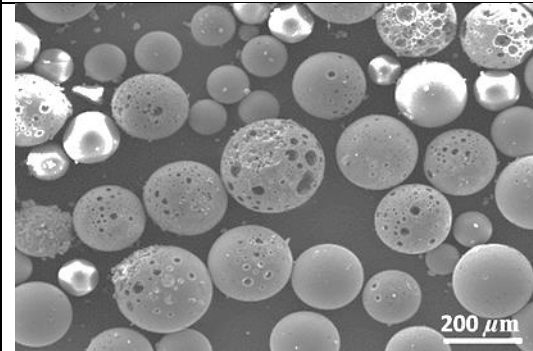
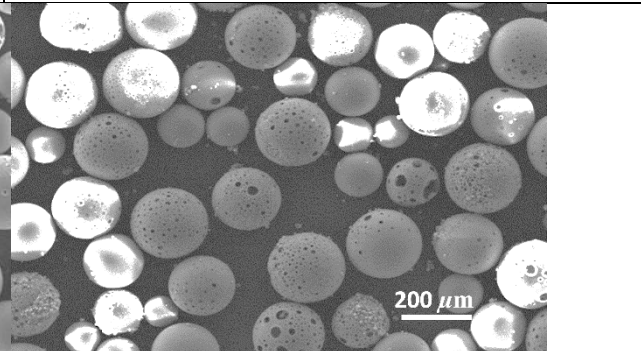
Figure 6.10: (a), (b), (c) & (d) SEM images showing the outcomes of using a 2 stage spheroidisation process where porogen was mixed with porous microspheres pre spheroidisation and put through the flame a second time.

6.4.4 Porogen binding methods

An alternate method of introducing the porogen was experimented with by using Cellosize as an adhesive to attach porogen of various sizes to the glass microparticles before being dried and subjected to the oxy-propane flame spheroidisation apparatus. Two different binding methods were investigated where; i) porogen in the size range of $<5 \mu\text{m}$ (Fisher Scientific) were bound to

glass microparticle in the size range of 100-200 μm at a glass microparticle to porogen ratio of 1: 0.1 and ii) porogen size range of $<5 \mu\text{m}$ (Fisher Scientific) were bound to non-porous glass microspheres in the size range 100-200 μm at the same ratio. The smaller size range of $<5 \mu\text{m}$ was chosen since this would allow the porogen to coat the outer surface of the glass particle and would provide the most contact. Table 6.2 illustrates the outcome of this binding method.

Table 6.2: The effect on binding porogen to glass particles using Cellosize before spheroidisation and the effect of binding porogen to non-porous microspheres

<i>Binding method i – porogen bound to microparticles via cellosize pre spheroidisation</i>	<i>Binding method ii – porogen bound to non-porous microspheres via cellosize pre spheroidisation</i>
	
	

The additional step of using Cellosize to bind the porogen to either the microparticles or non-porous microspheres pre spheroidisation, had no added benefit to both the porous microsphere yield and/or porosity achieved for each microsphere when qualitatively examining the SEM images. Therefore, this method was deemed ineffective and discontinued.

6.4.5 Oxy-acetylene assisted spheroidisation

The next set of trials were conducted using an oxy-acetylene spray gun set up (MK74 Thermal Spray gun, Metallisation Ltd., UK). This particular set up was experimented with due to its main advantage and capability of achieving higher flame temperatures and the in-built powder feeder as shown in Figure 6.11 (b), which would eliminate the need to control the powder feeding parameter.

However, the in-built powder feeder was not utilised due to the narrow aperture of the powder feeder which led to restricted powder flow and blockage. The flame length characteristics and feeder are displayed in Figure 6.11. Achieving higher flame temperatures when manufacturing porous microspheres was considered important since thermal decomposition of CaCO_3 is endothermic, thus increasing the porogen quantity could also affect the flame temperature.

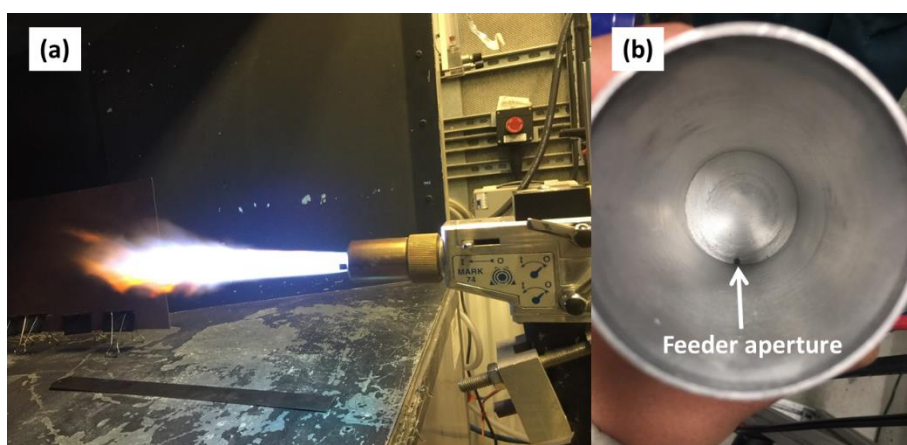


Figure 6.11: (a) flame length of oxy-acetylene flame, and (b) in built powder feeder.

Figure 6.12 displays the yield of non-porous microspheres after spheroidising via the oxy-acetylene spray gun. Porous microspheres were now manufactured using the MK74 thermal spray gun where the porogen was mixed with the glass microparticles and fed through the vibratory funnel feeder at a controlled rate. The microparticle size range was further narrowed following initial trials to 63-125 μm due to the broad size distribution observed in Figure 6.4 (e). Again, the ratio of glass microparticles to porogen were investigated in order to investigate the effects of pore formation and yield of porous spheres as displayed in Figure 6.13.

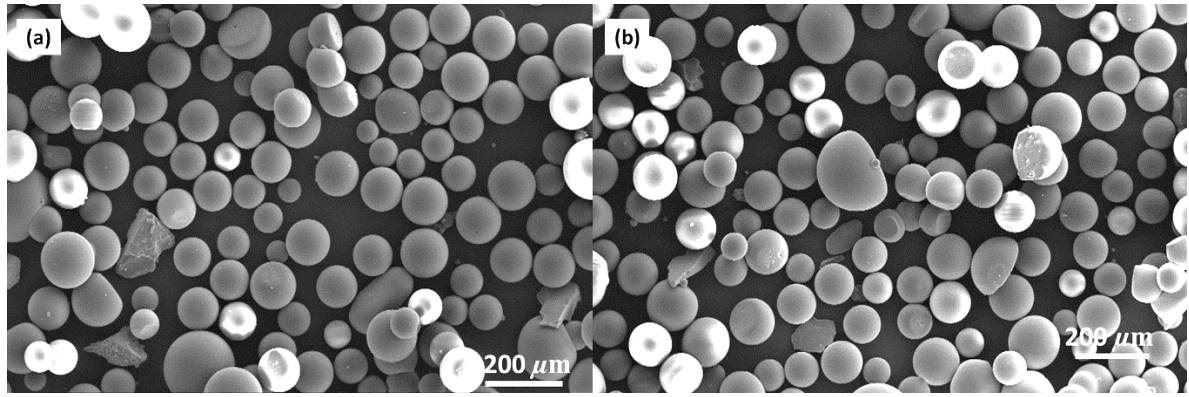
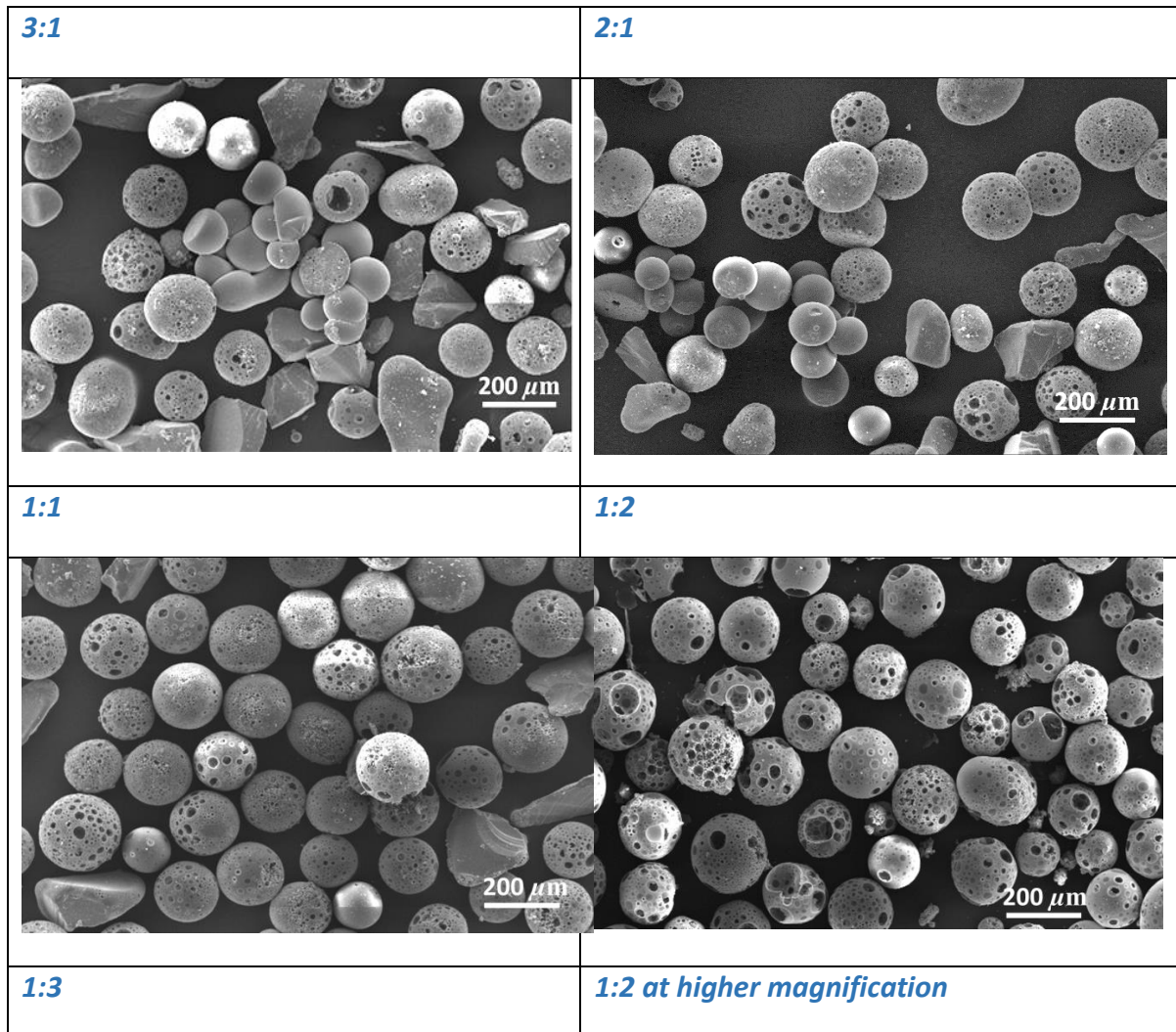


Figure 6.12: (a) & (b) SEM images showing yield of non-porous microspheres using the oxy-acetylene spray gun.



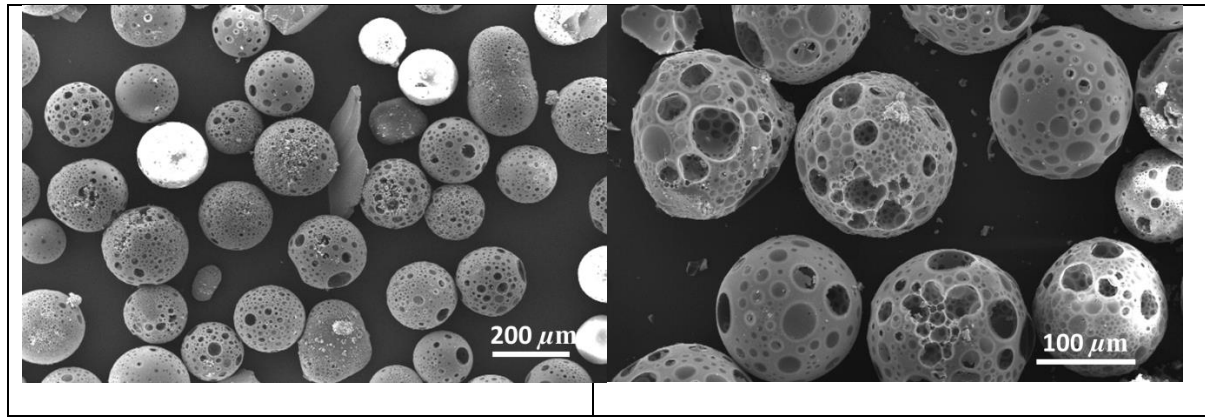
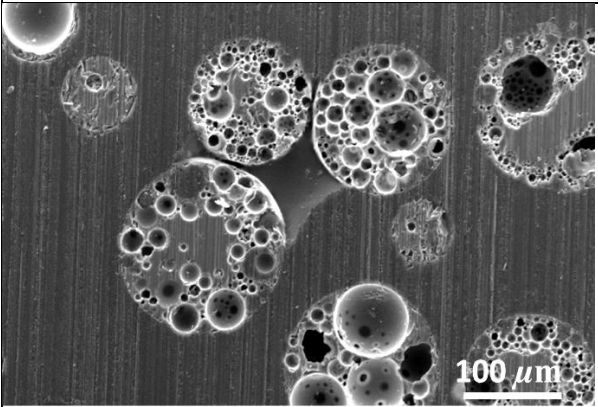
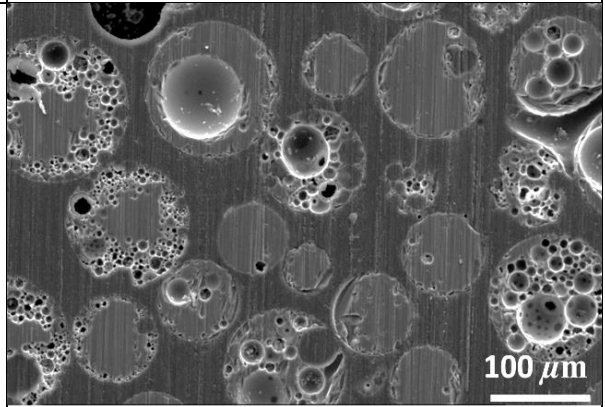
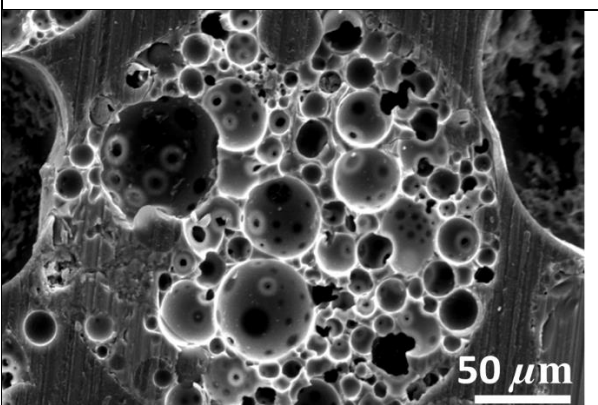
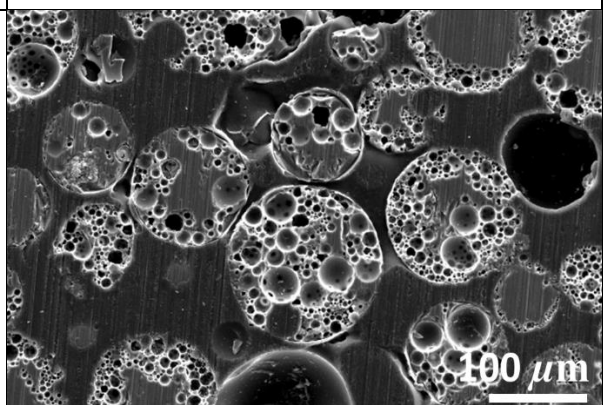
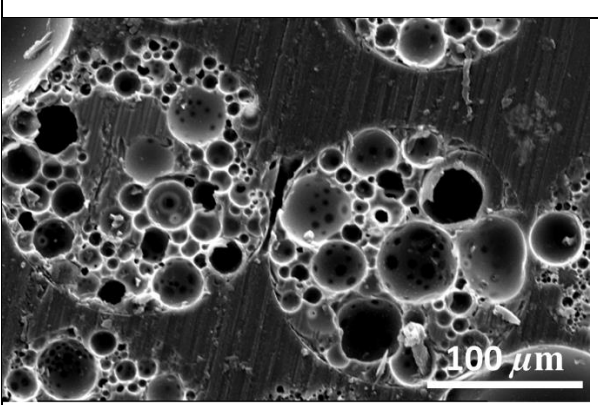
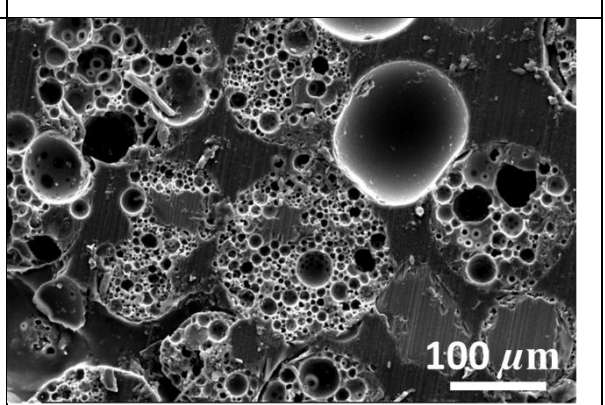


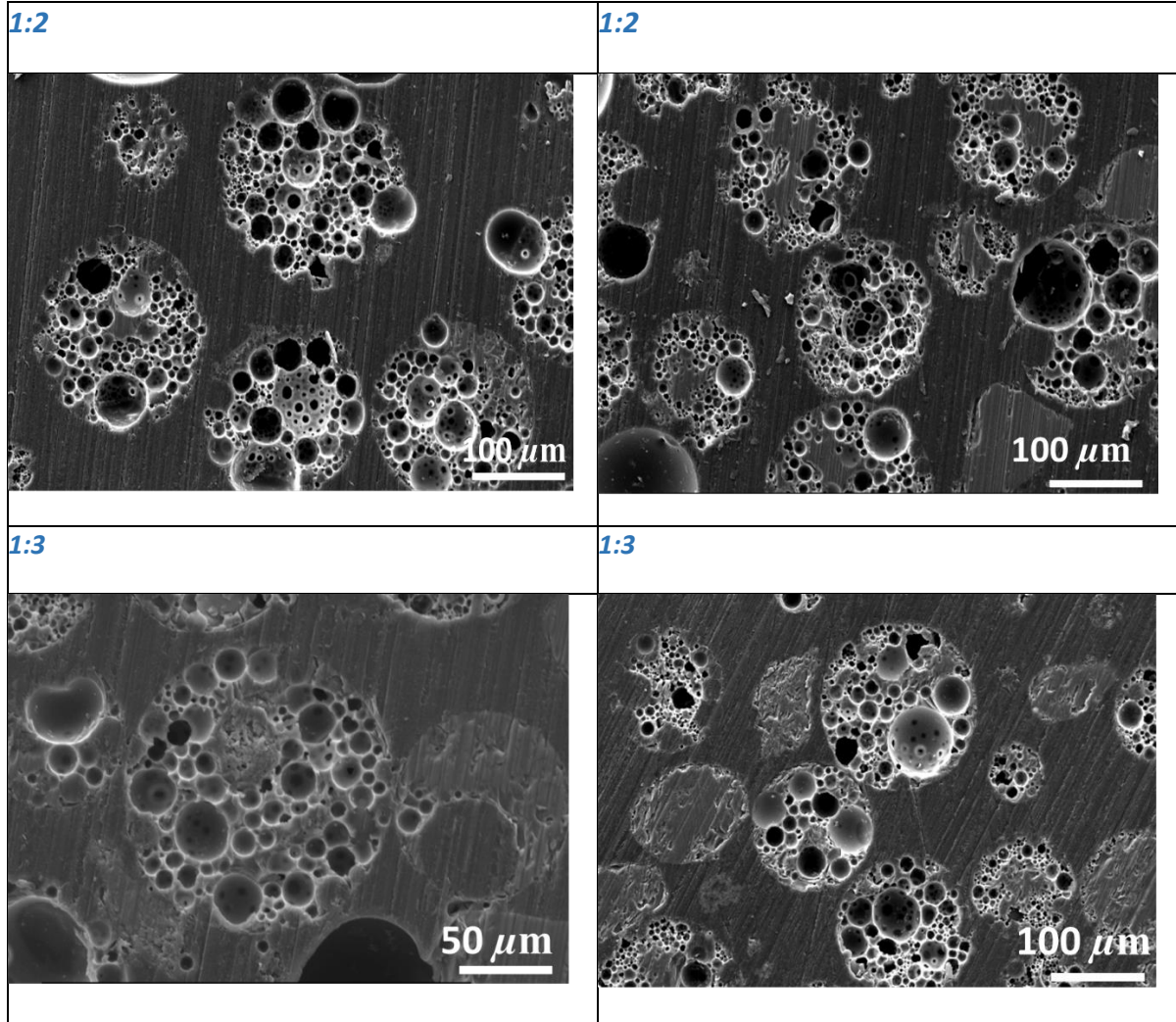
Figure 6.13: Displaying the effects of altering glass microparticle (63-125 μm) to porogen (45-63 μm) ratio on porosity and yield.

The results showed that higher glass microparticle to porogen ratios could be used to successfully fabricate porous microspheres, and that the most effective glass microparticle to porogen ratio was 1:2, thus all microspheres were fabricated using this porogen ratio going forward.

In order to qualitatively examine the internal structure of the porous microspheres, cross sections were taken by embedding the microspheres in a cold setting epoxy resin and ground and polished using SiC paper and a diamond cloth. It must be noted that this method cannot determine at what section the microspheres internal structure is revealed, i.e. does not show a true cross section, however can provide a qualitative level of detail on the internal structure of the spheres to determine open/closed porosity and interconnectivity. Table 6.3 shows cross sections of porous microspheres with various glass microparticle to porogen ratios.

Table 6.3: SEM images displaying internal features of porous microspheres manufactured using various glass microparticle to porogen ratios.

<p>3:1</p> 	<p>3:1</p> 
<p>2:1</p> 	<p>2:1</p> 
<p>1:1</p> 	<p>1:1</p> 



At lower glass microparticle to porogen ratios such as 3:1, some microspheres revealed porosity to be present at the surface edges of the spheres or not present at all. This behaviour has previously been observed in porous poly(lactic-co-glycolic acid)/CaCO₃ microspheres where a solid centre and macroporous surface was observed.^[133] Cross sectional views revealed that both interconnected and closed porosity was present in the microspheres. True (skeletal) density measurements by helium pycnometry complimented this observation as a decrease in density was observed with the addition of porogen from 2.71 g cm⁻³ for the quenched glass to 2.46 g cm⁻³ for the porous microspheres at a glass microparticle to porogen ratio of 1:2 as displayed in Figure 6.14.

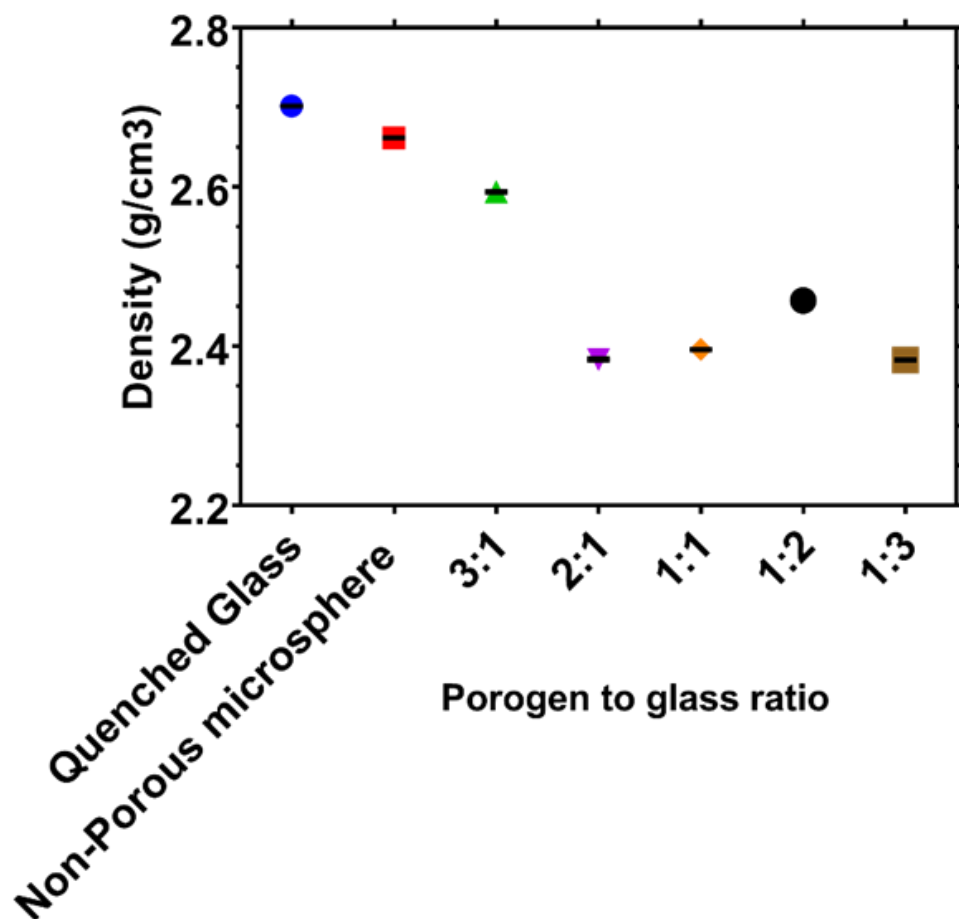


Figure 6.14: True density of porous microspheres with varying porogen quantities.

The spheroidisation efficiency of both non-porous and porous microspheres manufactured using the oxy-acetylene set up was calculated using equation 20 (chapter 6, section 6.3.1).

Where A is equal to the total number of particles counted in 8 SEM images at 200x magnification, and B is the number of spherical particles. All irregular particles such as those shown in Figure 6.15 (a) were excluded in parameter B for bulk microspheres, and all irregular and non-porous particles as shown in Figure 6.15 (b) were excluded in parameter B for porous microsphere calculations. The spheroidisation efficiency of non-porous and porous microspheres was calculated to be 94% and 91% respectively.

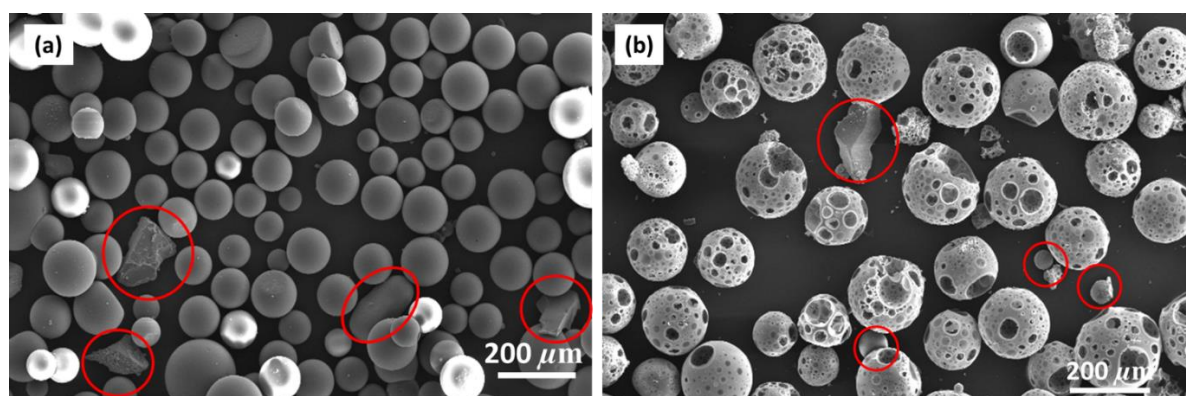


Figure 6.15: SEM images of (a) bulk and (b) porous microspheres where irregular and non-porous particles which were not included in parameter B in equation 20 are circled in red.

6.5 Microsphere characterisation

XRD was used to determine if the resultant microspheres remained amorphous after spheroidisation. Figure 6.16 (a) shows the XRD traces of the glass samples investigated and that the non-porous microspheres remained amorphous. However, the porous microspheres produced all showed crystalline peaks. This was further investigated as shown in Figure 6.16 (b), where the porous microspheres (1:2) were compared to the as received neat porogen and porogen that had been introduced to the flame spheroidisation equipment in the same way as the porous microspheres (processed porogen).

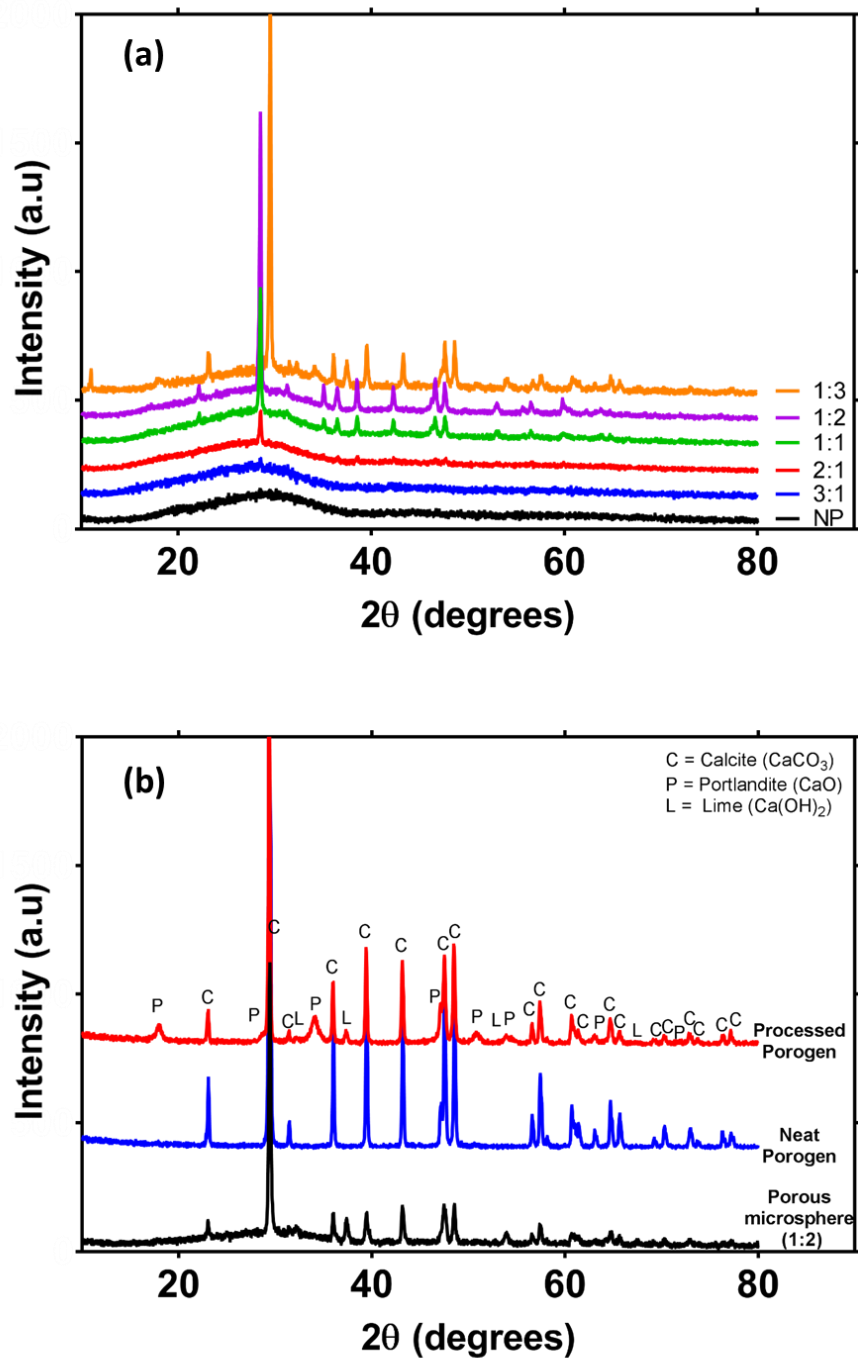


Figure 6.16: (a) XRD trace of non-porous (NP) and porous microspheres with varying porogen percent, (b) XRD trace of porous microsphere (1:2) compared to neat and processed porogen.

From the XRD traces it was apparent that the microspheres contained residual amounts of porogen as evident by the presence of calcite, portlandite and lime. The source of porogen could have been from either the presence of residual porogen trapped within the pores of the microspheres or remnants of porogen

could have been present along with the batch of microspheres sampled. The presence of porogen was confirmed by the DSC trace where an endothermic peak was observed beginning 345°C for the porous microspheres which was not present for the non-porous and microparticles of the same composition as displayed in Figure 6.17. The processed porogen also showed endothermic activity beginning at *c.a.* 308°C and continuing until just after 345°C confirming the presence of porogen amongst the porous microspheres.

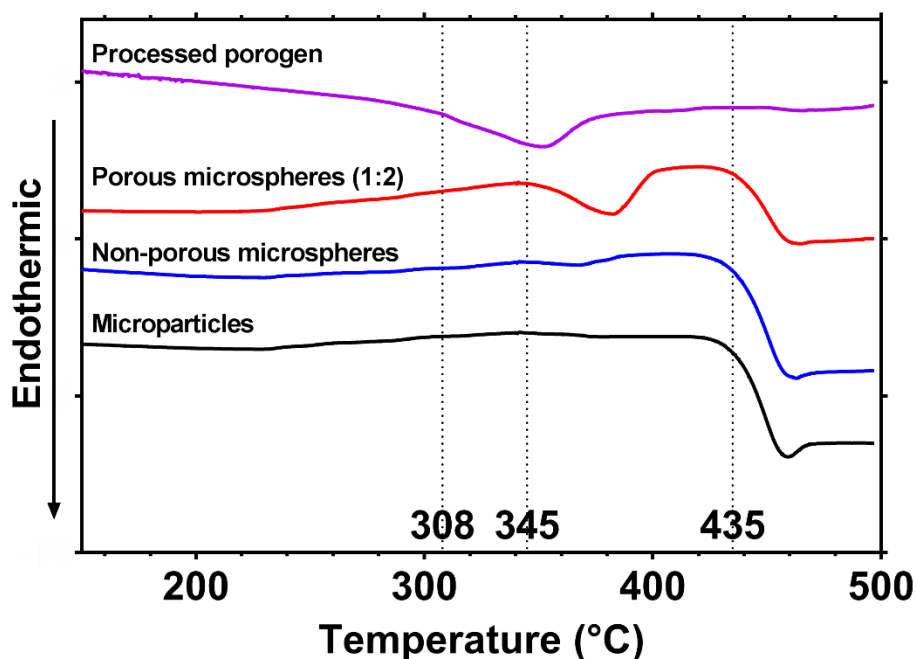


Figure 6.17: Thermal trace showing T_g of processed porogen, porous and non-porous microsphere and microparticles.

Further to this, EDX analysis on cross sections of the porous microspheres showed a higher concentration of CaO at the pore edges compared to the bulk material as indicated in Figure 6.18.

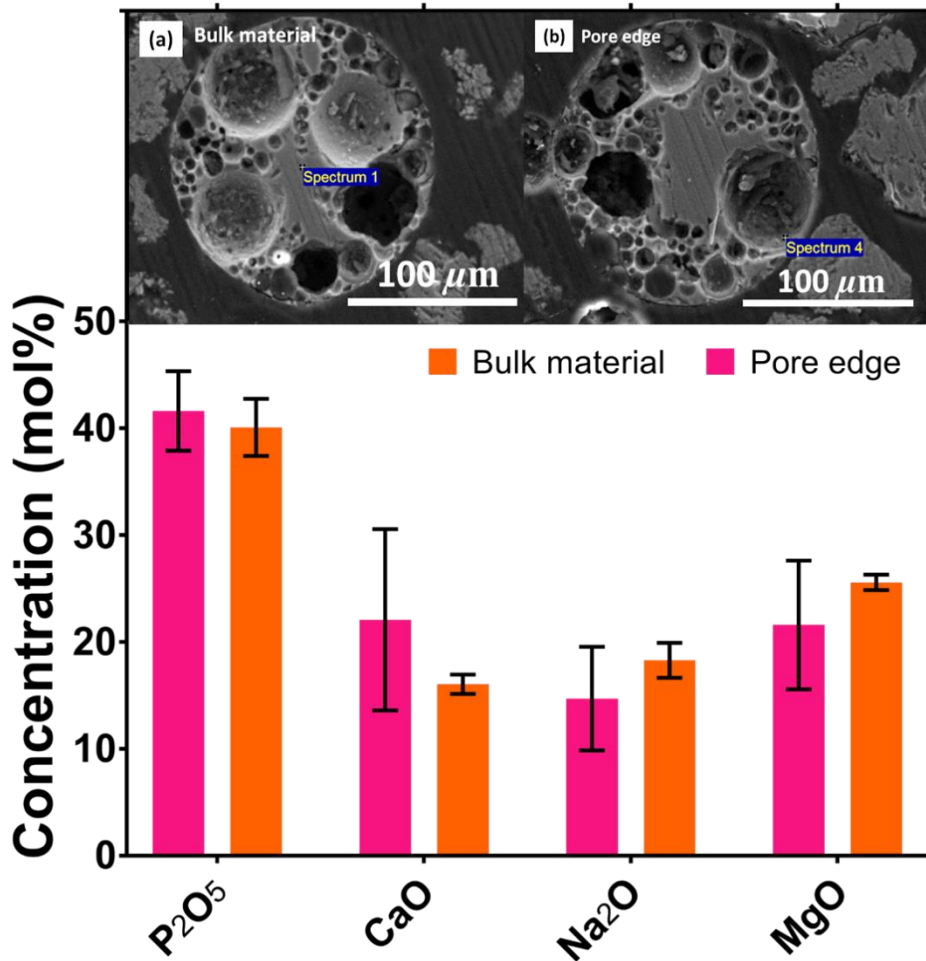


Figure 6.18: (a) & (b) SEM images showing bulk material and pore edge respectively, and EDX analysis of these areas from microsphere cross sections.

In order to confirm that the CaO rich regions around the pore edges were an effect of the porogen and not due to inhomogeneity in melting the glass, porous microspheres were attempted for manufacture using SrCO₃ as the porogen source (at a microparticle to porogen ratio of 1:2). Figure 6.19 showed the presence of SrO around the pore edges as determined by EDX. The porogen SrCO₃ was not used for the following experiments as the level of porosity in terms of yield of porous microspheres and pore distribution was inferior to that seen with CaCO₃. However, this was sufficient to confirm that additional ions could be incorporated into the microspheres via careful selection of porogen materials.

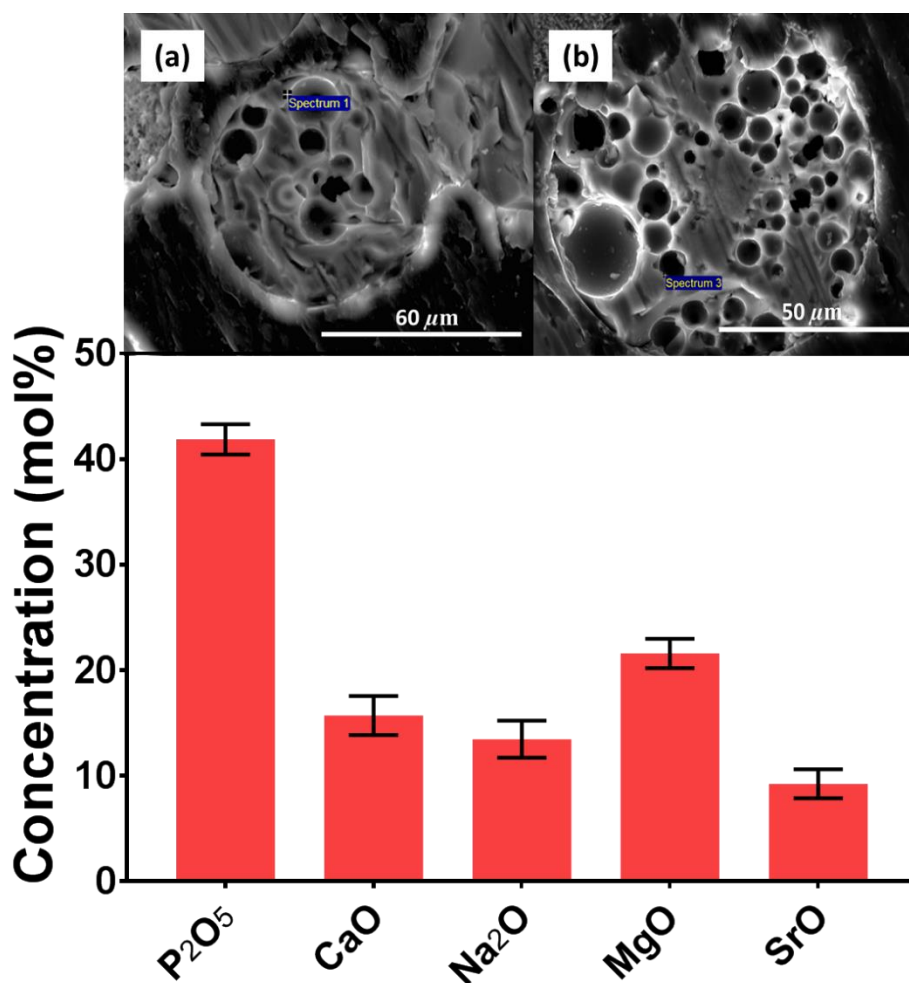


Figure 6.19: (a) & (b) SEM cross sections of porous microspheres using SrCO₃ as a porogen source, and the EDX analysis of the pore edges shown in (a) and (b).

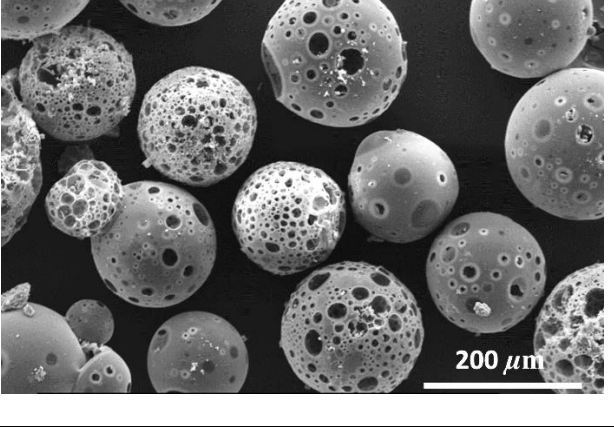
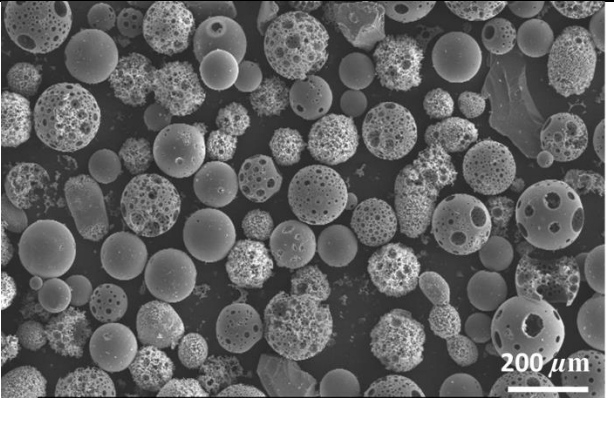
Although suggestion of residual CaCO₃ was present in the porous microspheres as indicated by the EDX analysis, this is not thought to have a cytotoxic effect on the cells or hinder the biocompatibility of the material as has previously been found in studies involving HeLa cells and porous spherical CaCO₃ microparticles.^[234]

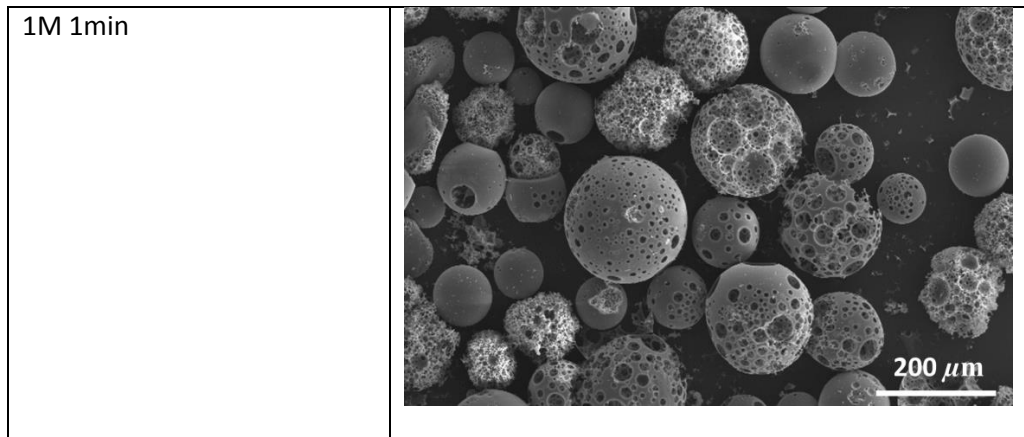
6.5.1 Post processing porous microspheres

In order to address the effect of residual porogen, a series of acid washes were developed where the porous microspheres (1:2) were subjected to certain concentrations of acetic acid for specific time points. This procedure was developed based on the findings of a previous study where CaCO_3 was dissolved using acetic acid with the aim of removing calcium carbonate crystals which tend to form in the pipelines of blast furnaces.^[235]

Studies began by investigating the effect of 2M and 1M concentrations of acetic acid for 2 and 1 minutes respectively. These concentrations appeared to be too strong and caused some damage to the glass spheres as shown in Table 6.4, where pore struts and “fuzzy” textured microspheres remained.

Table 6.4: SEM images displaying the effect of acid washing porous microspheres in 2M and 1M of acetic acid for 1 and 2 minutes respectively

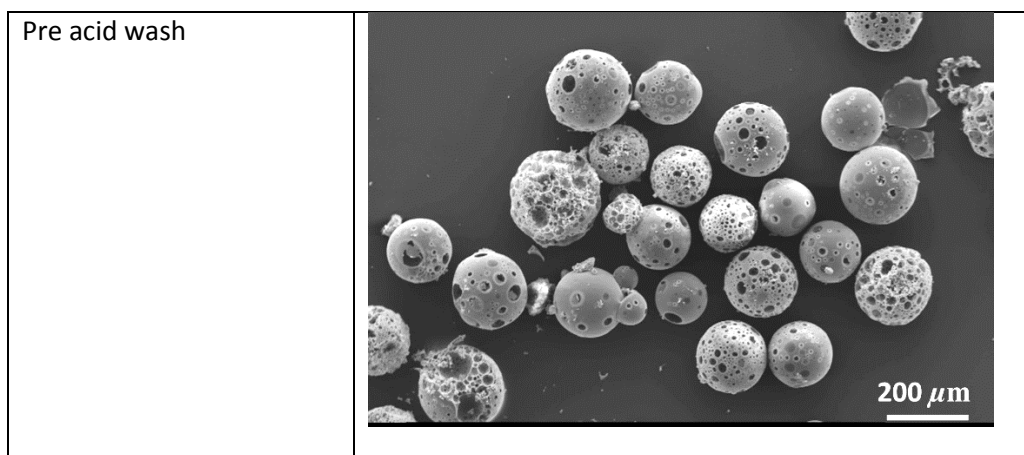
Pre-acid wash	
2M 2min	

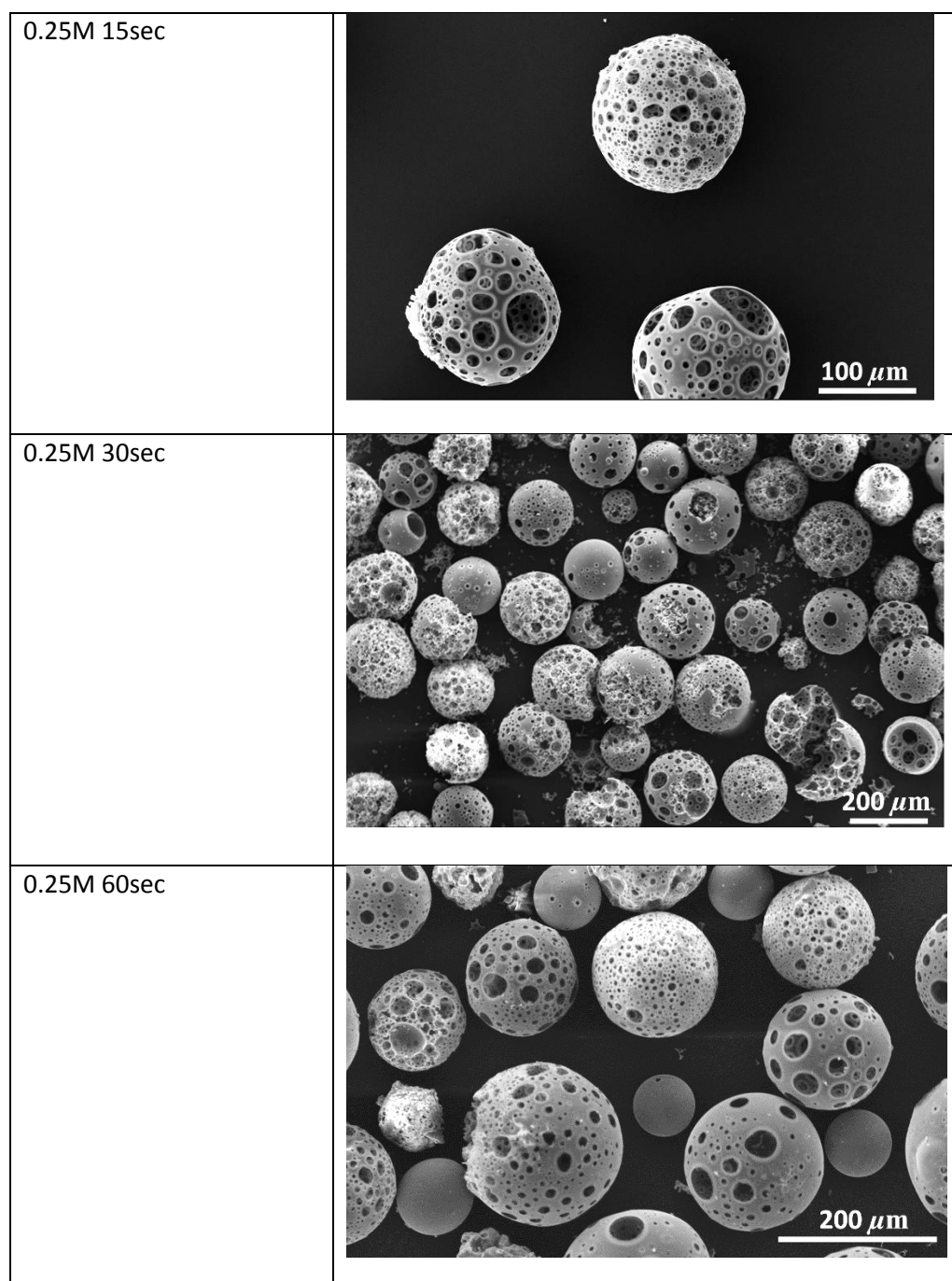


The smooth topography of the acid washed microspheres appeared to be altered displaying exposed pore struts. Thinning and loss of a large majority of pore struts would be likely to cause a loss in mechanical properties, adding further to the inherent brittle nature of glasses. The disruption in sphericity and the exposed pore struts would be deemed undesirable when trying to deliver these microspheres in a clinical setting as the free-flowing nature of spheres would be disrupted.

Following this, a lower concentration of 0.25M was investigated for a reduced period of time as shown in Table 6.5.

Table 6.5: SEM images displaying the effect of acid washing porous microspheres in 0.25M of acetic acid for various time points





Subjecting the microspheres to the reduced concentration of acetic acid appeared to have no detrimental effects on the microsphere surfaces when observed via SEM, however, some porogen remained and debris was also observed attached to the microspheres. The presence of residual porogen was confirmed again by the crystalline peaks (particularly prominent when 2 Theta is 30) in the XRD traces post acid wash process as shown in Figure 6.20.

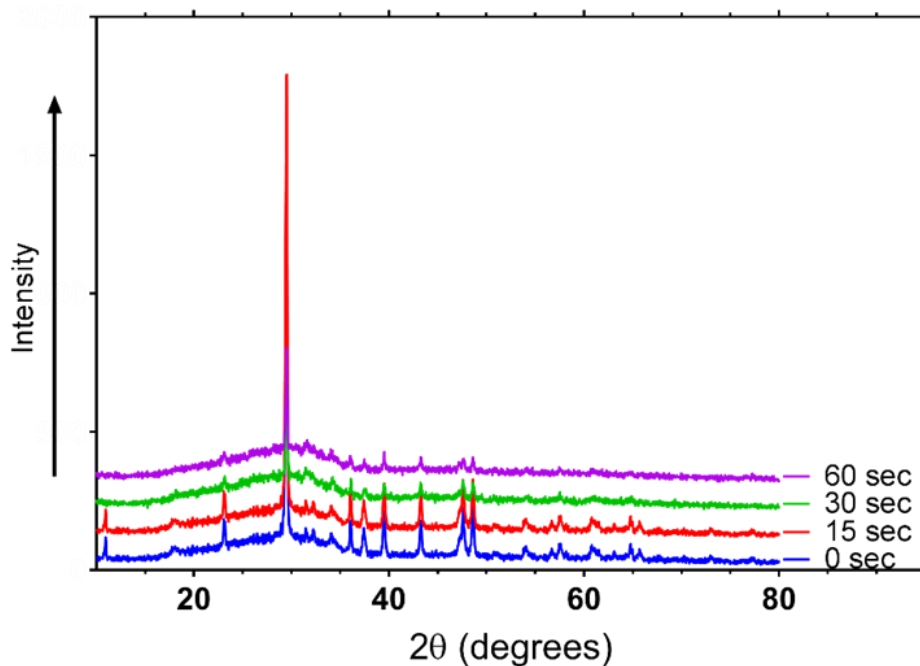
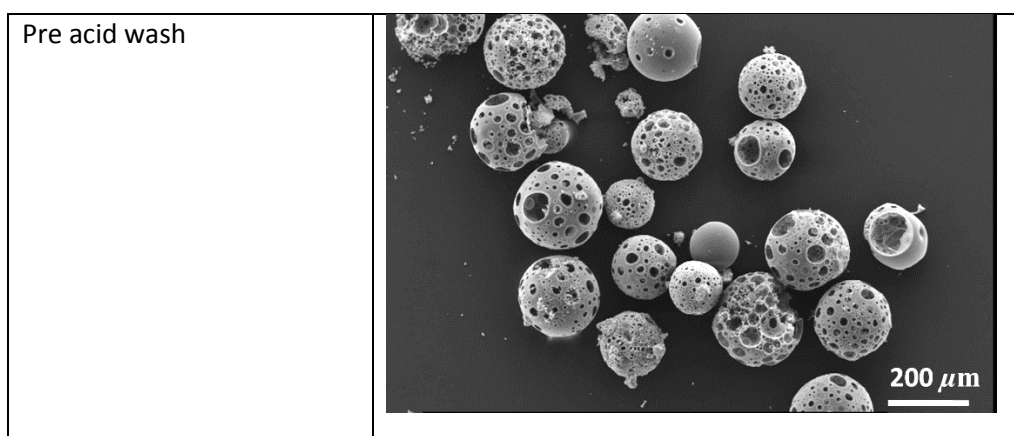
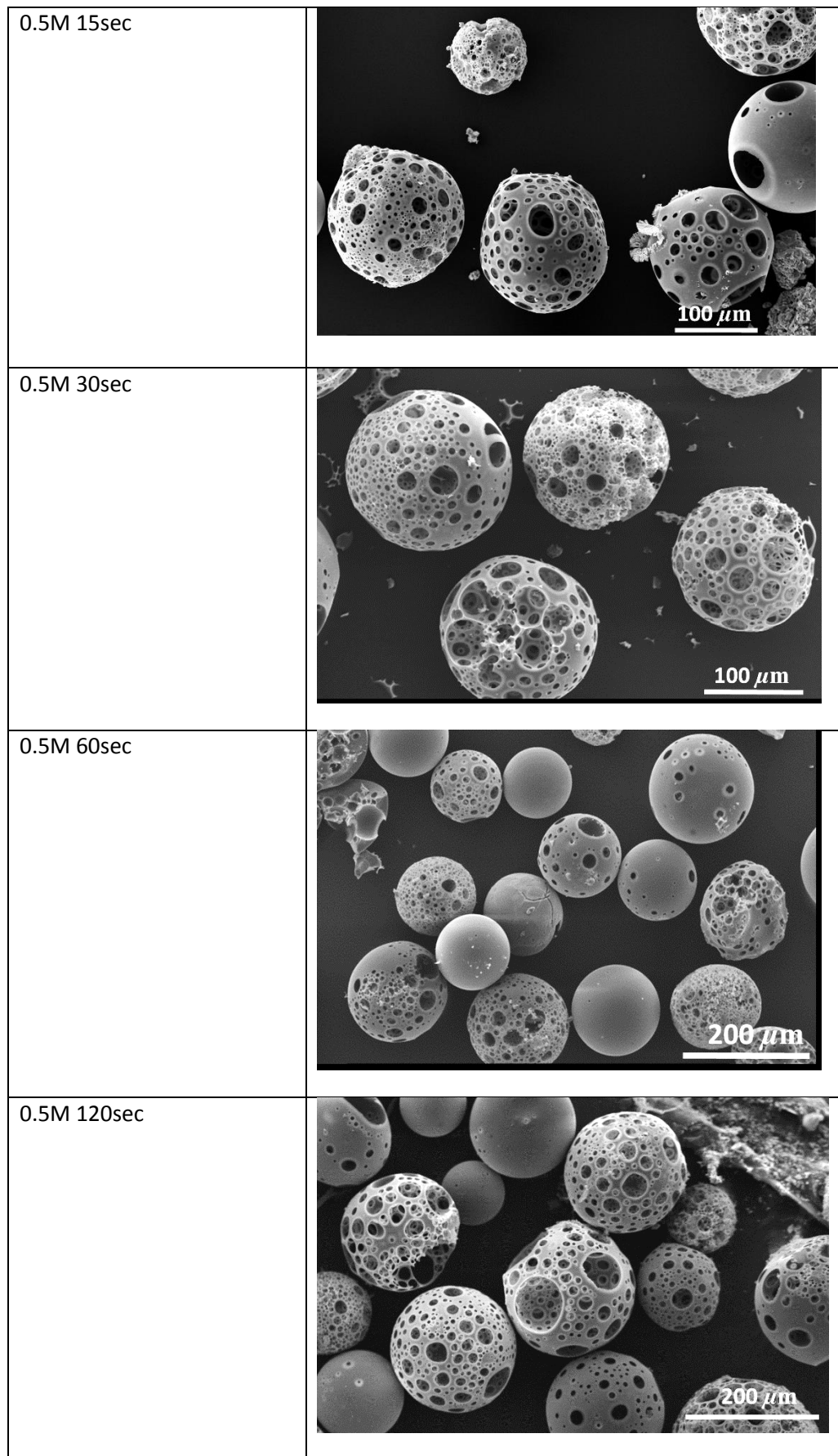


Figure 6.20: XRD trace of porous microspheres after acid washing in 0.25M acetic acid for 15, 30 and 60 seconds.

Therefore, the concentration of acetic acid was doubled to 0.5M and a further time point was tested as displayed in Table 6.6. Again, no detrimental destruction of the microspheres surface was observed.

Table 6.6: SEM images displaying the effect of acid washing porous microspheres in 0.5M of acetic acid for various time points





The XRD traces shown in Figure 6.21 indicated successful removal of residual porogen using acetic acid concentration of 0.5M for 120 seconds. Thus, going forward an acid wash step was included post manufacturing porous microspheres which involved submerging the porous microspheres (1:2) in 0.5M acetic acid for 120 seconds.

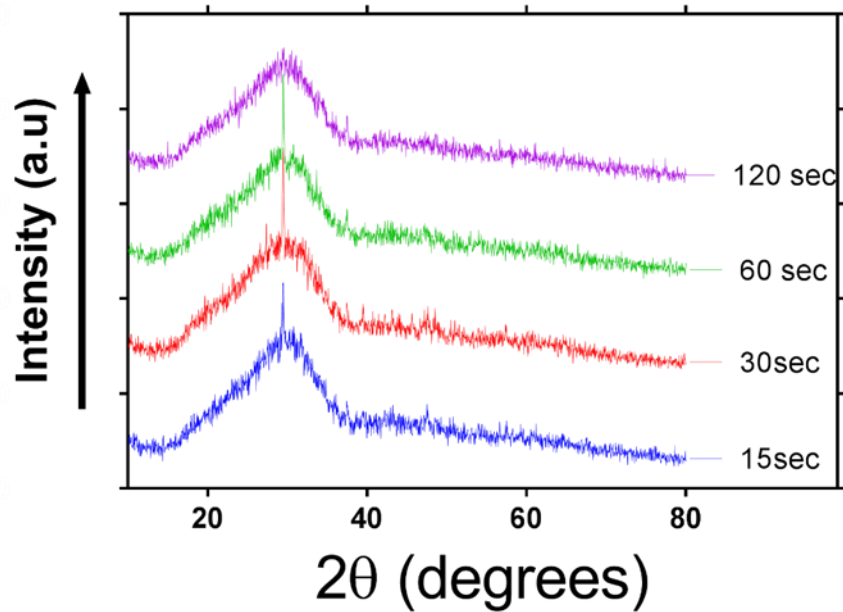


Figure 6.21: XRD trace of porous microspheres after been subjected to acid wash in 0.5M acetic acid for 15, 30, 60 and 120 seconds.

6.5.2 Optimised manufacturing procedure

Below (Figure 6.22) shows a flow diagram of the optimised standard operating procedure developed for the manufacture of novel porous microspheres.

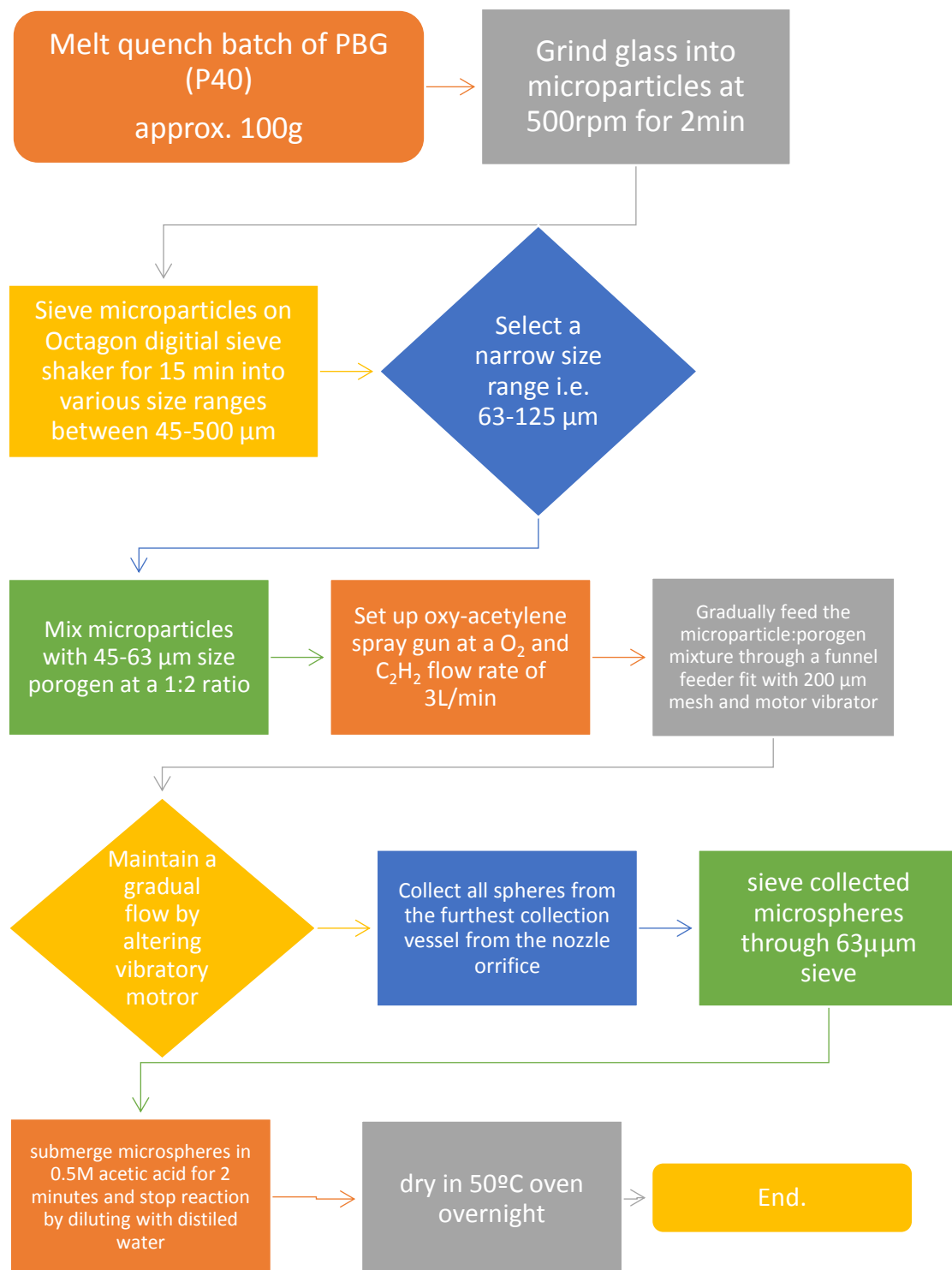


Figure 6.22: Flow diagram showing procedure of manufacturing porous microspheres.

6.5.3 Hypothesis on porosity formation within glass microspheres

After carrying out initial trials, optimising manufacturing procedures and qualitatively analysing porous microspheres via SEM image analysis, the process of porosity production has been hypothesised as illustrated in Figure 6.23.

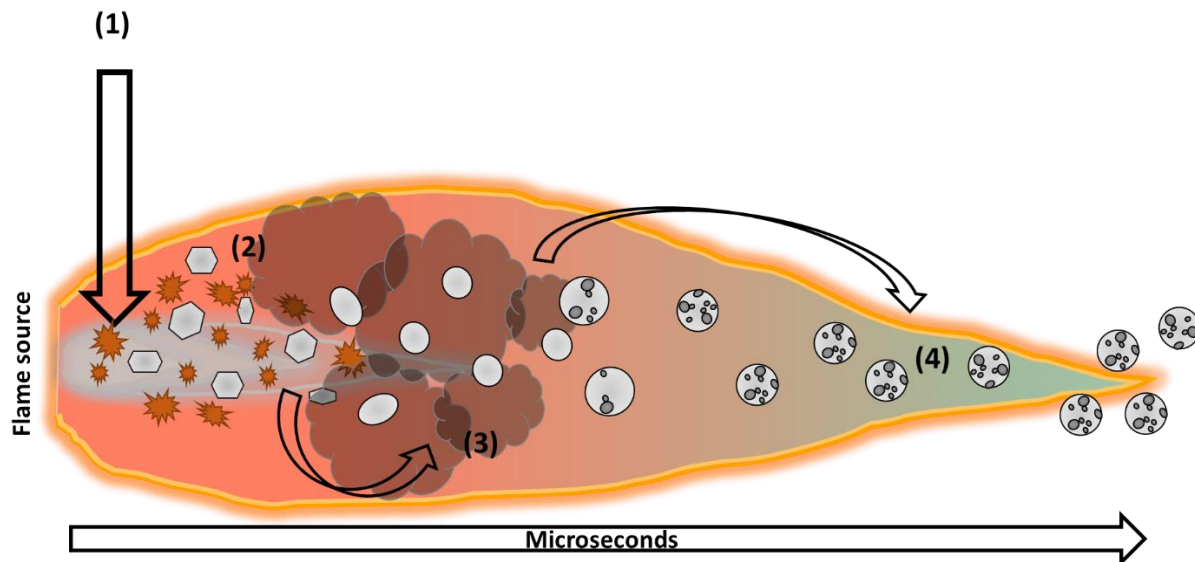


Figure 6.23: Schematic of the hypothesised process of porosity formation within the microspheres. The inner blue cone in the orange region indicates the hottest part of the flame and the blue tip of the flame indicates the coolest part of the flame.

Figure 6.23 can be summarised as follows:

- (1) Microparticle and porogen mixture enters the flame at the hottest part (inner cone)
- (2) Porogen instantly decomposes at the high temperatures as indicated by change in flame colour from blue to a bright orange/red flame. The viscosity of the glass decreases

- (3) The molten glass particles become surrounded by pockets of CO₂ gas. As the molten particles move through the flame trajectory, a spherical morphology is formed due to the surface tension. The flame temperature is expected to get cooler along its trajectory the further away it is from the source, thus CO₂ gas pockets becomes entrapped in the softened, viscous liquid as CO₂ is more soluble in the glass melt at lower temperatures as has been seen for silica glass melts.^[233]
- (4) As microspheres are ejected from the flame trajectory, they instantly cool, in turn “freezing” the CO₂ pockets in the glass microspheres.

These gas pockets are also spherical in morphology due to the surface forces, and these pores contain gasses characteristic to the melting atmosphere. The surrounding gasses would not have only been from the CO₂ released as a result of CaCO₃ decomposition but could also result from other soluble gasses present in the flame such as H₂O.^[32] On burning a mixture of oxygen and acetylene, flame temperatures can reach up to 3480°C in a two stage reaction:^[236]

- i) Oxygen and acetylene react to form carbon monoxide and hydrogen near the end of the torch tip



- ii) Carbon monoxide and hydrogen then react with oxygen from the atmosphere forming carbon dioxide and water vapour



The above hypothesis on formation of porosity is based on the assumption that the microparticle/ porogen mixture hits the centre of the hottest part of the flame each time for optimum energy transfer. However, in reality, this is highly dependent on the particle flow rate and velocity of the flame. Figure 6.24 illustrates the predicted flow paths of particles injected at different rates.

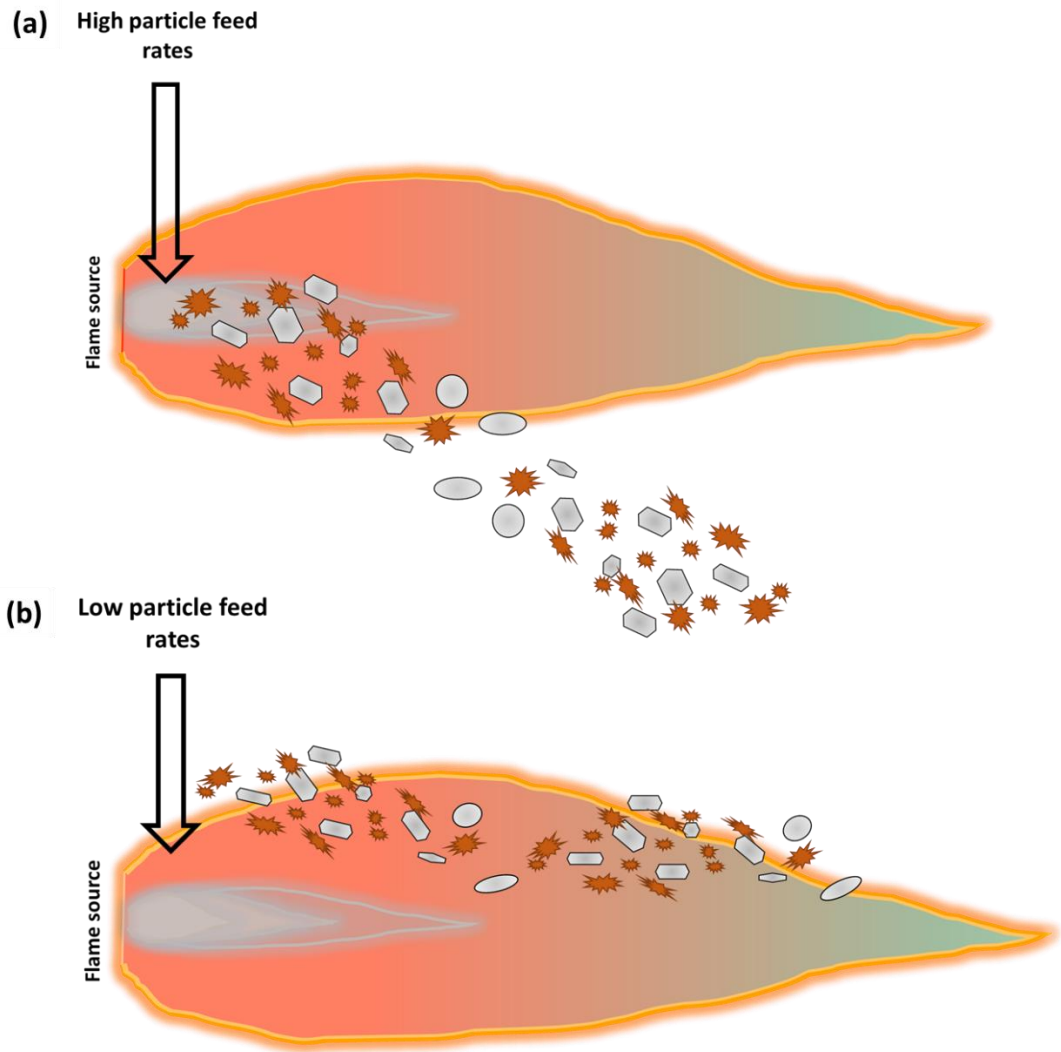


Figure 6.24: Illustration showing the effect of (a) high powder feeding rates and (b) low powder feeding rates.

Figure 6.24 shows that high powder feeding rates resulted in over injection of particles which fall through the flame, avoiding spheroidisation. Low powder feeding rates resulted in under injection, avoiding the ideal hot spot of the flame where particle temperature and velocity were optimised. Instead the particles flowed through the outer envelope of the flame which tend to have lower temperatures compared to the core, resulting in incomplete spheroidisation and scattering of particles.

6.5.4 Particle size analysis

The particle size distribution of the porogen, glass microparticle, non-porous, porous and acid washed microspheres were compared using a Mastersizer 2000. The comparison histogram can be seen in Figure 6.25.

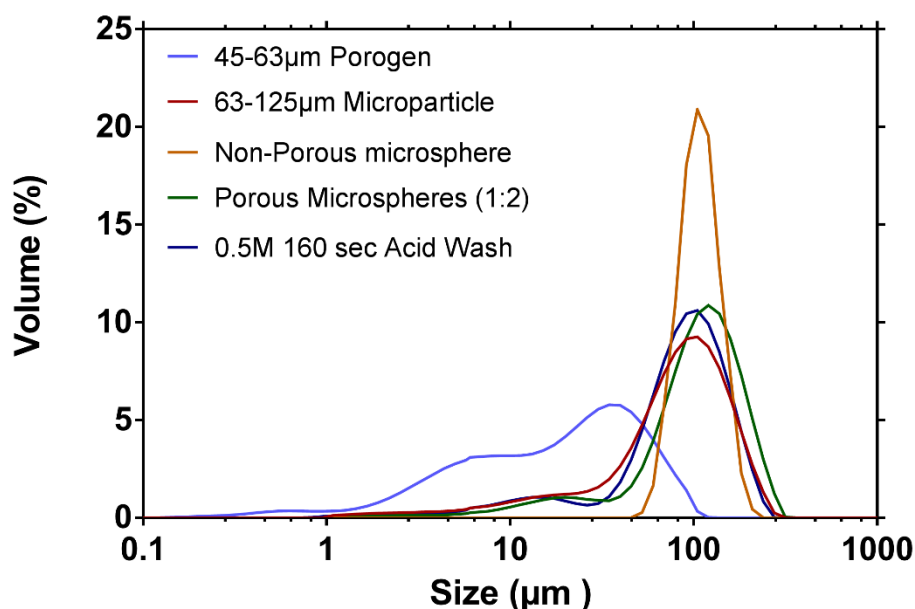


Figure 6.25: Histogram showing particle size distribution of the porogen, microparticles, non-porous, porous and acid washed microspheres.

Figure 6.25 showed that the porogen particles displayed a broad bimodal size distribution with the two modal sizes observed at *c.a.* 6 µm and *c.a.* 39 µm although the porogen was screened between 45-63 µm meshes. This can be explained by the fact that the porogen particles have irregular morphologies and the results are expressed in terms of equivalent spheres i.e. Mie theory presumes that the measured particles are perfect spheres, thus the measurement of irregular particles in this instance were defined by a single dimension, however, irregular particles are three-dimensional with more than one aspect ratio.

In order to compliment the laser particle size analysis, image analysis can be combined with this technique since this method can measure the particle projection and no assumption on shape is made.

Glass microparticles are angular particles thus also appear to show a fairly bimodal distribution, however the modal size distribution was found at 91 μm . In contrast non-porous microspheres showed a monomodal size distribution ranging between 52- 208 μm , with a modal particle size of 104 μm . The mono dispersity in particle size can be explained by the fact that all microspheres were characterised from the furthest collection vessel, thus are likely to have a more uniform size. There is also a possibility that smaller particles combined within the flame trajectory forming larger spheres.

A shift in the bimodal peak for the porous microspheres was also observed. This was due to the fact that the light scatters between the particles and the air, and so when the light encounters a pore, two phase boundaries are detected causing light to scatter again, i.e. second phase scattering is caused by the grain boundaries. Light is scattered back into the microsphere or at a wider angle, causing a deviation in the particle size analysis.^[237] There is also a possibility of the porous microspheres expanding as a result of spheroidisation process which entraps the gasses released (CO_2) by the porogen and within the flame (H_2O). It was interesting to see that the bimodal size distribution of the acid washed porous microspheres appeared to have shifted back to a similar position as the glass microparticles. Again, this could be due to the deviation cause in the laser diffraction analysis associated with porous materials or possibly due to a reduction in microsphere size caused by the acid washing step.

6.5.5 Density, surface area and pore size

Helium pycnometry was used in order to determine the effects of porosity on true (skeletal) density. Figure 6.26 (a) compares the skeletal density of the as quenched glass which contains no voids or bubbles to the non-porous, porous and acid washed microspheres. It was interesting to note that non-porous microspheres showed an unexpected minor decrease in density from 2.71 g cm^{-3} to 2.65 g cm^{-3} . This minor decrease was attributed to the fact that not all the non-porous microspheres were completely solid as shown in Figure 6.26 (b). When examining cross sections of the non-porous microspheres some hollow regions within the microsphere core were observed, possibly caused by the entrapment of air/gas from the oxy-acetylene breakdown products, during the spheroidisation process. It was clear that the introduction of porosity resulted in a decrease in density caused by the presence of closed porosity as confirmed in Figure 6.26 (c). Subjecting the microspheres to an acid wash resulted in a slight increase in density when compared to the porous microspheres. This suggested that some closed porosity in the structure may have opened after this step, increasing interconnectivity. Figure 6.26 (d) displayed the microspheres after acid washing showed a higher degree of interconnectivity and thinner struts.

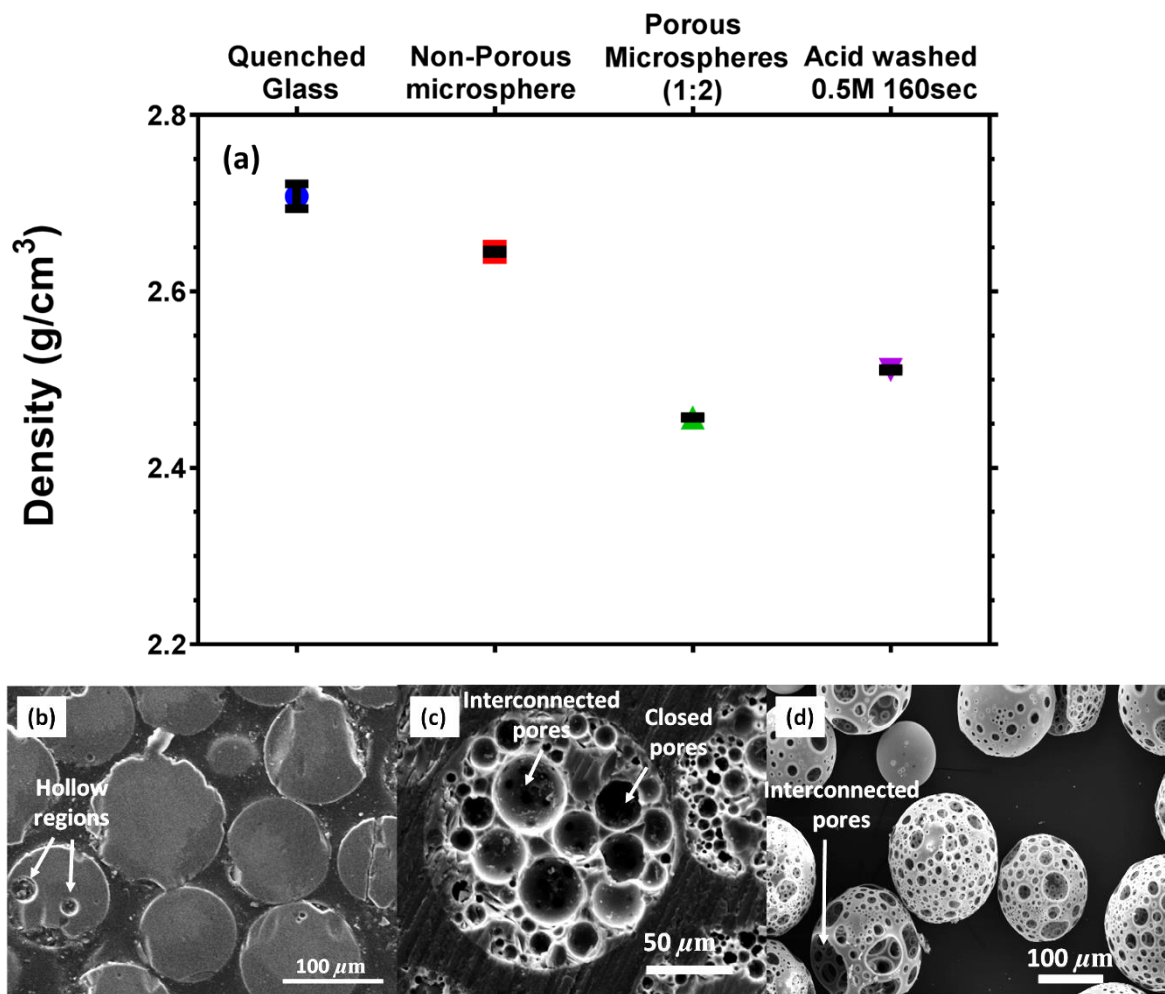


Figure 6.26: (a) showing density values of non-porous, porous and acid washed microspheres compared to the as quenched glass, and SEM images of cross sections of (b) non-porous spheres, (c) porous spheres and (d) SEM image of acid washed spheres.

The surface area (SA) of the microspheres were analysed via BET. Sorption properties in macroporous materials differed from micro- and mesoporous materials in that they have been considered to behave in a similar way to the sorption properties of flat surfaces due to their wide pore. Nitrogen or argon adsorption experiments (at 77.4K and 87.3K respectively) are limited by the detection limits, hence krypton (at 77.4K) was used to improve the detection limits allowing absolute surface areas to be measured down to 0.05m² or less.

When looking at low surface areas, the number of unabsorbed nitrogen molecules in the void volume of the cell can be larger than the number of absorbed molecules on the surface of the sample. In order to avoid this, the number of molecules contained within the void volume of the sample must be

reduced. This can be done using an adsorptive with a lower vapour pressure such as Krypton.^[238]

Table 6.7 displays the surface area of non-porous, porous and acid washed microspheres. The surface area of the porous microspheres was found to be almost four times greater than that of the bulk microsphere equivalent as expected. The surface area of the non-porous microspheres were found to be comparable to Quartz SE-10.^[239] Interestingly the surface area of the porous microspheres manufactured using a glass microparticle to porogen ratio of 1:3 resulted in a slight decrease, this may be due to an increased number of closed pores with increasing porogen quantity. Further to this, the acid washed microspheres also showed a decrease in the surface area, which was attributed to: i) opening up of porosity which may have resulted in some pore struts collapsing, reducing the volume of material or ii) the presence of residual porogen in the as prepared porous microspheres contributing to the overall surface area of the sample. The surface area for the porous microspheres was almost four times greater than that of the non-porous microspheres, confirming that introduction of porosity increased the surface area as expected.

Table 6.7: Surface area of microspheres as measured by BET

<i>Sample</i>	<i>BET Surface Area (m² g)</i>
Non-porous microsphere	0.0871
Porous microsphere (1:2)	0.3443
Porous microsphere (1:3)	0.3337
Porous acid washed	0.3060

Porosity and pore size distribution measurements were determined using mercury porosimetry. It should be noted that mercury porosimetry determines the largest entrance to a pore as pore size and not the actual “pore size”.^[240] All experiments were run in triplicate using samples from the same batch. The cumulative intrusion curves are displayed in Figure 6.27, showing that all three runs of the bulk microspheres followed the same trend. These results showed convincing reproducibility of the non-porous microspheres. Figure 6.27 also displayed each inflection points corresponding to the filling of specific areas of the microspheres. The cumulative intrusion curve of the porous microspheres appeared to differ slightly in comparison to the non-porous microspheres suggesting variability of porosity and packing within the batch. Samples also appeared to withstand high pressures over *c.a.* 1000 psi before showing signs of possible sample compression. The cumulative intrusion curves for the acid washed porous microspheres showed even greater variability in porosity of the batch compared to the porous microspheres and possible sample compression was seen at lower pressures of just over *c.a.* 100 psi as indicated by the dotted line in Figure 6.27. Although the acid wash step resulted in a density decrease as a result of the removal of residual porogen and displayed amorphous behaviour, opening up of pores may have resulted in the formation of thinner pore struts which would easily collapse when subjected to high pressures.

Compressibility effects can also be determined via mercury porosimetry when plotting cumulative intrusion as each inflection point can be used to determine mercury filling as displayed in Figure 6.27.^[240, 241]

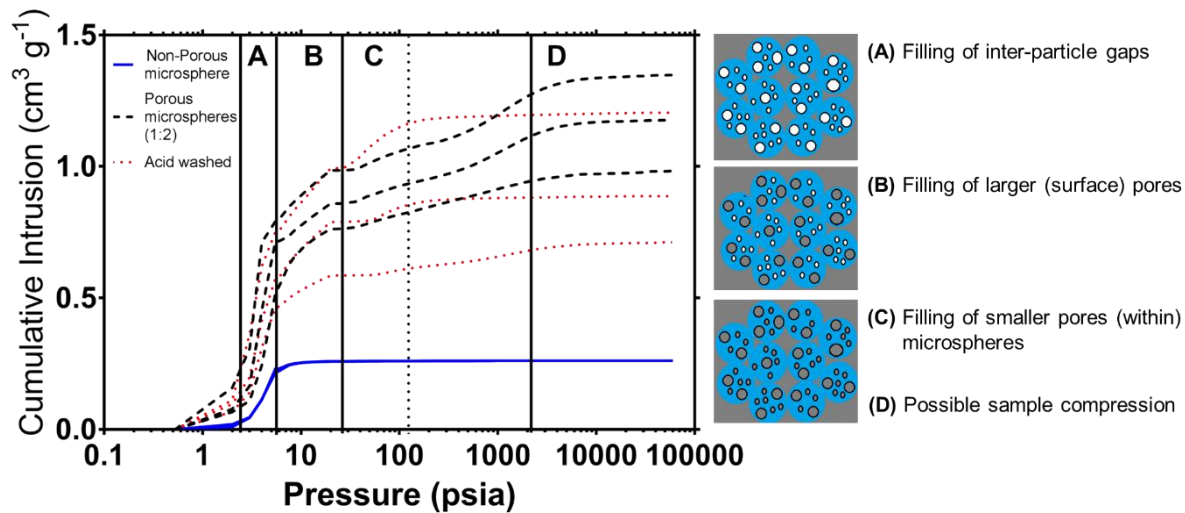


Figure 6.27: Displaying the cumulative intrusion of non-porous, porous and acid washed microspheres as obtained from mercury porosimetry, and their possible corresponding inflection points.

Figure 6.28 showed the pore diameters of the measured samples against the log differential pore volume. The non-porous microspheres displayed a bimodal distribution where each sample followed a closely related pattern. This narrow distribution complimented the particle size analysis and suggested that the interparticulate gaps have a modal size of *c.a.* 34 μm for the first peak and 24 μm for the second prominent peak. All three pore diameter distributions for the porous microspheres also displayed similar bimodal size distributions with the first prominent peak showing a modal value of *c.a.* 45 μm and the second peak at *c.a.* 24 μm . A trimodal behaviour was observed with the acid washed microspheres with the first two prominent peaks displaying a modal pore diameter of *c.a.* 45 μm and *c.a.* 24 μm . The modal pore diameter for the third smaller peak appeared at *c.a.* 3 μm and may have been related to fragments which resulted from sample compression. The pore diameters displayed in figure 6.28 suggest the presence of porosity *c.a.* 100nm and below, in the range of 10nm.

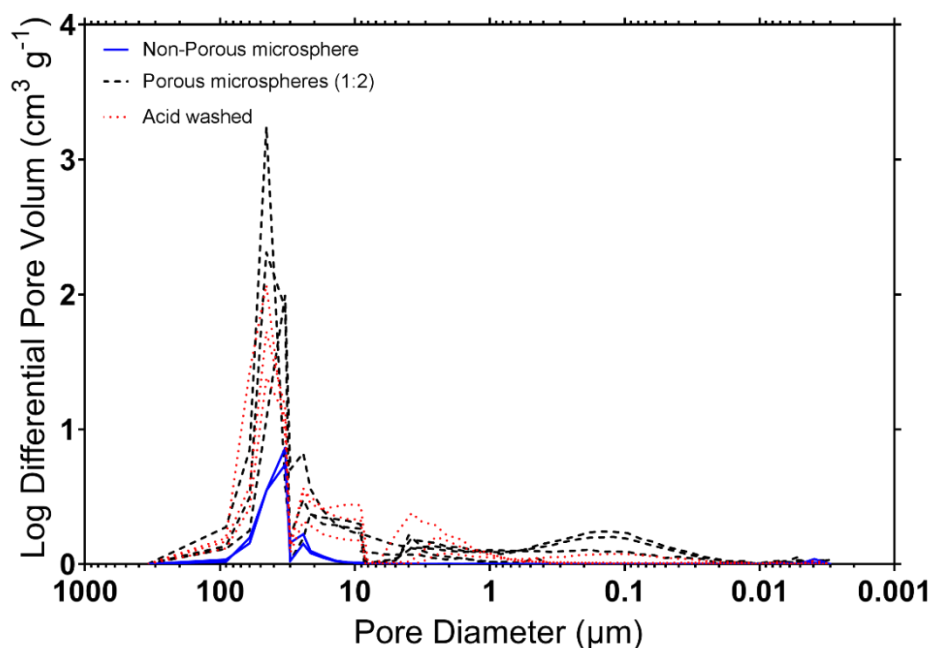


Figure 6.28: Pore diameter against Log differential pore volume of non-porous, porous and acid washed microspheres.

The porosity values of the porous and acid washed microspheres were given as $71\% \pm 2$ and $68\% \pm 4$ respectively.

6.5.6 Micro CT analysis

Figure 6.29 shows 2D slices of a selected microsphere for 3D reconstruction. The 2D slices showed that several microspheres revealed 1-2 large internal pores which were not seen in the embedded and polished microspheres for SEM. These large internal pores are displayed in the 3D reconstruction shown in Figure 6.30 (a) and (b), where the complete microsphere and a cross section are shown respectively. The inner pore dimension was $92 \mu\text{m}$ with smaller interconnected pores of size c.a. $14 \mu\text{m}$ as shown in Figure 6.31 (a) and (b) respectively. The pore strut also varied in size as shown in Figure 6.31 (c) with a randomly measured size of $6.37 \mu\text{m}$.

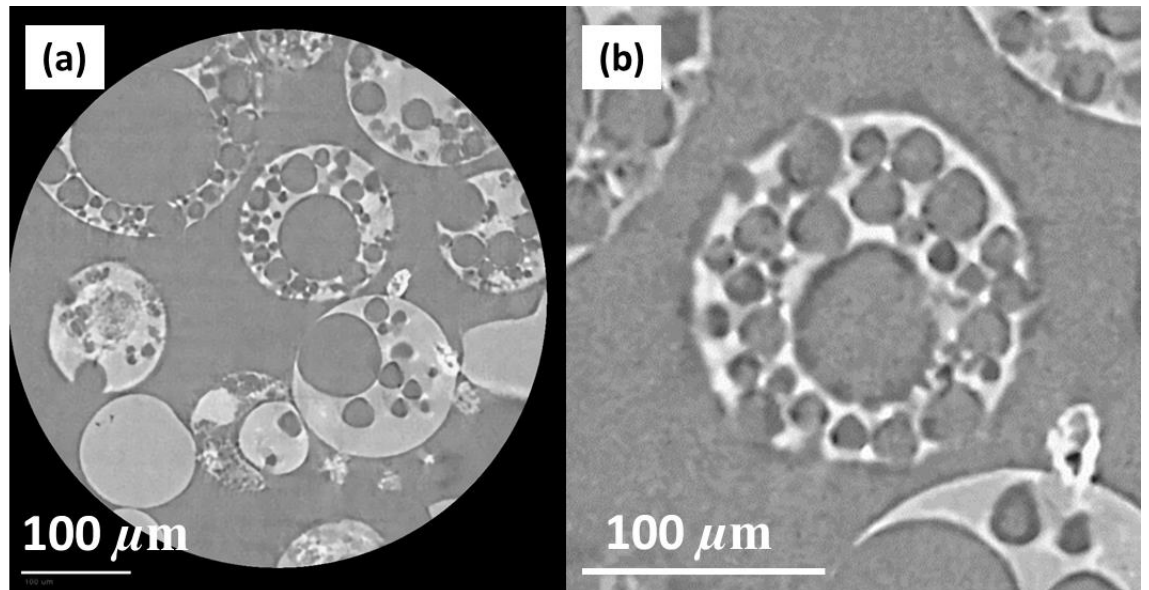


Figure 6.29: (a) grayscale image of 2D slice of high resolution imaged microspheres, (b) single selected full microsphere for analysis.

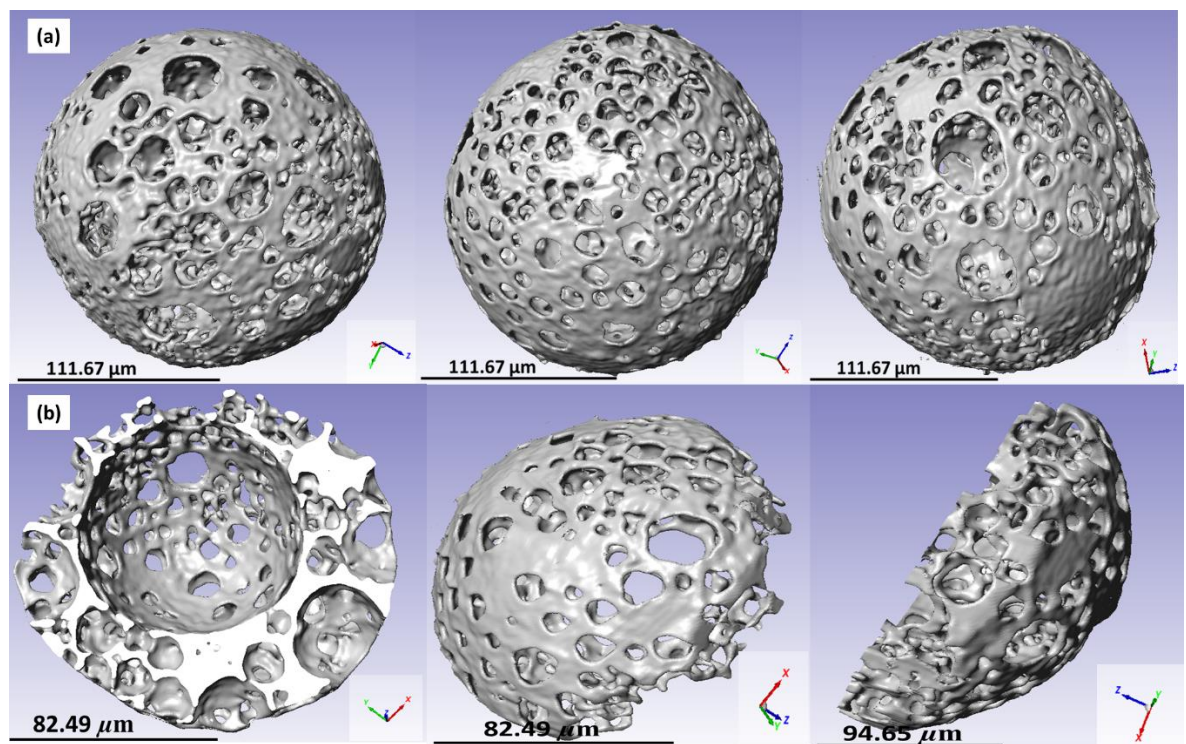


Figure 6.30: 3D construction (a) of porous microsphere, and (b) cross section of porous microsphere.

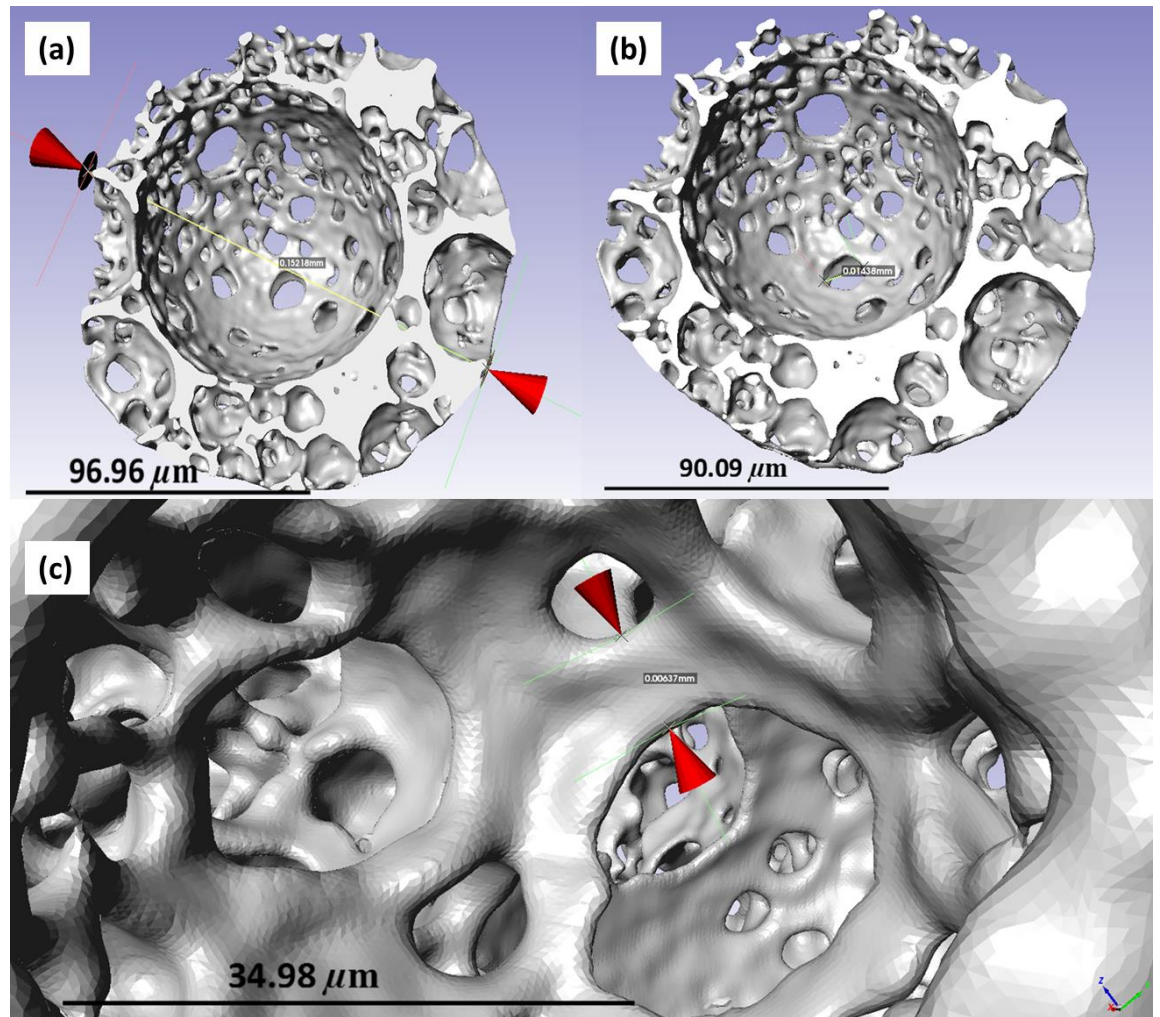


Figure 6.31: 3D reconstruction of porous microsphere showing (a) dimension of large inner pore, (b) dimension of an interconnected pore, and (c) pore strut size.

From the 3D reconstruction of the microsphere it was possible to obtain a porosity value by dividing the bulk volume of the material by the total volume. This resulted in a porosity value of 64%, which was less than that obtained via mercury porosimetry which was *c.a.* 71%.

Such a discrepancy can be attributed to the fact that this porosity value was associated with a single, random porous microsphere, which is not representative of the entire sample groups. Mercury porosimetry also takes into account all the spheres within a sample batch as well as the interparticulate spaces, however, micro CT is capable of accounting for closed, non-connected porosity which mercury porosimetry is not. Such results provide further evidence of a random distribution in porosity and pore sizes for each individual microsphere.

The 3D reconstructions in Figures 6.30 and 6.31 also confirmed the interconnectivity of the pores. In order to investigate this further, a specific section within the microspheres was analysed. Figure 6.32 shows a specific area within the single microsphere which is not a representation of all the microspheres. However, this section showed a 3D representation of the pore connectivity. The 2D slices displayed the connectivity of pores, where the struts or pore windows could clearly be seen. A higher density of connections were observed for the smaller pores, whereas the two larger pores were connected via fewer, larger struts.

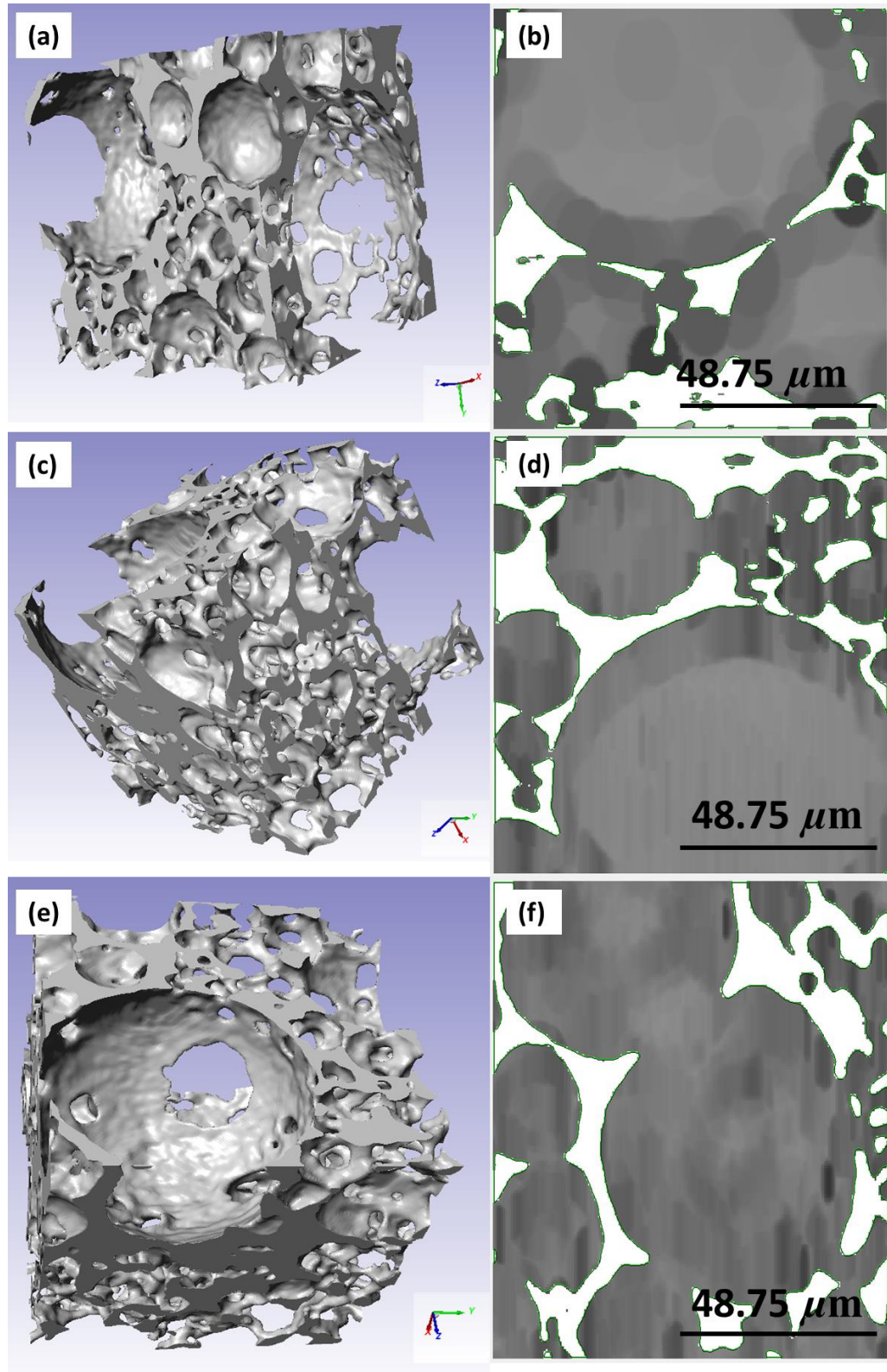


Figure 6.32: (a), (c) and (e) Micro CT images of a specific area within a single porous microsphere showing interconnectivity, (b), (d) and (f) 2D slices of the specific area showing interconnectivity of pores. Cubic constant element for (a), (c) and (e) $x=y = 0.0965$ mm, $z = 0.106$ mm.

The higher density of connections observed for the smaller pore sizes are displayed clearly in Figure 6.33 where several small connection points can be seen in the area of the smaller pores and larger connections are observed between the two larger pores.

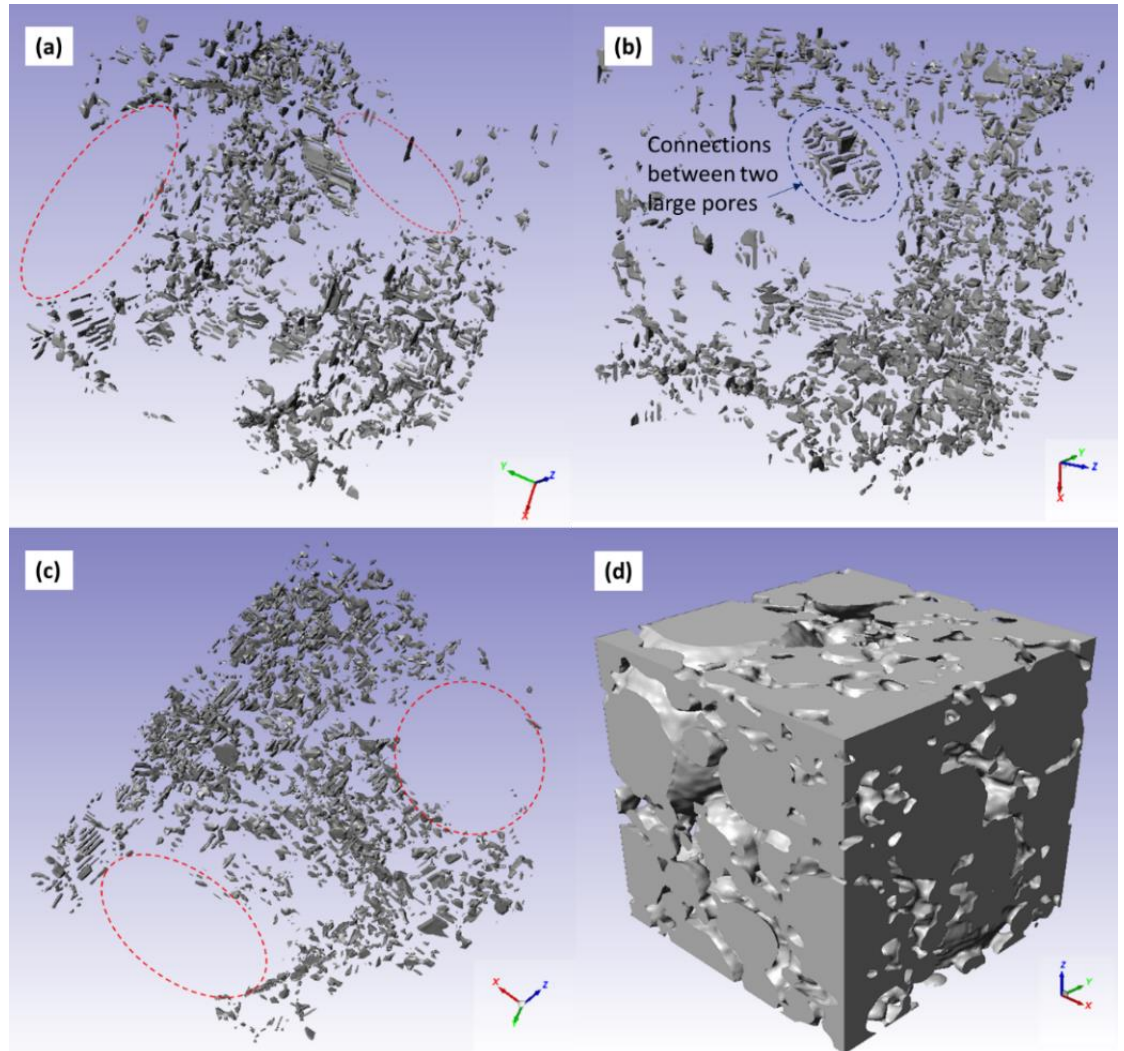


Figure 6.33: (a), (b) and (c) Micro CT images showing connection points between pores, the red dashed lines represent the space occupied by larger pores. (d) Inverse of Micro CT skeleton showing points of connectivity. Cubic constant element for (a), (b), (c) and (d), $x=y = 0.0965 \text{ mm}$, $z = 0.106 \text{ mm}$.

In order to observe the pore morphology within the specific area of the single microsphere examined, a watershed process was used in order to separate the pores from each other as shown in Figure 6.34.

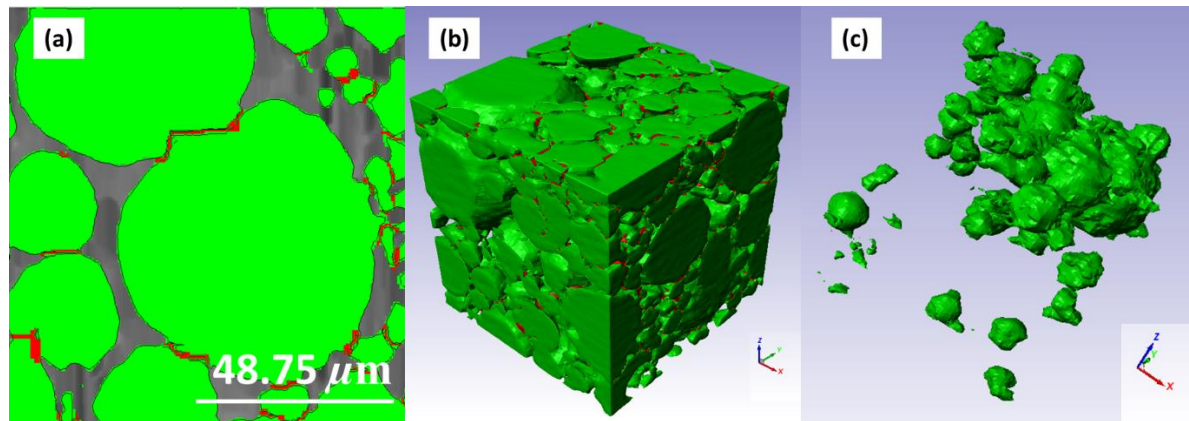


Figure 6.34: (a) 2D slice showing pore separation, where the red outlines show points of connection, (b) 3D reconstruction of pore separation, and (c) 3D reconstruction of separated pore morphology. Cubic constant element for (b) and (c), $x=y=0.0965$ mm, $z=0.106$ mm.

The 3D reconstruction of the pore morphology showed the pores to be spherical complementing that seen in the SEM images.

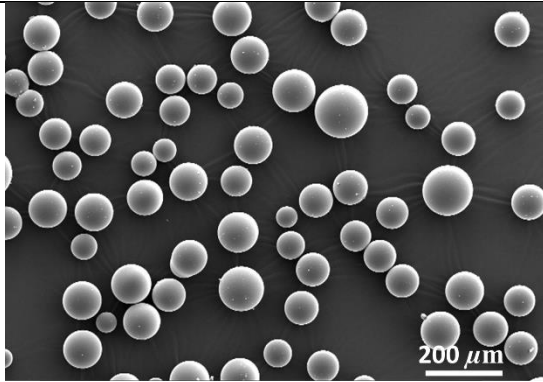
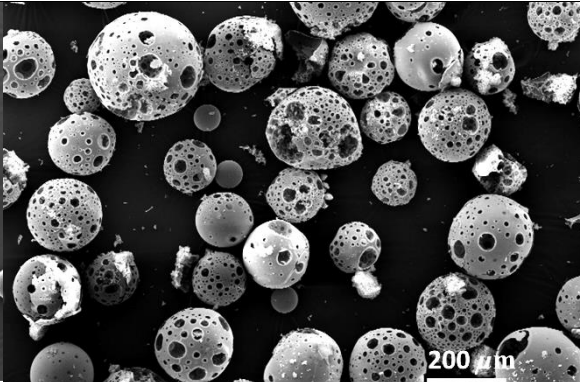
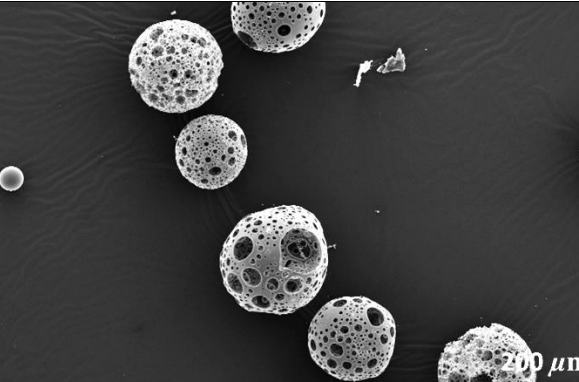
6.6 Degradation study of PBG microspheres

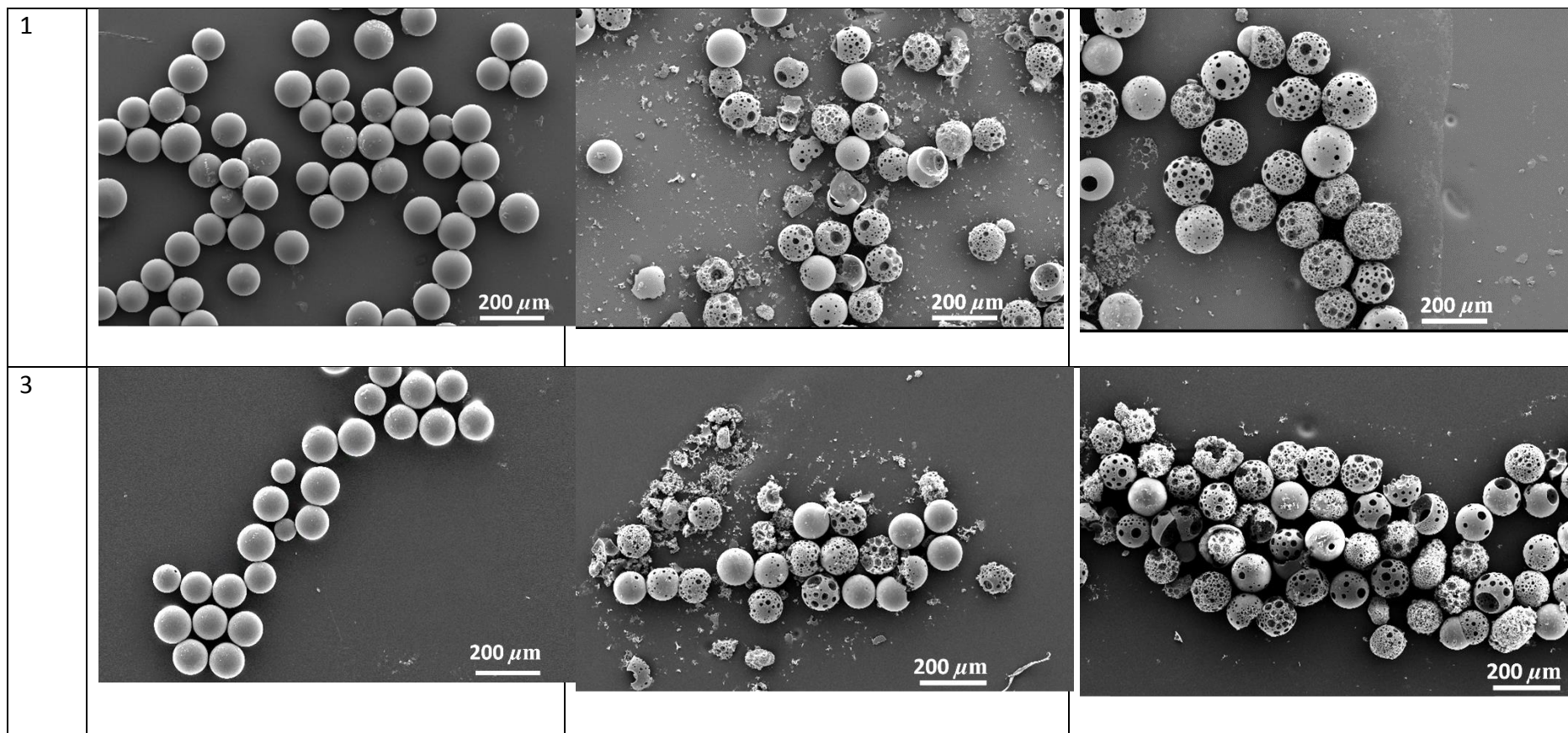
A degradation study in ultra-pure water on P40 non-porous and porous (pre and post acid washing) microspheres was conducted using a narrowed particle size range of 100-125 μm . Table 6.8 displays representative SEM images of the microspheres at each time point. Dissolution of phosphate based glasses generally follow three steps: i) acid/base catalysis where which the glass surface becomes saturated with acid H^+ or base OH^- ions linearly increasing in time until no more uptake is possible ii) hydration followed by iii) hydrolysis. The hydration process is initiated at the weakest bond between the NBO and metal ions (e.g. Na^+).^[242, 243] Although, F. Döhler *et al.*^[53] have previously shown phosphate networks to dissolve via P-O-P bond hydrolysis, and glasses consisting of phosphate chains to dissolve via hydration of entire chains however, hydrolysis did also occur. The formation of an additional layer was observed in some non-porous microspheres from as early as day 3 as shown at higher magnification in Figure 6.35. As time proceeded, this layer appeared to form a shell-like structure which eroded by peeling or pitting. Pitting of phosphate glass has previously been observed by Delahaye *et al.*^[244] and was attributed to polishing defects on the surface of the glass, however these samples were not polished. Past research on the degradation of PBG fibres with

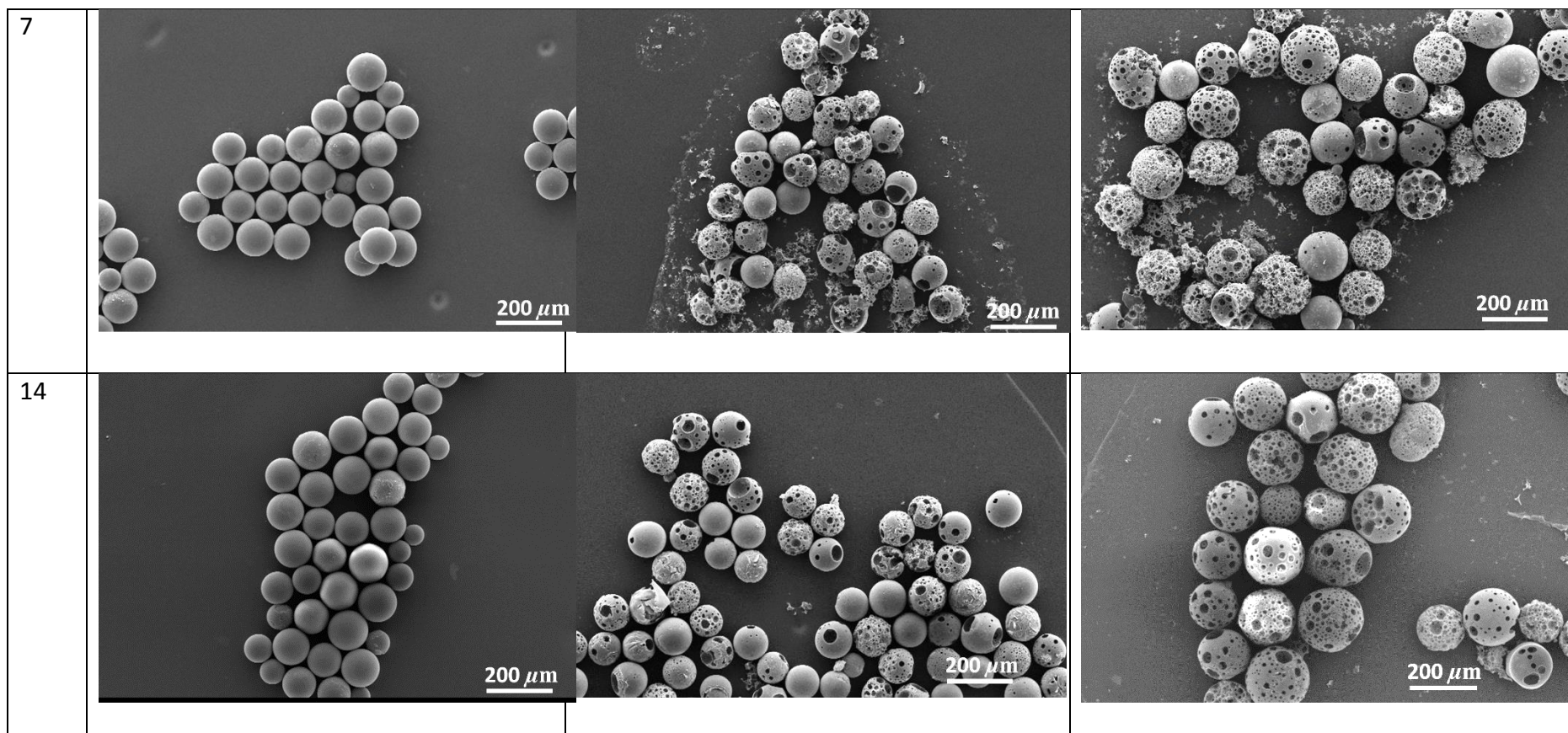
40 mol% P_2O_5 has also shown pitting corrosion during degradation,^[245, 246] which was suggested to occur simultaneously with the hydration mechanism as was also apparent in this study. The formation of these surface-reaction limited corrosion pits have been observed by Ma^[247] and their surface composition were found to be similar to those of the original glass as was seen in this study, indicated in Figure 6.36.

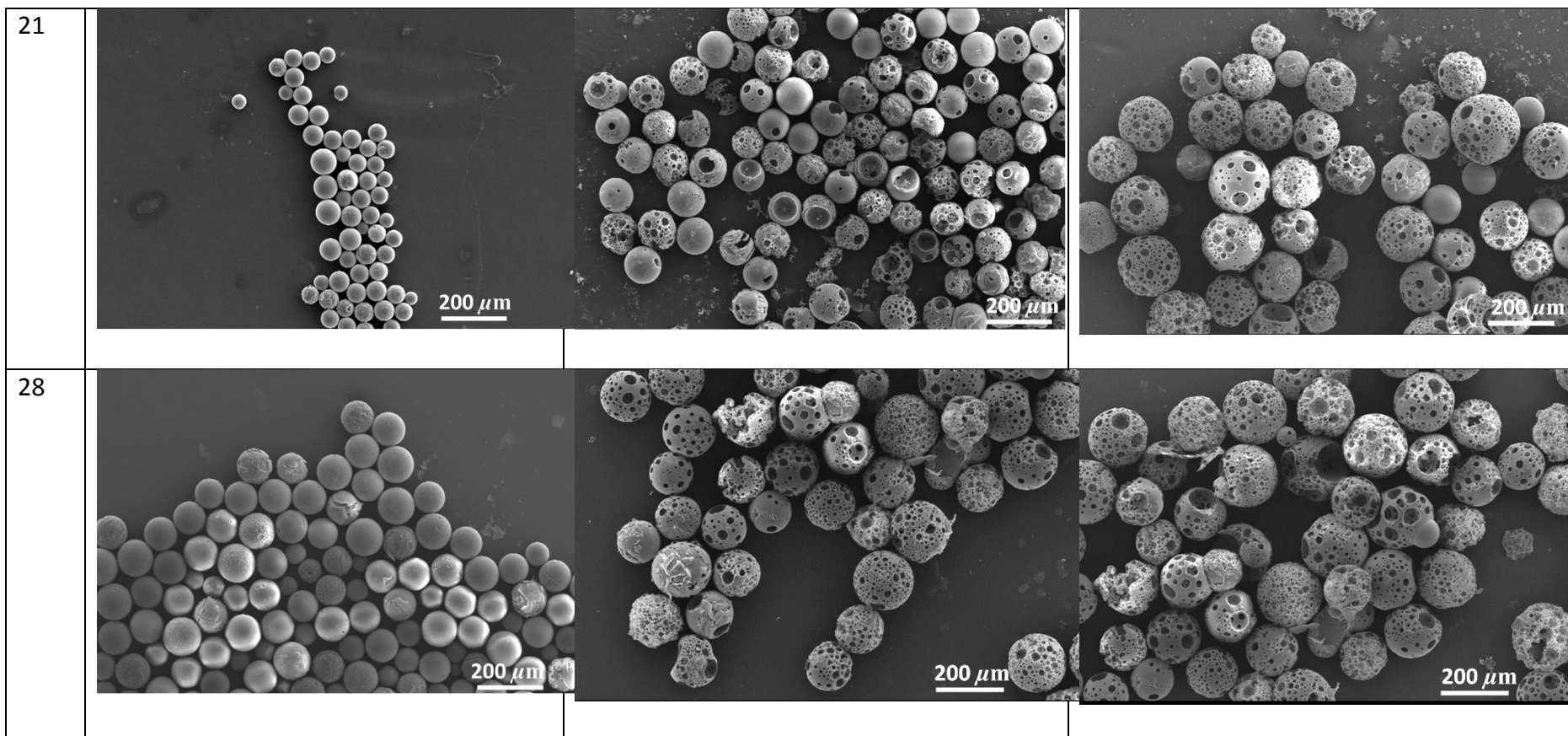
Some of the layers seen on the surface of these microspheres in Figure 6.35 were classed as hydration layers, since EDX analysis showed the composition of some of these layers to be the same as the bulk glass (Figure 6.36). The hydrated layer composition formed on phosphate glass is known to be the same as the bulk glass.^[244] The formation of precipitation was also suggested as a compositional difference in this layer compared to the bulk glass which was observed as shown in Figure 6.36 (b). The Ca/P ratio of the bulk glass was ~ 0.4 compared to that of the layer shown in spectrum 3 in Figure 6.36 (b), which had a Ca/P ratio of 0.66. Substitution of phosphate ions by hydrogen for phosphate (HPO_4^{2-}) has previously led to the formation of calcium deficient apatite. Calcium deficient apatite has been show to form via precipitation or hydrolysis methods.^[248, 249] It should be mentioned that a polished, flat cross section of the degraded microspheres would provide further insight of the formation of both a hydration and precipitation layer and their compositions.

Table 6.8: SEM images displaying representative samples of degraded non-porous, porous and acid washed microspheres at each time point after degrading in ultra-pure water.

Day	Non-porous microspheres	Porous microspheres	Porous Acid washed
0			







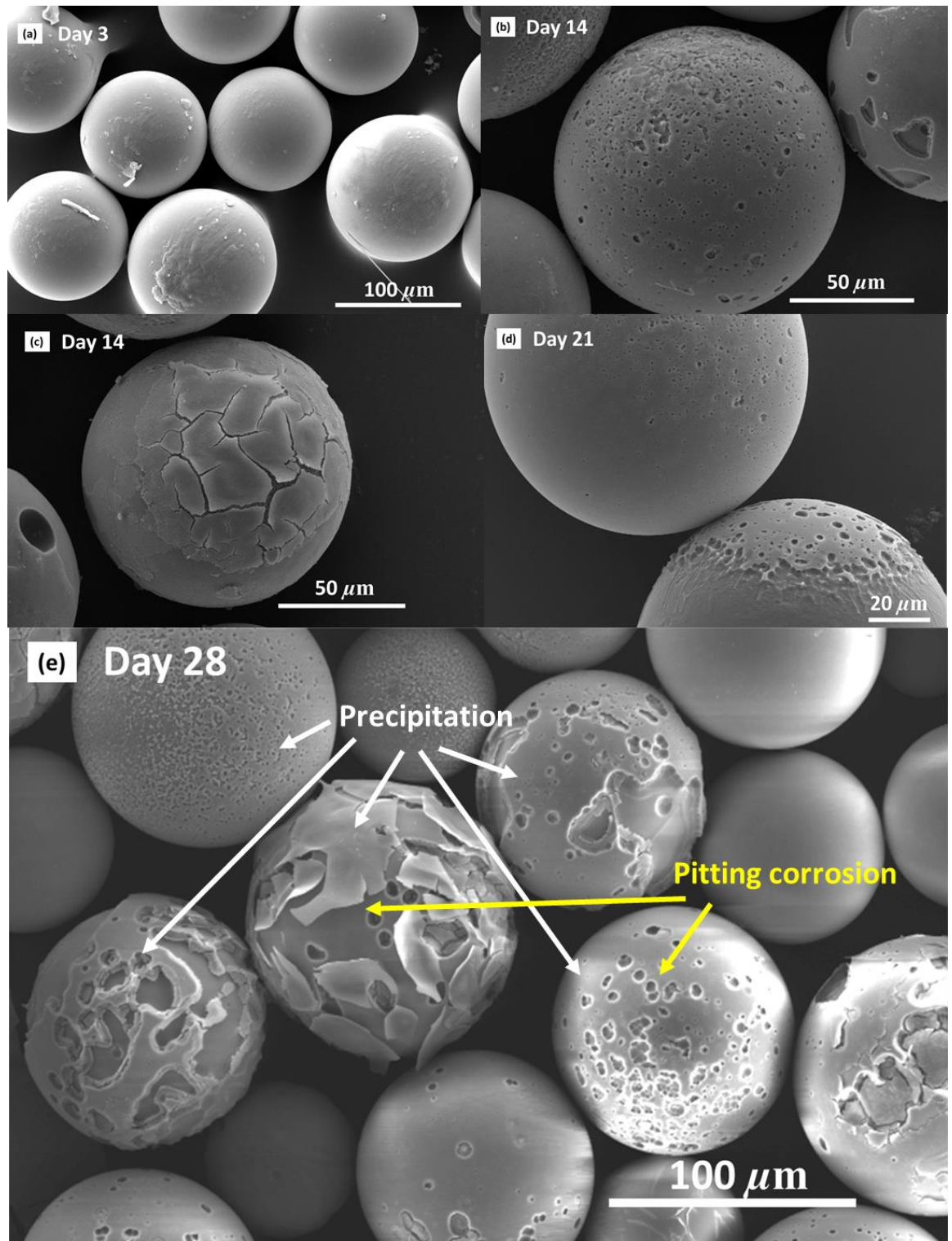


Figure 6.35: SEM images of degraded non-porous microspheres at various time points showing the formation of precipitation and pitting corrosion as indicated by the arrows.

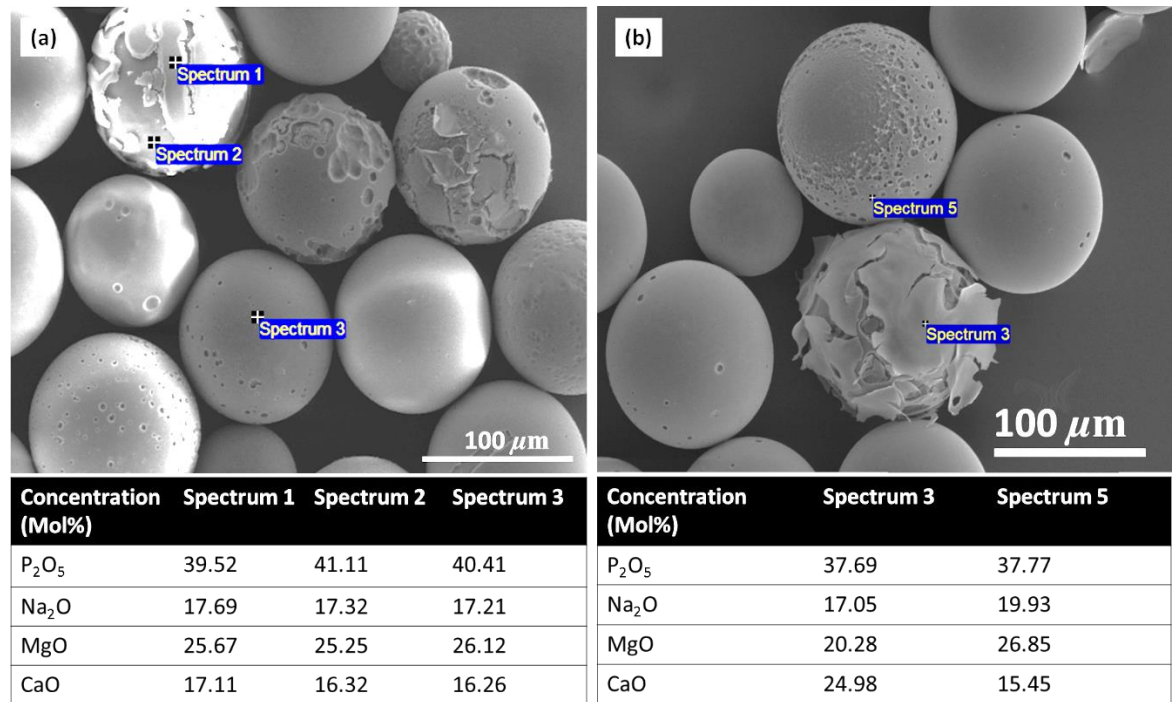


Figure 6.36: EDX analysis of degraded bulk microspheres at day 28 showing a possible hydration layer and the formation of precipitation.

Further evidence which suggested the formation of precipitation shells are shown in Figure 6.37. As mentioned earlier, the precipitation layer forms at early stages of degradation and appears to mask the real decrease in the diameter of the spheres, as shown by the modal diameter of the microspheres, which remained *c.a.* 110 μm. However, when looking at the histograms of the diameter shown in Figure 6.38, no real trend can be seen. This could be attributed to the formation of a precipitation layer as a result of the saturation of the dissolution media with the ions released as degradation by-products. The glass core uniformly shrinks and the reaction interface moves inwards towards the glass particle.^[247] This precipitation layer may form at different rates depending on the size of the microsphere and solution saturation levels. Furthermore, at each time point the media was changed which can disrupt the formation of this layer and begin to form a new layer at the surface between the glass microsphere and the previously formed precipitation layer, or even remove the first layer. The formation of the concentric precipitation layers is displayed in Figure 6.39, where a hollow core was observed.

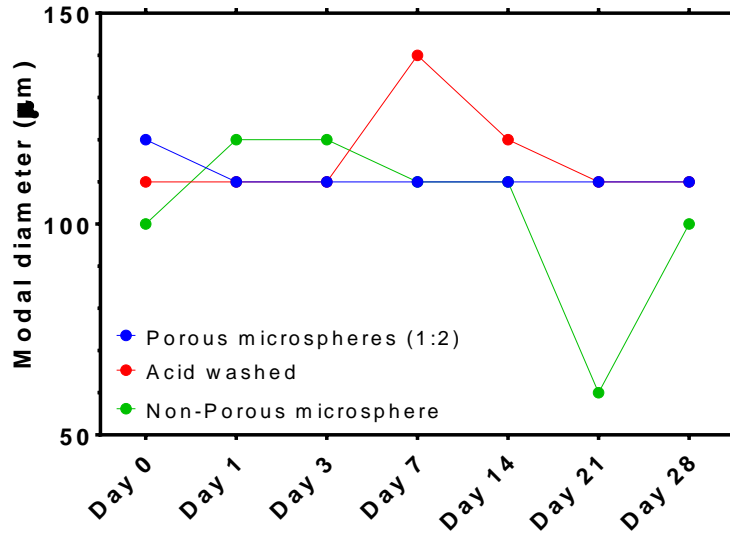


Figure 6.37: Modal diameter of degraded microspheres as measured via ImageJ

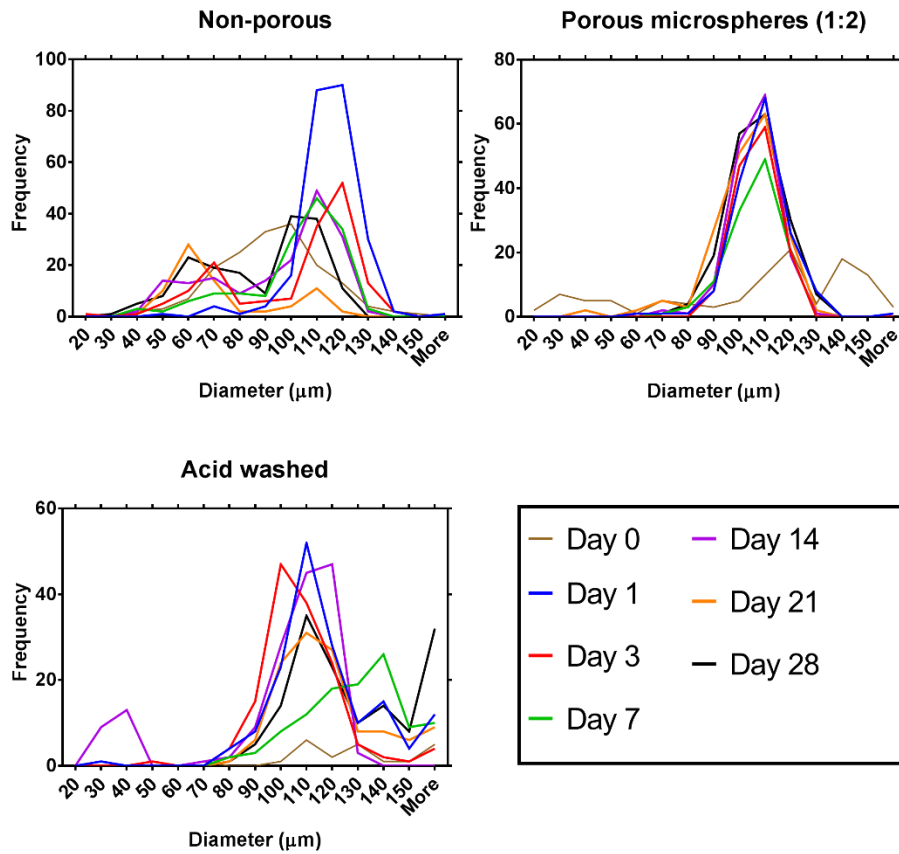


Figure 6.38: Histogram displaying diameters of degraded microspheres as measured by ImageJ.

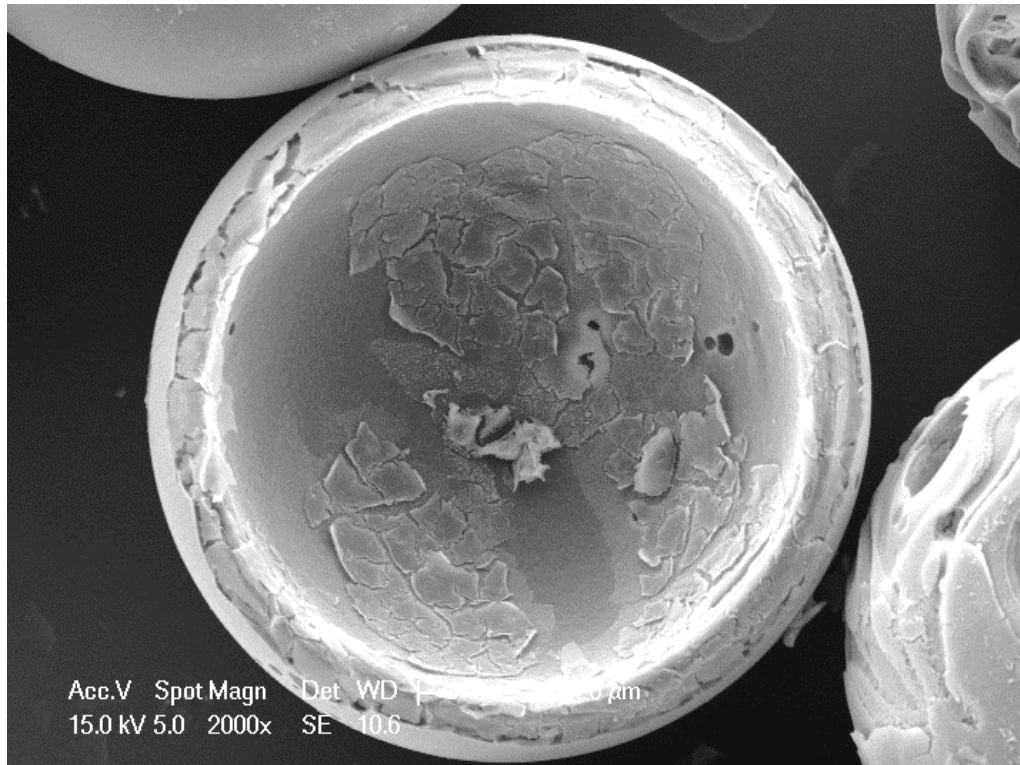


Figure 6.39: SEM image of microsphere at day 14 showing the possible formation of precipitation shells with several layers.

Previous studies on bioactive glasses such as 13-93 fibres have also shown the formation of a Ca-P layer when immersed in SBF from 1 week. Similarly, brittle layers of Ca-P were formed resulting in the formation of core structures.^[250] Other examples where Ca-P shell formation has been observed was by Radin *et al.*^[251] when examining bioactive glass (45S5) granules *in vivo*. This study found three layers were present on the bioactive glass granules after a week when immersed in serum free tris hydroxymethyl aminomethane-buffered solution supplemented with plasma electrolyte (TE); the inner core which was the unreacted bioglass, silica rich subsurface layer and the outer Ca-P rich layer. This outer Ca-P rich layer was shown to be covered in densely packed globular precipitate. Hollow Ca-P shell layers were also observed when the bioglass granules were immersed in a serum rich solution. This layer was formed of loosely packed (porous) precipitate which was attributed to the formation of a calcium deficient apatite layer as was suggested in this study. Complimentary observations were also made by Liu *et al.*^[252] where a calcium deficient carbonate apatite layer was observed when degrading a calcium phosphate

cement- bioactive glass composite in TE. Dissolution of the sample and formation of an amorphous Ca-P layer was thought to occur simultaneously as seen in this study. Figure 6.40 confirmed the precipitation formed on the non-porous microspheres at day 28, showing loosely packed precipitate formation and clear evidence of layer formation. Cracking of this delicate outer layer was thought to occur due to drying of the sample and sample preparation. Nevertheless, the cracks provide further evidence of surface layer formation and properties which differed from the parent glass, as these features were not seen on the starting material.

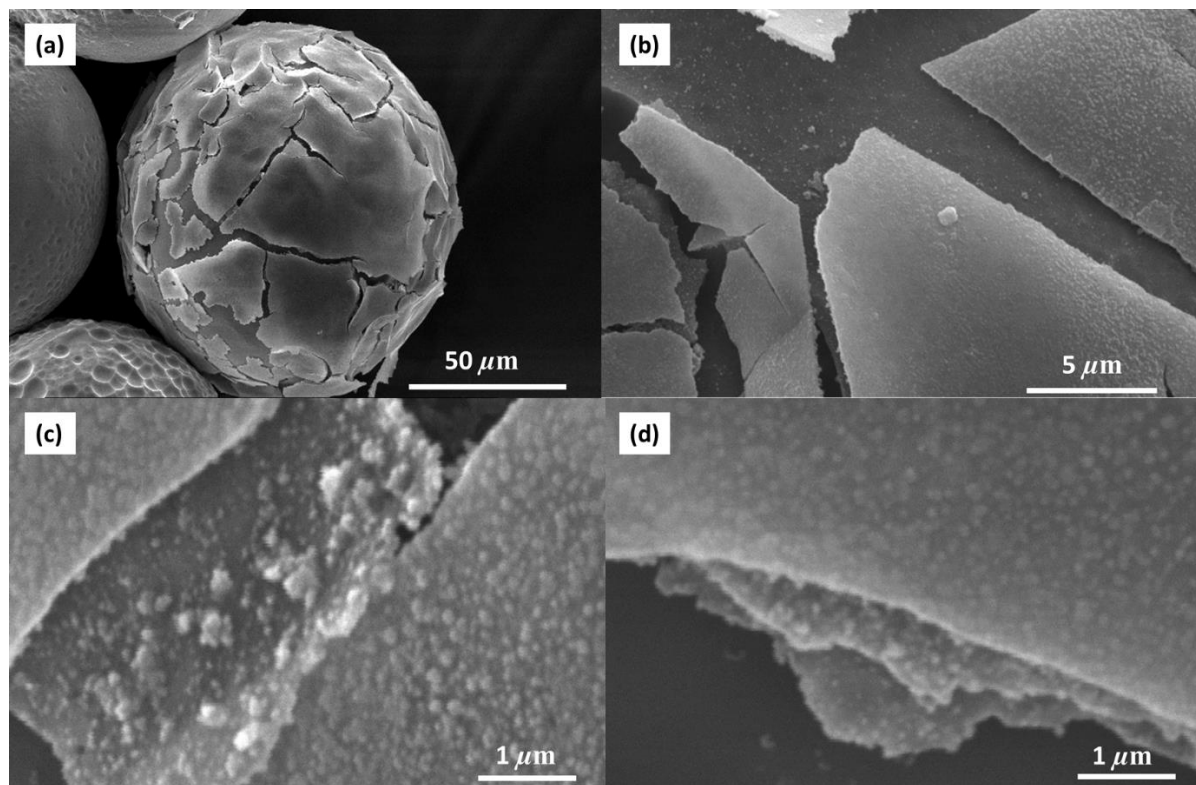


Figure 6.40: SEM images at day 28 after degradation showing (a) brittle precipitation layers formed on the outside of a P40 non-porous microsphere at low magnification (b) and (c) showing globular, loosely packed precipitation formation at high magnification, and (d) precipitation layer formation at high magnification

When considering the degradation mechanism for the porous microspheres (including acid washed), the dissolution media is not only limited to attacking the outer surface of the microspheres as is in the case of non-porous microspheres, but is also able to penetrate the internal structure of the porous microsphere. The internal structure has greater surface area compared to the outer surface which can be attacked by water, thus resulting in a faster

reduction in pore strut sizes and internal collapse in relation to the outer surface as shown in Figure 6.41. This can explain the constant value observed for the modal diameter of the porous microspheres.

Furthermore, dissolution of the internal structure resulted in a more fragile microsphere which can easily be damaged at each time when replenishing the dissolution media. Additionally, Figure 6.41 also showed evidence of a hydration/ precipitation layer formation as was observed for the non-porous microspheres.

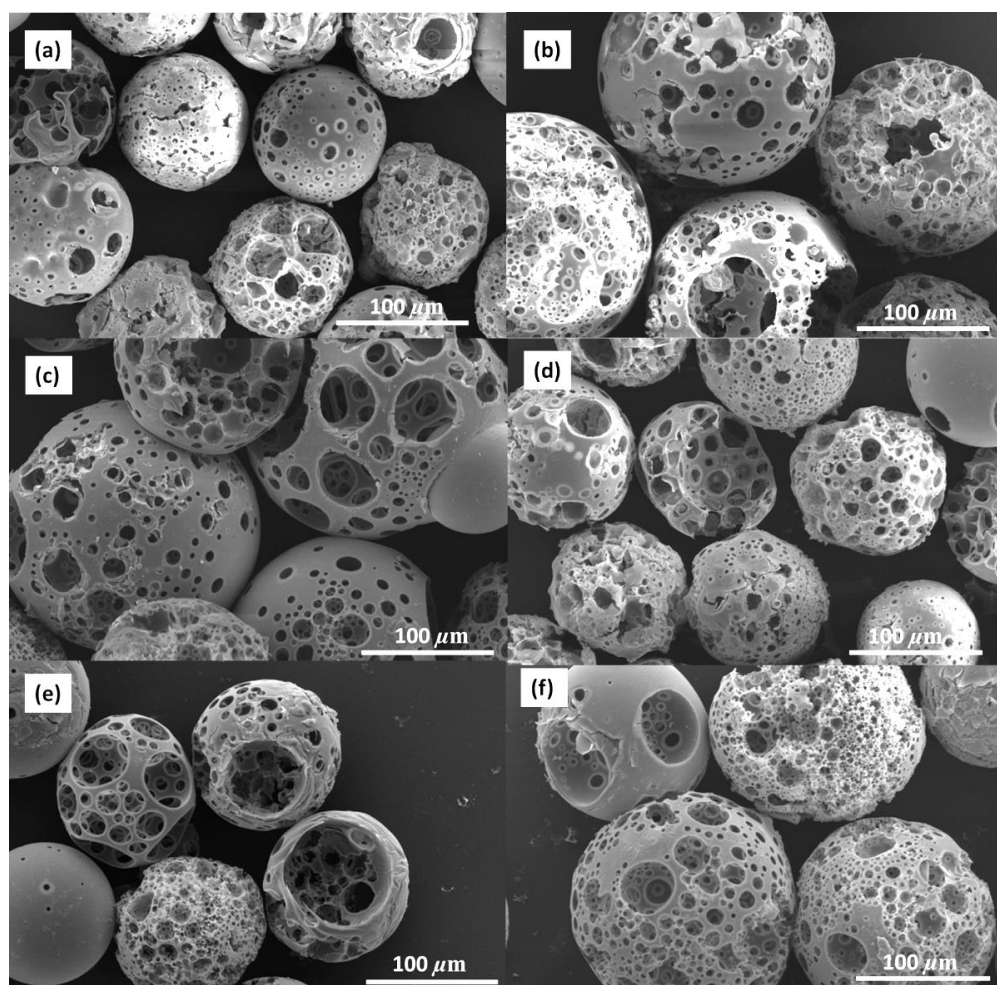


Figure 6.41: SEM images of degraded (a), (b), (c), and (d) porous microspheres at day 28, and (e) and (f) porous acid washed microspheres at day 14 and 21 respectively.

The ion release profiles displayed in Figure 6.42 all show linear trends with increasing ion release over time. The release rate of Na^+ for all three microsphere types was greater than of Mg^{2+} and Ca^{2+} by 1.5 ± 1 ppm/day. For all cations the release rate from the acid washed microspheres was over 1

ppm/day greater than for the non-porous and porous microspheres. For both the Na^+ and Mg^{2+} ion release profiles, the acid washed microspheres appeared to release the highest concentration of ions followed by the porous and non-porous microspheres. However, for the Ca^{2+} ion release profiles, the porous microspheres appeared to release a higher concentration of ions compared to the acid washed microspheres. This was attributed to the contribution from the residual porogen which was also apparent in the pH readings shown in Figure 6.43.

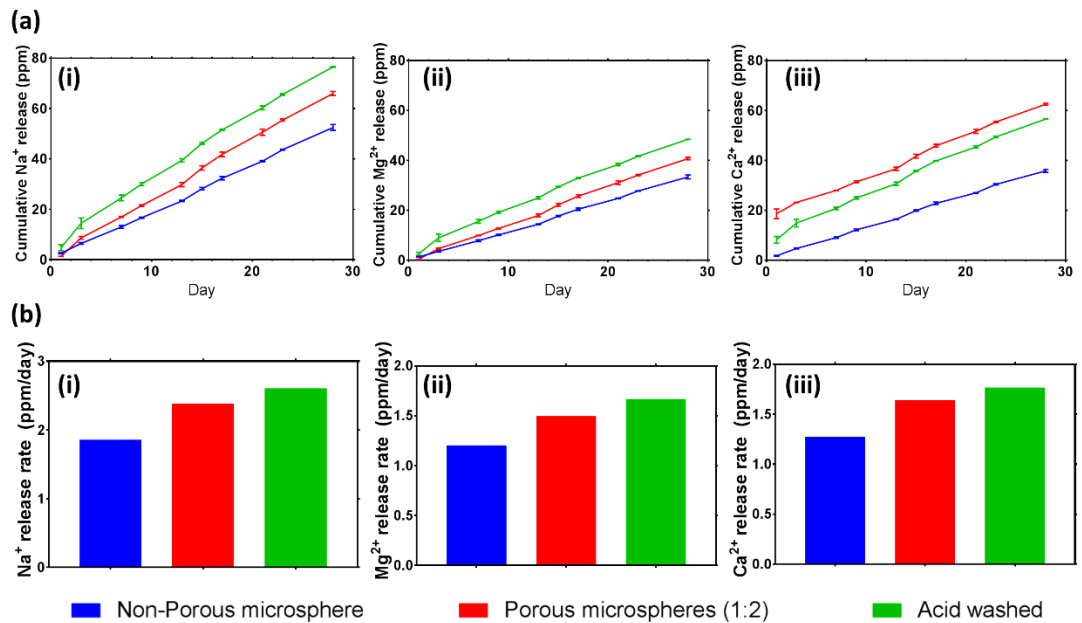


Figure 6.42: (a) Cumulative cation release profiles and (b) release rate profiles for non-porous, porous and acid washed microspheres degraded in ultra-pure water.

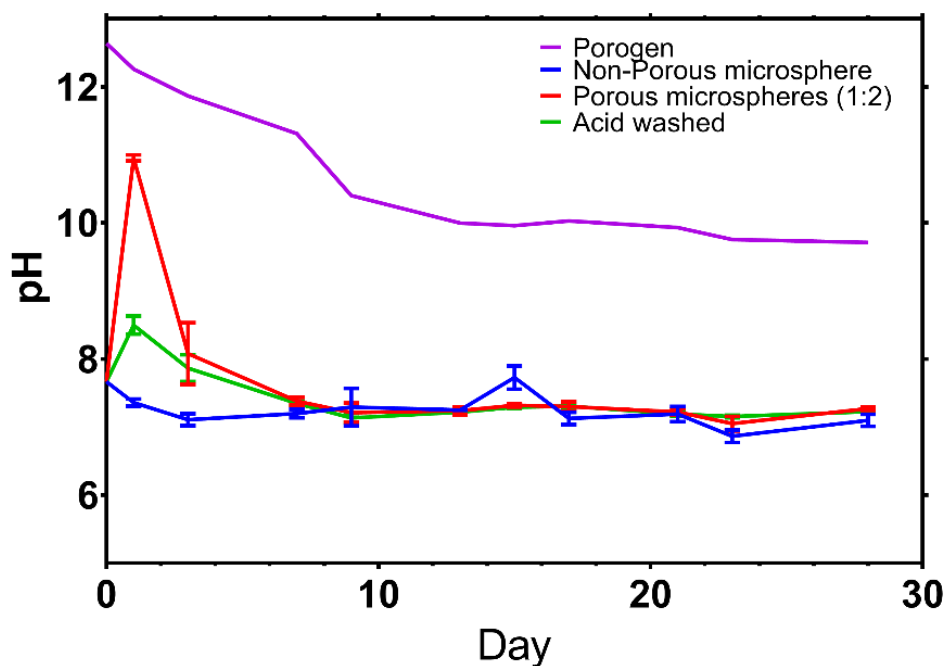


Figure 6.43: pH of porogen, non-porous, porous and acid washed microspheres during degradation study in ultra-pure water.

Figure 6.40 shows a large increase in pH for the porous microspheres at early time points, which later stabilised towards a neutral pH. Similarly, the acid washed microspheres also had a slight increase in pH at earlier time points, both of which were attributed to the presence of residual porogen.

6.7 Summary

This chapter has outlined for the first time a novel manufacturing technique for the production of highly porous, resorbable microspheres. The optimum glass microparticle to porogen ratio was found to be 1:2 resulting in a high yield of porous microspheres, each with a high level of porosity. This single stage manufacturing process enables porosity values of *c.a.* 71% to be achieved, resulting in interconnected, spherical pore morphologies as observed via Micro CT and SEM image analysis. This study has shown that interconnectivity can be enhanced via a post processing method which involves submersion of the microspheres in 0.5M acetic acid for 120 seconds.

This study has found that the level of porosity can be somewhat controlled by; i) altering the size of the porogen, ii) altering the amount of porogen mixed pre-spheroidisation, iii) altering the type of porogen used e.g. SrCO_3 instead of

CaCO₃, iv) and by subjecting the microspheres to a post processing method i.e. acid washing.

Degradation of the non-porous microspheres have revealed the formation of hollow, shell-like precipitation layers as opposed to the previously believed “peeling effect” of the outer hydrated layer as seen with PBG fibres.^[42, 253, 254] This degradation mechanism suggests porous microspheres to maintain their spherical morphology during degradation if they are not subjected to mechanical forces.

These novel, porous inorganic microspheres hold the potential to be used in a vast number of applications both inside and out of the biomedical field.

CHAPTER 7: CONCLUSIONS AND FUTURE DIRECTIONS

7.1 Conclusions

The purpose of this work was to manufacture and characterise novel PBG compositions which could release therapeutic ions as degradation by products for use in orthopaedic applications. In doing so, two new glass systems were developed:

- (i) $40\text{P}_2\text{O}_5 \cdot (16-x)\text{CaO} \cdot 20\text{Na}_2\text{O} \cdot 24\text{MgO} \cdot x\text{SrO}$, where x is 0, 4, 8, 12 and 16 mol%
- (ii) $(40-x)\text{P}_2\text{O}_5 \cdot 16\text{CaO} \cdot 20\text{Na}_2\text{O} \cdot 24\text{MgO} \cdot x\text{TiO}_2$, where $x = 3, 5, 7, 10$ and 12

Physico-chemical characterisation of the glasses in the first system (i) was carried out via XRD, EDX, DSC, helium pycnometry, dissolution studies in PBS, ultra-pure and deionised water and cation and anion release was also evaluated. In addition, cytocompatibility studies were conducted using the MG63 cell line via a direct contact method, and an osteoclast feasibility study was conducted using human peripheral blood monocytes. Structural characterisation of this glass system was carried out via FTIR, ^{31}P and ^{23}Na MAS NMR, and neutron diffraction. This study also provided comprehensive analysis on the properties and structure of $40\text{P}_2\text{O}_5 \cdot (16-x)\text{CaO} \cdot 20\text{Na}_2\text{O} \cdot 24\text{MgO} \cdot x\text{SrO}$, where x is 0, 4, 8, 12 and 16 mol% glass via neutron diffraction.

Thermal analysis showed substitution of Sr for Ca had little effect on T_g . An increase in T_{onset} , T_c , and thermal processing window was observed with initial substitution of Sr for Ca, followed by a gradual decrease with increasing substitution. This initial increase was attributed to an increase in cross-linking with the addition of a fifth cation to the glass network, whilst further addition resulted in a decrease in temperatures due to the smaller field strength of Sr^{2+} compared to Ca^{2+} .

This study also found that substituting Sr for Ca did not alter the structure of the glass as evidenced from the consistent results in the FTIR and NMR (^{31}P and ^{23}Na) spectra. The ^{31}P MAS NMR spectra showed an equal number of PO_4 tetrahedra present as Q^1 and Q^2 species, suggesting that all the modifier cations in the glass (Ca, Sr, Mg and Na) played the role of network modifiers and not network formers.

Neutron diffraction studies were performed on relevant binary metaphosphate glasses (CaP_2O_6 , SrP_2O_6 , MgP_2O_6 and NaPO_3) to aid in the interpretation of the $40\text{P}_2\text{O}_5 \cdot (16-x)\text{CaO} \cdot 20\text{Na}_2\text{O} \cdot 24\text{MgO} \cdot x\text{SrO}$, where x was 0, 4, 8, 12 and 16 mol% (i.e. multicomponent). The M-O coordination (M= Mg, Ca, Sr and Na) in the binary metaphosphate compositions showed a broad asymmetric distribution of bond lengths, with coordination numbers which were smaller than those in the corresponding crystals. The Ca-O and Sr-O coordination numbers were determined as 5.01(9) and 5.10(6) respectively, and it was suggested that most likely the Sr-O distribution included an additional contribution at longer distance. However, this was beyond the range that was able to be probed. The neutron correlation functions for the multicomponent glasses were consistent with a structural model in which the coordination of Ca, Sr and Na were the same as in the binary metaphosphate glasses. The Mg-O bonds on the other hand showed a shift to longer distance than for the binary metaphosphate glass.

The glasses with five components revealed a lower dissolution rate than the four-component glasses, and this was attributed to the increased cross-linking and packing density arising from the addition of SrO, or to the increased structural frustration associated with the larger number of components. The results suggested that phosphate glasses with compositions close to invert formulations (i.e. fixed with 40 mol% P₂O₅) provided a means of releasing controlled quantities of Sr²⁺ ions without significantly hindering the degradation rate.

The substitution of Sr for Ca showed no toxic effects when cultured with MG63 cells. The higher Sr containing compositions (Sr12 and Sr16) showed the greatest cell viability at later time points compared to the other compositions. Direct seeding of human peripheral blood monocytes on to glass discs was achieved in the osteoclast feasibility study and primary results suggested a dose dependent effect of Sr on osteoclastogenesis, however further validation is required.

A second series of invert glasses in the system (40-x)P₂O₅·16CaO·20Na₂O·24MgO·xTiO₂, where x = 3, 5, 7, 10 and 12 were investigated with an aim of developing high pyrophosphate containing units. In order to analyse the physico-chemical properties of this glass series EDX, XRD, helium pycnometry, DSC, ³¹P MAS NMR, dissolution studies in ultra-pure water and anion and cation release were conducted.

As shown in the literature review, the lowest P_2O_5 content reported without traces of crystallinity has been 30mol%. This study successfully manufactured a fully amorphous glass with a phosphate content as low as 28 mol%. All glass compositions were found to be invert i.e. consisting of short ortho- or pyrophosphate units. ^{31}P MAS NMR results suggested Ti behaved as a network former at lower concentrations of 3 mol%. However, addition of 5 mol% TiO_2 and above, suggested that Ti behaved as network modifiers. Thermal analysis showed an increase in T_g with increasing TiO_2 concentration which was attributed to increased cross linking and charge to size ratio of Ti ions.

Dissolution and ion release studies were conducted on the P33Ti7 and P30Ti10 glass compositions since the ^{31}P MAS NMR studies showed these formulations had the highest pyrophosphate units. Dissolution rates of both compositions were drastically reduced compared to the Ti free glass composition (P40) which was reflected in the low ion release concentrations detected. None the less P33Ti7 was observed to release pyrophosphate units as degradation by products.

This project also aimed to manufacture both non-porous and porous microspheres from PBGs in order to provide added advantages of the spherical morphology such as better flow properties compared to irregular shaped particles and more efficient packing into defects, as well as enabling the incorporation of biologics such as stem cells into the highly porous structures. The high porosity would also provide potential for enhanced diffusion of nutrients and waste products throughout the entire construct.

This project successfully developed a novel manufacturing process to create both non-porous and highly porous microspheres with fully interconnected porosity from PBGs between the size ranges of 63-125 μm . The manufacturing process used a porogen at a specific ratio which resulted in porosity values of *c.a.* 71%. An additional stage of washing the porous microspheres in 0.5M acetic acid for 160 seconds resulted in improvement of interconnectivity and removal of residual porogen as evidenced by the density, XRD and EDX results. Degradation studies of the non-porous and porous microspheres in ultra-pure water suggested the formation of a precipitation shell in static degradation conditions as evident by SEM images of the non-porous microspheres. SEM images of the degraded microspheres up to 28 days also showed that the majority of the microspheres retained their spherical shape during degradation.

This study is the first to show the manufacture of highly porous PBG microspheres with interconnected porosity. These have the potential to be used in several applications both inside and outside the biomedical field. For example, delivery of drugs and biologics directly to the site of interest, the high surface areas could be utilised in improving sensitivity of point of care testing devices, furthermore the high porosity and packing efficiency could be utilised in water treatment and filtration. Furthermore, the resorbable properties and spherical morphology could also be taken advantage of in veterinary applications, for example for the treatment of ion deficiencies in cattle and livestock which could replace the need of treatment via large boluses.

7.2 Future work

Based on the developments of this work, the following suggestions have been made for future studies:

- Conduct in depth investigation on the effect of varying Sr concentrations on osteoclast behaviour and determine an optimum composition.
- Optimise the invert glass series by removing TiO_2 and increasing the CaO or Na_2O content, in order to increase the dissolution rate and release of therapeutic pyrophosphate units. Alternatively, remove TiO_2 and replace with several additional modifying cations in order to develop the glass with the aim of preventing the onset of crystallisation.
- Spheroidise and characterise porous microspheres in the Sr series and Ti series range. Initial feasibility trials were carried out by Dr Zakir Hossain using the composition Sr8, and the following Ti glass compositions; $40\text{P}_2\text{O}_5 \cdot 16\text{CaO} \cdot 17.5\text{Na}_2\text{O} \cdot 24\text{MgO} \cdot 2.5\text{TiO}_2$, and $40\text{P}_2\text{O}_5 \cdot 38\text{CaO} \cdot 19\text{Na}_2\text{O} \cdot 2\text{MgO} \cdot 1\text{TiO}_2$, showing successful manufacture of porous microspheres (63-125 μm) as shown in Figure 7.1.

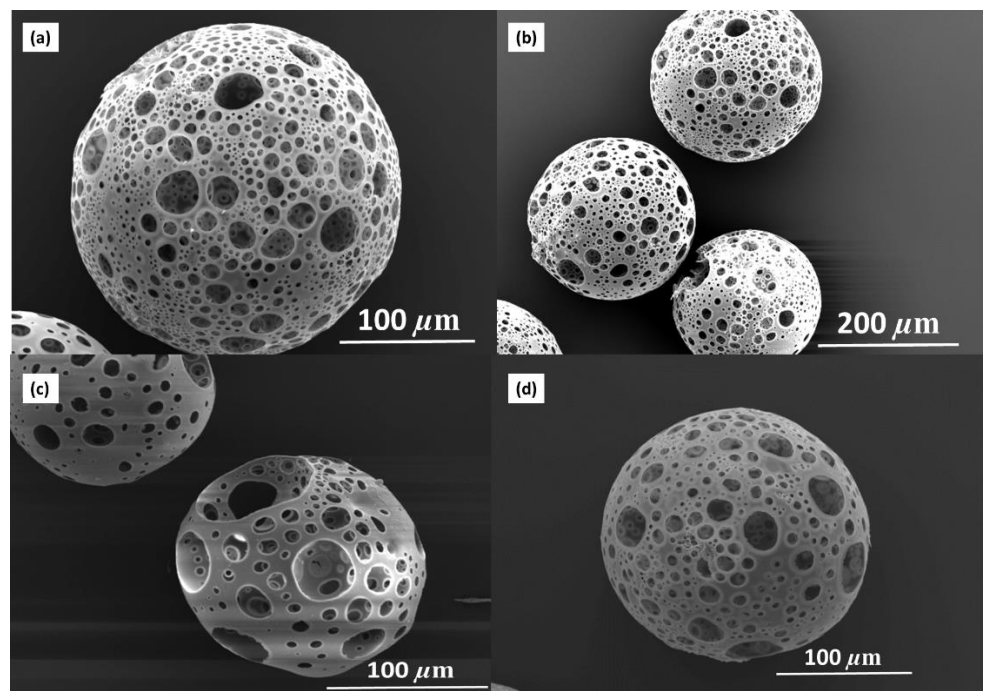
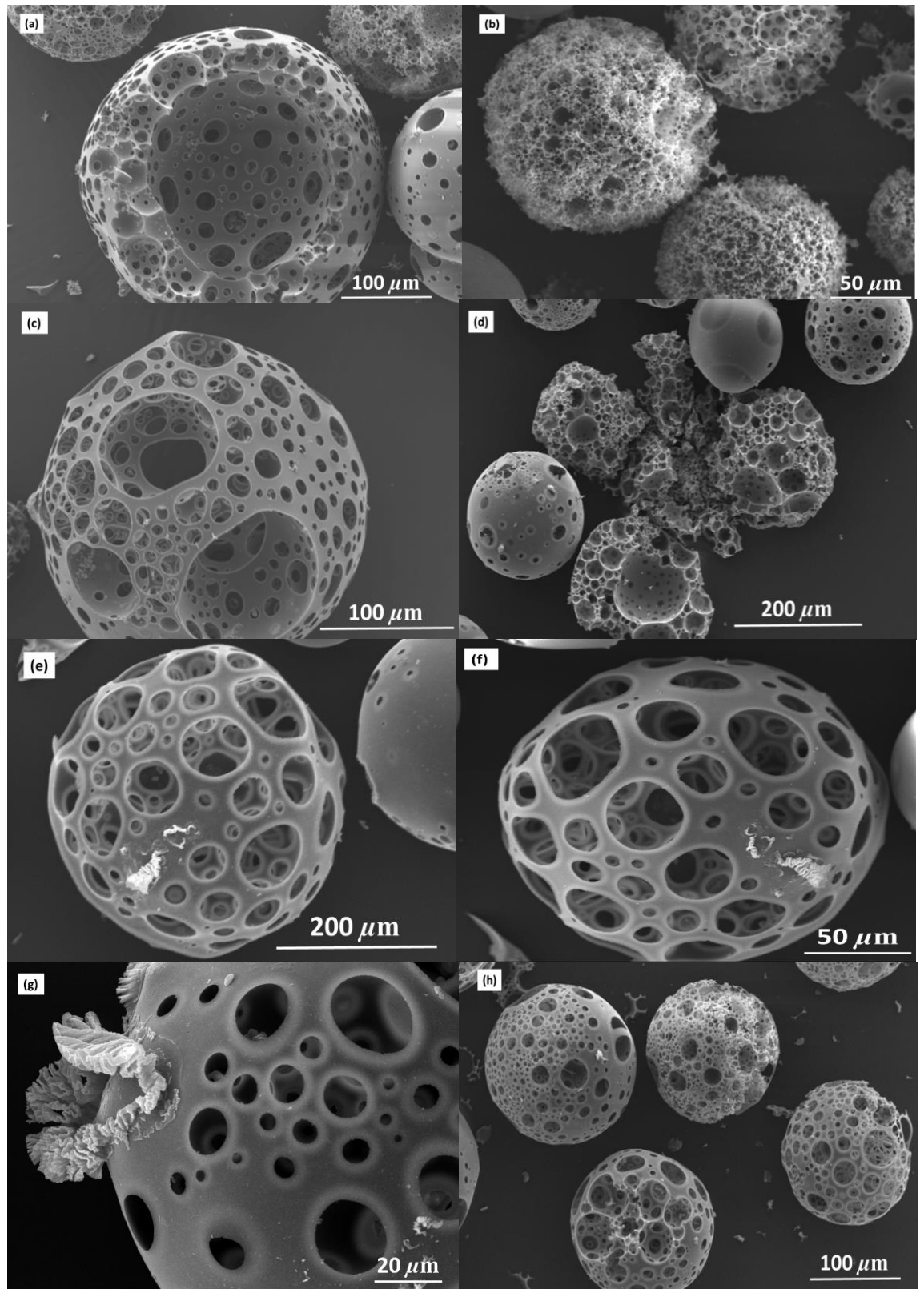


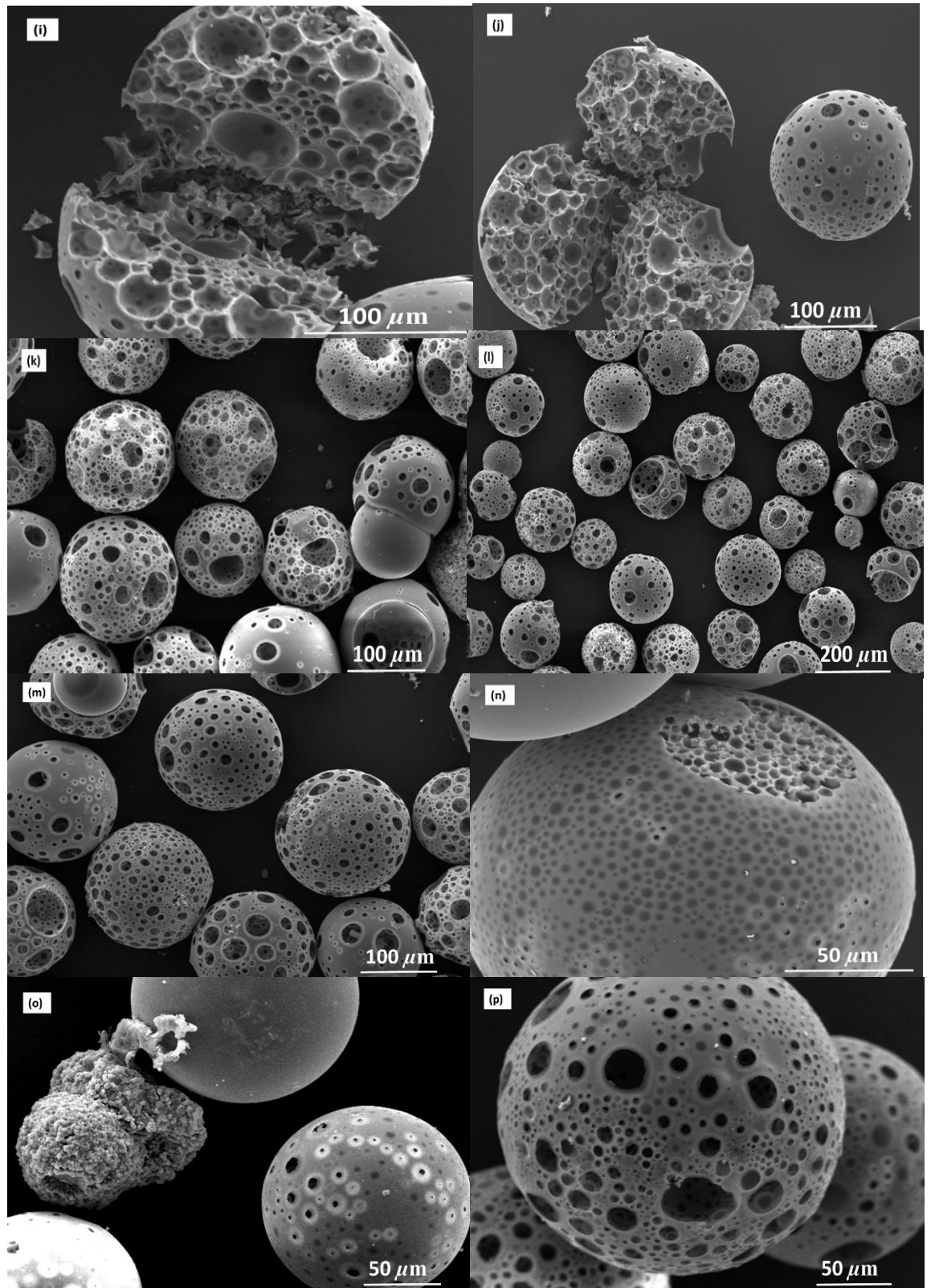
Figure 7.1: SEM images of porous microspheres trialled with the compositions (a) and (b) Sr8, (c) $40\text{P}_2\text{O}_5 \cdot 38\text{CaO} \cdot 19\text{Na}_2\text{O} \cdot 2\text{MgO} \cdot 1\text{TiO}_2$ and (d) $40\text{P}_2\text{O}_5 \cdot 16\text{CaO} \cdot 17.5\text{Na}_2\text{O} \cdot 24\text{MgO} \cdot 2.5\text{TiO}_2$.

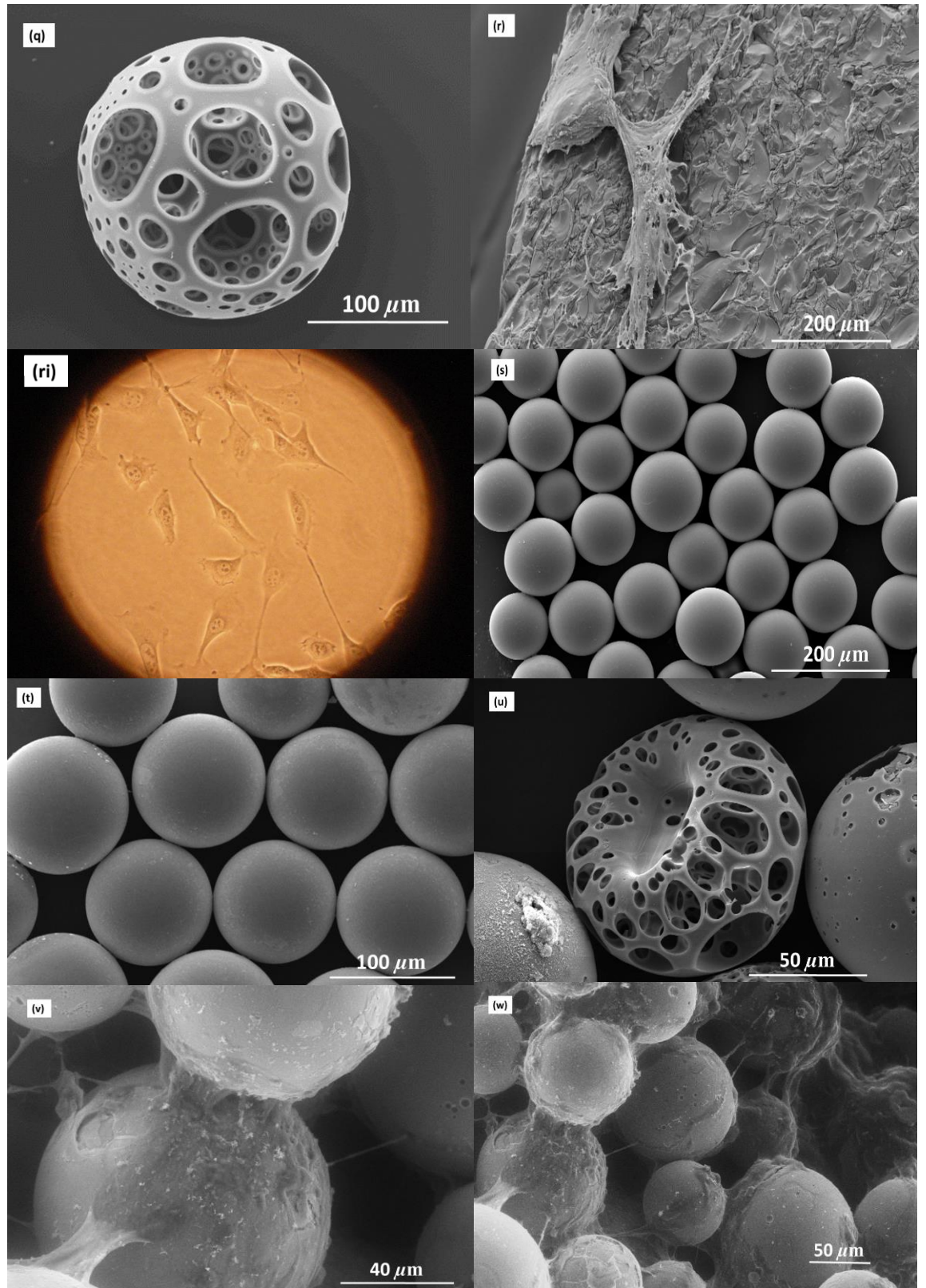
- Additional studies could investigate the effect of combining the porous microspheres with alternate biologics such as stem cells, drugs or hormones. This may involve an additional step for example surface functionalising or coating the microspheres in polymers or hydrogels in order to combine drugs and other therapeutics such as growth factors.
- A strategic investigation into the effects of combining several PBG microspheres of varying compositions on the effect of degradation profiles, ions release and stem cell differentiation would also be of significant interest as this would allow for the release of several therapeutic ions at controlled rates, which could encourage cells down specific lineages. This may be achieved for example by combining faster degrading porous microspheres such as binary composition, with slower degrading compositions such as multicomponent invert glass series.
- Additionally, investigation into varying the microsphere size range (unimodal, bimodal, or multimodal size distributions) could have on packing efficiency and degradation would also be of interest. Furthermore, modelling of flow through the porous microspheres and the interparticulate gaps would aid in understanding interconnectivity and media flow through the porous constructs.

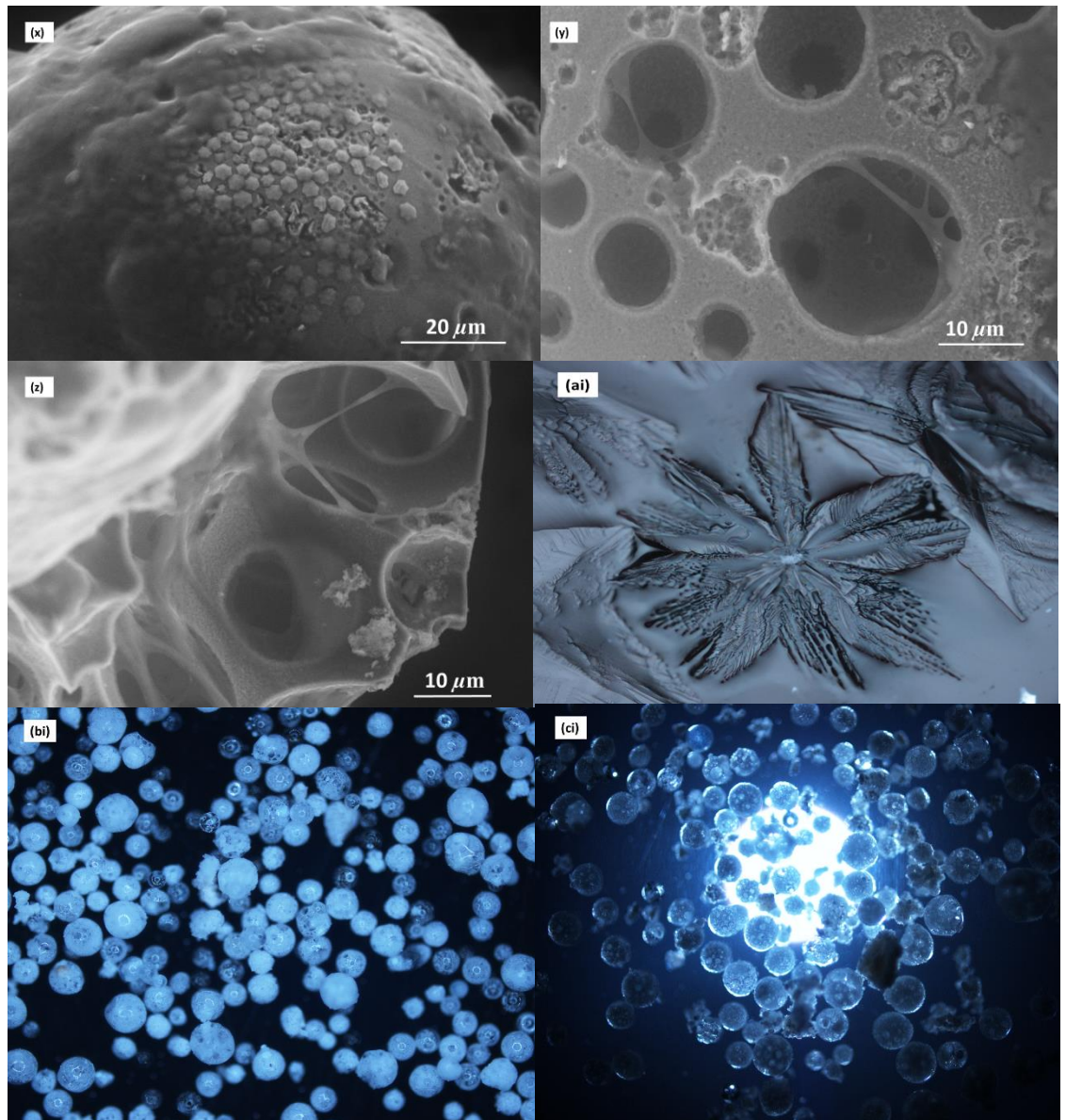
7.3 A collection of images

Below is a collection of my favourite images collated throughout this project.









- (a) Acid washed P40 porous microsphere
- (b) P40 porous microspheres Acid washed for 1min in 1M acetic acid
- (c) Acid washed P40 porous microsphere
- (d) P40 porous microsphere (crushed)
- (e) P40 porous microspheres Acid washed for 0.5 min in 0.25M acetic acid
- (f) P40 porous microspheres Acid washed for 0.5 min in 0.25M acetic acid
- (g) P40 porous microspheres Acid washed for 15 sec in 0.5M acetic acid
- (h) P40 porous microspheres Acid washed for 0.5 min in 0.5M acetic acid
- (i) P40 porous microsphere (crushed)
- (j) P40 porous microspheres Acid washed for 1 min in 0.5M acetic acid
- (k) P40 porous microspheres Acid washed for 1 min in 1M acetic acid
- (l) P40 porous microspheres Acid washed for 20 min in 2.5 M acetic acid
- (m) P40 porous microspheres Acid washed for 10 min in 0.25M acetic acid
- (n) P40 porous microspheres re-spheroidised using cellosize as a porogen binding agent
- (o) P40 porous microsphere and porogen
- (p) P40 porous microsphere
- (q) P40 porous microsphere
- (r) MG63 cells cultured on P40 disc at day 14
- (ri) MG63 cells culture on tissue culture plastic at day 1
- (s) P40 microspheres degraded in ultra pure water at day 1
- (t) P40 microspheres degraded in ultra pure water at day 7
- (u) P40 porous microspheres degraded in ultra pure water at day 7
- (v) eSEM image of P40 microspheres culture with human mesenchymal stem cells
- (w) eSEM image of P40 microspheres culture with human mesenchymal stem cells
- (x) eSEM image of P30 porous microspheres culture with human mesenchymal stem cells
- (y) eSEM image of P30 porous microspheres culture with human mesenchymal stem cells
- (z) eSEM image of P30 porous microspheres culture with human mesenchymal stem cells
- (ai) Light microscope image of surface crystal on Sr16 disc
- (bi) Light microscope image of P40 porous microspheres
- (ci) Light microscope image of P40 porous microspheres

REFERENCES

1. Society, N.O. *Key Facts & Figures*. [cited 2014 20/05/2014]; Available from: <http://www.nos.org.uk/page.aspx?pid=328>.
2. Ahmed, I., et al., *Phosphate glasses for tissue engineering: Part 1. Processing and characterisation of a ternary-based P(2)O(5)-CaO-Na(2)O glass system*. *Biomaterials*, 2004. **25**(3): p. 491-499.
3. Ahmed, I., et al., *Phosphate glasses for tissue engineering: Part 2. Processing and characterisation of a ternary-based P(2)O(5)-CaO-Na(2)O glass fibre system*. *Biomaterials*, 2004. **25**(3): p. 501-507.
4. Ahmed, I., et al., *Quantification of anion and cation release from a range of ternary phosphate-based glasses with fixed 45 mol% P(2)O(5)*. *Journal of Biomaterials Applications*, 2005. **20**(1): p. 65-80.
5. Hasan, M.S., et al., *Material characterisation and cytocompatibility assessment of quinary phosphate glasses*. *Journal of Materials Science-Materials in Medicine*, 2012. **23**(10): p. 2531-2541.
6. Sharmin, N., et al., *Effect of Boron Addition on the Thermal, Degradation, and Cytocompatibility Properties of Phosphate-Based Glasses*. *Biomed Research International*, 2013. **902427**.
7. Donaldson, L.J., et al., *The epidemiology of fractures in England*. *Journal of Epidemiology and Community Health*, 2008. **62**(2): p. 174-180.
8. Johnell, O. and J.A. Kanis, *An estimate of the worldwide prevalence and disability associated with osteoporotic fractures*. *Osteoporosis International*, 2006. **17**(12): p. 1726-1733.
9. Giannoudis, P.V., H. Dinopoulos, and E. Tsiridis, *Bone substitutes: An update*. *Injury-International Journal of the Care of the Injured*, 2005. **36**: p. 20-27.
10. Sharif, P.S., M. Abdollahi, and B. Larijani, *Current, new and future treatments of osteoporosis*. *Rheumatology International*, 2011. **31**(3): p. 289-300.
11. Hench, L.L. and J.M. Polak, *Third-generation biomedical materials*. *Science*, 2002. **295**(5557): p. 1014-+.
12. Narayan, R.J., *The next generation of biomaterial development PREFACE*. *Philosophical Transactions of the Royal Society a-Mathematical Physical and Engineering Sciences*, 2010. **368**(1917): p. 1831-1837.
13. Toolan, B.C., *Current concepts review: Orthobiologics*. *Foot & Ankle International*, 2006. **27**(7): p. 561-566.
14. Roberts, T.T. and A.J. Rosenbaum, *Bone grafts, bone substitutes and orthobiologics The bridge between basic science and clinical advancements in fracture healing*. *Organogenesis*, 2012. **8**(4): p. 114-124.
15. Gerard J. Tortora, B.H.D., *Principles of Anatomy and Physiology: Organization, Support and Movement, and Control Systems of the Human Body, Twelfth Edition*. Vol. 1. 2009.
16. Olszta, M.J., et al., *Bone structure and formation: A new perspective*. *Materials Science & Engineering R-Reports*, 2007. **58**(3-5): p. 77-116.
17. Little, N., B. Rogers, and M. Flannery, *Bone formation, remodelling and healing*. *Surgery (Medicine Publishing)*, 2011. **29**(4): p. 141-145.
18. Kanis, J.A., et al., *Assessment of Fracture Risk and Its Application to Screening for Postmenopausal Osteoporosis - Synopsis of a Who Report*. *Osteoporosis International*, 1994. **4**(6): p. 368-381.
19. Excellence, N.N.I.f.H.a.C. *CG146 Osteoporosis: assessing the risk of fragility fractures*. 2012 [cited 2014 10/06/2014]; Available from: <http://publications.nice.org.uk/osteoporosis-assessing-the-risk-of-fragility-fracture-cg146#close>.

20. Organization, W.H. *WHO scientific group on the assessment of osteoporosis at primary health care level 2004*.
21. Jakob, F., et al., *Bone tissue engineering in osteoporosis*. *Maturitas*, 2013. **75**(2): p. 118-24.
22. Korpi-Steiner, N., D. Milhorn, and C. Hammett-Stabler, *Osteoporosis in men*. *Clin Biochem*, 2014.
23. Langdahl, B.L. and T. Harsløf, *Medical Treatment of Osteoporotic Vertebral Fractures*. *Therapeutic Advances in Musculoskeletal Disease*, 2011. **3**(1): p. 17-29.
24. Kennel, K.A. and M.T. Drake, *Adverse Effects of Bisphosphonates: Implications for Osteoporosis Management*. *Mayo Clinic Proceedings*, 2009. **84**(7): p. 632-638.
25. Drake, M.T., B.L. Clarke, and S. Khosla, *Bisphosphonates: Mechanism of action and role in clinical practice*. *Mayo Clinic Proceedings*, 2008. **83**(9): p. 1032-1045.
26. Hansdottir, H., *Raloxifene for older women: a review of the literature*. *Clinical Interventions in Aging*, 2008. **3**(1): p. 45-50.
27. McClung, M., *Role of RANKL inhibition in osteoporosis*. *Arthritis Research & Therapy*, 2007. **9**.
28. Boivin, G., A. Doublier, and D. Farlay, *Strontium ranelate - a promising therapeutic principle in osteoporosis*. *Journal of Trace Elements in Medicine and Biology*, 2012. **26**(2-3): p. 153-156.
29. Sunyecz, J.A., *The use of calcium and vitamin D in the management of osteoporosis*. *Ther Clin Risk Manag*, 2008. **4**(4): p. 827-36.
30. Zanchetta, J.R., et al., *Effects of teriparatide [recombinant human parathyroid hormone (1-34)] on cortical bone in postmenopausal women with osteoporosis*. *Journal of Bone and Mineral Research*, 2003. **18**(3): p. 539-543.
31. Jiang, Y.B., et al., *Recombinant human parathyroid hormone (1-34) [Teriparatide] improves both cortical and cancellous bone structure*. *Journal of Bone and Mineral Research*, 2003. **18**(11): p. 1932-1941.
32. Shelby, J.E., *Introduction to Glass Science and Technology 1997*, UK: The Royal Society of Chemistry.
33. Rao, K.J., *Structural Chemistry of Glasses*. 2002: Elsevier.
34. Pickup, D.M., et al., *The structure of phosphate glass biomaterials from neutron diffraction and P-31 nuclear magnetic resonance data*. *Journal of Physics-Condensed Matter*, 2007. **19**(41): p. 415116.
35. Burnie, J., et al., *Controlled release glasses (C.R.G.) for biomedical uses*. *Biomaterials*, 1981. **2**(4): p. 244-246.
36. Liu, X., M.N. Rahaman, and D.E. Day, *In Vitro Degradation and Conversion of Melt-Derived Microfibrous Borate (13-93B3) Bioactive Glass Doped with Metal Ions*. *Journal of the American Ceramic Society*, 2014. **97**(11): p. 3501-3509.
37. Bitar, M., et al., *Soluble phosphate glasses: in vitro studies using human cells of hard and soft tissue origin*. *Biomaterials*, 2004. **25**(12): p. 2283-2292.
38. Mourino, V., J.P. Cattalini, and A.R. Boccaccini, *Metallic ions as therapeutic agents in tissue engineering scaffolds: an overview of their biological applications and strategies for new developments*. *Journal of the Royal Society Interface*, 2012. **9**(68): p. 401-419.
39. Hoppe, A., V. Mourino, and A.R. Boccaccini, *Therapeutic inorganic ions in bioactive glasses to enhance bone formation and beyond*. *Biomaterials Science*, 2013. **1**(3): p. 254-256.

40. Franks, K., et al., *The effect of MgO on the solubility behavior and cell proliferation in a quaternary soluble phosphate based glass system*. Journal of Materials Science-Materials in Medicine, 2002. **13**(6): p. 549-556.
41. Ahmed, I., et al., *Cytocompatibility and effect of increasing MgO content in a range of quaternary invert phosphate-based glasses*. J Biomater Appl, 2010. **24**(6): p. 555-75.
42. Abou Neel, E.A., et al., *Effect of iron on the surface, degradation and ion release properties of phosphate-based glass fibres*. Acta Biomaterialia, 2005. **1**(5): p. 553-563.
43. Ahmed, I., et al., *Processing, characterisation and biocompatibility of iron-phosphate glass fibres for tissue engineering*. Biomaterials, 2004. **25**(16): p. 3223-3232.
44. Abou Neel, E.A., et al., *Characterisation of antibacterial copper releasing degradable phosphate glass fibres*. Biomaterials, 2005. **26**(15): p. 2247-2254.
45. Stahli, C., M. James-Bhasin, and S.N. Nazhat, *Three-dimensional endothelial cell morphogenesis under controlled ion release from copper-doped phosphate glass*. Journal of Controlled Release, 2015. **200**: p. 222-232.
46. Ahmed, I., et al., *Antimicrobial effect of silver-doped phosphate-based glasses*. Journal of Biomedical Materials Research Part A, 2006. **79A**(3): p. 618-626.
47. Lee, I.H., et al., *Development, characterisation and biocompatibility testing of a cobalt-containing titanium phosphate-based glass for engineering of vascularized hard tissues*. Materials Science & Engineering C-Materials for Biological Applications, 2013. **33**(4): p. 2104-2112.
48. Brow, R.K., *Review: the structure of simple phosphate glasses*. Journal of Non-Crystalline Solids, 2000. **263**(1-4): p. 1-28.
49. Knowles, J.C., *Phosphate based glasses for biomedical applications*. Journal of Materials Chemistry, 2003. **13**(10): p. 2395-2401.
50. Lippmaa, E., et al., *Structural studies of silicates by solid-state high-resolution silicon-29 NMR*. Journal of the American Chemical Society, 1980. **102**(15): p. 4889-4893.
51. Hoppe, U., et al., *The P-O bond lengths in vitreous P2O5 probed by neutron diffraction with high real-space resolution*. Journal of Physics-Condensed Matter, 1998. **10**(2): p. 261-270.
52. Suzuya, K., et al., *Structure of vitreous P2O5 and alkali phosphate glasses*. Journal of Non-Crystalline Solids, 1998. **232**: p. 650-657.
53. Dohler, F., et al., *P-31 NMR characterisation of phosphate fragments during dissolution of calcium sodium phosphate glasses*. Journal of Materials Chemistry B, 2015. **3**(6): p. 1125-1134.
54. Ainsworth, R.I., J.K. Christie, and N.H. de Leeuw, *On the structure of biomedical silver-doped phosphate-based glasses from molecular dynamics simulations*. Physical Chemistry Chemical Physics, 2014. **16**(39): p. 21135-21143.
55. Kirkpatrick, R.J. and R.K. Brow, *Nuclear-Magnetic-Resonance Investigation of the Structures of Phosphate and Phosphate-Containing Glasses - a Review*. Solid State Nuclear Magnetic Resonance, 1995. **5**(1): p. 9-21.
56. A.C. Hannon, i.M.A.E., *Modern Glass Characterization*, ed. M. Affatigato. 2015, United States of America: Wiley.
57. Kiani, A., et al., *Titanium-containing bioactive phosphate glasses*. Philosophical Transactions of the Royal Society a-Mathematical Physical and Engineering Sciences, 2012. **370**(1963): p. 1352-1375.
58. Jones, J.R. and A.G. Clare, *Bio-Glasses: An Introduction*. 2012, Chichester: Wiley.

59. Marie, P.J., et al., *Mechanisms of action and therapeutic potential of strontium in bone*. *Calcified Tissue International*, 2001. **69**(3): p. 121-129.
60. Bonnelye, E., et al., *Dual effect of strontium ranelate: Stimulation of osteoblast differentiation and inhibition of osteoclast formation and resorption in vitro*. *Bone*, 2008. **42**(1): p. 129-138.
61. Dahl, S.G., et al., *Incorporation and distribution of strontium in bone*. *Bone*, 2001. **28**(4): p. 446-453.
62. Fredholm, Y.C., et al., *Influence of strontium for calcium substitution in bioactive glasses on degradation, ion release and apatite formation*. *Journal of the Royal Society Interface*, 2012. **9**(70): p. 880-889.
63. O'Donnell, M.D., et al., *Materials characterisation and cytotoxic assessment of strontium-substituted bioactive glasses for bone regeneration*. *Journal of Materials Chemistry*, 2010. **20**(40): p. 8934-8941.
64. Abou Neel, E.A., et al., *Structure and properties of strontium-doped phosphate-based glasses*. *Journal of the Royal Society Interface*, 2009. **6**(34): p. 435-446.
65. Gorustovich, A., et al., *Osteoconductivity of strontium-doped bioactive glass particles*. *Bone*, 2007. **41**(6): p. S4-S4.
66. Gentleman, E., et al., *The effects of strontium-substituted bioactive glasses on osteoblasts and osteoclasts in vitro*. *Biomaterials*, 2010. **31**(14): p. 3949-3956.
67. Fujikura, K., et al., *Influence of strontium substitution on structure and crystallisation of Bioglass (R) 45S5*. *Journal of Materials Chemistry*, 2012. **22**(15): p. 7395-7402.
68. Martin, R.A., et al., *An examination of the calcium and strontium site distribution in bioactive glasses through isomorphic neutron diffraction, X-ray diffraction, EXAFS and multinuclear solid state NMR*. *Journal of Materials Chemistry*, 2012. **22**(41): p. 22212-22223.
69. *Public Health Service Agency for Toxic Substances and Disease Registry, Toxicological Profile for Strontium. Department of Health and Human Services. 2004 28/09/16]; Available from: <https://www.atsdr.cdc.gov/toxprofiles/tp159.pdf>.*
70. Price, C.T., J.R. Langford, and F.A. Liporace, *Essential Nutrients for Bone Health and a Review of their Availability in the Average North American Diet*. *Open Orthop J*, 2012. **6**: p. 143-9.
71. Cabrera, W.E., et al., *Strontium and bone*. *Journal of Bone and Mineral Research*, 1999. **14**(5): p. 661-668.
72. Querido, W., A.L. Rossi, and M. Farina, *The effects of strontium on bone mineral: A review on current knowledge and microanalytical approaches*. *Micron*, 2016. **80**: p. 122-134.
73. Al Qaysi, M., et al., *Strontium- and calcium-containing, titanium-stabilised phosphate-based glasses with prolonged degradation for orthopaedic tissue engineering*. *J Biomater Appl*, 2015. **30**(3): p. 300-10.
74. Lee, S., et al., *Dissolution behavior and cell compatibility of alkali-free MgO-CaO-SrO-TiO₂-P₂O₅ glasses for biomedical applications*. *Biomedical Glasses*, 2015. **1**(1): p. 151-158.
75. Aina, V., et al., *Sr-containing hydroxyapatite: morphologies of HA crystals and bioactivity on osteoblast cells*. *Materials Science & Engineering C-Materials for Biological Applications*, 2013. **33**(3): p. 1132-1142.
76. Lin, K.L., et al., *Strontium substituted hydroxyapatite porous microspheres: Surfactant-free hydrothermal synthesis, enhanced biological response and sustained drug release*. *Chemical Engineering Journal*, 2013. **222**: p. 49-59.

77. Ni, G.X., et al., *The effect of strontium incorporation into hydroxyapatites on their physical and biological properties*. Journal of Biomedical Materials Research Part B-Applied Biomaterials, 2012. **100B**(2): p. 562-568.
78. Capuccini, C., et al., *Interaction of Sr-doped hydroxyapatite nanocrystals with osteoclast and osteoblast-like cells*. Journal of Biomedical Materials Research Part A, 2009. **89A**(3): p. 594-600.
79. Boanini, E., et al., *Osteopenic bone cell response to strontium-substituted hydroxyapatite*. Journal of Materials Science-Materials in Medicine, 2011. **22**(9): p. 2079-2088.
80. Pouria, A., et al., *Physicochemical Properties and Cellular Responses of Strontium-Doped Gypsum Biomaterials*. Bioinorganic Chemistry and Applications, 2012.
81. Lakhkar, N., et al., *Titanium and Strontium-doped Phosphate Glasses as Vehicles for Strontium Ion Delivery to Cells*. Journal of Biomaterials Applications, 2011. **25**(8): p. 877-893.
82. Walter, G., et al., *The structure of CaO–Na₂O–MgO–P₂O₅ invert glass*. Journal of Non-Crystalline Solids, 2001. **296**(3): p. 212-223.
83. Kasuga, T. and Y. Abe, *Calcium phosphate invert glasses with soda and titania*. Journal of Non-Crystalline Solids, 1999. **243**(1): p. 70-74.
84. Vogel, W., *Glass Chemistry*. 1994, Berlin: Springer Verlag.
85. Brauer, D.S., et al., *Effect of degradation rates of resorbable phosphate invert glasses on in vitro osteoblast proliferation*. Journal of Biomedical Materials Research Part A, 2006. **77A**(2): p. 213-219.
86. Brauer, D.S., et al., *Effect of TiO₂ addition on structure, solubility and crystallisation of phosphate invert glasses for biomedical applications*. Journal of Non-Crystalline Solids, 2010. **356**(44-49): p. 2626-2633.
87. Walter, G., et al., *The structure of CaO–Na₂O–MgO–P₂O₅ invert glass*. Journal of Non-Crystalline Solids, 2001. **296**(3): p. 212-223.
88. Walter, G., et al., *Structural study of magnesium polyphosphate glasses*. Journal of Non-Crystalline Solids, 2003. **320**(1-3): p. 210-222.
89. Kasuga, T., et al., *Apatite formation on calcium phosphate invert glasses in simulated body fluid*. Journal of the American Ceramic Society, 2001. **84**(2): p. 450-452.
90. Lee, S., A. Obata, and T. Kasuga, *Ion release from SrO–CaO–TiO₂–P₂O₅ glasses in Tris buffer solution*. Journal of the Ceramic Society of Japan, 2009. **117**(1369): p. 935-938.
91. Suzuya, K., et al., *The structure of magnesium phosphate glasses*. Journal of Physics and Chemistry of Solids, 1999. **60**(8-9): p. 1457-1460.
92. Fayon, F., et al., *³¹P NMR study of magnesium phosphate glasses*. Journal of Non-Crystalline Solids, 2001. **283**(1-3): p. 88-94.
93. Lee, S., et al., *Structure and dissolution behavior of MgO–P₂O₅–TiO₂/Nb₂O₅ (Mg/P ≥ 1) invert glasses*. Journal of the Ceramic Society of Japan, 2015. **123**(1442): p. 942-948.
94. Segawa, H., et al., *Properties and structures of TiO₂–ZnO–P₂O₅ glasses*. Journal of the Ceramic Society of Japan, 2010. **118**(1376): p. 278-282.
95. Brauer, D.S., et al., *Effect of degradation rates of resorbable phosphate invert glasses on in vitro osteoblast proliferation*. Journal of Biomedical Materials Research Part A, 2006. **77A**(2): p. 213-219.
96. Abou Neel, E.A. and J.C. Knowles, *Physical and biocompatibility studies of novel titanium dioxide doped phosphate-based glasses for bone tissue engineering applications*. Journal of Materials Science-Materials in Medicine, 2008. **19**(1): p. 377-386.

97. Rajendran, V., et al., *Physicochemical studies of phosphate based P2O5-Na2O-CaO-TiO2 glasses for biomedical applications*. Journal of Non-Crystalline Solids, 2007. **353**(1): p. 77-84.
98. Vitale-Brovarone, C., et al., *Novel phosphate glasses with different amounts of TiO2 for biomedical applications Dissolution tests and proof of concept of fibre drawing*. Materials Science & Engineering C-Materials for Biological Applications, 2011. **31**(2): p. 434-442.
99. Choi, S.W., et al., *Biodegradable porous beads and their potential applications in regenerative medicine*. Journal of Materials Chemistry, 2012. **22**(23): p. 11442-11451.
100. Cai, Y.P., et al., *Porous microsphere and its applications*. International Journal of Nanomedicine, 2013. **8**: p. 1111-1120.
101. Freiberg, S. and X. Zhu, *Polymer microspheres for controlled drug release*. International Journal of Pharmaceutics, 2004. **282**(1-2): p. 1-18.
102. Wu, C. and H. Zreiqat, *Porous bioactive diopside (CaMgSi2O6) ceramic microspheres for drug delivery*. Acta Biomaterialia, 2010. **6**(3): p. 820-829.
103. Lakhkar, N.J., et al., *Titanium phosphate glass microspheres for bone tissue engineering*. Acta Biomaterialia, 2012. **8**(11): p. 4181-4190.
104. Sene, F.F., J.R. Martinelli, and E. Okuno, *Synthesis and characterization of phosphate glass microspheres for radiotherapy applications*. Journal of Non-Crystalline Solids, 2008. **354**(42-44): p. 4887-4893.
105. Bohner, M., et al., *Synthesis of spherical calcium phosphate particles for dental and orthopedic applications*. Biomatter, 2013. **3**(2).
106. Kim, K. and D. Pack, *Microspheres for Drug Delivery*, in *BioMEMS and Biomedical Nanotechnology*, M. Ferrari, A. Lee, and L.J. Lee, Editors. 2006, Springer US. p. 19-50.
107. Fu, H.L., M.N. Rahaman, and D.E. Day, *Effect of Process Variables on the Microstructure of Hollow Hydroxyapatite Microspheres Prepared by a Glass Conversion Method*. Journal of the American Ceramic Society, 2010. **93**(10): p. 3116-3123.
108. Huang, W.H., et al., *Strength of hollow hydroxyapatite microspheres prepared by a glass conversion process*. Journal of Materials Science-Materials in Medicine, 2009. **20**(1): p. 123-129.
109. Todea, M., et al., *XPS analysis of aluminosilicate microspheres bioactivity tested in vitro*. Applied Surface Science, 2013. **270**: p. 777-783.
110. Conzone, S.D., et al., *In vitro and in vivo dissolution behavior of a dysprosium lithium borate glass designed for the radiation synovectomy treatment of rheumatoid arthritis*. Journal of Biomedical Materials Research, 2002. **60**(2): p. 260-268.
111. Conzone, S.D., et al., *Biodegradable radiation delivery system utilizing glass microspheres and ethylenediaminetetraacetate chelation therapy*. Journal of Biomedical Materials Research Part A, 2004. **70A**(2): p. 256-264.
112. Conzone, S.D. and D.E. Day, *Preparation and properties of porous microspheres made from borate glass*. Journal of Biomedical Materials Research Part A, 2009. **88A**(2): p. 531-542.
113. Wang, Q., et al., *Preparation of hollow hydroxyapatite microspheres*. Journal of Materials Science-Materials in Medicine, 2006. **17**(7): p. 641-646.
114. Wang, Q., W.H. Huang, and D.P. Wang, *Preparation of hollow porous HAP microspheres as drug delivery vehicles*. Journal of Wuhan University of Technology-Materials Science Edition, 2007. **22**(1): p. 174-177.
115. Hench, L.L., *The story of Bioglass (R)*. Journal of Materials Science-Materials in Medicine, 2006. **17**(11): p. 967-978.

116. Jones, J.R., *Review of bioactive glass: From Hench to hybrids*. Acta Biomaterialia, 2013. **9**(1): p. 4457-4486.
117. Rahaman, M.N., et al., *Bioactive glass in tissue engineering*. Acta Biomaterialia, 2011. **7**(6): p. 2355-2373.
118. Fu, H.L., et al., *Long-term conversion of 45S5 bioactive glass-ceramic microspheres in aqueous phosphate solution*. Journal of Materials Science-Materials in Medicine, 2012. **23**(5): p. 1181-1191.
119. Martinelli, J.R., et al., *Synthesis and characterization of glass-ceramic microspheres for thermotherapy*. Journal of Non-Crystalline Solids, 2010. **356**(44-49): p. 2683-2688.
120. Bortot, M.B., S. Prastalo, and M. Prado, *Production and Characterization of Glass Microspheres for Hepatic Cancer Treatment*. 11th International Congress on Metallurgy & Materials Sam/Conamet 2011, 2012. **1**: p. 351-358.
121. Liu, H., et al., *Preparation of Porous Hollow SiO₂ Spheres by a Modified Stober Process Using MF Microspheres as Templates*. Journal of Cluster Science, 2012. **23**(2): p. 273-285.
122. Kawashita, M., et al., *Preparation of antibacterial silver-doped silica glass microspheres*. Journal of Biomedical Materials Research Part A, 2003. **66A**(2): p. 266-274.
123. Masuda, N., M. Kawashita, and T. Kokubo, *Antibacterial activity of silver-doped silica glass microspheres prepared by a sol-gel method*. Journal of Biomedical Materials Research Part B-Applied Biomaterials, 2007. **83B**(1): p. 114-120.
124. Sharmin, N., et al., *Effect of boron oxide addition on the viscosity-temperature behaviour and structure of phosphate-based glasses*. Journal of Biomedical Materials Research Part B: Applied Biomaterials, 2016.
125. Zhu, C., *Scale-up Manufacture and Characterisation of Resorbable Phosphate Based Glass Fibre for Textile Production*, in Faculty of Engineering 2016, University of Nottingham: UK.
126. Novajra, G., et al., *Phosphate glass fibre scaffolds: Tailoring of the properties and enhancement of the bioactivity through mesoporous glass particles*. Materials Science & Engineering C-Materials for Biological Applications, 2016. **67**: p. 570-580.
127. Guedes, J.C., et al., *TiO₂-doped phosphate glass microcarriers: A stable bioactive substrate for expansion of adherent mammalian cells*. Journal of Biomaterials Applications, 2013. **28**(1): p. 3-11.
128. Lakhkar, N.J., et al., *Titanium phosphate glass microcarriers induce enhanced osteogenic cell proliferation and human mesenchymal stem cell protein expression*. Journal of Tissue Engineering, 2015. **6**.
129. Sene, F.F., J.R. Martinelli, and E. Okuno, *Synthesis and characterization of phosphate glass microspheres for radiotherapy applications*. Journal of Non-Crystalline Solids, 2008. **354**(42-44): p. 4887-4893.
130. Rouquerol, J., et al., *Recommendations for the characterization of porous solids (Technical Report)*. Pure and Applied Chemistry, 1994. **66**(8): p. 1739-1758.
131. Krämer, F., *Solubility of Gases in Glass Melts*, in *Properties of Glass-Forming Melts*. 2005, CRC Press.
132. Simao, L., et al., *Permeability of porous ceramic based on calcium carbonate as pore generating agent*. Ceramics International, 2015. **41**(3): p. 4782-4788.
133. Cheng, D.L., et al., *Superficially porous poly(lactic-co-glycolic acid)/calcium carbonate microsphere developed by spontaneous pore-forming method for bone repair*. Rsc Advances, 2013. **3**(19): p. 6871-6878.

134. Wojdyr, M., *Fityk: a general-purpose peak fitting program*. Journal of Applied Crystallography, 2010. **43**: p. 1126-1128.
135. Carlile, B.T.M.W.a.C.J., *Experimental Neutron Scattering 2009*, United States: Oxford University Press.
136. Hannon, A.C., *Results on disordered materials from the General Materials diffractometer, GEM, at ISIS*. Nuclear Instruments & Methods in Physics Research Section a-Accelerators Spectrometers Detectors and Associated Equipment, 2005. **551**(1): p. 88-107.
137. Williams, W.G., et al., *GEM - General Materials Diffractometer at ISIS*. Physica B-Condensed Matter, 1997. **241**: p. 234-236.
138. Hannon, A.C., *Neutron Diffraction Techniques for Structural Studies of Glasses*. Modern Glass Characterization, 2015: p. 158-240.
139. Soper, A.K., *GudrunN and GudrunX: Programs for Correcting Raw Neutron and X-ray Diffraction Data to Differential Scattering Cross Section*. 2011, Rutherford Appleton Laboratory Technical Report.
140. Hannon, A.C., Howells, W.S., Soper, A.K., *Atlas - a Suite of Programs for the Analysis of Time-of-Flight Neutron-Diffraction Data from Liquid and Amorphous Samples*. IOP Conf. Ser., 1990. **107**(107): p. 193-211.
141. Placzek, G., *The Scattering of Neutrons by Systems of Heavy Nuclei*. Physical Review, 1952. **86**(3): p. 377-388.
142. Lorch, E., *Neutron diffraction by germania, silica and radiation-damaged silica glasses*. Journal of Physics C: Solid State Physics, 1969. **2**(2): p. 229-237.
143. Rigby, S.P. and P.I. Chigada, *MF-DFT and Experimental Investigations of the Origins of Hysteresis in Mercury Porosimetry of Silica Materials*. Langmuir, 2010. **26**(1): p. 241-248.
144. Rouquerol, J., et al., *The characterization of macroporous solids: An overview of the methodology*. Microporous and Mesoporous Materials, 2012. **154**: p. 2-6.
145. Otaru, A.J. and A.R. Kennedy, *The permeability of virtual macroporous structures generated by sphere packing models: Comparison with analytical models*. Scripta Materialia, 2016. **124**: p. 30-33.
146. Schindelin, J., et al., *Fiji: an open-source platform for biological-image analysis*. Nature Methods, 2012. **9**(7): p. 676-682.
147. Morikawa, H., et al., *Effects of magnesium for calcium substitution in P2O5-CaO-TiO2 glasses*. Journal of Non-Crystalline Solids, 2013. **380**: p. 53-59.
148. Ahmed, I., et al., *Comparison of phosphate-based glasses in the range 50P(2)O(5)-(50-x)CaO-xNa(2)O prepared using different precursors*. Glass Technology-European Journal of Glass Science and Technology Part A, 2008. **49**(2): p. 63-72.
149. Shannon, R.D., *Revised Effective Ionic Radii and Systematic Studies of Interatomic Distances in Halides and Chalcogenides*. Acta Cryst., 1976. **A32**: p. 751-767.
150. Lakhkar, N.J., et al., *Strontium oxide doped quaternary glasses: effect on structure, degradation and cytocompatibility*. Journal of Materials Science-Materials in Medicine, 2009. **20**(6): p. 1339-1346.
151. Brauer, D.S., R.M. Wilson, and T. Kasuga, *Multicomponent phosphate invert glasses with improved processing*. Journal of Non-Crystalline Solids, 2012. **358**(14): p. 1720-1723.
152. Dietzel, A., *Die Kationenfeldstärken und ihre Beziehungen zu Entglasung Vorgängen, zur Verbindungsbildung und zu den Schmelzpunkten von Silikaten*. Z. Elektrochem, 1942. **48**: p. 9-23.

153. Parsons, A.J., et al., *Neutron scattering and ab initio molecular dynamics study of cross-linking in biomedical phosphate glasses*. Journal of Physics-Condensed Matter, 2010. **22**(48): p. 485403.
154. Massera, J., et al., *Thermal properties and surface reactivity in simulated body fluid of new strontium ion-containing phosphate glasses*. J Mater Sci Mater Med, 2013. **24**(6): p. 1407-16.
155. Christie, J.K., R.I. Ainsworth, and N.H. de Leeuw, *Investigating structural features which control the dissolution of bioactive phosphate glasses: Beyond the network connectivity*. Journal of Non-Crystalline Solids, 2016. **432 Part A**: p. 31-34.
156. Christie, J.K., et al., *Nanoscale Chains Control the Solubility of Phosphate Glasses for Biomedical Applications*. Journal of Physical Chemistry B, 2013. **117**(36): p. 10652-10657.
157. Caverzasio, J., *Strontium ranelate promotes osteoblastic cell replication through at least two different mechanisms*. Bone, 2008. **42**(6): p. 1131-1136.
158. Fonseca, J.E. and M.L. Brandi, *Mechanism of action of strontium ranelate: what are the facts?* Clinical Cases in Mineral and Bone Metabolism, 2010. **7**(1): p. 17-18.
159. Brennan, T.C., et al., *Osteoblasts play key roles in the mechanisms of action of strontium ranelate*. British Journal of Pharmacology, 2009. **157**(7): p. 1291-1300.
160. Caverzasio, J. and C. Thouverey, *Activation of FGF Receptors is a new Mechanism by which Strontium Ranelate Induces Osteoblastic Cell Growth*. Cellular Physiology and Biochemistry, 2011. **27**(3-4): p. 243-250.
161. Boanini, E., et al., *Combined effect of strontium and zoledronate on hydroxyapatite structure and bone cell responses*. Biomaterials, 2014. **35**(21): p. 5619-5626.
162. Tian, A., et al., *Osteoblast Response to Titanium Surfaces Coated with Strontium Ranelate-Loaded Chitosan Film*. International Journal of Oral & Maxillofacial Implants, 2014. **29**(6): p. 1446-1453.
163. Lian, J.B. and G.S. Stein, *Concepts of Osteoblast Growth and Differentiation - Basis for Modulation of Bone Cell-Development and Tissue Formation*. Critical Reviews in Oral Biology & Medicine, 1992. **3**(3): p. 269-305.
164. Andrews, N.A., *Strontium ranelate: A new tune, or just more heavy metal?* IBMS BoneKEy, 2007. **4**(7): p. 186-190.
165. Wornham, D.P., et al., *Strontium potently inhibits mineralisation in bone-forming primary rat osteoblast cultures and reduces numbers of osteoclasts in mouse marrow cultures*. Osteoporosis International, 2014. **25**(10): p. 2477-2484.
166. Mattila, P.K. and P. Lappalainen, *Filopodia: molecular architecture and cellular functions*. Nature Reviews Molecular Cell Biology, 2008. **9**(6): p. 446-454.
167. Assender, H., V. Bliznyuk, and K. Porfyrakis, *How surface topography relates to materials properties*. Science, 2002. **297**(5583): p. 973-976.
168. Yang, J.Y., et al., *Quantitative analysis of osteoblast-like cells (MG63) morphology on nanogrooved substrata with various groove and ridge dimensions*. Journal of Biomedical Materials Research Part A, 2009. **90A**(3): p. 629-640.
169. Curtis, A. and C. Wilkinson, *Topographical control of cells*. Biomaterials, 1997. **18**(24): p. 1573-1583.
170. Navarro, M., M.P. Ginebra, and J.A. Planell, *Cellular response to calcium phosphate glasses with controlled solubility*. Journal of Biomedical Materials Research Part A, 2003. **67A**(3): p. 1009-1015.

171. Skelton, K.L., et al., *Effect of ternary phosphate-based glass compositions on osteoblast and osteoblast-like proliferation, differentiation and death in vitro*. Acta Biomaterialia, 2007. **3**(4): p. 563-572.
172. Schumacher, M., et al., *Strontium substitution in apatitic CaP cements effectively attenuates osteoclastic resorption but does not inhibit osteoclastogenesis*. Acta Biomaterialia, 2016. **37**: p. 184-194.
173. Stenbeck, G., *Formation and function of the ruffled border in osteoclasts*. Seminars in Cell & Developmental Biology, 2002. **13**(4): p. 285-292.
174. Peng, S.L., et al., *The cross-talk between osteoclasts and osteoblasts in response to strontium treatment: Involvement of osteoprotegerin*. Bone, 2011. **49**(6): p. 1290-1298.
175. Martin, R.A., et al., *A structural investigation of the alkali metal site distribution within bioactive glass using neutron diffraction and multinuclear solid state NMR*. Physical Chemistry Chemical Physics, 2012. **14**(35): p. 12105-12113.
176. Hoppe, U., et al., *Variation in P-O bonding in phosphate glasses - A neutron diffraction study*. Zeitschrift Fur Naturforschung Section a-a Journal of Physical Sciences, 2000. **55**(3-4): p. 369-380.
177. Al-Hasni, B.M., G. Mountjoy, and E. Barney, *A complete study of amorphous iron phosphate structure*. Journal of Non-Crystalline Solids, 2013. **380**: p. 141-152.
178. Smith, J.M., et al., *Structural study of Al₂O₃-Na₂O-CaO-P₂O₅ bioactive glasses as a function of aluminium content*. Journal of Chemical Physics, 2013. **138**(3): p. 034501.
179. Moss, R.M., et al., *Structural characteristics of antibacterial bioresorbable phosphate glass*. Advanced Functional Materials, 2008. **18**(4): p. 634-639.
180. Moss, R.M., et al., *The effect of zinc and titanium on the structure of calcium-sodium phosphate based glass*. Journal of Non-Crystalline Solids, 2010. **356**(25-27): p. 1319-1324.
181. Wetherall, K.M., et al., *The structure of calcium metaphosphate glass obtained from x-ray and neutron diffraction and reverse Monte Carlo modelling*. Journal of Physics-Condensed Matter, 2009. **21**(3).
182. Pickup, D., R. Moss, and R. Newport, *NXFit: a program for simultaneously fitting X-ray and neutron diffraction pair-distribution functions to provide optimized structural parameters*. Journal of Applied Crystallography, 2014. **47**: p. 1790-1796.
183. Shih, P.Y., J.Y. Ding, and S.Y. Lee, *31P MAS-NMR and FTIR analyses on the structure of CuO-containing sodium poly- and meta-phosphate glasses*. Materials Chemistry and Physics, 2003. **80**(2): p. 391-396.
184. Ma, L.N., *Dissolution behavior of phosphate glasses*, in Faculty of the Graduate School of the. 2014, Missouri university of science and technology.
185. Jones, A.R., et al., *23Na, 29Si, and 13C MAS NMR Investigation of Glass-Forming Reactions between Na₂CO₃ and SiO₂*. J. Phys. Chem. B, 2005. **109**(49): p. 23154-23161.
186. Brow, R.K., R.J. Kirkpatrick, and G.L. Turner, *The short range structure of sodium phosphate glasses I. MAS NMR studies*. Journal of Non-Crystalline Solids, 1990. **116**(1): p. 39-45.
187. Tagg, S.L., R.E. Youngman, and J.W. Zwanziger, *The Structure of Sodium Tellurite Glasses - Sodium-Cation Environments from Na-23 Nmr*. J. Phys. Chem., 1995. **99**(14): p. 5111-5116.
188. Omrani, R.O., et al., *Structural and thermochemical properties of sodium magnesium phosphate glasses*. Journal of Alloys and Compounds, 2015. **632**: p. 766-771.

189. Moustafa, Y.M. and K. El-Egili, *Infrared spectra of sodium phosphate glasses*. Journal of Non-Crystalline Solids, 1998. **240**(1-3): p. 144-153.
190. Wright, A.C., *Longer range order in single component network glasses?* Physics and Chemistry of Glasses-European Journal of Glass Science and Technology Part B, 2008. **49**(3): p. 103-117.
191. Christie, J.K., S.N. Thraskin, and S.R. Elliott, *Positional disorder in lattices: a model for the structural order responsible for the first sharp diffraction peak in glasses*. Journal of Physics-Condensed Matter, 2004. **16**(44): p. S5109-S5120.
192. Christie, J.K., S.N. Taraskin, and S.R. Elliott, *Structural characteristics of positionally disordered lattices: Relation to the first sharp diffraction peak in glasses*. Physical Review B, 2004. **70**(13).
193. Pickup, D.M., et al., *The structure of phosphate glass biomaterials from neutron diffraction and P-31 nuclear magnetic resonance data*. Journal of Physics-Condensed Matter, 2007. **19**(41).
194. Grimley, D.I., A.C. Wright, and R.N. Sinclair, *Neutron scattering from vitreous silica IV. Time-of-flight diffraction*. Journal of Non-Crystalline Solids, 1990. **119**(1): p. 49-64.
195. Hoppe, U., et al., *Neutron and X-ray diffraction study on the structure of ultraphosphate glasses*. Zeitschrift Fur Naturforschung Section a-a Journal of Physical Sciences, 1997. **52**(3): p. 259-269.
196. W. Matz, D.S., E.A. Goremychkin, *The Structure of Alkaline Earth Metaphosphate Glasses Investigated by Neutron Diffraction*. Journal of Non-Crystalline Solids, 1988. **101**: p. 80-89.
197. Matsubara, E., et al., *Structural Study of Binary Phosphate-Glasses with Mgo, Zno, and Cao by X-Ray-Diffraction*. Journal of Non-Crystalline Solids, 1988. **103**(1): p. 117-124.
198. U. Hoppe, G.W.a.D.S., Silikattechnik, 1990. **41**: p. 227-230.
199. Hoppe, U., D. Stachel, and D. Beyer, *The Oxygen Coordination of Metal-Ions in Phosphate and Silicate-Glasses Studied by a Combination of X-Ray and Neutron-Diffraction*. Physica Scripta, 1995. **T57**: p. 122-126.
200. Hoppe, U., et al., *Combined neutron and X-ray scattering study of phosphate glasses*. Journal of Non-Crystalline Solids, 2001. **293**: p. 158-168.
201. Lindberg, A.G.N.a.K.B., *The Crystal Structure of Magnesium Tetrametaphosphate, Mg₂P₄O₁₂*. Acta Chem. Scand. A, 1975. **29**: p. 1-6.
202. Kohara, S., et al., *Glass formation at the limit of insufficient network formers*. Science, 2004. **303**(5664): p. 1649-1652.
203. Brese, N.E. and M. O'keeffe, *Bond-Valence Parameters for Solids*. Acta Cryst, B, 1991. **47**: p. 192-197.
204. Rothammel, W., H. Burzlaff, H. and R. Specht, *Structure of calcium metaphosphate Ca(PO₃)₂*. Acta Crystallogr. Sect. C-Cryst. Struct. Commun., 1989. **45**: p. 551-553.
205. Graia, M., Driss, A., and Jouini, T., *Polyphosphates de strontium Sr (P O₃)₂ formes beta et gamma*. Acta Crystallogr. Sect. C-Cryst. Struct. Commun., 1999. **55**: p. 1395-1398.
206. U. Hoppe, et al., Phosphorus Res. Bull, 1999. **10**: p. 546-551.
207. McAdam, A., Jost, K.H., and Beagley, B, *Refinement of the structure of sodium Kurrol salt (NaPO₃)_x, type A*. Acta Crystallogr. Sect. B-Struct. Sci., 1968. **24**: p. 1621-1622.
208. Karakassides, M.A., A. Saranti, and I. Koutselas, *Preparation and structural study of binary phosphate glasses with high calcium and/or magnesium content*. Journal of Non-Crystalline Solids, 2004. **347**(1-3): p. 69-79.

209. Poole, K.E. and J.E. Compston, *Bisphosphonates in the treatment of osteoporosis*. British Medical Journal, 2012. **344**.
210. Lee, S., A. Obata, and T. Kasuga, *Structure of CaO-SrO-TiO₂-P₂O₅ Glasses and Their Ion-releasing Abilities in Tris Buffer Solution*. Thermec 2009 Supplement, 2010. **89-91**: p. 342.
211. Kasuga, T., et al., *Calcium phosphate invert glasses and glass-ceramics with apatite-forming ability*. Bioceramics 15, 2003. **240-2**: p. 265-268.
212. Hashimoto, T., H. Nasu, and K. Kamiya, *Ti³⁺-free multicomponent titanophosphate glasses as ecologically sustainable optical glasses*. Journal of the American Ceramic Society, 2006. **89**(8): p. 2521-2527.
213. Devi, A.V.G., V. Rajendran, and N. Rajendran, *Structure, solubility and bioactivity in TiO₂-doped phosphate-based bioglasses and glass-ceramics*. Materials Chemistry and Physics, 2010. **124**(1): p. 312-318.
214. Kiani, A., et al., *Structural characterization and physical properties of P₂O₅-CaO-Na₂O-TiO₂ glasses by Fourier transform infrared, Raman and solid-state magic angle spinning nuclear magnetic resonance spectroscopies*. Acta Biomaterialia, 2012. **8**(1): p. 333-340.
215. Abou Neel, E.A., W. Chrzanowski, and J.C. Knowles, *Effect of increasing titanium dioxide content on bulk and surface properties of phosphate-based glasses*. Acta Biomaterialia, 2008. **4**(3): p. 523-534.
216. Abou Neel, E.A., et al., *Doping of a high calcium oxide metaphosphate glass with titanium dioxide*. Journal of Non-Crystalline Solids, 2009. **355**(16-17): p. 991-1000.
217. Monem, A.S., et al., *In vivo behavior of bioactive phosphate glass-ceramics from the system P₂O₅-Na₂O-CaO containing TiO₂*. Journal of Materials Science: Materials in Medicine, 2008. **19**(3): p. 1097-1108.
218. Brow, R.K., et al., *Spectroscopic studies of the structure of titanophosphate and calcium titanophosphate glasses*. Physics and Chemistry of Glasses, 1997. **38**(6): p. 300-306.
219. Nocun, M., *Structural studies of phosphate glasses with high ionic conductivity*. Journal of Non-Crystalline Solids, 2004. **333**(1): p. 90-94.
220. Aderibigbe, B., I. Aderibigbe, and P. Popoola, *Design and Biological Evaluation of Delivery Systems Containing Bisphosphonates*. Pharmaceutics, 2016. **9**(1).
221. Russell, R.G.G., et al., *Mechanisms of action of bisphosphonates: similarities and differences and their potential influence on clinical efficacy*. Osteoporosis International, 2008. **19**(6): p. 733-759.
222. Russell, R.G.G., *Determinants of structure-function relationships among bisphosphonates*. Bone, 2007. **40**(5): p. S21-S25.
223. Russell, R.G.G., et al., *The influence of pyrophosphate, condensed phosphates, phosphonates and other phosphate compounds on the dissolution of hydroxyapatite in vitro and on bone resorption induced by parathyroid hormone in tissue culture and in thyroparathyroidectomised rats*. Calcified Tissue Research, 1970. **6**(1): p. 183-196.
224. Kiani, A., et al., *Physical properties and MAS-NMR studies of titanium phosphate-based glasses*. Materials Chemistry and Physics, 2010. **120**(1): p. 68-74.
225. Shaharuddin, S.I.S., et al., *Investigation on the thermal properties, density and degradation of quaternary iron and titanium phosphate based glasses*. 2nd International Manufacturing Engineering Conference and 3rd Asia-Pacific Conference on Manufacturing Systems (Imec-Apcoms 2015), 2016. **114**.

226. Al Qaysi, M., et al., *Strontium- and calcium-containing, titanium-stabilised phosphate-based glasses with prolonged degradation for orthopaedic tissue engineering*. Journal of Biomaterials Applications, 2015. **30**(3): p. 300-310.
227. Vogel, J., P. Wange, and P. Hartmann, *Effect of composition changes on the structure and properties of phosphate glasses in the pyrophosphate region*. Glastechnische Berichte-Glass Science and Technology, 1997. **70**(1): p. 23-27.
228. Lee, S., Obata, A., and Kasua, T., *Ion Releasing Abilities of Phosphate Invert Glasses Containing MgO, CaO or SrO in Tris Buffer Solution*. Bioceramics Development and Applications, 2010. **1**: p. D110148.
229. Watts, S.J., et al., *Influence of magnesia on the structure and properties of bioactive glasses*. Journal of Non-Crystalline Solids, 2010. **356**(9-10): p. 517-524.
230. Murphy, W.L., T.C. McDevitt, and A.J. Engler, *Materials as stem cell regulators*. Nature Materials, 2014. **13**(6): p. 547-557.
231. Kallmes, D.F., et al., *Vertebroplasty in the mid- and upper thoracic spine*. American Journal of Neuroradiology, 2002. **23**(7): p. 1117-1120.
232. Hossain, M.M., Y. Yao, and T. Watanabe, *A numerical study of plasma-particle energy exchange dynamics in induction thermal plasmas for glassification*. Materials science and technology-association for iron and steel technology-, 2007. **3**.
233. Klouzek, J., et al., *Determination of gas properties in glass melts*. Ceramics-Silikaty, 2008. **52**(2): p. 66-71.
234. Zhang, Y., et al., *Biocompatibility of porous spherical calcium carbonate microparticles on hela cells*. World Journal of Nano Science and Engineering, 2012. **2**(01): p. 25.
235. Blinkova, E.V. and E.I. Eliseev, *Dissolution of calcium carbonate in aqueous solutions of acetic acid*. Russian Journal of Applied Chemistry, 2005. **78**(7): p. 1064-1066.
236. Shanmugam, G., *Basic Mech Engg, 3E Tnc Syllb*. 2000: McGraw-Hill Education (India) Pvt Limited.
237. Xu, R., *Particle Characterization: Light Scattering Methods*. 2006: Springer Netherlands.
238. S. Lowell, J.E.S., Martin A. Thomas, Matthias Thommes, *Characterization of porous solids and powders: Surface area, pore size and density*. 2004.
239. M.P. Gómez-Tena, J.G., J. Toledo, and C.M. E. Zumaquero, *Relationship between the specific surface area parameters determined using different analytical techniques*, in *Qualicer 14*. 2014.
240. Giesche, H., *Mercury porosimetry: A general (practical) overview*. Particle & Particle Systems Characterization, 2006. **23**(1): p. 9-19.
241. Webb, P.A., *An introduction to the physical characterization of materials by mercury intrusion porosimetry with emphasis on reduction and presentation of experimental data*. 2001: Micromeritics Instrument Corp.
242. Bunker, B.C., G.W. Arnold, and J.A. Wilder, *Phosphate-Glass Dissolution in Aqueous-Solutions*. Journal of Non-Crystalline Solids, 1984. **64**(3): p. 291-316.
243. Gao, H.S., T.N. Tan, and D.H. Wang, *Dissolution mechanism and release kinetics of phosphate controlled release glasses in aqueous medium*. Journal of Controlled Release, 2004. **96**(1): p. 29-36.
244. Delahaye, F., et al., *Acid dissolution of sodium-calcium metaphosphate glasses*. Journal of Non-Crystalline Solids, 1998. **242**(1): p. 25-32.
245. Cozien-Cazuc, S., et al., *Real-time dissolution of P40Na20Ca16Mg24 phosphate glass fibers*. Journal of Non-Crystalline Solids, 2009. **355**(50-51): p. 2514-2521.

246. Haque, P., et al., *Degradation properties and microstructural analysis of 40P2O5–24MgO–16CaO–16Na2O–4Fe2O3 phosphate glass fibres*. Journal of Non-Crystalline Solids, 2013. **375**: p. 99-109.
247. Ma, L.N., *Dissolution behaviour of phosphate glasses* in *Materials Science and Engineering* 2014, Missouri University of Science and Technology: US.
248. Legeros, R.Z., et al., *Biphasic calcium phosphate bioceramics: preparation, properties and applications*. Journal of Materials Science-Materials in Medicine, 2003. **14**(3): p. 201-209.
249. Raynaud, S., E. Champion, and D. Bernache-Assollant, *Calcium phosphate apatites with variable Ca/P atomic ratio II. Calcination and sintering*. Biomaterials, 2002. **23**(4): p. 1073-1080.
250. Pirhonen, E., et al., *Manufacturing, mechanical characterization, and in vitro performance of bioactive glass 13–93 fibers*. Journal of Biomedical Materials Research Part B: Applied Biomaterials, 2006. **77B**(2): p. 227-233.
251. Radin, S., et al., *In vitro transformation of bioactive glass granules into Ca-P shells*. Journal of Biomedical Materials Research, 2000. **49**(2): p. 264-272.
252. Liu, C.S., C.W. Chen, and P. Ducheyne, *In vitro surface reaction layer formation and dissolution of calcium phosphate cement-bioactive glass composites*. Biomedical Materials, 2008. **3**(3).
253. Sharmin, N., et al., *Effect of boron oxide addition on fibre drawing, mechanical properties and dissolution behaviour of phosphate-based glass fibres with fixed 40, 45 and 50 mol% P(2)O(5)*. Journal of Biomaterials Applications, 2014. **29**(5): p. 639-653.
254. Ahmed, I., et al., *Core/Clad Phosphate Glass Fibres Containing Iron and/or Titanium*, in *Biomedical glasses*. 2015.